TIME- AND DEPTH-VARYING CROSS-SHORE CURRENTS: NUMERICAL MODELING AND LABORATORY MEASUREMENTS

by

JANE McKEE SMITH
AND
IB A. SVENDSEN

RESEARCH REPORT NO. CACR-96-04
APRIL, 1996

CENTER FOR APPLIED COASTAL RESEARCH
OCEAN ENGINEERING LABORATORY
UNIVERSITY OF DELAWARE
NEWARK, DE 19716

TABLE OF CONTENTS

LIST OF FIGURES iv
LIST OF TABLES ix
ABSTRACT x
ACKNOWLEDGEMENT xi

Chapter

1 INTRODUCTION 1

1.1 Background 3
1.2 Thesis Content 7

2 DERIVATION OF GOVERNING EQUATIONS 9

2.1 Depth-Integrated Equations of Continuity and Momentum 9

2.1.1 Continuity equation 9
2.1.2 Momentum equations 12

2.2 Depth-Varying *x*-Momentum Equation 18

3 DEPTH-INTEGRATED MODEL FOR INFRAGRAVITY WAVES . 22

3.1 Numerical Solution 24

3.1.1 Predictor-Corrector model 24
3.1.2 Lax-Wendroff model 31

3.2 Input/Output Parameters 33

3.2.1 Input Parameters 34
3.2.2 Output Parameters 36

3.3 Example 36

4 PROFILE MODEL FOR INFRAGRAVITY WAVES 41

4.1 Eigenfunction Expansion 42

4.1.1 Solution satisfying boundary conditions in z 43
4.1.2 Homogeneous solution 43
4.1.3 Particular solution 47
4.1.4 Full solution for velocity profile 49
4.1.5 f independent of z 49

4.2 Input/Output Parameters 52

4.2.1 Input Parameters 52
4.2.2 Output Parameters 55

4.3 Example 55

5 MODEL APPLICATION WITH ANALYTICAL SURF BEAT FORCING 62

5.1 Schäffer and Svendsen Surf Beat Model 62

5.1.1 Surf beat model description 63
5.1.2 Model input and output 69
5.1.3 Depth-integrated model surf beat results 72
5.1.4 Profile model surf beat results 95

5.2 Putrevu and Svendsen Periodic Profile Model 99

5.2.1 Putrevu-Svendsen model description 99
5.2.2 Application of Putrevu-Svendsen and eigenfunction profile models to surf beat 103

6 SUPERTANK LABORATORY DATA COLLECTION PROJECT . 116

6.1 Experiment Overview 117
6.2 Hydrodynamic Data Collection 121

6.2.1 Instrument description 121
6.2.2 Instrument location 122
6.2.3 Instrument characteristics 124
6.2.4 Experiment procedures 126
6.2.5 Calibration and zero reference 128

6.2.6 Sampling 129

6.3 Data Analysis 129

6.3.1 Analysis procedure 130
6.3.2 Long-wave motion in two SUPERTANK runs 133
6.3.3 Short- and long-wave reflection 143
6.3.4 Wave groups 147

7 MODELING TIME- AND DEPTH-VARYING CURRENTS AT SUPERTANK 154

7.1 SUPERTANK Runs A0509A and A2007B 154
7.2 Depth-Integrated Model 157

7.2.1 Model input and set up 157
7.2.2 Model results 162

7.3 Profile Model 175

7.3.1 Model input and set up 175
7.3.2 Model results 176
7.3.3 Profile parameters 188

8 SUMMARY AND CONCLUSIONS 194

8.1 Research Results 194
8.2 Future Work 200

REFERENCES 202

LIST OF FIGURES

2.1 Definition Sketch 10

3.1 Predictor-Corrector results with surf beat forcing. Oscillations are due to a disjoint numerical solution 30

3.2 Predictor-Corrector finite-difference molecule 32

3.3 Lax-Wendroff finite-difference molecule 33

3.4 Example standing wave results at cell 11 39

3.5 Example standing wave results at cell 51 40

4.1 Predictor-Corrector depth-integrated results for plane beach with steady forcing discussed in Section 4.3 59

4.2 Eigenfunction velocity profiles for a plane beach with steady forcing discussed in Section 4.3 . . . . 60, 61

5.1 Sketch of bottom topography and short-wave modulation for $\kappa = 0$ and 1 in region I, II, and III for Schäffer-Svendsen surf beat model 67

5.2 Case 1: nondimensional surf beat envelope for Schäffer-Svendsen model, $\pm|\xi_1/(\delta a_\infty)|$ -- solid line, $\xi_1/(\delta a_\infty)$ at $t = 0$ and $-T/4$ -- dashed and chain-dot lines 75

5.3 Case 1 snap shots of water surface elevation from depth-integrated and analytic Schäffer-Svendsen models 76

5.4 Case 1 time series of water surface from depth-integrated and analytic Schäffer-Svendsen models for selected locations 79

5.5 Case 1 snap shots of depth-integrated velocity from depth-integrated and analytic Schäffer-Svendsen models 80

5.6 Case 1 time series of depth-integrated velocity from depth-integrated and analytic Schäffer-Svendsen models for selected locations 81

5.7 Case 2: nondimensional surf beat envelope for Schaffer-Svendsen model, $\pm|\xi_1/(\delta a_\infty)|$ -- solid line, $\xi_1/(\delta a_\infty)$ at $t = 0$ and $-T/4$ -- dashed and chain-dot lines 83

5.8 Case 2 snap shots of water surface elevation from depth-integrated and analytic Schäffer-Svendsen models 84

5.9 Case 2 time series of water surface from depth-integrated and analytic Schäffer-Svendsen models for selected locations 86

5.10 Case 2 snap shots of depth-integrated velocity from depth-integrated and analytic Schäffer-Svendsen models 87

5.11 Case 2 time series of depth-integrated velocity from depth-integrated and analytic Schäffer-Svendsen models for selected locations 88

5.12 Case 3: nondimensional surf beat envelope for Schäffer-Svendsen model, $\pm|\xi_1/(\delta a_\infty)|$ -- solid line, $\xi_1/(\delta a_\infty)$ at $t = 0$ and $-T/4$ -- dashed and chain-dot lines 90

5.13 Case 3 snap shorts of water surface elevation from depth-integrated and analytic Schäffer-Svendsen models 91

5.14 Case 3 time series of water surface from depth-integrated and analytic Schäffer-Svendsen models for selected locations 92

5.15 Case 3 snap shots of depth-integrated velocity from depth-integrated and analytic Schäffer-Svendsen models 93

5.16 Case 3 time series of depth-integrated velocity from depth-integrated and analytic Schäffer-Svendsen models for selected locations 94

5.17 Case 2 surf beat velocity profiles from eigenfunction profile model at locations outside and through the surf zone 96

5.18 Case 3 surf beat velocity profiles from eigenfunction profile model at locations outside and through the surf zone 97

5.19 Case 2: velocity profile parameters, top: solid line -- f_a/g, dashed line -- $P_1 = \sqrt{2}\ T_s\ \beta/(\rho g)$, bottom: solid line -- BA, dashed line -- $f_{cw}\ u_o/(2\ \nu_t\ \beta)$, chain dot line -- Δ/π 105

5.20 Relative strength of surface stress to depth-uniform surf beat forcing for Case 2 106

5.21 Putrevu-Svendsen time-varying velocity profiles for Case 2 surf beat forcing for locations outside and through the surf zone 108

5.22 Eigenfunction time-varying velocity profiles for Case 2 surf beat forcing for locations outside and through the surf zone 109

5.23 Case 3: velocity profile parameters, top: solid line -- f_a/g, dashed line -- $P_1 = \sqrt{2}\ T_s\ \beta/(\rho g)$, bottom: solid line BA, dashed line -- $f_{cw}\ u_o/(2\ \nu_t\ \beta)$, chain dot line -- Δ/π 112

5.24 Relative strength of surface stress to depth-uniform surf beat forcing for Case 3 113

5.25 Putrevu-Svendsen time-varying velocity profiles for Case 3 surf beat forcing for locations outside and through the surf zone 114

5.26 Eigenfunction time-varying velocity profiles for Case 3 surf beat forcing for locations outside and through the surf zone 115

6.1 View of the OSU wave channel during SUPERTANK 118

6.2 Current meter mounting configuration 125

6.3 Period response of the low-pass filter for cutoff period 6 sec 132

6.4 Summary of wave transformation and mean cross-shore currents for Run A2007B 135

6.5 Summary of wave transformation and mean cross-shore currents for Run A0509A 136

6.6 Time series of raw and low-pass water surface elevation for Gauge 3, Run A2007B 137

6.7 Wave spectra for the raw, low-pass, and high-pass water surface elevation for Gauge 3, Run A2007B 138

6.8 Current meter raw spectrum and time series of the raw and low-pass signal for Channel 30, Run A2007B 140

6.9 High-pass and low-pass significant wave heights for Run A0509A 142

6.10 Total, incident, and reflected low-pass water surface elevation for Run A2007B 146

6.11 High-pass and low-pass wave heights as a function of time 148

6.12 Incident wave energy and low-pass surface elevation offshore, seaward of incipient breaking, and surf zone 149

6.13 Correlation of the incident wave energy and the low-pass surface elevation at a location just seaward of the incipient breaker zone 151

6.14 Time series of incident wave energy, low-pass surface elevation, and low-pass velocity 151

6.15 Correlation of the long-wave surface elevation and the long-wave velocity at a location just seaward of the incipient breaker zone 153

6.16 Correlation of the long-wave surface elevation and the long-wave velocity at a location in the mid surf zone 153

7.1 Bathymetry and current meter positions for SUPERTANK Run A0509A 155

7.2 Bathymetry and current meter positions for SUPERTANK Run A2007B 155

7.3 Infragravity surface elevations for Run A0509A, t = 0-250 sec 163

7.4 Depth-integrated velocities for Run A0509A, t = 0-250 sec 163

7.5 Infragravity surface elevations for Run A0509A, t = 250-500 sec 164

7.6 Depth-integrated velocities for Run A0509A, t = 250-500 sec 164

7.7 Infragravity surface elevations for Run A0509A, t = 500-750 sec 165

7.8 Depth-integrated velocities for Run A0509A, t = 500-750 sec 165

7.9 Infragravity surface elevations for Run A2007B, t = 0-250 sec 166

7.10 Depth-integrated velocities for Run A2007B, t = 0-250 sec 166

7.11 Infragravity surface elevations for Run A2007B, t = 250-500 sec 167

7.12 Depth-integrated velocities for Run A2007B, t = 250-500 sec 167

7.13 Infragravity surface elevations for Run A2007B, t = 500-750 sec 168

7.14 Depth-integrated velocities for Run A2007B, t = 500-750 sec 168

7.15 Velocity profiles at x = 25.6 m for Run A0509A 177

7.16 Velocity profiles at x = 36.6 m for Run A0509A 177

7.17 Velocity profiles at x = 40.2 m for Run A0509A 178

7.18 Velocity profiles at x = 43.9 m for Run A0509A 178

7.19 Velocity profiles at x = 36.6 m for Run A2007B 179

7.20 Velocity profiles at x = 37.2 m for Run A2007B 179

7.21 Velocity profiles at x = 40.2 m for Run A2007B 180

7.22 Velocity profiles at x = 43.9 m for Run A2007B 180

7.23 Calculated profiles for Run A0509A, t = 500-750 sec 181

7.24 Calculated profiles for Run A2007B, t = 500-750 sec 182

7.25 Relative strength of surface stress and depth-uniform forcing, βh, and relative phase of surface stress and depth-uniform forcing for Run A0509A . . . 190

7.26 Relative strength of surface stress and depth-uniform forcing, βh, and relative phase of surface stress and depth-uniform forcing for Run A2007B . . . 191

LIST OF TABLES

3.1 rms error in standing wave model computations 38

4.1 rms error in plane-beach velocity profile computations 58

5.1 Surf beat model input 72

5.2 Lax-Wendroff error for Case 1 78

5.3 Lax-Wendroff error for Case 2 85

5.4 Lax-Wendroff error for Case 3 95

7.1 Wave and grid parameters for Runs A0509A and A2007B 157

7.2 Depth-integrated model means and rms errors for Run A0509A 169

7.3 Depth-integrated model means and rms errors for Run A2007B 170

7.4 Profile model mean values and rms errors for Run A0509A 184

7.5 Profile model mean values and rms errors for Run A2007B 185

ABSTRACT

Time- and depth-varying cross-shore currents forced by gravity and infragravity waves in the nearshore are numerically modeled. Model evaluation is made with analytical solutions and laboratory data.

Cross-shore flow is simulated with two linked models: a depth-integrated model and an eigenfunction solution for velocity distribution over depth. Water surface gradients generated by the depth-integrated model are used to drive the profile model. Both models are time dependent. Two numerical schemes are used for the depth-integrated model, Predictor-Corrector and Lax-Wendroff. The Predictor-Corrector scheme exhibited water surface and velocity oscillations in space when executed with only linear terms. Two disjoint solutions in space were generated.

The depth-integrated and profile models were applied to an analytical, depth-integrated surf beat solution (Schäffer and Svendsen 1988 and Schäffer 1990, 1993). The solution includes both forced infragravity waves propagating toward the shoreline and free infragravity waves released in the breaking process and reflected from shore. Mean radiation stress forcing was added to the model. The depth-integrated model results compared well with the analytical solution. The eigenfunction profile model results were compared to the periodic analytical profile model of Putrevu and Svendsen (1995) for the time-varying portion of the surf beat solution. The results were identical.

Laboratory data to evaluate the depth-integrated and profile models were collected at the SUPERTANK Laboratory Project. Wave and current data were collected in a large-scale wave channel with a sand beach. The models did not represent mean cross-shore currents well due to limitations in the radiation stress calculation. Time-varying flows were represented fairly well.

Characteristics exhibited by the profile model differed outside and inside the surf zone. Outside the surf zone, most vertical variation in the cross-shore current occurs near the water surface, velocities near the surface and bottom are out of phase, and profile variation over depth is fairly symmetric. Inside the surf zone, the mean undertow profile is the dominant feature, time variation of the velocity is fairly constant over depth, and in the inner surf zone, velocity profiles are uniform over depth.

ACKNOWLEDGEMENT

This research was supported by the Army Research Office through University Research Initiative Grant No. DAAL-03-92-G-0116 and the NOAA Office of Sea Grant, Department of Commerce, Award No. NA16RG0162.

Chapter 1

INTRODUCTION

As gravity waves approach a beach, they steepen and break in water depths approximately equal to the wave height. Breaking waves dissipate energy and induce nearshore currents (longshore and cross-shore) and changes in the water level. The *surf zone* is the region from the shoreline to the seaward boundary of wave breaking. This zone is the most dynamic coastal region with sediment transport and bathymetry change driven by breaking waves and wave-induced currents. The surf zone also serves as the interface between humans and the ocean, so surf zone processes greatly impact the human-ocean inter-relationship.

By the year 2000, 45 percent of the U.S. population will live in coastal communities (Senate Coastal Coalition 1995) that are vulnerable to coastal erosion, flooding, and pollution problems. U.S. beaches contribute substantially to the U.S. economy with tourism producing $50 billion in tax revenue, contributing $746 billion to the Gross Domestic Product in 1995, and supporting more than 14 million jobs. Eighty-five percent of all tourism-generated revenue is the U.S. comes from coastal states (Houston 1995a, b). U.S. beaches are the key element protecting these coastal communities and generating tourism dollars. An understanding of nearshore coastal processes is the basis for engineers and scientists to make wise decisions when endeavoring to "solve" problems of shoreline and bathymetry change (erosion/accretion), coastal flooding, and pollutant transport. Engineering tools used in decision making take the form of empirical relationships, physical models, and numerical models. In this thesis, all three types of tools are exploited, although the major emphasis is numerical modeling. Numerical modeling is increasingly the tool of choice due to its flexibility and efficiency.

Although the most dramatic nearshore feature observed by someone on the beach is the breaking gravity waves, the related processes of nearshore circulation and infragravity waves exhibit higher correlation to sediment and pollutant transport. Infragravity waves, oscillations with periods of tens to hundreds of seconds, increase in amplitude near the shoreline, in the region where gravity waves (short waves) have been dissipated. The energy in infragravity frequencies can be substantial, even exceeding energy in short-wave frequencies (Wright et al. 1982, Guza and Thornton 1982).

Nearshore currents are composed of motions at many scales, forced by several processes. Currents are composed of wave-driven currents, tidal currents, wind-driven currents, and gravity and infragravity wave oscillations. This study focuses on the wave-driven and infragravity wave components of nearshore currents. The time- and depth-dependent cross-shore flow is modeled under the forcing of gravity and infragravity waves.

The following section gives background information on nearshore circulation and infragravity wave modeling. Section 1.2 provides an overview of the material covered in the following chapters.

1.1 Background

The study of nearshore circulation was revolutionized by the introduction of the concept of radiation stress. Radiation stress was applied to calculate mean water elevations and currents, undertow, and wave-group forced infragravity waves.

In the early 1960s, Longuet-Higgins and Stewart (1962, 1963, 1964) introduced the concept of *radiation stress*, a stress tensor associated with gravity waves. Gradients in radiation stress, due to non-uniform wave amplitudes, induce currents and changes in water level. Radiation stress forcing has been applied to problems of wave setup and setdown, longshore currents, undertow, and wave-group forced infragravity waves. Radiation stress is an additional term in the momentum equation for the solution of water surface elevation and velocity.

Nearshore circulation is generally modeled with the depth-integrated equations of mass and momentum. The equations are short-wave averaged, and formulated much like tidal circulation models with additional short-wave forcing. Radiation stress is calculated externally and then imposed as an external force. Generally the models are formulated to be time-dependent, but in practice are used with steady-state forcing. The steady-state limitation stems from the use of steady-state short-wave models that provide the radiation stress forcing. Depth-integrated circulation models provide water-levels and depth-integrated currents over a one- or two-dimensional-horizontal domain.

Nearshore circulation models are used to study longshore current distributions, wave setup, two-dimensional current patterns (including rip currents and cell circulation), and ultimately predict sediment transport and bathymetry change. Examples of nearshore circulation models include steady longshore current models, e.g., Bowen (1969), Longuet-Higgins (1970a, b), Thornton (1970), Thornton and Guza (1986), and Larson and Kraus (1991); and steady and time-dependent two-dimensional-horizontal circulation models, e.g., Noda (1974), Birkemeier and Dalrymple (1975), Keely and Bowen (1977), Ebersole and Dalrymple (1979), Vemulakonda (1984), Wind and Vreugdenhill (1986), and Cialone et al. (1994). Examples of linked wave, current, and sediment transport models are discussed by de Vriend et al. (1993).

Longshore currents are generally relatively constant over depth. Wave setup, the vertical nonuniformity of radiation stress, and mass transport combine to generate a depth-varying cross-shore flow or *undertow*. The mean undertow profile is parabolic with a maximum offshore flow near the bottom and an onshore flow above trough level. Undertow may be relatively strong, generally eight to ten percent of $\sqrt{g\,h}$ near the bottom, where g is gravitation acceleration and h is the water depth. The vertical profile of the undertow is determined as a balance between radiation stress, the pressure gradient from the sloping mean water surface, and vertical mixing. The first quantitative analysis of undertow was given by Dyhr-Nielsen and Sorensen (1970). Solutions for the undertow profile are given by Dally and Dean (1984), Hansen and Svendsen (1984), Stive and Wind (1986), and Svendsen et al. (1987).

The quasi-three-dimensional modeling approach has been used successfully to extract steady undertow and longshore current profiles based on local wave and water level forcing (de Vriend and Stive 1987, Svendsen and Lorenz 1989, Svendsen and Putrevu 1990, Sanchez-Arcilla et al. 1992, and Svendsen and Putrevu 1994). The quasi-3-D approach provides information on current variation through the vertical without the complication of a full 3-D model. The modeling approach has more recently been applied to situations with time-varying forcing. Van Dongeren et al. (1994) calculated the development of undertow and longshore current profiles from zero to steady-state forcing using a quasi-steady approach. Steady-state profiles are solved analytically using the method of Svendsen and Putrevu (1994). A quasi-3-D approach has been used to extract time-varying profiles in large-scale circulation models (e.g., Davies 1987, 1980). Putrevu and Svendsen (1995) develop an analytic solution for time-varying infragravity wave velocity profiles in the surf zone, assuming constant periodicity in all forcing. Time-varying profiles have not been compared to laboratory or field measurements.

Infragravity waves fall into three categories: (a) forced long waves, (b) edge waves, and (c) leaky waves. Forced long waves are generated by gradients in radiation stress found in wave groups causing a lowering of the mean water level under high waves and a raising under low waves (Longuet-Higgins and Stewart 1962). The forced wave travels at the group speed of the short waves, hence is bound to the wave group. Edge waves are freely propagating long waves which reflect from the shoreline and are trapped along the shore by refraction. Long waves may be progressive or standing along the shore. Edge waves travel alongshore with an antinode at the shoreline, and the amplitude decays exponentially offshore. Leaky waves are also freely propagating long waves or standing waves, but they reflect from the shoreline to deep water and are not trapped by the bathymetry. Proposed generation mechanisms for propagating long waves include time-varying break point of groupy waves (Symonds et al. 1982), release of forced waves through wave breaking (Longuet-Higgins and Stewart 1964), and nonlinear wave-wave interactions (Gallagher 1971).

Field studies have clearly identified forced long waves and edge waves in the nearshore (see Huntley et al. 1981 and Oltman-Shay and Hathaway 1989). The relative amount of infragravity energy and incident gravity wave energy is often considered a function of the surf similarity parameter (Holman and Sallenger 1985, Holman 1986), with infragravity energy dominating for low values of the surf similarity parameter (< 1.5). For low surf similarity values, the energy spectrum at incident frequencies is generally saturated (the spectral energy density is independent of the offshore wave height, due to wave breaking), but at infragravity frequencies, the energy density increases linearly with increasing offshore wave height (Guza and Thornton 1982, Mase 1988). This implies that short-wave forcing is a significant source of infragravity wave forcing (Svendsen and Putrevu 1996). Storm conditions with high steepness waves tend to have low-valued surf similarity parameters, so infragravity waves are prevalent in storms. Svendsen and Putrevu (1996) suggest that a substantial amount of infragravity wave generation takes place in the surf zone, based on recent measurements of free infragravity waves in the offshore (e.g., Elgar et al. 1992 and Herbers et al. 1992) and proposed surf zone generation mechanisms.

1.2 Thesis Content

The purpose of this study is to numerically model the time- and depth-varying cross-shore current forced by gravity waves and infragravity waves in the nearshore. The model results are compared to analytic solutions and laboratory measurements.

First, the governing depth-integrated equations of mass and momentum and the depth-dependent momentum equations are derived in Chapter 2. These equations serve as the basis for model development in the following chapters. Chapter 3 describes the formulation of a depth-integrated model, including gravity and infragravity wave forcing. The finite-difference model calculates water surface elevations and depth-integrated currents. Chapter 4 describes the formulation of an eigenfunction solution for calculation of the local velocity profile. The profile model is forced with output from the depth-integrated model.

The depth-integrated and profile models are applied using forcing from the analytical surf beat model of Schäffer and Svendsen (1988) and Schäffer (1990, 1993). The analytical surf beat model provides the offshore long-wave input and the time-varying short-wave forcing required to execute the depth-integrated and profile models. The depth-integrated model is compared to the analytic surf beat solution and errors are evaluated. The profile model, with the surf beat forcing, is compared to the periodic profile model of Putrevu and Svendsen (1995).

Chapter 6 describes data collected during the SUPERTANK Laboratory Data Collection Project. SUPERTANK was a large-scale, nearshore hydrodynamic and beach profile change study conducted at Oregon State University. The chapter describes how the data were collected and analyzed. Sample data are also presented. The SUPERTANK data are applied in Chapter 7 to drive the depth-integrated and profile models and to evaluate model results. Last, Chapter 8 summarizes the study and provides conclusions, limitations, and suggestions for further study.

Chapter 2

DERIVATION OF GOVERNING EQUATIONS

The purpose of this chapter is to derive and discuss the equations that govern the nearshore circulation. The depth-integrated continuity and momentum equations and equation for variation of flow over depth are derived. These equations will be used in Chapters 3 and 4 to develop models for depth-integrated and depth-varying flows, respectively.

2.1 Depth-Integrated Equations of Continuity and Momentum

The equations governing the nearshore flow are the wave-averaged continuity and momentum equations.

2.1.1 Continuity equation

The continuity equation, assuming incompressible flow, is given by

$$\frac{\partial u}{\partial x} + \frac{\partial v}{\partial y} + \frac{\partial w}{\partial z} = 0 \tag{2.1}$$

where u is the cross-shore velocity, v is the longshore velocity, w is the vertical velocity, ρ is the water density, and t is time. The right-handed coordinate system is defined with x in the on-shore direction, y in the longshore direction, and z

vertical, measured from the still-water surface (see Figure 2.1). Integrating Equation 2.1 from the bottom, $z = -h_0$, to the water surface, $z = \zeta$, and using Leibnitz's Theorem gives

$$\begin{aligned}&\frac{\partial}{\partial x}\int_{-h_0}^{\zeta} u\,dz + \frac{\partial}{\partial y}\int_{-h_0}^{\zeta} v\,dz - u_{\zeta}\frac{\partial \zeta}{\partial x} - v_{\zeta}\frac{\partial \zeta}{\partial y} \\ &- u_{-h_0}\frac{\partial h_0}{\partial x} - v_{h_0}\frac{\partial h_0}{\partial y} + w_{\zeta} - w_{-h_0} = 0\end{aligned} \tag{2.2}$$

The subscripts $-h_0$ and ζ denote that the variable is evaluated at these z elevations.

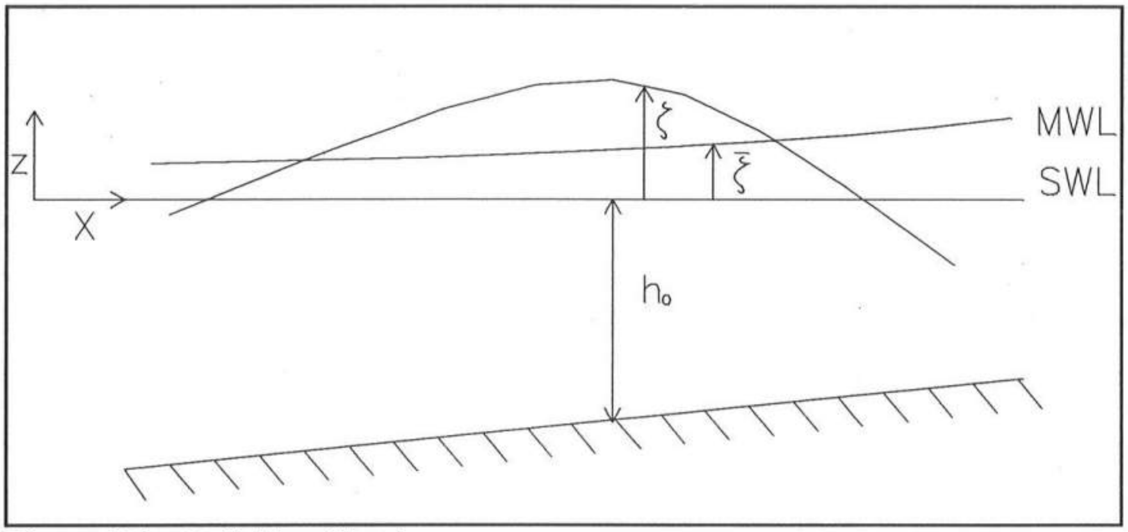

Figure 2.1. Definition Sketch

Next, the kinematic boundary conditions (no flow through the interface) are applied. The kinematic free surface boundary condition is

$$w_{\zeta} = \frac{\partial \zeta}{\partial t} + u_{\zeta}\frac{\partial \zeta}{\partial x} + v_{\zeta}\frac{\partial \zeta}{\partial y} \tag{2.3}$$

The bottom boundary condition, assuming the bottom position does not change with time, is

$$(w_w + W)_{-h_0} = -(u_w + U)_{-h_0}\frac{\partial h_0}{\partial x} - (v_w + V)_{-h_0}\frac{\partial h_0}{\partial y} \tag{2.4}$$

where u_w, v_w, and w_w are short-wave velocities, and U, V, and W are short-wave-averaged velocities. Applying the boundary conditions (Equations 2.3 and 2.4), Equation 2.2 becomes

$$\frac{\partial}{\partial x}\int_{-h_0}^{\zeta} u\,dz + \frac{\partial}{\partial y}\int_{-h_0}^{\zeta} v\,dz + \frac{\partial \zeta}{\partial t} - \left(u'\frac{\partial h_0}{\partial x} + v'\frac{\partial h_0}{\partial y} + w'\right)_{-h0} = 0 \tag{2.5}$$

where u', v', and w' denote turbulent fluctuations.

Velocity is divided into three components: a) short-wave-averaged component (U, V, 0), b) short-wave component (u_w, v_w, w_w), and c) turbulent fluctuation (u', v', w'). Substituting these components into Equation 2.5 and time averaging (over the short-wave period) gives

$$\frac{\partial}{\partial x}\int_{-h_0}^{\overline{\zeta}} U\,dz + \frac{\partial}{\partial y}\int_{-h_0}^{\overline{\zeta}} V\,dz + \frac{\partial \overline{\zeta}}{\partial t} + \overline{\frac{\partial}{\partial x}\int_{\zeta_t}^{\zeta} u_w\,dz} + \overline{\frac{\partial}{dy}\int_{\zeta_t}^{\zeta} v_w\,dz} = 0 \tag{2.6}$$

where ζ_t is the short-wave trough elevation. The overline denotes short-wave-averaged components. The time-averaged short-wave velocities are zero below trough level

$$\overline{u_w} = \overline{v_w} = \overline{w_w} = 0 \qquad \text{below trough level} \tag{2.7}$$

For the region above trough level, the integral of the short-wave velocities u_w and v_w are x and y components of wave-induced mass transport, which will be denoted as Q_{wx} and Q_{wy}, respectively. The first two terms in Equation 2.6 are the volume fluxes below mean water level and are defined as

$$\begin{aligned} \int_{-h_0}^{\overline{\zeta}} U dz &\equiv Q_x - Q_{wx} \\ \int_{-h_0}^{\overline{\zeta}} V dz &\equiv Q_y - Q_{wy} \end{aligned} \tag{2.8}$$

Applying these definitions reduces Equation 2.6 to

$$\frac{\partial Q_x}{\partial x} + \frac{\partial Q_y}{\partial y} + \frac{\partial \overline{\zeta}}{\partial t} = 0 \tag{2.9}$$

2.1.2 Momentum equations

The momentum equations, neglecting viscous stresses, are given by

$$\frac{\partial u}{\partial t} + \frac{\partial u^2}{\partial x} + \frac{\partial uv}{\partial y} + \frac{\partial uw}{\partial z} = -\frac{1}{\rho}\frac{\partial P}{\partial x} \tag{2.10}$$

$$\frac{\partial v}{\partial t} + \frac{\partial uv}{\partial x} + \frac{\partial v^2}{\partial y} + \frac{\partial vw}{\partial z} = -\frac{1}{\rho}\frac{\partial P}{\partial y} \tag{2.11}$$

$$\frac{\partial w}{\partial t} + \frac{\partial uw}{\partial x} + \frac{\partial vw}{\partial y} + \frac{\partial w^2}{\partial z} = -\frac{1}{\rho}\frac{\partial P}{\partial z} - g \tag{2.12}$$

where P is pressure and g is gravitational acceleration. Integrating Equations 2.10-12 over depth and using Leibnitz's Theorem gives

$$\frac{\partial}{\partial t}\int_{-h_0}^{\zeta} u\,dz - \frac{d\zeta}{dt}u_\zeta + \frac{d(-h_0)}{dt}u_{-h_0} + \frac{\partial}{\partial x}\int_{-h_0}^{\zeta}(u^2+\frac{P}{\rho})dz + \frac{\partial}{\partial y}\int_{-h_0}^{\zeta} uv\,dz - \frac{d\zeta}{dx}(u^2+\frac{P}{\rho})_\zeta$$
$$+ \frac{d(-h_0)}{dx}(u^2 + \frac{P}{\rho})_{-h_0} - \frac{d\zeta}{dy}(uv)_\zeta + \frac{d(-h_0)}{dy}(uv)_{-h_0} + (uw)_\zeta - (uw)_{-h_0} = 0 \tag{2.13}$$

$$\frac{\partial}{\partial t}\int_{-h_0}^{\zeta} v\,dz - \frac{d\zeta}{dt}v_\zeta + \frac{d(-h_0)}{dt}v_{-h_0} + \frac{\partial}{\partial y}\int_{-h_0}^{\zeta}(v^2+\frac{P}{\rho})dz + \frac{\partial}{\partial x}\int_{-h_0}^{\zeta} uv\,dz - \frac{d\zeta}{dy}(v^2+\frac{P}{\rho})_\zeta \tag{2.14}$$
$$+ \frac{d(-h_0)}{dy}(v^2 + \frac{P}{\rho})_{-h_0} - \frac{d\zeta}{dx}(uv)_\zeta + \frac{d(-h_0)}{dx}(uv)_{-h_0} + (vw)_\zeta - (vw)_{-h_0} = 0$$

$$\frac{\partial}{\partial t}\int_{-h_0}^{\zeta} w\,dz + \frac{\partial}{\partial x}\int_{-h_0}^{\zeta} uw\,dz + \frac{\partial}{\partial y}\int_{-h_0}^{\zeta} vw\,dz + g(\zeta + h_0) - \frac{P_{-h_0}}{\rho} \tag{2.15}$$
$$+w_\zeta(w_\zeta - \frac{\partial\zeta}{\partial t} - u_\zeta\frac{\partial\zeta}{\partial x} - v_\zeta\frac{\partial\zeta}{\partial y}) - w_{-h_0}(w_{-h_0} + u_{-h_0}\frac{dh_0}{dx} + v_{-h_0}\frac{dh_0}{dy}) = 0$$

Applying the kinematic boundary conditions (Equations 2.3 and 2.4), assuming that bed level is constant in time, simplifies Equations 2.13-15 to

$$\frac{\partial}{\partial t}\int_{-h_0}^{\zeta} u\,dz + \frac{\partial}{\partial x}\int_{-h_0}^{\zeta}(u^2 + \frac{P}{\rho})dz + \frac{\partial}{\partial y}\int_{-h_0}^{\zeta} uv\,dz - \frac{P_{-h_0}}{\rho}\frac{\partial h_0}{\partial x} \tag{2.16}$$
$$- \frac{\partial h_0}{\partial x}(u'^2)_{-h_0} - \frac{\partial h_0}{\partial y}(u'v')_{-h_0} - (u'w')_{-h_0} = 0$$

$$\frac{\partial}{\partial t}\int_{-h_0}^{\zeta} v\,dz + \frac{\partial}{\partial y}\int_{-h_0}^{\zeta}(v^2 + \frac{P}{\rho})dz + \frac{\partial}{\partial x}\int_{-h_0}^{\zeta} uv\,dz - \frac{P_{-h_0}}{\rho}\frac{\partial h_0}{\partial y} \tag{2.17}$$
$$- \frac{\partial h_0}{\partial y}(v'^2)_{-h_0} - \frac{\partial h_0}{\partial x}(v'u')_{-h_0} - (v'w')_{-h_0} = 0$$

$$\frac{\partial}{\partial t}\int_{-h_0}^{\zeta} w\,dz + \frac{\partial}{\partial x}\int_{-h_0}^{\zeta} uw\,dz + \frac{\partial}{\partial y}\int_{-h_0}^{\zeta} vw\,dz + g(\zeta + h_0) - \frac{P_{-h_0}}{\rho} - w_{-h_0}\left(w' + u'\frac{\partial h_0}{\partial x} + v'\frac{\partial h_0}{\partial y}\right)_{-h_0} = 0 \tag{2.18}$$

The last three terms on the left-hand sides of Equation 2.16-18 represent turbulent stresses at the top of the bottom boundary layer. The bottom boundary condition (Equation 2.4) applies only to the wave-averaged and short-wave components of velocity, and thus the turbulent stresses do not cancel out when the boundary condition is applied. The notation τ_{bx}/ρ, τ_{by}/ρ, and τ_{bz}/ρ will be used to represent these bottom stresses, respectively.

Time averaging Equations 2.16-18 results in

$$\frac{\partial}{\partial t}\overline{\int_{-h_0}^{\zeta} u\,dz} + \frac{\partial}{\partial x}\overline{\int_{-h_0}^{\zeta} (u^2 + \frac{P}{\rho})\,dz} + \frac{\partial}{\partial y}\overline{\int_{-h_0}^{\zeta} uv\,dz} = \frac{\overline{P_{-h_0}}}{\rho}\frac{\partial h_0}{\partial x} - \frac{\tau_{bx}}{\rho} \tag{2.19}$$

$$\frac{\partial}{\partial t}\overline{\int_{-h_0}^{\zeta} v\,dz} + \frac{\partial}{\partial y}\overline{\int_{-h_0}^{\zeta} (v^2 + \frac{P}{\rho})\,dz} + \frac{\partial}{\partial x}\overline{\int_{-h_0}^{\zeta} uv\,dz} = \frac{\overline{P_{-h_0}}}{\rho}\frac{\partial (h_0)}{\partial y} - \frac{\tau_{by}}{\rho} \tag{2.20}$$

$$\frac{\partial}{\partial t}\overline{\int_{-h_0}^{\zeta} w\,dz} + \frac{\partial}{\partial x}\overline{\int_{-h_0}^{\zeta} uw\,dz} + \frac{\partial}{\partial y}\overline{\int_{-h_0}^{\zeta} vw\,dz} + g(\overline{\zeta} + h_0) = \frac{\overline{P_{-h_0}}}{\rho} - \frac{\tau_{bz}}{\rho} \tag{2.21}$$

The time average of the vertical velocity is zero, so the first term in Equation 2.21 is zero. Equation 2.21 can be rewritten as

$$\frac{\overline{P_{-h_0}}}{\rho} = g(\overline{\zeta} + h_0) + \frac{\partial}{\partial x}\overline{\int_{-h_0}^{\zeta} uw\,dz} + \frac{\partial}{\partial y}\overline{\int_{-h_0}^{\zeta} vw\,dz} + \frac{\tau_{bz}}{\rho} \tag{2.22}$$

The second and third terms on the right-hand side of Equation 2.22 are zero by linear theory due to the time integration. These terms will be neglected. The last term on the right-hand side of Equation 2.22 is much smaller than the horizontal bottom stresses, τ_{bx} and τ_{by}, in Equations 2.19 and 2.20 and thus will be neglected. Substituting Equation 2.22 into 2.19 yields,

$$\frac{\partial}{\partial t}\overline{\int_{-h_0}^{\zeta} u\,dz} + \frac{\partial}{\partial x}\overline{\int_{-h_0}^{\zeta} (u^2 + \frac{P}{\rho})dz} + \frac{\partial}{\partial y}\overline{\int_{-h_0}^{\zeta} uv\,dz} = g(\overline{\zeta} + h_0)\frac{\partial h_0}{\partial x} - \frac{\tau_{bx}}{\rho} \tag{2.23}$$

Note that

$$g(\overline{\zeta} + h_0)\frac{\partial h_0}{\partial x} = \frac{g}{2}\frac{\partial}{\partial x}(\overline{\zeta} + h_0)^2 - (\overline{\zeta} + h_0)\frac{\partial \overline{\zeta}}{\partial x} \tag{2.24}$$

and Equation 2.23 becomes

$$\frac{\partial}{\partial t}\overline{\int_{-h_0}^{\zeta} u\,dz} + \frac{\partial}{\partial x}\overline{\int_{-h_0}^{\zeta} (u^2 + \frac{P}{\rho})dz} + \frac{\partial}{\partial y}\overline{\int_{-h_0}^{\zeta} uv\,dz} = \frac{g}{2}\frac{\partial}{\partial x}(\overline{\zeta} + h_0)^2 - (\overline{\zeta} + h_0)\frac{\partial \overline{\zeta}}{\partial x} - \frac{\tau_{bx}}{\rho} \tag{2.25}$$

Similarly, Equation 2.20 becomes

$$\frac{\partial}{\partial t}\overline{\int_{-h_0}^{\zeta} v\,dz} + \frac{\partial}{\partial y}\overline{\int_{-h_0}^{\zeta} (v^2 + \frac{P}{\rho})dz} + \frac{\partial}{\partial x}\overline{\int_{-h_0}^{\zeta} uv\,dz} = \frac{g}{2}\frac{\partial}{\partial y}(\overline{\zeta} + h_0)^2 - (\overline{\zeta} + h_0)\frac{\partial \overline{\zeta}}{\partial y} - \frac{\tau_{by}}{\rho} \tag{2.26}$$

The wave-induced radiation stress components are defined as

$$S_{xx} = \overline{\int_{-h_0}^{\zeta} (\rho u_w^{\,2} + P) dz} - \frac{1}{2} \rho g (h_0 + \overline{\zeta})^2 \tag{2.27}$$

$$S_{yx} = \overline{\int_{-h_0}^{\zeta} \rho u_w v_w dz} \tag{2.28}$$

$$S_{yy} = \overline{\int_{-h_0}^{\zeta} (\rho v_w^2 + P) dz} - \frac{1}{2} \rho g (h_0 + \overline{\zeta}) \tag{2.29}$$

Inserting the time-averaged, short-wave, and turbulent velocity components (U, u_w, u', V, v_w, v', w_w, w') into Equations 2.25 and 2.26, using the definitions given by Equations 2.27-2.29, gives

$$\begin{aligned}
&\frac{\partial Q_x}{\partial t} + \frac{\partial}{\partial x}\overline{\int_{-h_0}^{\zeta} U^2 \; dz} + \frac{\partial}{\partial y}\overline{\int_{-h_0}^{\zeta} UV dz} + \frac{\partial}{\partial x}\overline{\int_{\zeta_t}^{\zeta} 2 u_w U dz} + \frac{\partial}{\partial y}\overline{\int_{\zeta_t}^{\zeta} (v_w U + u_w V) dz} \\
&+ g(\overline{\zeta} + h_0)\frac{\partial \overline{\zeta}}{\partial x} + \frac{\partial}{\partial x}\left(\frac{S_{xx}}{\rho} - \overline{\int_{-h_0}^{\zeta} u'u' dz}\right) + \frac{\partial}{\partial y}\left(\frac{S_{yx}}{\rho} - \overline{\int_{-h_0}^{\zeta} u'v' dz}\right) + \frac{\tau_{bx}}{\rho} = 0
\end{aligned} \tag{2.30}$$

$$\begin{aligned}
&\frac{\partial Q_y}{\partial t} + \frac{\partial}{\partial y}\overline{\int_{-h_0}^{\zeta} V^2 \; dz} + \frac{\partial}{\partial x}\overline{\int_{-h_0}^{\zeta} UV dz} + \frac{\partial}{\partial y}\overline{\int_{\zeta_t}^{\zeta} 2 v_w V dz} + \frac{\partial}{\partial x}\overline{\int_{\zeta_t}^{\zeta} (u_w V + v_w U) dz} \\
&+ g(\overline{\zeta} + h_0)\frac{\partial \overline{\zeta}}{\partial y} + \frac{\partial}{\partial y}\left(\frac{S_{yy}}{\rho} - \overline{\int_{-h_0}^{\zeta} v'v' dz}\right) + \frac{\partial}{\partial x}\left(\frac{S_{yx}}{\rho} - \overline{\int_{-h_0}^{\zeta} u'v' dz}\right) + \frac{\tau_{by}}{\rho} = 0
\end{aligned} \tag{2.31}$$

The turbulent shear stresses (Reynolds stresses) will be parameterized by

$$\overline{\int_{-h_0}^{\zeta} u'u'dz} = 2\nu_{xx}\rho(\overline{\zeta} + h_0)\frac{\partial \overline{U}}{\partial x} \tag{2.32}$$

$$\overline{\int_{-h_0}^{\zeta} u'v'dz} = \nu_{xy}\rho(\overline{\zeta} + h_0)\left(\frac{\partial \overline{U}}{\partial y} + \frac{\partial \overline{V}}{\partial x}\right) \tag{2.33}$$

$$\overline{\int_{-h_0}^{\zeta} v'v'dz} = 2\nu_{yy}\rho(\overline{\zeta} + h_0)\frac{\partial \overline{V}}{\partial y} \tag{2.34}$$

where ν is the eddy viscosity, and $\overline{U}$ and $\overline{V}$ are depth-integrated short-wave-averaged velocities. The turbulent normal stresses (Equations 2.32 and 2.34) are typically small and will be neglected. The x and y momentum equations become

$$\begin{gathered}\frac{\partial Q_x}{\partial t} + \frac{\partial}{\partial x}\overline{\int_{-h_0}^{\zeta} U^2\ dz} + \frac{\partial}{\partial y}\overline{\int_{-h_0}^{\zeta} UVdz} + \frac{\partial}{\partial x}\overline{\int_{\eta_t}^{\zeta} 2u_w Udz} + \frac{\partial}{\partial y}\overline{\int_{\eta_t}^{\zeta}(v_w U + u_w V)dz} \\ + g(\overline{\zeta} + h_0)\frac{\partial \overline{\zeta}}{\partial x} + \frac{\partial}{\partial x}\left(\frac{S_{xx}}{\rho}\right) + \frac{\partial}{\partial y}\left(\frac{S_{yx}}{\rho} - \nu_{xy}(\overline{\zeta} + h_0)\left(\frac{\partial \overline{U}}{\partial y} + \frac{\partial \overline{V}}{\partial x}\right)\right) + \tau_{bx} = 0\end{gathered} \tag{2.35}$$

$$\begin{gathered}\frac{\partial Q_y}{\partial t} + \frac{\partial}{\partial y}\overline{\int_{-h_0}^{\eta} V^2\ dz} + \frac{\partial}{\partial x}\overline{\int_{-h_0}^{\eta} UVdz} + \frac{\partial}{\partial y}\overline{\int_{\eta_t}^{\eta} 2v_w Vdz} + \frac{\partial}{\partial x}\overline{\int_{\eta_t}^{\eta}(u_w V + v_w U)dz} \\ + g(\overline{\eta} + h_0)\frac{\partial \overline{\eta}}{\partial y} + \frac{\partial}{\partial y}\left(\frac{S_{yy}}{\rho}\right) + \frac{\partial}{\partial x}\left(\frac{S_{yx}}{\rho} - \nu_{xy}(\overline{\eta}\ h_0)\left(\frac{\partial \overline{U}}{\partial y} + \frac{\partial \overline{V}}{\partial x}\right)\right) + \tau_{by} = 0\end{gathered} \tag{2.36}$$

The bottom stress terms will be parameterized by

$$\tau_{bx} = \rho \frac{f_{cw}}{\pi}(u_o U)_{-h_0} \tag{2.37}$$

$$\tau_{by} = \rho \frac{f_{cw}}{\pi}(v_o V)_{-h_0} \tag{2.38}$$

where f_{cw} is the bottom friction coefficient, and u_o and v_o are the short-wave velocity amplitudes. This formulation is a linearized version of the standard quadratic bottom friction (e.g., Jonsson 1966) which assumes a weak current, i.e., $u_o >> U$ and $v_o >> V$.

2.2 Depth-Varying *x*-Momentum Equation

Returning to Equation 2.10, prior to depth integrating the x-momentum equation, and substituting the three velocity components (short-wave averaged, short wave, and turbulent), gives

$$\begin{aligned}\frac{\partial(U+u_w)}{\partial t} + \frac{\partial(U+u_w)^2}{\partial x} + \frac{\partial[(U+u_w)(V+v_w)]}{\partial y} + \frac{\partial(U+u_w)w_w}{\partial z} \\ = -\frac{1}{\rho}\frac{\partial P}{\partial x} - \frac{\partial(u')^2}{\partial x} - \frac{\partial u'v'}{\partial y} - \frac{\partial u'w'}{\partial z}\end{aligned} \tag{2.39}$$

Integrating the z momentum equation (Equation 2.12) to an arbitrary elevation z, time averaging, and applying the kinematic free surface boundary condition gives

$$\frac{\overline{P}}{\rho} = g(\overline{\zeta} - z) - w_w^{\,2} - w'^2 + \frac{\partial}{\partial x}\overline{\int_z^{\zeta} uw\,dz} + \frac{\partial}{\partial y}\overline{\int_z^{\zeta} vw\,dz} \tag{2.40}$$

The last two terms on the right-hand side of Equation 2.40 are second order and are neglected, as discussed previously. Time averaging Equation 2.39 and substituting the mean pressure from Equation 2.40 into 2.39 yields

$$\begin{aligned}\frac{\partial U}{\partial t} + \frac{\partial U^2}{\partial x} + \frac{\partial UV}{\partial y} + \frac{\partial(\overline{u_w^{\,2}} - \overline{w_w^{\,2}})}{\partial x} + \frac{\partial \overline{u_w v_w}}{\partial y} + \frac{\partial \overline{u_w w_w}}{\partial z} \\ = -g\,\frac{\partial \overline{\zeta}}{\partial x} - \frac{\partial(\overline{u'^2} - \overline{w'^2})}{\partial x} - \frac{\partial \overline{u'v'}}{\partial y} - \frac{\partial \overline{u'w'}}{\partial z}\end{aligned} \tag{2.41}$$

Since the wave motion is periodic, the short-wave average of the short-wave components equal zero (Equation 2.7).

We are considering only the cross-shore flow, so we assume the bottom contours are straight and parallel in the longshore direction. This means that the terms $\partial/\partial y = 0$, and Equation 2.41 reduces to

$$\begin{aligned}\frac{\partial U}{\partial t} + \frac{\partial U^2}{\partial x} + \frac{\partial(\overline{u_w^{\,2}} - \overline{w_w^{\,2}})}{\partial x} + \frac{\partial \overline{u_w w_w}}{\partial z} \\ = -g\,\frac{\partial \overline{\zeta}}{\partial x} - \frac{\partial(\overline{u'^2} - \overline{w'^2})}{\partial x} - \frac{\partial \overline{u'w'}}{\partial z}\end{aligned} \tag{2.42}$$

Stive and Wind (1982) showed that the turbulent apparent normal stress term, $(u'^2 - w'^2)$, is approximately 5% of the wave-induced apparent normal stress term in surf zone. Thus, they concluded that the effects of breaking-induced turbulence are weak. This term will be neglected. The term $u_w w_w$ represents the horizontal shear stress created by the oscillatory wave component and is also typically neglected in nearshore current modeling. See Putrevu and Svendsen (1993) for discussion. The term is identically zero for horizontal-bottom wave theories except in the bottom boundary layer (Battjes et al. 1990).

Next, we introduce a Reynolds stress closure for the turbulent shear stress $u'w'$, where the turbulent shear stress is related directly to the mean flow through the eddy viscosity, ν_t,

$$\overline{u'w'} = -\nu_t \frac{\partial U}{\partial z} \tag{2.43}$$

The eddy viscosity is assumed here to be constant over depth. Applying this closure and neglecting the terms $(u'^2 - w'^2)$ and $u_w w_w$ reduces Equation 2.42 to

$$\frac{\partial U}{\partial t} - \frac{\partial}{\partial z}\left(\nu_t \frac{\partial U}{\partial z}\right) = -g \frac{\partial \bar{\zeta}}{\partial x} - \frac{\partial(\overline{u_w^2} - \overline{w_w^2})}{\partial x} - \frac{\partial U^2}{\partial x} \tag{2.44}$$

The first term in Equation 2.44 represents the time variation in the cross-shore flow. Typically undertow has only been analyzed for steady situations ($\partial U/\partial t = 0$). The purpose of this study is to extend analysis to unsteady flow, where $\partial U/\partial t$ is important. The second term in Equation 2.44 represents the "stiffness" of the water column. The value of the eddy viscosity will determine to what extent surface stresses are transferred through the water column. The terms on the right-hand side of Equation 2.44 will be treated as the driving forces of the cross-shore flow. The first term on the right-hand side is the dominant forcing term. This is the setup term, and it has no vertical structure (constant over depth). The second term on the right-hand side is the wave radiation stress term. This term has a significant vertical variation with a large concentration above the wave trough level and a fairly uniform vertical distribution below trough level. This variation over the vertical, to a large part, drives the undertow. The last term in Equation 2.44 is the momentum flux from the cross-shore current, and it is typically neglected in cross-shore current modeling. Svendsen et al. (1987) showed that this term can be significant, although it is smaller in magnitude than the setup and radiation stress terms. This term would typically be included on the left side of the equation and not as a driving term on the right-hand side. For simplicity, we will be treating it as a known quantity (from the depth-integrated model) that is averaged over depth.

Chapter 3

DEPTH-INTEGRATED MODEL FOR INFRAGRAVITY WAVES

This chapter describes the first of two model components used to calculate the horizontal and vertical variations in the time-varying infragravity wave velocity field. The approach used is quasi-three-dimensional, where the depth-integrated velocity is solved for the domain first, and then, as described in Chapter 4, the horizontal velocity components at several elevations in the vertical are solved locally. The local solution over the vertical is more efficient computationally than a full three-dimensional model. Quasi-three-dimensional models provide information on velocity variation over the vertical with only marginally more computational effort than a depth-integrated model. For the depth-integrated model, this chapter provides discussion of the model assumptions, solution techniques, input and output parameters, and an example application.

The depth-integrated model is based on the equations of continuity and momentum given in Equations 2.9, 2.35, and 2.36. For the present application, additional simplifications have been made to the equations. The first assumption is longshore homogeneity ($\partial/\partial y = 0$). This assumption is made because the model will be applied to data taken in a long, narrow wave channel. The second assumption is that the cross-shore and longshore components of momentum flux ($\partial U^2/\partial x$ and $\partial V^2/\partial y$) are small. In the SUPERTANK laboratory measurements, $\partial U^2/\partial x$ is small. The effect of one current component on the other (UV terms) will also be neglected, although Svendsen and Putrevu (1994) found that the nonlinear interaction has a dispersion effect on the longshore current. The third assumption is to neglect the wave-current interaction which in the momentum equations occur in the trough-to-crest region. The U and V velocities are undefined in this region, and presently, no guidance exists on specifying these values. Under these assumptions, Equations 2.9, 2.35, and 2.36, respectively, become:

$$\frac{\partial Q_x}{\partial x} + \frac{\partial \overline{\zeta}}{\partial t} = 0 \tag{3.1}$$

$$\frac{\partial Q_x}{\partial t} + g(\overline{\zeta} + h_0)\frac{\partial \overline{\zeta}}{\partial x} + \frac{\partial}{\partial x}\left(\frac{S_{xx}}{\rho}\right) + \frac{\tau_{bx}}{\rho} = 0 \tag{3.2}$$

$$\frac{\partial Q_y}{\partial t} + \frac{\partial}{\partial x}\left(\frac{S_{yx}}{\rho} - \nu_{xy}(\overline{\zeta}\ h_0)\left(\frac{\partial \overline{V}}{\partial x}\right)\right) + \frac{\tau_{by}}{\rho} = 0 \tag{3.3}$$

For the applications in this thesis, waves are normally incident and $S_{yx} = 0$. Thus, the longshore flux (Q_y) and velocity ($\overline{V}$) are also zero.

3.1 Numerical Solution

Two numerical schemes have been used: a two-dimensional (*x*-*y*) Predictor-Corrector method and a one-dimensional (*x*) Lax-Wendroff scheme. Both methods are second-order accurate, and the solutions are explicit.

3.1.1 Predictor-Corrector model

The Predictor-Corrector model SHORECIRC (Van Dongeren et al. 1994) was used as the baseline model. An absorbing-generating offshore boundary condition was implemented for arbitrary, time-varying surface elevation.

The model uses the following definitions:

$$E = -\left(\frac{\partial Q_x}{\partial x}\right) \tag{3.4}$$

$$F = -g(\overline{\zeta} + h_0)\frac{\partial \overline{\zeta}}{\partial x} - \frac{\partial}{\partial x}\left(\frac{S_{xx}}{\rho}\right) - \frac{\tau_{bx}}{\rho} \tag{3.5}$$

$$G = - \frac{\partial}{\partial x}\left(\frac{S_{yx}}{\rho} - \nu_{xy}(\overline{\zeta} h_0)\left(\frac{\partial \overline{V}}{\partial x}\right)\right) - \frac{\tau_{by}}{\rho} \tag{3.6}$$

The spatial derivatives are calculated with second-order, central finite differences. At the offshore grid boundary, second-order forward differences are applied, and at the shore boundary, second-order backward differences are applied.

The predictor step is:

$$\overline{\zeta}^{*}_{i,j} = \overline{\zeta}^{n}_{i,j} + \frac{\Delta t}{2}\left(3E^{n}_{i,j} - E^{n-1}_{i,j}\right) \tag{3.7}$$

$$Q_{x_{i,j}}^{*} = Q_{x_{i,j}}^{n} + \frac{\Delta t}{2}\left(3F_{i,j}^{n} - F_{i,j}^{n-1}\right) \tag{3.8}$$

$$Q_{y_{i,j}}^{*} = Q_{y_{i,j}}^{n} + \frac{\Delta t}{2}\left(3G_{i,j}^{n} - G_{i,j}^{n-1}\right) \tag{3.9}$$

where i, j subscripts represent the x, y grid indices where the variable is evaluated, the superscripts represent the time step (e.g., n and $n-1$) when the variable is evaluated, the * superscript represents an intermediate time step, and Δt is the time step. The corrector step is:

$$\overline{\zeta}_{i,j}^{n+1} = \overline{\zeta}_{i,j}^{n} + \frac{\Delta t}{12}\left(5E_{i,j}^{*} + 8E_{i,j}^{n} - E_{i,j}^{n-1}\right) \tag{3.10}$$

$$Q_{x_{i,j}}^{n+1} = Q_{x_{i,j}}^{n} + \frac{\Delta t}{12}\left(5F_{i,j}^{*} + 8F_{i,j}^{n} - F_{i,j}^{n-1}\right) \tag{3.11}$$

$$Q_{y_{i,j}}{}^{n+1} = Q_{y_{i,j}}{}^{n} + \frac{\Delta t}{12}\left(5G_{i,j}{}^{*} + 8G_{i,j}{}^{n} - G_{i,j}{}^{n-1}\right) \tag{3.12}$$

The boundary conditions applied in the model include a no-flux condition at the beach (no flow into the beach), an absorbing-generating offshore boundary condition, and periodicity at the lateral boundaries.

Boundary conditions

Initially, the offshore boundary was specified as the measured total infragravity wave surface elevation $\overline{\zeta}$. Although this condition is theoretically correct, practically, it requires that the reflected wave generated in the model exactly matches the measured reflected wave. If the calculated and measured reflected waves differed, the difference was re-reflected into the model from the boundary. Also, this mode of operation requires that the "solution," the total surface elevation at the boundary, be known a priori. Therefore, an absorbing-generating offshore boundary condition was developed.

The offshore boundary generates a specified incoming wave and absorbs the outgoing reflected wave using the method of characteristics (Kobayashi et al. 1987, Van Dongeren et al. 1994). Assuming shallow-water conditions with

$$c = \sqrt{gh} \tag{3.13}$$

where $h = h_0 + \overline{\zeta}$, the continuity equation (Equation 3.1) can be rewritten as

$$\frac{\partial 2c}{\partial t} + c\frac{\partial \overline{U}}{\partial x} + \overline{U}\frac{\partial 2c}{\partial x} = 0 \tag{3.14}$$

and the x-momentum equation (Equation 3.2) can be rewritten as

$$\frac{\partial \overline{U}}{\partial t} + \overline{U}\frac{\partial \overline{U}}{\partial x} + c\frac{\partial 2c}{\partial x} = -\frac{\partial}{\partial x}\left(\frac{S_{xx}}{\rho}\right) - \frac{\tau_{bx}}{\rho} \tag{3.15}$$

Note that the longshore momentum flux term has been re-introduced.

Adding and subtracting Equations 3.14 and 3.15 generates the characteristic form of the equations. Using the definitions $\alpha = \overline{U} + 2c$ and $\beta = \overline{U}$ - $2c$, the characteristic equations are

$$\frac{\partial \alpha}{\partial t} + (\overline{U} + c)\frac{\partial \alpha}{\partial x} = -\frac{\partial}{\partial x}\left(\frac{S_{xx}}{\rho}\right) - \frac{\tau_{bx}}{\rho} \tag{3.16}$$

$$\frac{\partial \beta}{\partial t} + (\overline{U} - c)\frac{\partial \beta}{\partial x} = -\frac{\partial}{\partial x}\left(\frac{S_{xx}}{\rho}\right) - \frac{\tau_{bx}}{\rho} \tag{3.17}$$

Equation 3.17, the β-equation, gives the relationship between $\overline{U}$ and h on the offshore boundary at $x = 0$.

The β-equation can be written as

$$\beta = (\overline{U_i} + \overline{U_r} + \overline{U_m}) - 2c \tag{3.18}$$

where $\overline{U}_i$ is the velocity associated with the incoming or incident long wave, $\overline{U}_r$ is the velocity associated with the outgoing or reflected long wave, and $\overline{U}_m$ is the time-mean velocity at $x = 0$. Again applying the shallow-water assumptions

$$\overline{U_i} = \sqrt{\frac{g}{h}}\,\overline{\zeta_i}\,, \qquad \overline{U_r} = -\sqrt{\frac{g}{h}}\,\overline{\zeta_r} \tag{3.19}$$

Equation 3.18 becomes

$$\beta = \sqrt{\frac{g}{h}}\,(\overline{\zeta_i} - \overline{\zeta_r}) + \overline{U_m} - 2\sqrt{gh} \tag{3.20}$$

The first two terms of the binomial expansion of h, assuming $\overline{\zeta}_i + \overline{\zeta}_r << h_0$ at $x = 0$, is

$$\sqrt{h} = \sqrt{h_0}\left(1 + \frac{\overline{\zeta_i} + \overline{\zeta_r}}{2h_0}\right) \tag{3.21}$$

Applying Equation 3.21, the β-equation becomes

$$\beta = \frac{\sqrt{g}\,(\overline{\zeta_i} - \overline{\zeta_r})}{\sqrt{h_0}\left(1 + \dfrac{\overline{\zeta_i} + \overline{\zeta_r}}{gh_0}\right)} + \overline{U_m} - 2\sqrt{gh_0}\left(1 + \frac{\overline{\zeta_i} + \overline{\zeta_r}}{2h_0}\right) \tag{3.22}$$

The term $(1 + (\overline{\zeta}_i + \overline{\zeta}_r)/(2h_0))^{-1}$ can be expressed as the geometric series $1 - (\overline{\zeta}_i + \overline{\zeta}_r)/(2h_0)$, neglecting terms of order $\overline{\zeta}^2$ and higher. The β-equation then simplifies to

$$\beta = -2\sqrt{\frac{g}{h_0}}\,\overline{\zeta_r} + \overline{U_m} - 2\sqrt{gh_0} \tag{3.23}$$

The reflected wave amplitude is given by solving Equation 3.23 for $\overline{\zeta}_r$

$$\overline{\zeta_r} = -\frac{1}{2}\sqrt{\frac{h_0}{g}}\,\beta - C(t) - h_0 \tag{3.24}$$

where $C(t) = -0.5\ (h_0/g)^{0.5}\ \overline{U}_m$. The total depth, h, is the sum of $h_0 + \overline{\zeta}_i + \overline{\zeta}_r$, where $\overline{\zeta}_r$ is given by Equation 3.24

$$h = \overline{\zeta_i} - \frac{1}{2}\sqrt{\frac{h_0}{g}}\,\beta - C(t) \tag{3.25}$$

and the velocity, using the definition of β, is given by

$$\overline{U} = \beta + 2\sqrt{gh} \tag{3.26}$$

To implement the absorbing-generating boundary condition, the Predictor-Corrector method is used to solve for β^{n+1} using Equation 3.13. Next, the values of $\overline{\zeta}_i$ and $C(t)$ at $n+1$ are specified. Then, Equation 3.25 is solved for h^{n+1}, and Equation 3.26 is solved for $\overline{U}^{n+1}$. These values are then used as the offshore boundary conditions in the Predictor-Corrector scheme illustrated in Equations 3.4-3.12. This form of the absorbing-generating boundary condition assumes that the incoming infragravity wave is propagating in the $+x$ direction. A more general formulation in given by Van Dongeren et al. (1994). A periodicity condition is applied to the lateral boundaries. This assumes the longshore wavenumber is a multiple of the grid width in the y direction. For the problems studied in this thesis, no longshore forcing is applied and $\overline{V}$ is always zero. Also, since we are simulating a closed wave tank, $C(t)$ is zero.

Solution oscillation

For application of the Predictor-Corrector model with surf beat forcing (Schäffer and Svendsen 1988, Schäffer 1993, see also Chapter 5), the solutions for $\overline{\zeta}$ and Q_x oscillated from grid point to grid point in the cross-shore direction. The Schäffer and Svendsen analytic solution is linear ($h = h_0$) with no bottom friction, and the model was run under these same conditions. The oscillations did not become unbounded, but started from zero at the cold start and quickly reached a bounded value (up to approximately 30 percent of Q_x). The amplitudes of the oscillations were reduced slightly by reducing the grid spacing, but were not eliminated. Figures 3.1a and b show Predictor-Corrector results for a plane beach with Schäffer and Svendsen surf beat forcing.

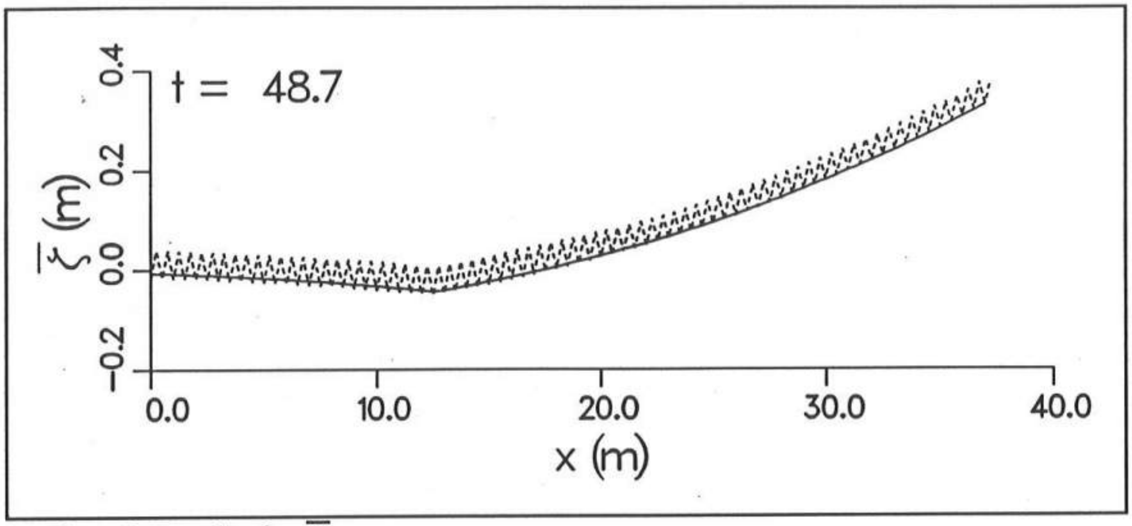

a. Sample results for $\overline{\zeta}$

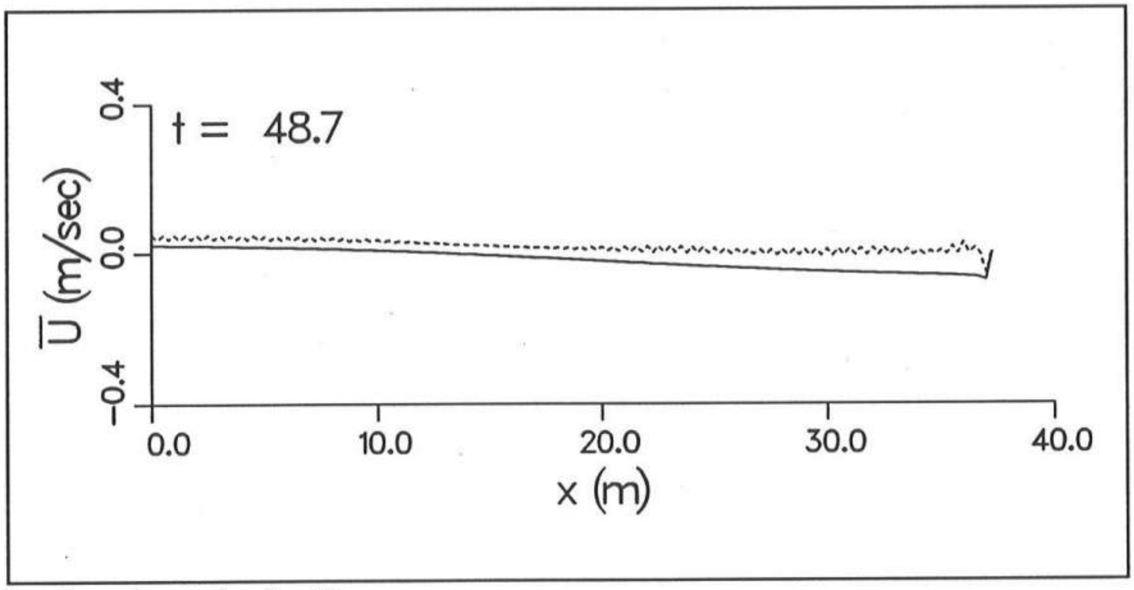

b. Sample results for *U*

Figure 3.1. Predictor-Corrector results with surf beat forcing (solid line -- Schaffer-Svendsen analytic solution, dashed line -- model results). Oscillations are due to a disjoint numerical solution (see page 31 for discussion).

The cause of this spatial oscillation of the solution is analogous to the time splitting instability found in the "leap frog" numerical scheme (Roach 1982). In the time-splitting problem, the solution jumps back and forth between two solutions on alternating time steps. This occurs because the time derivatives use function values at time levels $n-1$ and $n+1$, while spatial derivative are taken at time level n, and thus the solutions for even and odd time steps are disjoint.

The second-order Predictor-Corrector scheme applied here has similar construction in the horizontal plane. For example consider the solution for $\overline{\zeta}$, in both the predictor and corrector steps, $\overline{\zeta}_i^{n+1}$ depends only on $\overline{\zeta}_i^{n}$ and Q_x evaluated at $i+1$ and $i-1$ for time levels $n-1$, n, $n+1$, and *. Thus, at even spatial steps $\overline{\zeta}$ is disjoint from the odd spatial step solution for $\overline{\zeta}$, and vice versa. Two disjoint solutions can develop and the values of $\overline{\zeta}$ and Q_x oscillate between these solutions. Figure 3.2 illustrates the finite-difference molecule for the Predictor-Corrector method. When the depth nonlinearity is included, the oscillation disappears because the nonlinear term links solutions for $\overline{\zeta}$ and Q_x at steps $i-1$, i, and $i+1$.

3.1.2 Lax-Wendroff model

As an alternate solution scheme, the two-step Lax-Wendroff method was applied. For simplicity, the model was developed in only one horizontal direction (Equations 3.1 and 3.2 only). The first step of the solution is given by

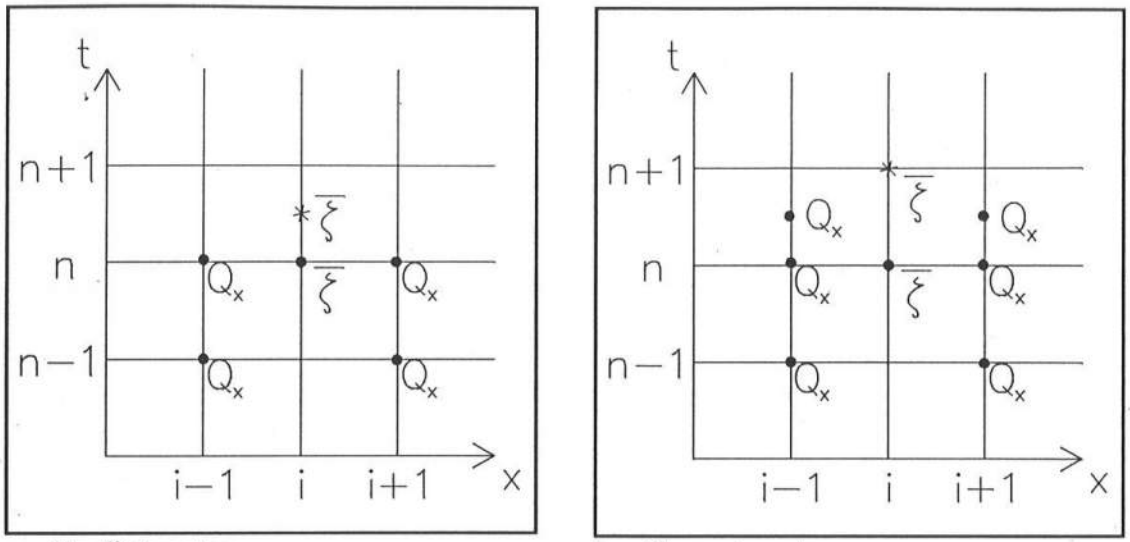

a. Predictor step

b. Corrector step

Figure 3.2. Predictor-Corrector finite-difference molecule

$$\overline{\zeta}^{n+\frac{1}{2}}_{i+\frac{1}{2}} = \frac{\overline{\zeta}^{n}_{i+1} + \overline{\zeta}^{n}_{i}}{2} - \frac{\Delta t}{2\,\Delta x}(Q^{\,n}_{x_{i+1}} - Q^{\,n}_{x_i}) \tag{3.27}$$

$$Q^{\,n+\frac{1}{2}}_{x_{i+\frac{1}{2}}} = \frac{Q^{\,n}_{x_{i+1}} + Q^{\,n}_{x_i}}{2} - \frac{g h_{i+\frac{1}{2}} \Delta t}{2\,\Delta x}(\overline{\zeta}^{n}_{i+1} - \overline{\zeta}^{n}_{i}) - \frac{\Delta t}{2\rho}\left(\frac{dS_{xx}}{dx}\right)^{n+\frac{1}{2}}_{i+\frac{1}{2}} \tag{3.28}$$

The second step is:

$$\overline{\zeta}^{n+1}_{i} = \overline{\zeta}^{n}_{i} - \frac{\Delta t}{\Delta x}(Q^{\,n+\frac{1}{2}}_{x_{i+\frac{1}{2}}} - Q^{\,n+\frac{1}{2}}_{x_{i-\frac{1}{2}}}) \tag{3.29}$$

$$Q^{\,n+1}_{x_i} = Q^{\,n}_{x_i} - \frac{g h_i \Delta t}{\Delta x}(\overline{\zeta}^{n+\frac{1}{2}}_{i+\frac{1}{2}} - \overline{\zeta}^{n+\frac{1}{2}}_{i-\frac{1}{2}}) - \frac{\Delta t}{\rho}\left(\frac{dS_{xx}}{dx}\right)^{n+\frac{1}{2}}_{i} \tag{3.30}$$

Figure 3.3 shows the finite difference molecule for the Lax-Wendroff method (for Equations 3.27 and 3.29). Note that the nonlinearity in water depth and bottom friction have been neglected in Equations 3.27-3.30. This is because this scheme is applied only to the Schäffer-Svendsen surf beat solution, which also neglects these components.

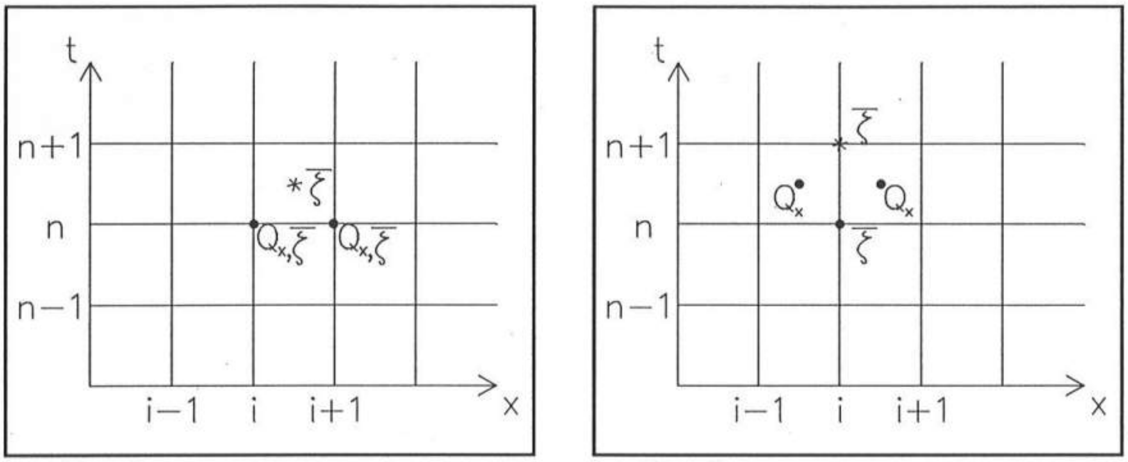

a. Step 1 b. Step 2

Figure 3.3. Lax-Wendroff finite-difference molecule

The boundary conditions for the Lax-Wendroff model are the same as used in the Predictor-Corrector model: an absorbing-generating offshore boundary condition and a no-flux condition at the beach. The Lax-Wendroff model is used for applications using the Schäffer-Svendsen surf beat forcing in Chapter 4. The Predictor-Corrector model is used for applications to the SUPERTANK data in Chapter 5.

3.2 Input/Output Parameters

Both the Predictor-Corrector and Lax-Wendroff models require the same input and produce the same output. The input includes the forcing functions of the incident infragravity wave elevations and the radiation stress forcing throughout the grid. A bottom friction coefficient and some short-wave information are also required to calculate bottom friction, when bottom friction is included. Parameters must also be specified to define the grid domain. The output includes the infragravity wave surface elevations and depth-integrated velocities throughout the grid.

3.2.1 Input parameters

Incident infragravity surface elevation

The absorbing-generating boundary condition at the offshore boundary requires the input of the time series of the incident infragravity wave elevation $\overline{\zeta}_i$. This boundary condition can be specified from an analytic solution or from measurements. If measurements are used, the incident and reflected wave components must be separated (see Hughes 1993 and Section 6.3.3).

Radiation stress

A time series of the radiation stress is required at each grid point. This is the most difficult input to supply to the model because a general model to predict the temporal and spatial radiation stress variation, commensurate with the level of effort employed in the depth-integrated model, is not available. For applications in this thesis, radiation stress was calculated/interpolated from wave measurements or calculated using the analytic model of Schäffer and Svendsen (1988). Radiation stress is calculated based on linear theory as

$$S_{xx} = \frac{\rho g H^2}{8}\left(\frac{2C_g}{C} - \frac{1}{2}\right) \tag{3.31}$$

where H is wave height, C_g is wave group celerity, and C is wave celerity. For SUPERTANK applications, shallow water is also assumed, so $C_g = C$. The wave height varies as a function of x and t.

Bottom friction

The linear bottom friction formulation is given in Equation 2.37. This formulation requires an input bottom friction coefficient f_{cw} and an estimate of the short-wave velocity amplitude at the bottom u_o. The short-wave velocity amplitude is estimated for each grid point based on linear theory, an input short-wave amplitude and period (treated as a constant), and the local still-water depth. The bottom friction coefficient is a function of bottom roughness and bottom velocity (laminar or smooth turbulent boundary layer). Typical bottom friction coefficients used in previous steady-state current studies range from approximately 0.005 to 0.05, based on the Equation 2.37 (e.g., Jonsson 1966, Thornton 1970, Noda 1974, Ebersole and Dalrymple 1979, Thornton and Guza 1981, and Smith et al. 1992). Coefficient values of 0.01 and 0.05 were applied with the SUPERTANK data with minor variations in the results. The bottom friction coefficient in both the depth-integrated and profile models is treated as a constant, and a value of 0.01 is used. The coefficient could be used as a calibration parameter.

Grid domain

The grid domain is specified by the number of cells in the x and y coordinates, nx and ny, and the cell spacings, Δx and Δy. The number of time steps nt and the step increment Δt must also be specified. The still-water depth h_0 must be specified throughout the domain.

3.2.2 Output parameters

The model output parameters are the time series of $\overline{\zeta}$ and $\overline{U}$ for each grid point. These output parameters provide the forcing for the profile model to extract the distribution of $\overline{U}$ over depth. The reflected infragravity wave at the offshore boundary can also be estimated.

3.3 Example

As an example model application illustrating the absorbing-generating boundary condition, a standing wave is generated with no radiation stress forcing and no bottom friction. The Predictor-Corrector model is used for this example. The offshore boundary condition is given by

$$\overline{\zeta}_i = a_i \cos(kx - \sigma t) \qquad (3.32)$$

where a_i is the incident infragravity wave amplitude, k is wave number, and σ is wave frequency. The parameter values specified are $a_i = 0.05$ m and wave length $L = 50$ m (from which k and σ are calculated using linear theory). The domain is 100 m in length and is specified with $nx = 101$, $ny = 5$, $\Delta x = \Delta y = 1$ m, and Δt

= 0.25 sec. A constant depth of h_0 = 0.5 m is applied over the entire grid. The incident infragravity wave input was linearly ramped up over the first 20 time steps.

The analytic solution for this case is given by

$$\overline{\zeta} = a_i[\cos(kx - \sigma t) + \cos(kx + \sigma t)] \tag{3.33}$$

and

$$\overline{U} = a_i \frac{\sigma}{kh_0}[\cos(kx - \sigma t) - \cos(kx + \sigma t)] \tag{3.34}$$

The solution has antinodes in $\overline{\zeta}$ at each of the boundaries. The maximum water surface amplitude is 0.05 m at the antinodes, and the maximum horizontal velocity is 0.44 m/sec at the nodes. Example plots of the results at cell 11 and 51 are given in Figures 3.4 and 3.5. The plots show a flat portion at the beginning of the record, prior to the wave reaching the cell from a cold start. Then, the incident wave reaches the cell, and finally the wave reflected from the end of the grid returns to the cell. A close match to the analytic solution is reached after about 100 sec at cell 11 and after 80 sec at cell 51. The small errors in amplitude and phase are due to a small re-reflection at the absorbing-generating boundary.

Root-mean-square (rms) errors in the calculated solution for time steps 500-1000 (t = 125-250 sec) are given in Table 3.1, for selected grid cells. The rms error is defined

$$E_{\alpha,rms} = \sqrt{\frac{\Sigma \; (\alpha_a - \alpha_n)^2}{N}} \tag{3.35}$$

where α represents the variable ($\overline{\zeta}$ or $\overline{U}$), the subscript a denotes the analytic solution, n denotes the numerical solution, and N is the number of points in the summation. The relative error is expressed as the rms error divided by the local maximum of the analytic solution, $E_{\overline{\zeta},\, rms}/\overline{\zeta}_{max}$ and $E_{\overline{U},\, rms}/\overline{U}_{max}$.

Table 3.1. rms error in standing wave model computations

Grid Cell	1	2	11	26	41	51	61	76	91	100	101
x/L	0.0	0.02	0.2	0.5	0.8	1.0	1.2	1.5	1.8	1.98	2.0
$E_{\overline{\zeta},\, rms}$ (m)	.0076	.0077	.0039	.0076	.0036	.0077	.0035	.0078	.0035	.0079	.0078
$E_{\overline{\zeta},\, rms}/\overline{\zeta}_{max}$ (%)	7.6	7.8	12.6	7.6	11.6	7.7	11.3	7.8	11.3	7.8	7.8
$E_{\overline{U},\, rms}$ (m/sec)	.0135	.0134	.0366	.0113	.0338	.0086	.0337	.0057	.0377	.0067	.0
$E_{\overline{U},\, rms}/\overline{U}_{max}$ (%)	∞	24.4	8.0	∞	8.1	∞	8.0	∞	8.0	12.2	0.

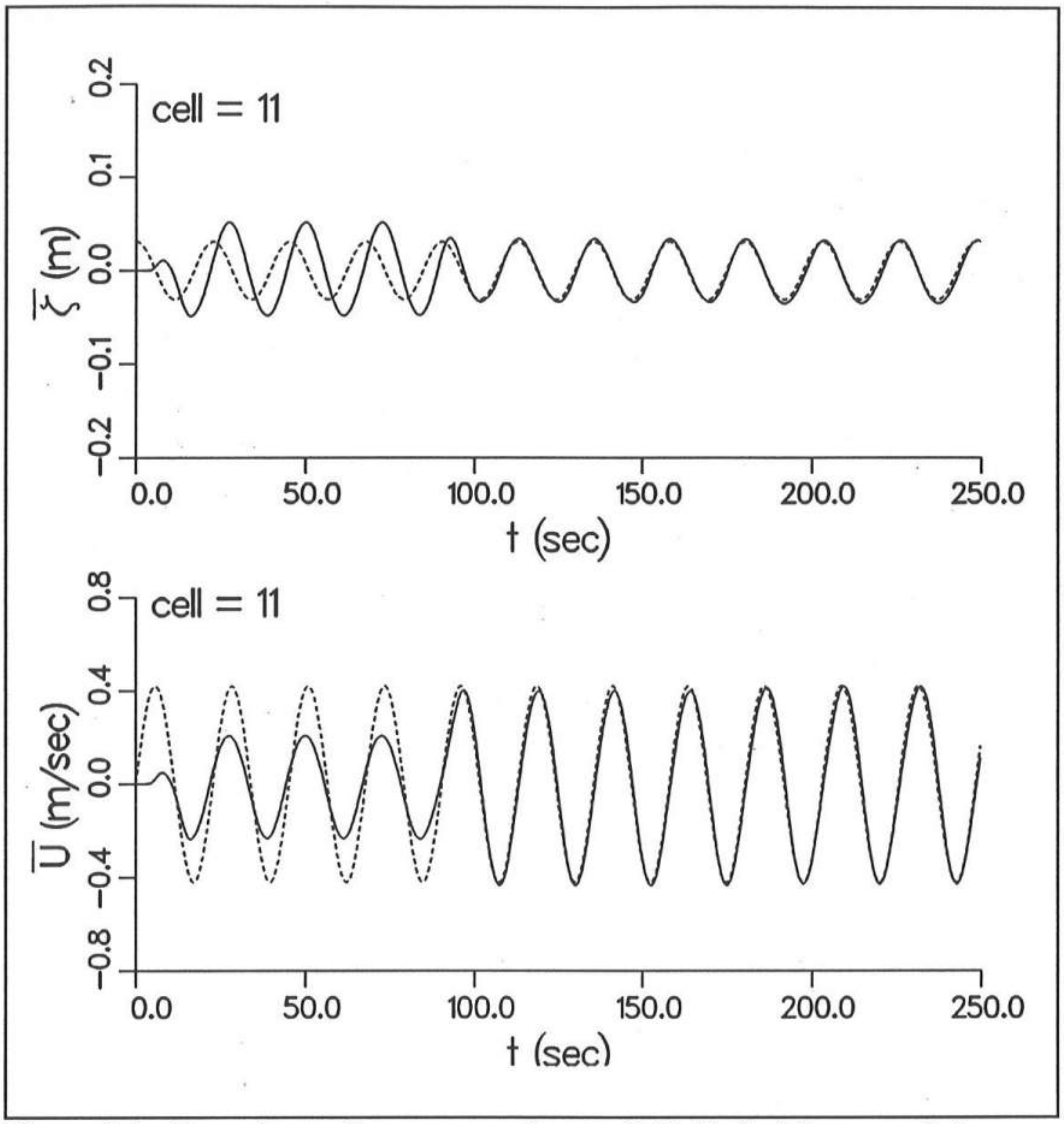

Figure 3.4. Example standing wave results at cell 11 (dashed line -- analytic solution, solid line -- model results)

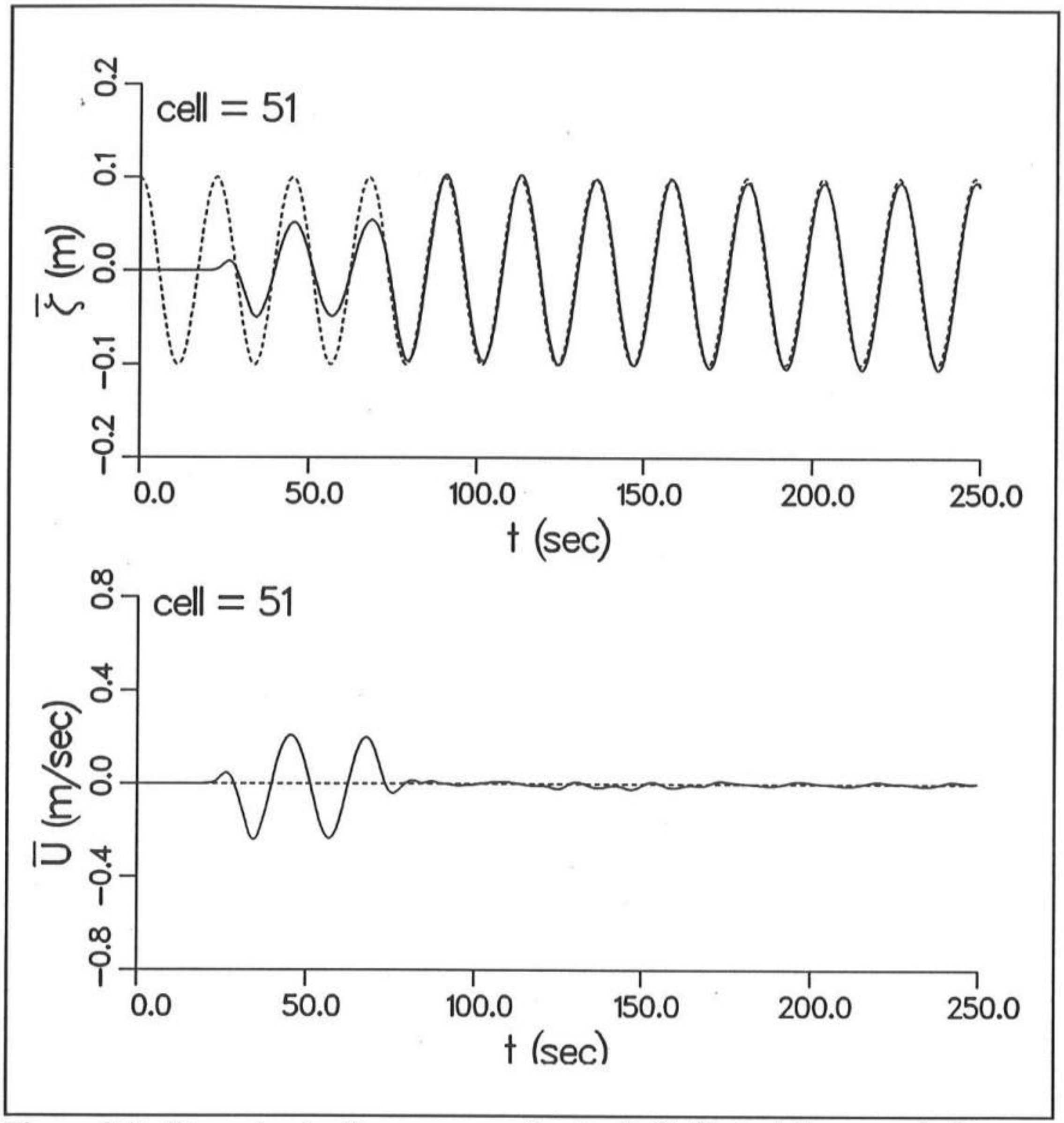

Figure 3.5. Example standing wave results at cell 51 (dashed line -- analytic solution, solid line -- model results)

Chapter 4

PROFILE MODEL FOR INFRAGRAVITY WAVES

This chapter describes the model component, called the profile model, used to calculate the vertical variations in the time-varying infragravity wave velocity field. The water column is divided into three regions: a bottom boundary layer, a central layer (from the bottom boundary layer to the mean water surface), and an upper layer (above the mean water surface). The velocity profiles are solved in the central layer with the boundary conditions of bottom and surface stresses representing bottom and upper layers. This chapter provides discussion of the model assumptions, solution technique, input and output parameters, and example applications for the profile model.

The profile model is based on the cross-shore momentum equation given in Equation 2.44. The only additional assumption applied is that the term $\partial U^2/\partial x$ is neglected, as was assumed for the depth-integrated model (see Chapter 3). Equation 2.44 then becomes

$$\frac{\partial U}{\partial t} - \frac{\partial}{\partial z}\left(\nu_t \frac{\partial U}{\partial z}\right) = -g\frac{\partial \overline{\zeta}}{\partial x} - \frac{\partial(\overline{u_w^{\ 2}} - \overline{w_w^{\ 2}})}{\partial x} \qquad (4.1)$$

The right-hand side of Equation 4.1 is the forcing function, defined as *f(t)*. The bottom, surface, and initial boundary conditions are:

$$\rho \nu_t \frac{\partial U}{\partial z} - \frac{\rho}{\pi} f_{cw} u_o U = 0 \quad \text{at} \quad z = -h_0 \tag{4.2}$$

$$\frac{\partial U}{\partial z} = \frac{\tau_s(t)}{\rho \nu_t} \quad \text{at} \quad z = \overline{\zeta} \tag{4.3}$$

and

$$U = U_o(z) \quad \text{at} \quad t = 0 \tag{4.4}$$

where $\tau_s(t)$ is the time-varying stress at the mean water surface and $U_o(z)$ is the initial condition. The surface stress is due to radiation stress above mean water level and wind stress (which is neglected for the applications in this thesis). The eddy viscosity is assumed constant over depth.

4.1 Eigenfunction Expansion

Equation 4.1 is solved using separation of variables and the Sturm-Liouville approach. This approach involves determining the solution in two parts: u which satisfies the boundary conditions in z, and v which is broken into a homogeneous solution (for $f = 0$) and a particular solution, v_p.

4.1.1 Solution satisfying boundary conditions in *z*

The first step is to choose a partial solution *u(z,t)* which satisfies the boundary conditions in *z*

$$u(z,t) = \frac{\tau_s}{\rho \nu_t}\left(h_0 + z + \frac{\pi \nu_t}{f_{cw} u_o}\right) \tag{4.5}$$

The solution for Equation 4.1 then becomes

$$U(z,t) = u(z,t) + v(z,t) \tag{4.6}$$

4.1.2 Homogeneous solution

Combining Equations 4.5 and 4.6 and substituting into 4.1, gives the governing equation for v

$$\frac{\partial v}{\partial t} - \nu_t \frac{\partial^2 v}{\partial z^2} = f^*(t) \tag{4.7}$$

where

$$f^*(t) = f(t) - \frac{\partial u}{\partial t} = f(t) - \frac{1}{\rho \nu_t}\frac{\partial \tau_s}{\partial t}(h_0 + z + \frac{\pi \nu_t}{f_{cw} u_o}) \tag{4.8}$$

The boundary conditions for Equation 4.7 are given by substituting Equations 4.5 and 4.6 into the boundary conditions (Equations 4.2-4) for Equation 4.1. The boundary conditions are given by

$$\frac{\partial v}{\partial z} = 0 \qquad \text{at} \quad z = \overline{\zeta} \tag{4.9}$$

$$\rho \, \nu_t \frac{\partial v}{\partial z} - \frac{\rho}{\pi} f_{cw} u_o v = 0 \qquad \text{at} \quad z = -h_0 \tag{4.10}$$

and

$$v(z,0) = U_o^*(z) \qquad t = 0 \tag{4.11}$$

The homogeneous equation for v

$$\frac{\partial v}{\partial t} - \nu_t \frac{\partial^2 v}{\partial z^2} = 0 \tag{4.12}$$

is solved by the method of separation of variables, in the form $v = Z(z)T(t)$, where Z and T are to be determined. Substituting the assumed form of v into Equation 4.12 gives

$$Z\frac{dT}{dt} - \nu_t \frac{d^2 Z}{dz^2} T = 0 \tag{4.13}$$

To separate the variables, Equation 4.13 is divided by $\nu_t ZT$ and the first term is moved to the right-hand side

$$\frac{\left(\dfrac{d^2Z}{dz^2}\right)}{z} = \frac{\left(\dfrac{dT}{dt}\right)}{\nu_t T} = -\kappa^2 \tag{4.14}$$

Since z and t are independent, both sides of Equation 4.14 must be equal to a constant, which is defined as $-\kappa^2$. The separation procedure produces two ordinary differential equations

$$\frac{d^2Z}{dz^2} + \kappa^2 Z = 0 \tag{4.15}$$

$$\frac{dT}{dt} + \nu_t \kappa^2 T = 0 \tag{4.16}$$

The general solutions for Equations 4.15 and 4.16 are given by

$$Z = \begin{cases} A\cos\kappa z + B\sin\kappa z \\ C + Dz \end{cases} \tag{4.17}$$

$$T = \begin{cases} Ee^{-\nu_t \kappa^2 t} \\ F \end{cases} \tag{4.18}$$

where A, B, C, D, E, and F are constants. The general solution for v is

$$v = ZT = (A\cos\kappa z + B\sin\kappa z)e^{-\nu_t \kappa^2 t} + C + Dz \tag{4.19}$$

where the constant coefficients have been redefined (E has been absorbed into A and B, and F has been absorbed into C and D). The solutions for $\kappa^2 \neq 0$ and $\kappa^2 = 0$ have been summed.

To simplify Equation 4.19, we define $\xi = z - \overline{\zeta}$. Then Equation 4.19 becomes

$$v = ZT = (A\cos\kappa\xi + B\sin\kappa\xi)e^{-\nu_t\kappa^2 t} + C + D\xi \tag{4.20}$$

The boundary conditions are applied to determine the coefficient values. At $\xi = 0$,

$$\frac{\partial v}{\partial \xi} = 0 = (B\kappa)e^{-\nu_t\kappa^2 t} + D \tag{4.21}$$

Since the first and second term on the right-hand side of Equation 4.21 are linearly independent, $B = D = 0$. At $\xi = -(h_0 + \overline{\zeta})$,

$$\begin{gathered} \rho\,\nu_t\frac{\partial v}{\partial \xi} - \frac{\rho}{\pi}f_{cw}u_o v = 0 \\ \rho\,\nu_t(-A\kappa\sin\kappa\xi\ e^{-\nu_t\kappa^2 t}) - \frac{\rho}{\pi}f_{cw}u_o(A\cos\kappa\xi\ e^{-\nu_t\kappa^2 t} + C) = 0 \end{gathered} \tag{4.22}$$

Again, due to linear independence of solution, $C = 0$ and

$$-\nu_t\kappa\ \sin\kappa\xi = \frac{f_{cw}u_o}{\pi}\cos\kappa\xi \tag{4.23}$$

or, the characteristic equation for κ is

$$\frac{\pi \nu_t \kappa}{f_{cw} u_o} = \frac{1}{\tan \kappa (h_0 + \overline{\zeta})} \tag{4.24}$$

The comprehensive homogeneous solution for v is

$$v(z,t) = \sum_{n=1}^{N} A_n \cos \kappa_n (z - \overline{\zeta}) \; e^{-\nu_t \kappa_n^2 t} \tag{4.25}$$

4.1.3 Particular solution

Returning to Equation 4.7 to determine the particular solution for v, we first express the forcing term as an eigenfunction expansion. We define

$$F_n(t) = \frac{\left\langle f - \frac{1}{\rho \nu_t} \frac{\partial \tau_s}{\partial t} (h_0 + z + \frac{\pi \nu_t}{f_{cw} u_o}),\ \cos \kappa_n (z - \overline{\zeta}) \right\rangle}{\left\langle \cos \kappa_n (z - \overline{\zeta}),\ \cos \kappa_n (z - \overline{\zeta}) \right\rangle} \tag{4.26}$$

where the triangular brackets represent the inner product of the two enclosed functions (Greenberg 1988), then

$$f^*(t) = \sum_{n=1}^{N} F_n(t) \cos \kappa (z - \overline{\zeta}) \tag{4.27}$$

We determine the particular solution by the method of variation of parameters. Starting from

$$v_p = \sum_{n=1}^{N} A_n(t) \cos\kappa_n(z - \overline{\zeta})\, e^{-\nu_t\kappa_n^2 t} \tag{4.28}$$

Substituting into Equation 4.7 yields

$$\frac{\partial A_n}{\partial t}\cos\kappa_n(z - \overline{\zeta})e^{-\nu_t\kappa_n^2 t} - \nu_t\kappa_n^2 A_n\cos\kappa_n(z - \overline{\zeta})e^{-\nu_t\kappa_n^2 t} + \nu_t\kappa^2 A_n\cos\kappa_n(z - \overline{\zeta})e^{\nu_t\kappa} = F_n\cos\kappa_n(z - \overline{\zeta}) \tag{4.29}$$

which simplifies to

$$\frac{\partial A_n}{\partial t}e^{-\nu_t\kappa_n^2 t} = F_n \tag{4.30}$$

or

$$A_n = \int_0^t F_n e^{\nu_t\kappa_n^2\tau}\, d\tau \tag{4.31}$$

Substituting Equation 4.31 into 4.28 provides the particular solution

$$v_p = \sum_{n=1}^{N} \int_0^t F_n e^{\nu_t\kappa_n^2(\tau-t)} d\tau \, \cos\kappa_n(z - \zeta_t) \tag{4.32}$$

The complete solution for v is the sum the homogeneous and particular solutions

$$v = \sum_{n=1}^{N}[A_n e^{-\nu_t\kappa_n^2 t} + \int_0^t F_n e^{\nu_t\kappa_n^2(\tau-t)} d\tau] \cos\kappa_n(z - \overline{\zeta}) \tag{4.33}$$

4.1.4 Full solution for velocity profile

Returning to Equation 4.6, the solution for the cross-shore velocity profile is the sum of Equations 4.5 and 4.33

$$U = \frac{\tau_s}{\rho \nu_t}\left(h_0 + z + \frac{\pi \nu_t}{f_{cw} u_o}\right) + \sum_{n=1}^{N} [A_n e^{-\nu_t \kappa_n^2 t} + \int_0^t F_n e^{\nu_t \kappa_n^2 (\tau - t)} d\tau] \cos \kappa_n (z - \overline{\zeta}) \tag{4.34}$$

4.1.5 *f* independent of *z*

It is convenient to consider the case of *f*, the forcing function on the right hand side of Equation 4.1, independent of *z*. The first term on the right hand side of Equation 4.1 is independent of *z*, and the second term has a weak dependence in shallow water. The assumption of *f* independent of *z* is used often in the literature (Svendsen and Lorenz 1989, Svendsen and Putrevu 1990, Sanchez-Arcilla et al. 1992, and Putrevu and Svendsen 1993,1995) and simplifies the analytical integration in Equation 4.26. The solution for F_n, assuming *f* is not a function of *z*, is given by the solution of Equation 4.26

$$F_n = \frac{\left(f - \frac{\partial \tau_s}{\partial t}\frac{\pi}{\rho f_{cw} u_o}\right) \sin \kappa_n (h_0 + \overline{\zeta}) + \frac{1}{\rho \nu_t}\frac{\partial \tau_s}{\partial t}\left(\frac{\cos \kappa_n (h_0 + \overline{\zeta}) - 1}{\kappa_n}\right)}{\frac{\kappa_n}{2}(h_0 + \overline{\zeta}) + \frac{1}{4}\sin 2\kappa_n (h_0 + \overline{\zeta})} \tag{4.35}$$

The solution for A_n is given by

$$A_n = \frac{(U_o - \frac{\tau_s(0)\,\pi}{\rho f_{cw} u_o}) \sin\kappa_n (h_0 + \overline{\zeta}) + \frac{\tau_s(0)}{\rho\,\nu_t}\left(\frac{\cos\kappa_n (h_0 + \overline{\zeta}) - 1}{\kappa_n}\right)}{\frac{\kappa_n}{2}(h_0 + \overline{\zeta}) + \frac{1}{4}\sin 2\kappa_n (h_0 + \overline{\zeta})} \tag{4.36}$$

The velocity distribution over the vertical, given by Equation 4.34, contains a time integration. An efficient method is required to evaluate the integral. Using integration by parts, the integral becomes:

$$\int_0^t F_n(\tau) e^{\nu_t \kappa_n^2 (\tau - t)} d\tau = \left(F_n(\tau) \frac{e^{\nu_t \kappa_n^2 (\tau - t)}}{\nu_t \kappa_n^2} \right)_0^t - \int_0^t \frac{F_n^{\prime}(\tau) e^{\nu_t \kappa_n^2 (\tau - t)}}{\nu_t \kappa_n^2} d\tau \tag{4.37}$$

where the prime denotes a time derivative. The integral in Equation 4.37, can be broken into two integrals

$$\int_0^t F_n(\tau) e^{\nu_t \kappa_n^2 (\tau - t)} d\tau = \int_0^{t-\Delta t} F_n(\tau) e^{\nu_t \kappa_n^2 (\tau - t)} d\tau + \int_{t-\Delta t}^{t} F_n(\tau) e^{\nu_t \kappa_n^2 (\tau - t)} d\tau \tag{4.38}$$

Pulling out the term $\exp(-\nu_t\, \kappa_n^{\,2} \Delta t)$, gives

$$\int_0^t F_n(\tau) e^{\nu_t \kappa_n^2 (\tau - t)} d\tau = e^{-\nu_t \kappa_n^2 \Delta t} \int_0^{t-\Delta t} F_n(\tau) e^{\nu_t \kappa_n^2 (\tau - \Delta t - t)} d\tau + \int_{t-\Delta t}^{t} F_n(\tau) e^{\nu_t \kappa_n^2 (\tau - t)} d\tau \tag{4.39}$$

If we define the integral I_n as

$$I_n(t) = \int_0^t e^{-\nu_t \kappa_n^2 (t - \tau)} F_n(\tau) d\tau \tag{4.40}$$

then, Equation 4.39 becomes

$$I_n(t) = e^{-\nu_t \kappa_n^2 \Delta t} I_n(t-\Delta t) + \int_{t-\Delta t}^{t} e^{-\nu_t \kappa_n^2 (t-\tau)} F_n(\tau) d\tau \tag{4.41}$$

Partial integration can be used repeatedly to evaluate the second term on the right-hand side of Equation 4.41, giving the following series

$$\int_{t-\Delta t}^{t} e^{-\nu_t \kappa_n^2 (t-\tau)} F_n(\tau) d\tau = \frac{F_n(t)}{\nu_t \kappa_n^2} - \frac{F_n(t-\Delta t) e^{\nu_t \kappa_n^2 (-\Delta t)}}{\nu_t \kappa_n^2} - \frac{F_n'(t)}{(\nu_t \kappa_n^2)^2} + \frac{F_n'(0)}{(\nu_t \kappa_n^2)^2} + \ldots \tag{4.42}$$

where κ is O(1) or larger and ν_t is O(0.01). Assuming that F_n varies slowly with time ($F_n' \approx 0$), Equation 4.42 is substituted for the integral in Equation 4.41 to give

$$I_n(t) = e^{-\nu_t \kappa_n^2 \Delta t} I_n(t-\Delta t) + F_n(t-\frac{\Delta t}{2}) \left(\frac{1 - e^{-\nu_t \kappa_n^2 \Delta t}}{\nu_t \kappa_n^2} \right) \tag{4.43}$$

The analytic profile model is given by Equations 4.34, 4.35, 4.36, and 4.43. The profile model is also used within the depth-integrated model to define the bottom velocity, $U(-h_0)$, for calculation of the bottom friction. It is important that the forcing/resisting functions (radiation stress and bottom friction) are the same in both models. If they are not, then $\overline{\zeta}$ from the depth-integrated model will not be in equilibrium with the radiation stress forcing and bottom friction in the profile model. Disequilibrium between models causes erroneous profile solutions and comparable solutions could not be obtained in the two models.

4.2 Input/Output Parameters

The input forcing functions for the profile model are water surface gradient from the depth-integrated model, radiation stress, and bottom friction. Additional input includes "grid"-like parameters defining the accuracy and resolution of the solution. The eddy viscosity coefficient is also required as input. Unlike the depth-integrated model, the input is not required globally, but is only required in the region where the profile solution is desired. The model output is the cross-shore velocity at specified locations over the vertical.

4.2.1 Input parameters

Water surface gradient

The infragravity wave water surface, $\overline{\zeta}$, is obtained from the output of the depth-integrated model. The gradient of $\overline{\zeta}$ is calculated using second-order, central finite differences. At the offshore and onshore boundaries of the depth-integrated model, forward and backward differences are used.

Radiation stress

Radiation stress is divided into two components to apply to the profile model: (a) a surface stress τ_s, and (b) a depth-uniform component. The radiation stress is defined by

$$S_{xx} = \overline{\int_{-h_0}^{\zeta} (\rho u_w^2 + P)\, dz} - \frac{\rho g}{2}(h_0 + \overline{\zeta})^2 \tag{4.44}$$

(Mei 1989). Substituting $P = p_D + \rho g(\overline{\zeta} - z)$ and $\eta = \zeta - \overline{\zeta}$ into Equation 4.44 yields

$$S_{xx} = \overline{\int_{-h_0}^{\zeta} (\rho u_w^2 + p_D)\, dz} + \frac{\rho g \overline{\eta^2}}{2} \tag{4.45}$$

where $p_D = -w_w^2$, assuming linear theory, or

$$S_{xx} = \overline{\int_{-h_0}^{\zeta} (\rho u_w^2 - w_w^2)\, dz} + \frac{\rho g \overline{\eta^2}}{2} \tag{4.46}$$

Applying the linear theory definitions of u_w, w_w, and η, integrating over depth, and taking the time average reduces Equation 4.46 to Equation 3.31 (the radiation stress applied to the depth-integrated model). The cross-shore gradient of the first term on the right-hand side of Equation 4.46 is equivalent to the second term on the right-hand side of Equation 4.1. Assuming shallow water, this term is uniform over depth and is calculated in the model as

$$\frac{\partial(\overline{u_w^2} - \overline{w_w^2})}{\partial x} = \frac{\rho g}{8h}\frac{\partial H^2}{\partial x} \tag{4.47}$$

assuming a mild slope. The surface stress term is calculated as

$$\tau_s = \frac{\rho g H^2}{16} \tag{4.48}$$

Using Equations 4.47 and 4.48, one-third of the stress is applied as the surface stress and two-thirds is applied uniformly over depth below the mean water surface. Wave height gradients are calculated with second-order, central finite differences (forward and backward differences at the boundaries).

Bottom friction

The bottom friction is specified as it was for the depth-integrated model. The formulation is given in Equation 2.37. A constant bottom friction coefficient of 0.01 is used. Choice of the bottom friction coefficient was discussed in Section 3.2.1. The same coefficient is used in both the depth-integrated and profile models.

"Grid"-like parameters

The number of solution points over depth must be specified. This determines the resolution of the solution. The *x*-*y* locations from the depth-integrated grid where current profiles are to be calculated must also be specified. The number of eigenfunctions, *N*, to be used in the solution is an additional input parameter. The number of eigenfunctions determines the accuracy of the solution. The resolution (number of points over depth) and accuracy (number of eigenfunctions) are unrelated in the analytic solution, unlike a numerical solution.

Eddy viscosity

The eddy viscosity has been assumed constant in the derivation of the profile model. A depth-varying eddy viscosity would require a numerical solution over the vertical instead of the present analytic solution. Svendsen and Putrevu's (1994) eddy viscosity parameterization is used for all cases studied in this thesis

$$\nu_t = \begin{cases} 0.01\, h_0 \sqrt{g\, h_0} & \text{inside surf zone} \\ \left[0.8 \left(\dfrac{h_0}{h_b} \right)^{-4} + 0.2 \right] \nu_{tb} & \text{outside surf zone} \end{cases} \tag{4.49}$$

where h_b is the depth at incipient breaking and $\nu_{tb} = 0.01\ h_b\ (g\ h_b)^{1/2}$. The breaking depth is estimated as $h_b = H_{mo}/0.8$, where H_{mo} is the incident zero-moment wave height.

4.2.2 Output parameters

The model output is the time series of U at specified elevations and x-y locations.

4.3 Example

As an example model application, steady short-wave forcing conditions are applied. The steady forcing case includes the processes of setdown seaward of the breakpoint, setup in the surf zone, and undertow. This example is selected because it is important to show that the depth-integrated and profile models are, at least approximately, in equilibrium, i.e., produce the same mean velocities for steady forcing. The profile model forcing includes the water surface slope from the depth-integrated model and the radiation stress forcing. If the profile model forcing differs from the depth-integrated model forcing, then the surface slope gradient will not balance the radiation stress forcing. In a steady case, this lack of equilibrium is highlighted by a profile solution that diverges from the depth-integrated solution. Also, for comparison, a simpler steady analytic solution for the velocity profile is derived for comparison.

The steady-state analytic solution is derived from Equation 4.1, neglecting the first term on the left-hand side of the equation, $\partial U/\partial t$. Integrating the equation twice gives

$$U = -\frac{f z^2}{2\nu_t} + C_1 z + C_2 \tag{4.50}$$

where f is the forcing function given by the right-hand side of Equation 4.1. C_1 and C_2 are integration constants. Applying the boundary conditions given in Equations 4.2 and 4.3, the constants are found to be

$$C_1 = \frac{1}{\nu_t}\left(\frac{\tau_s}{\rho} + f\nu_t\right) \tag{4.51}$$

and

$$C_2 = \frac{\pi}{f_{cw} U_{-h_0}} \left(f\,(h_0 + \overline{\zeta}) + \frac{\tau_s}{\rho} \right) + \frac{f\,h_0}{\nu_t} \left(\frac{h_0}{2} + \overline{\zeta} \right) + \frac{h_0 \tau_s}{\nu_t \rho} \tag{4.52}$$

Integrating Equation 4.50 over depth gives the mean velocity

$$\overline{U} = \frac{\tau_s}{\rho} \left(\frac{\overline{\zeta} - h_0}{2\nu_t} + \frac{\pi}{f_{cw} u_o} \right) + f \left(\frac{(\overline{\zeta} + h_0)^2}{3\nu_t} + \frac{\pi}{f_{cw} u_o} (h_0 + \overline{\zeta}) \right) \tag{4.53}$$

The depth-integrated model gives the same steady-state solution, neglecting the terms containing the eddy viscosity.

The example case is a beach configured with a 1-m deep, flat portion extending 3.66 m and then a 1:20 plane slope. The depth-integrated, Predictor-Corrector model was set up with $nx = 37$, $ny = 5$, $\Delta x = \Delta y = 0.6096$ m, and $\Delta t = 0.125$ sec. The minimum water depth was 0.13 m. With steady forcing, the cross-shore depth-integrated velocity is zero. The short-wave transformation, used to calculate the radiation stress forcing, was calculated for a monochromatic wave, using linear shoaling and the Dally et al. (1985) breaker/reformation model with an incipient breaker index of 0.8. The forcing was ramped up over 400 time steps (50 sec). The profile model was applied using 20 eigenvectors. Solutions were generated at 21 points over the vertical. The still-water level was used in place of the mean water level in the calculations.

The results of the depth-integrated model are given in Figure 4.1. The time series of $\overline{\zeta}$ and U are given for three grid locations: the offshore boundary, x

= 0.0 m, mid surf zone, x = 11.0 m, and near the onshore boundary, x = 21.9 m. The effects of the cold start and the 50-sec ramping are apparent in the first 60-70 sec, then the variables reach steady conditions.

The profile model results are given in Figure 4.2a and b. The vertical axis, Z, is dimensionless depth, $(h_0 + z)/h_0$. The plots show that the profile model solution (dotted line) oscillates around the steady profile (solid line) given by Equations 4.50-4.52 until about a time of 90 sec. Small amplitude oscillations continue until about 400 sec. The rms errors for selected grid cells for t = 400-750 sec are given in Table 3.2. The overall rms error was 0.031 m/sec for t = 200-750 sec and 0.026 m/sec for t = 400-750 sec.

Table 4.1 rms error in plane-beach velocity profile computations

Grid cell	1	7	13	19	25	31	37
$E_{U,rms}$ (m/sec)	0.067	0.0085	0.051	0.030	0.012	0.0066	0.0058

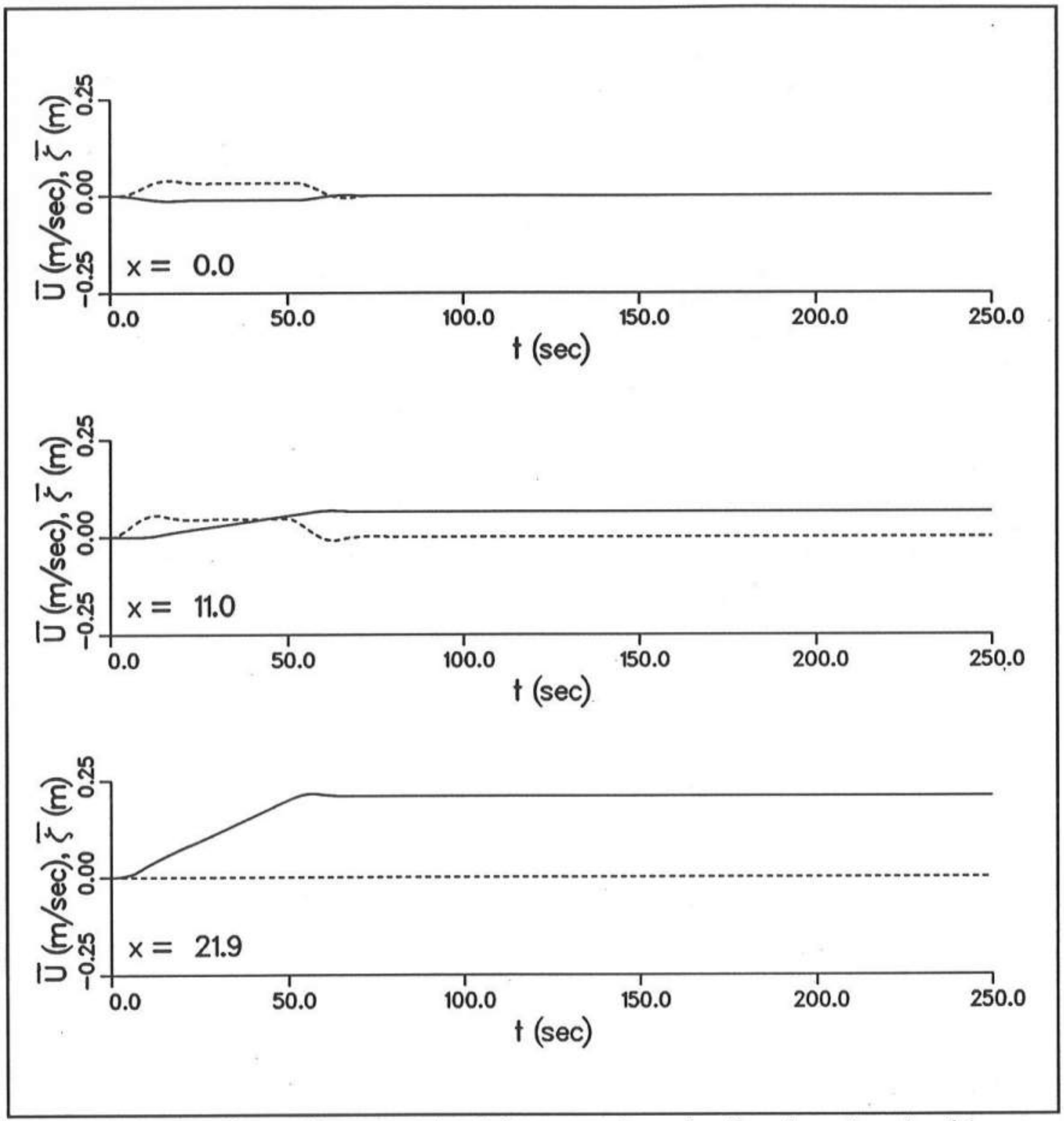

Figure 4.1. Predictor-Corrector depth-integrated results for plane beach with steady forcing (solid line -- $\overline{\zeta}$, dashed line -- $\overline{U}$) discussed in Section 4.3.

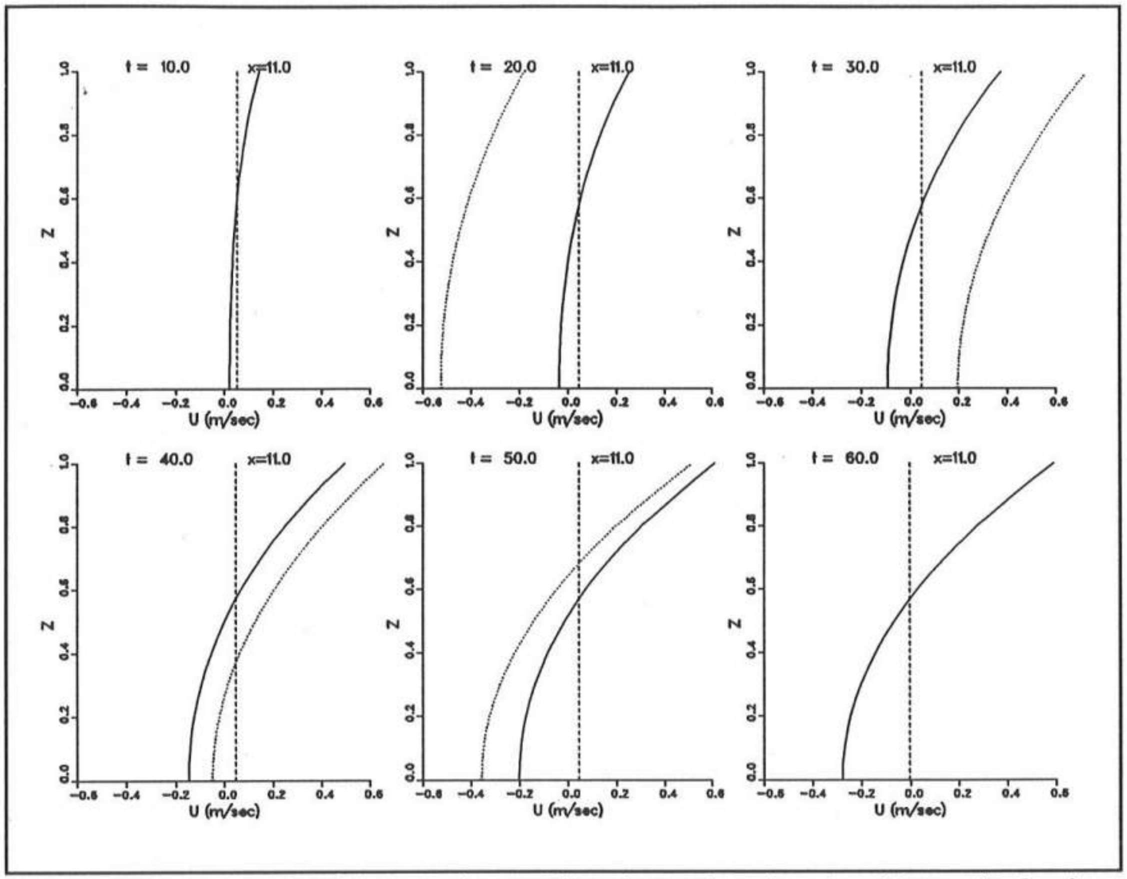

Figure 4.2a. Eigenfunction velocity profiles for a plane beach with steady forcing (solid line -- analytic steady solution, dashed line -- depth-integrated model results, dotted line -- Eigenfunction solution) discussed in Section 4.3

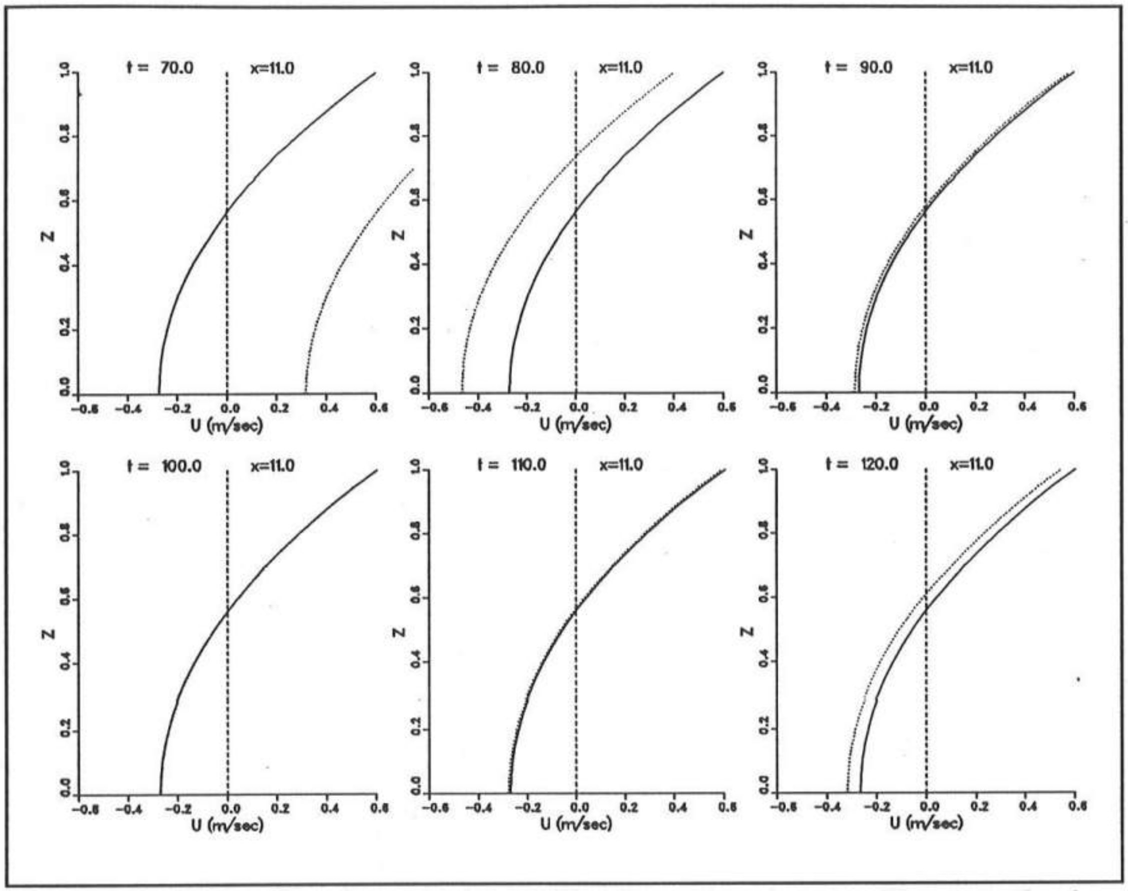

Figure 4.2b. Eigenfunction velocity profiles for a plane beach with steady forcing (solid line -- analytic steady solution, dashed line -- depth-integrated model results, dotted line -- Eigenfunction solution) discussed in Section 4.3

Chapter 5

MODEL APPLICATIONS WITH ANALYTICAL SURF BEAT FORCING

The purpose of this chapter is to investigate the models developed in Chapters 3 and 4 using surf beat forcing from the analytic model of Schäffer and Svendsen (1988) and Schäffer (1990, 1993). The depth-integrated model is compared directly to the Schäffer-Svendsen model. The profile model is also run for the Schäffer-Svendsen surf beat forcing. Profile model results are compared to the periodic infragravity wave profile model of Putrevu and Svendsen (1995).

5.1 Schäffer and Svendsen Surf Beat Model

Schäffer and Svendsen (1988) and Schäffer (1990) developed a theoretical two-dimensional model for surf beat generation by incident wave groups on a plane beach. The surf beat is forced by the modulation of radiation stress. Short waves are modulated both inside and outside the surf zone, i.e., wave breaking does not destroy the wave groups. The break point in this model was held constant. Schäffer (1993) extended the model to include both a constant break point with wave modulation in the surf zone and a varying break point position with no modulation in the surf zone, as suggested by Symonds et al. (1982).

5.1.1 Surf beat model description

The governing equations for the two-dimensional Schäffer-Svendsen surf beat model are Equations 3.1 and 3.2. The model neglects the bottom friction term and the depth nonlinearity in the momentum equation. The two equations were cross differentiated ($\partial/\partial x$ was taken of Equation 3.1 and $\partial/\partial t$ was taken of Equation 3.2) and combined to eliminate Q_x. The resulting surf beat governing equation is

$$\frac{\partial^2 \overline{\zeta_1}}{\partial t^2} - \frac{\partial}{\partial x}\left(g h_0 \frac{\partial \overline{\zeta_1}}{\partial x}\right) = \frac{1}{\rho}\frac{\partial^2 S_{xx,1}}{\partial x^2} \tag{5.1}$$

where the water surface elevation is divided into a time-mean component, $\overline{\zeta}_0$, and a time-varying component, $\overline{\zeta}_1$,

$$\overline{\zeta} = \overline{\zeta_0}(x) + \overline{\zeta_1}(x,t) \tag{5.2}$$

and likewise the radiation stress is divided into a time-mean component, $S_{xx,0}$, and a time-varying component, $S_{xx,1}$,

$$S_{xx} = S_{xx,0}(x) + S_{xx,1}(x,t) \tag{5.3}$$

Mean values of the variables have been neglected in Equation 5.1. The onshore boundary condition is full reflection of the infragravity wave. The solution is expressed as

$$\overline{\zeta_1} = \alpha\,\overline{\zeta_1^{(1)}} + \beta\,\overline{\zeta_1^{(2)}} + \overline{\zeta_1^{p}} \tag{5.4}$$

where the superscripts 1 and 2 denote two linearly independent homogeneous solutions, and the superscript p denotes a particular solution which is chosen to vanish at the shoreline. Full reflection is specified by $\alpha = \beta$. The offshore boundary condition is specified as a incoming bound wave

$$\overline{\zeta_1} = -\frac{S_{xx,1}}{\rho\,(g h_s - C_{gs}^2)} \tag{5.5}$$

where h_s is the shelf depth and C_{gs} is the group celerity in the offshore, shelf region. At the break point, matching conditions of continuity of mass

$$[\overline{\zeta_1}]_-^+ = 0 \tag{5.6}$$

and momentum

$$\left[\frac{\partial\overline{\zeta_1}}{\partial x}\right]_-^+ = -\frac{1}{\rho g h}\left[\frac{\partial S_{xx,1}}{\partial x}\right]_-^+ \tag{5.7}$$

are applied, where the square brackets indicate the difference in variables evaluated on the + and - x sides of the matching location.

The short-wave modulation is formed by two monochromatic waves with slightly different frequencies, $\omega_1 = \omega_s(1 + \epsilon)$ and $\omega_2 = \omega_s(1 - \epsilon)$. The mean frequency is ω_s and ϵ is a small perturbation. The difference frequency is defined as $\omega = \omega_1 - \omega_2$ and is the frequency of the infragravity wave. The amplitude of the first component is defined as a, and the amplitude of the second component is defined as δa. It is assumed that the short-wave height modulation is small, $\delta << 1$. The mean short-wave wavenumber is k, and the wavenumbers for the component waves are $k_1 = k\,(1 + \epsilon\, C/C_g)$ and $k_2 = k\,(1 - \epsilon\, C/C_g)$, where C and C_g are the wave celerity and group celerity, respectively. The time varying radiation stress is calculated from linear theory, which using Equation 5.3 yields

$$\frac{|S_{xx,1}|}{\rho} = \frac{g}{2}|A_1|^2\left(\frac{2C_g}{C} - \frac{1}{2}\right) \tag{5.8}$$

Neglecting terms of $O(\delta^2)$ and higher, the time varying wave amplitude is given by

$$|A_1|^2 = \begin{cases} \gamma^2 h_0^2 (1 - \kappa) 2\delta \exp\left(i\displaystyle\int_{x_b}^{x} \frac{\omega_s}{C_g} dx\right) & (x \leq x_b) \\ a^2 2\delta \exp\left(i\displaystyle\int_{x_b}^{x} \frac{\omega_s}{C_g} dx\right) & (x \geq x_b) \end{cases} \tag{5.9}$$

where x is measured from the shoreline, x_b is the location of the break point (which may be time varying), γ is the breaker index (ratio of wave amplitude to water depth at breaking), and κ is the parameter which determines wave groupiness in the surf zone. The integration in Equation 5.9 is calculated using trapezoidal integration.

For a value of $\kappa = 1$, the time-varying short-wave forcing in the surf zone is zero, as seen from Equation 5.9. This case is analogous to the model of Symonds et al. (1982). The position of the break point varies with time, as specified by the limiting condition $|A|^2 = \gamma^2 h_0^2$, where $|A|$ includes both the steady and time-varying short-wave components. Within the surf zone, wave amplitude is constant for each depth. For $\kappa = 0$, the groupiness in the surf zone is maintained, but the amplitude is reduced in proportion to water depth. This case is analogous to Schäffer and Svendsen (1988) and Schäffer (1990). Depth at the break point is constant and defined by $h_b = a/\gamma$. Visualizations of the short-wave modulation for $\kappa = 1$ and 0 are given in Figure 5.1. The three regions, marked I, II, and III in the figure, represent the surf zone, the shoaling region, and a constant depth "shelf" region, respectively. The region B, for $\kappa = 1$, is the zone where incipient breaking takes place.

The solution for the infragravity wave amplitude is given by

$$\begin{aligned} \xi^{(J)} = {} & \frac{i\pi}{2\rho g h_x} H_0^{(1)}(y') \left(-\alpha^{(J)} + \int_{x_t}^{x} H_0^{2}(y') \frac{d^2 S_{xx}^{(J)}}{dx^2} dx \right) \\ & - \frac{i\pi}{2\rho g h_x} H_0^{(2)}(y') \left(\beta^{(J)} + \int_{x_t}^{x} H_0^{1}(y') \frac{d^2 S_{xx}^{(J)}}{dx^2} dx \right) \end{aligned} \qquad \textbf{(5.10)}$$

where h_x is the beach slope, J = I and II for the region inside and outside the surf zone, respectively, $i = \sqrt{-1}$, $H_0^{(1)}$ and $H_0^{(2)}$ are Hankel functions of the first and second kind, and the argument of the Hankel functions is given by

$$y' = \frac{2\omega}{g h_x} \sqrt{g h_0} \qquad \textbf{(5.11)}$$

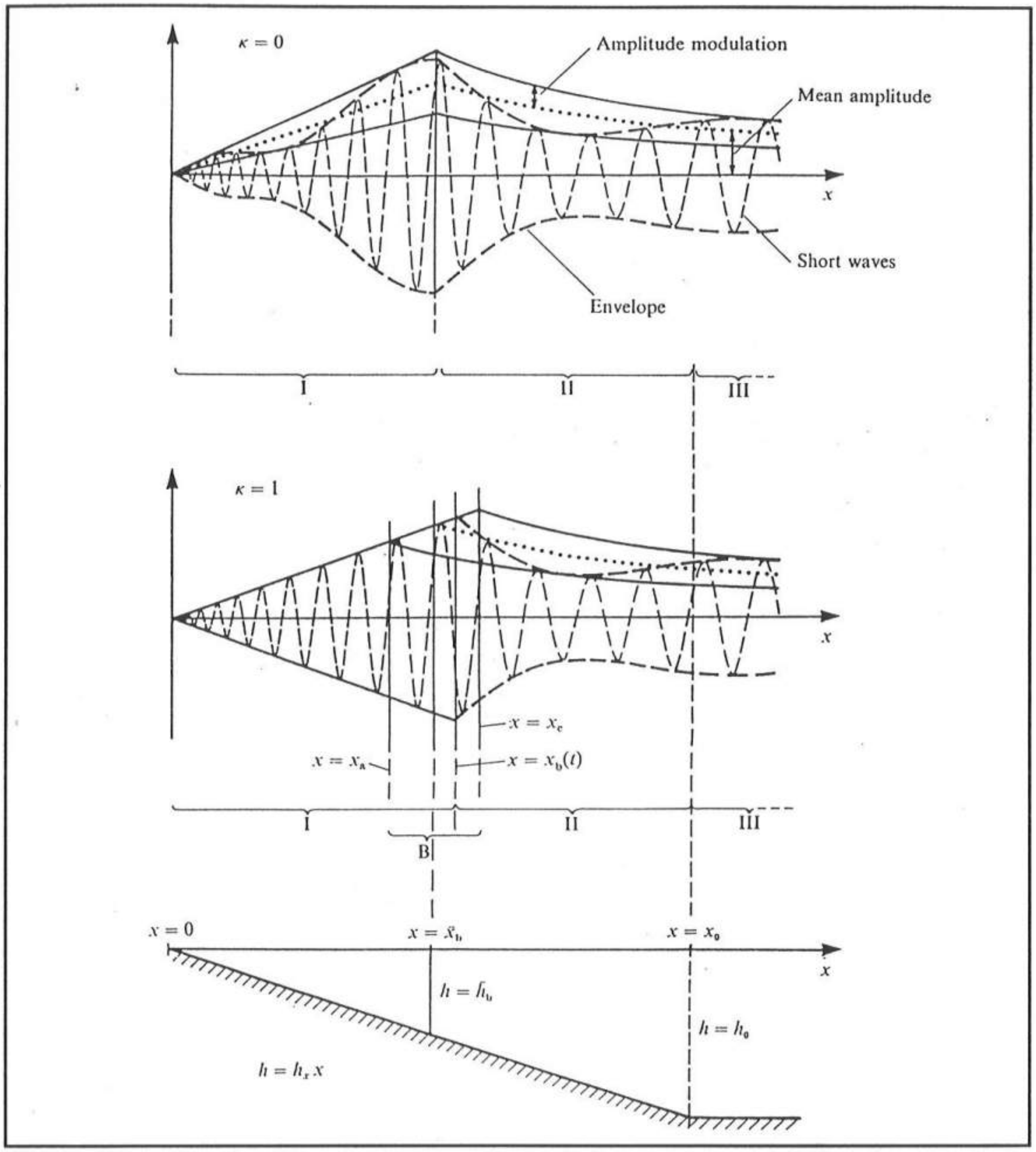

Figure 5.1. Sketch of bottom topography and short-wave modulation for $\kappa = 0$ and 1 in regions I, II, and III for Schäffer-Svendsen surf beat model (from Schäffer 1993)

The integrals in Equation 5.10 are evaluated using Simpson Rule integration. The radiation stress derivatives are calculated using second-order central finite differences. The amplitude of the infragravity wave in region III, the constant depth shelf region, is given by

$$\xi^{(III)} = \alpha^{(III)} e^{\left(\frac{i\omega}{\sqrt{gh_s}} x\right)} + \beta^{(III)} e^{\left(\frac{-i\omega}{\sqrt{gh_s}} x\right)} - \frac{S_{xx,1}^{(III)}}{\rho\left(gh_s - C_{gs}^2\right)} \tag{5.12}$$

The last term in Equation 5.12 is the input forced long wave (Longuet-Higgins and Stewart 1962, 1964). This assumes dynamic equilibrium between the radiation stress forcing and the forced long wave, i.e., a long propagation distance in the constant depth region. In very shallow water, the group velocity approaches the free wave velocity and a near-resonance condition exists.

The complex constants α and β in Equations 5.10 and 5.12 are determined by matching the solutions between regions I and II and regions II and III. At the shoreline, β is set equal to α, which equates the reflected and incident infragravity wave amplitudes at the shoreline, as stated earlier this is the condition of full reflection. The time-varying solution for the infragravity wave surface elevation is given by

$$\overline{\zeta_1} = \frac{1}{2}\left(\xi(x) e^{i\omega t} + *\right) \tag{5.13}$$

where * denotes the complex conjugate of the preceding term and ξ is given by Equation 5.10 or 5.12.

The mean (steady) radiation stress forcing was discussed by Schäffer (1993), but was not included in the model solution (Equations 5.10 and 5.12). The mean radiation stress is given by

$$\frac{S_{xx,0}}{\rho} = \begin{cases} \frac{g}{2}\left(\frac{2C_g}{C} - \frac{1}{2}\right)a^2 & x \geq x_b \\ \frac{g}{2}\left(\frac{2C_g}{C} - \frac{1}{2}\right)\gamma^2 h_0^2 & x \leq x_b \end{cases} \tag{5.14}$$

and the mean water surface elevation is given by

$$\overline{\zeta_0} = \begin{cases} -\frac{a^2 k}{2\sinh 2kh_0} & x \geq x_b \\ \left(\frac{1}{\frac{2}{3\gamma^2} + 1}\right)(h_b - h_0) - \frac{a_b^2 k_b}{2\sinh 2k_b h_b} & x \leq x_b \end{cases} \tag{5.15}$$

where the subscript *b* represents variables evaluated at the break point. Equations 5.14 and 5.15 have been added to the model to calculate mean radiation stress and mean water surface elevation.

5.1.2 Model input and output

The input required to run the surf beat model includes descriptions of the two short-wave trains, beach slope, shelf depth, the parameter κ, and parameters defining the solution grid. The output parameters for each grid cell are water depth, infragravity wave surface elevation and depth-integrated velocity, and radiation stress.

Input parameters

The input parameters defining the short-wave components are the wave amplitudes, a and δa, in meters and the wave frequencies, ω_1 and ω_2, in sec^{-1}. The beach configuration is defined by specifying the shelf depth in meters, h_s , and the beach slope, h_x. The computation grid is specified by the nondimensional depth change between grid steps, $\Delta\overline{h}$, which is defined as the depth change Δh in meters multiplied by the deepwater wavenumber, ω_s^2/g. The horizontal grid step and number of grid points are internally calculated based on beach slope and shelf depth. The dimensionless minimum and maximum depths for model output must also be specified. These depths are nondimensionalized using the deepwater wavenumber. Additional input parameters are the breaker index γ, gravitational acceleration g (SI units will be used throughout this study), and the parameter κ. Schäffer (1993) suggests that the value of κ is near unity. Values of $\kappa < 1$ represent continued wave grouping into the surf zone (see Equation 5.15). Values of $\kappa > 1$ represent a reversal of wave grouping into the surf zone, i.e., setdown under what was, prior to breaking, low waves and setup under what was high waves.

Output parameters

For each grid cell, the model output is the dimensionless still-water depth $h_0\,\omega_s^2/g$, the dimensionless mean water surface $\overline{\zeta}_0/(a_\infty\delta)$, the dimensionless time-varying water surface amplitude $|\xi|/(a_\infty\delta)$, the dimensionless mean radiation stress amplitude $S_{xx,0}/(a_\infty^2\,\delta)$, the dimensionless time-varying radiation stress amplitude $|S_{xx,1}|/(a_\infty^2\,\delta)$, and the dimensionless time-varying infragravity wave velocity amplitude $|U_1|/(i\;a_\infty(\omega_s/g))$. a_∞ is the deepwater wave amplitude that is equivalent to a.

Sample surf beat model output is shown in Figure 5.2. This figure reproduces Figure 5 given by Schäffer (1993). The figure shows the spatial variation of the time varying nondimensional surf beat envelope (+/- the amplitude) as a function of nondimensional depth, $h_0\,\omega^2/g$. The nondimensional surf beat for times t = 0 sec and -0.25 T sec, where T is the surf beat period, are also shown in the figure. The input parameters for this simulation are listed as Case 1 in Table 5.1.

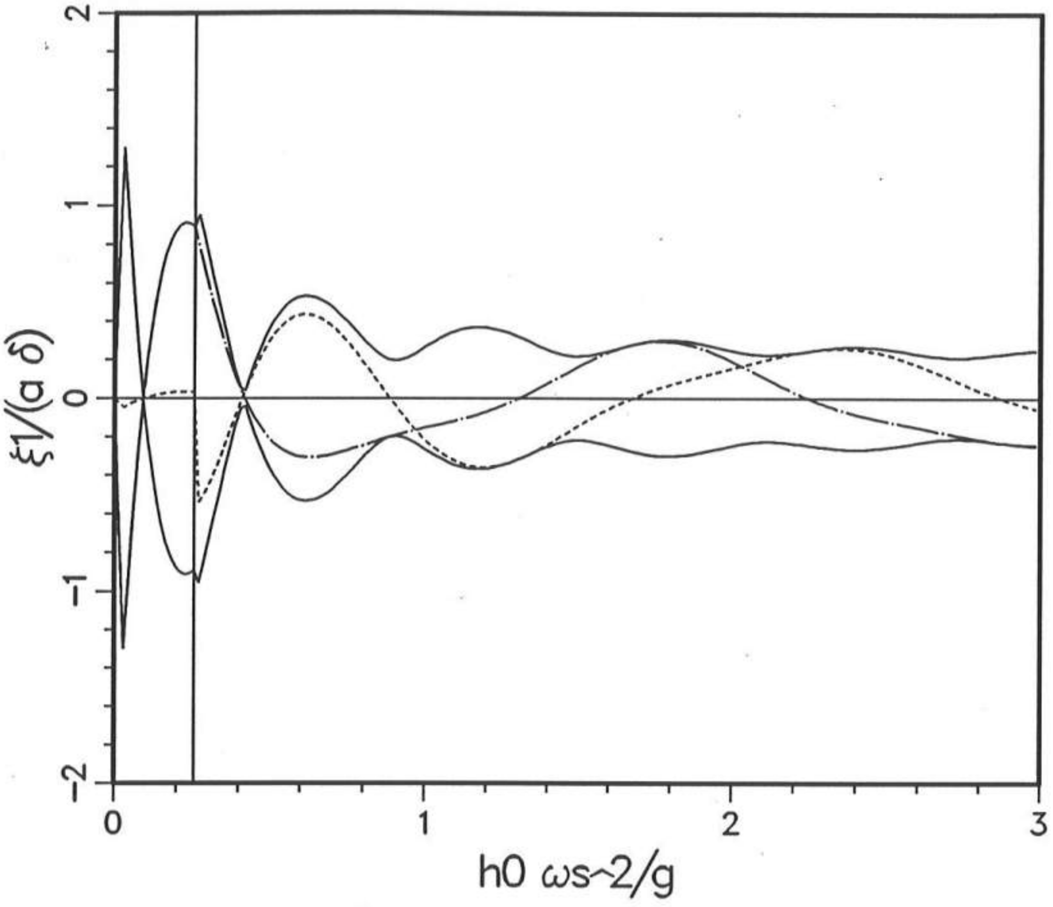

Figure 5.2. Case 1: nondimensional surf beat envelope for Schäffer-Svendsen model, $\pm|\xi_1/(\delta a_\infty)|$ -- solid line, $\xi_1/(\delta a_\infty)$ at $t = 0$ and $-T/4$ -- dashed and chain-dot lines

Table 5.1. Surf beat model input

Case	a, m	δa, m	ω_1, sec^{-1}	ω_2, sec^{-1}	h_s, m	h_x	γ	κ
1	0.62	0.062	1.375	1.125	18.835	0.05	0.4	1.0
2	0.80	0.08	2.18	2.02	3.0	0.08	0.4	0.0
3	0.80	0.08	2.25	1.95	3.0	0.08	0.4	0.0

5.1.3 Depth-integrated model surf beat results

The Schäffer-Svendsen surf beat model, with the additional calculation of mean radiation stress and water surface elevation, provides the input required to run the depth-integrated model described in Chapter 3. The surf beat model also provides an analytic solution to which the depth-integrated model results can be compared. In this section and in Section 5.2, the surf beat model output will be used to drive the depth-integrated and profile models. The periodic nature of the solution provides the opportunity to investigate model input parameters and output trends.

As discussed in Section 3.1.1 of Chapter 3, the Predictor-Corrector model gave results which oscillated from grid point to grid point in the cross-shore direction when executed with surf beat input (see Figure 3.1). The reason for this oscillation is a spatial splitting of the solution at alternating grid points when bottom friction and depth nonlinearity are neglected, as they are in the surf beat model described above. For the following comparisons, the Lax-Wendroff version of the depth-integrated model is used.

Three surf beat applications will be used for model comparisons: Case 1 is the application shown in Figure 5.2, and Cases 2 and 3 were chosen to approximate natural beach conditions similar to those occurring during the SUPERTANK laboratory project (see Chapter 6). The surf beat output of mean and time-varying radiation stress throughout the grid is used as input to the depth-integrated model along with the incident infragravity wave surface elevation at the offshore boundary given by Equations 5.12 and 5.15

$$\overline{\zeta_i} = -\frac{a^2 k}{2\sinh 2kh_s} - \frac{S_{xx,1}^{(III)}}{\rho(gh_s - C_{gs}^2)} \tag{5.16}$$

Case 1

The surf beat input conditions for Case 1 are listed in Table 5.1. The grid spacing used in the surf beat and Lax-Wendroff models was $\Delta x = 1.88$ m with $nx = 200$. The time step used in the Lax-Wendroff model was $\Delta t = 0.126$ sec. The maximum Courant number was 0.91. The Lax-Wendroff model was started from a cold start ($\overline{\zeta} = 0$ m and $Q_x = 0$ m/sec over the entire grid). The forcing functions ($\overline{\zeta_i}$ and S_{xx}) were linearly ramped from zero to the full values specified by the surf beat model over 500 time steps. Lax-Wendroff model results are given in two forms: "snapshots" which illustrate the entire domain at a given time step and time series plots for given x locations. The orientations of the x axis in the surf beat and Lax-Wendroff models are opposite. The example output plots use the x-axis orientation of the Lax-Wendroff model which is $x = 0$ at the offshore boundary and x increasing toward the shore.

Figure 5.2 gives an overview of the spatial variation of the surf beat forcing for Case 1. The majority of the model domain is outside the surf zone (the breaker point is shown with a vertical line). The figure shows six partial nodes in the surface elevation, with the nodes located inside and just outside the surf zone having almost zero amplitude. Antinodes exist near the breaker line and at the shoreline. Also, note the discontinuity in elevation at the breaker point. This is the narrow incipient breaker zone formed by the time-varying break point for $\kappa = 1$. The period of the infragravity wave is 25 sec. The short-wave modulation, δ, is 10 percent (see Table 5.1)

What is happening in the surf beat solution is that the short-wave height varies and creates a long wave (with a trough under high wave groups and a crest under low wave groups). The variation is driven by two short-wave trains with different amplitudes and frequencies. The infragravity wave frequency is equal to the difference in frequency of the short-wave trains.

Figures 5.3a - e give snapshots of the infragravity water surface elevations at 5 sec intervals over one wave period. The solid lines are the surf beat analytic solution and the dashed lines are the Lax-Wendroff model results.

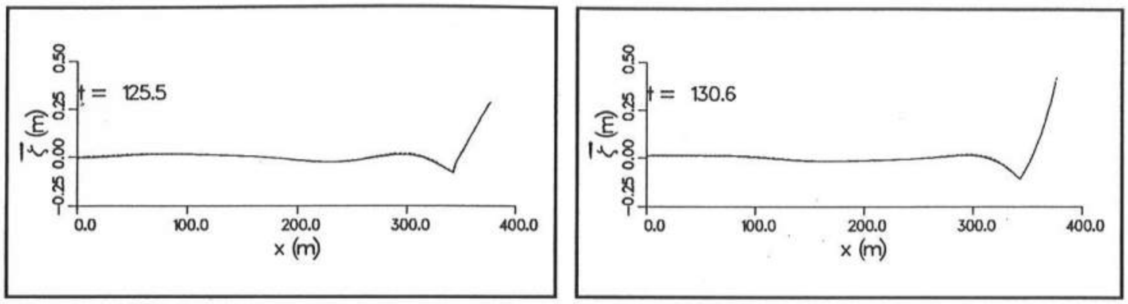

a. t = 125.5 sec b. t = 130.6 sec

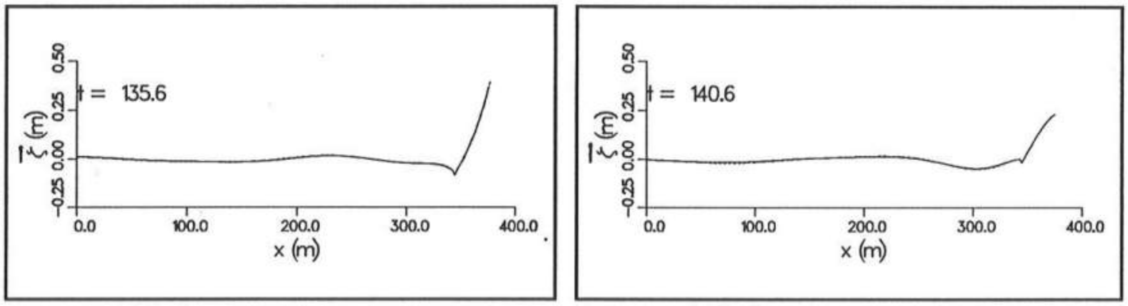

c. t = 135.6 sec d. t = 140.6 sec

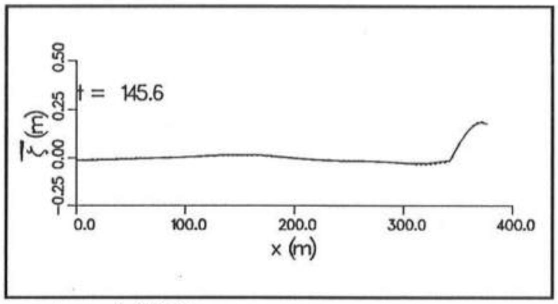

e. t = 145.6 sec

Figure 5.3. Case 1 snapshots of water surface elevation from depth-integrated and analytic Schäffer-Svendsen models (solid line -- analytic surf beat solution, dashed line -- numerical solution)

The times given at the top of the figures are in seconds, and start well after the ramp-up period (approximately 60 sec). The figures show small surface oscillations in the shoaling region, a strong mean setdown at the break point, and significant time-varying oscillation at the break point and shoreline (anti-nodes in the surf beat solution). The dimensionless mean and root-mean-square (rms) error for selected locations are given in Table 5.2. The dimensionless errors are defined as

$$
\begin{aligned}
E_{\overline{\zeta},m} &= \frac{\overline{\zeta}_{SS_{mean}} - \overline{\zeta}_{LW_{mean}}}{H_0} \; X\ 100, \quad E_{\overline{\zeta},rms} = \sqrt{\frac{\Sigma\ (\overline{\zeta}_{SS} - \overline{\zeta}_{LW})^2}{N\ H_0^2}} \; X\ 100 \\
E_{\overline{U},m} &= \frac{\overline{U}_{SS_{mean}} - \overline{U}_{LW_{mean}}}{\sqrt{g h_0}} \; X\ 100, \quad E_{\overline{U},rms} = \sqrt{\frac{\Sigma\ (\overline{U}_{SS} - \overline{U}_{LW})^2}{N\ g h_0}} \; X\ 100
\end{aligned}
\qquad (5.17)
$$

where *SS* represents the Schäffer-Svendsen surf beat solution, *LW* represents the Lax-Wendroff solution, and H_0 is the local mean wave height. The error calculations begin after 1000 time steps to avoid the effect of the numerical ramp-up time. The numerical Lax-Wendroff results match the analytic solution very well. The mean errors increase in magnitude from less than 0.001 % of H_0 (0.0001 m) in the offshore region to 0.01 m near the shoreline (where H_0 goes to zero) where both the mean and time-varying water surface amplitudes are largest. The largest rms errors occur where the gradient in the time-varying envelope are greatest, e.g., in the mid surf zone, which suggests that the errors are caused by inaccuracies in time integration, which cause small phase errors.

Table 5.2. Lax-Wendroff error for Case 1

x, m	82.9	167.6	252.4	344.7	363.5
$E_{\overline{\zeta},m}$, %	0.001	0.009	0.001	-0.01	-0.97
$E_{\overline{\zeta},rms}$, %	0.25	0.49	0.36	0.98	0.27
$E_{\overline{U},m}$, %	0.001	0.001	0.001	-0.01	-0.002
$E_{\overline{U},rms}$, %	0.06	0.02	0.07	0.07	0.34

Figures 5.4a-e give time series of the water surface elevations at five locations. These plots again show good agreement of the numerical solution with the analytic solution. There is a very small error in the period of the numerical solution resulting in a phase error developing in time.

Figures 5.5a-e give snapshots of the depth-integrated velocity for the same times shown in Figure 5.3. Again, the solid lines are the analytic solution and the dashed lines are the numerical solution. Errors in the computed velocities are again given in Table 5.2. The error is defined by Equation 5.17. Time series of the depth-integrated velocity are given in Figures 5.6a-e. As shown in the water surface elevation time series, a small phase error is developing.

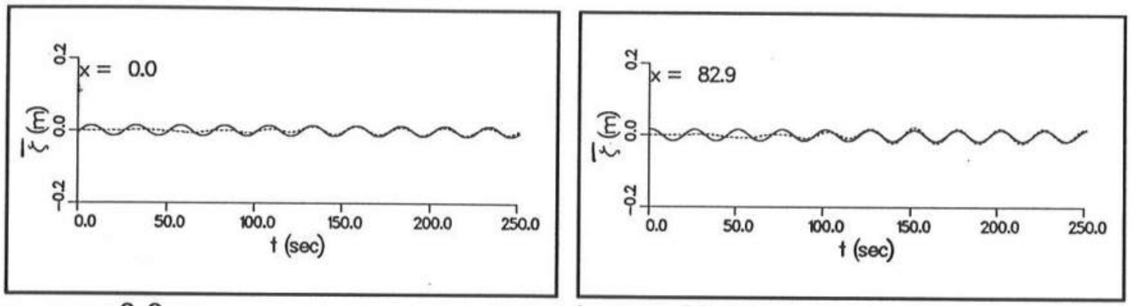

a. x = 0.0 m

b. x = 82.9 m

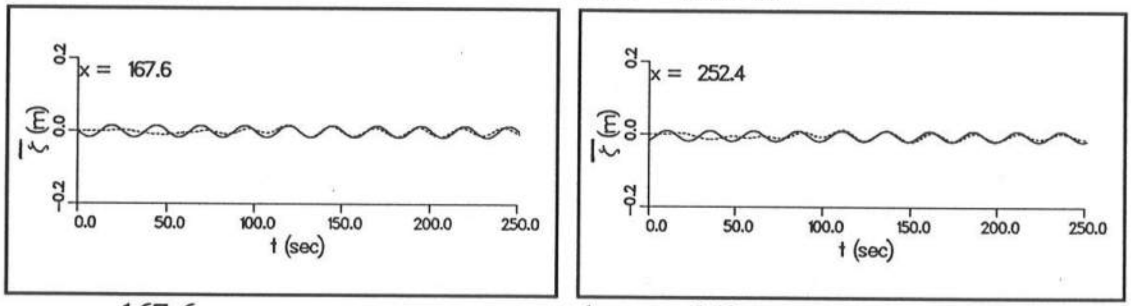

c. x = 167.6 m

d. x = 252.4 m

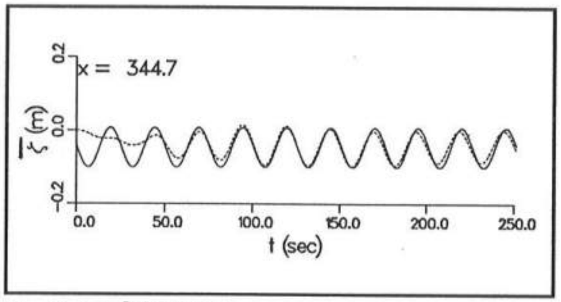

e. x = 344.7 m

Figure 5.4. Case 1 time series of water surface from depth-integrated and analytic Schäffer-Svendsen models for selected locations (solid line -- analytic surf beat solution, dashed line -- numerical solution)

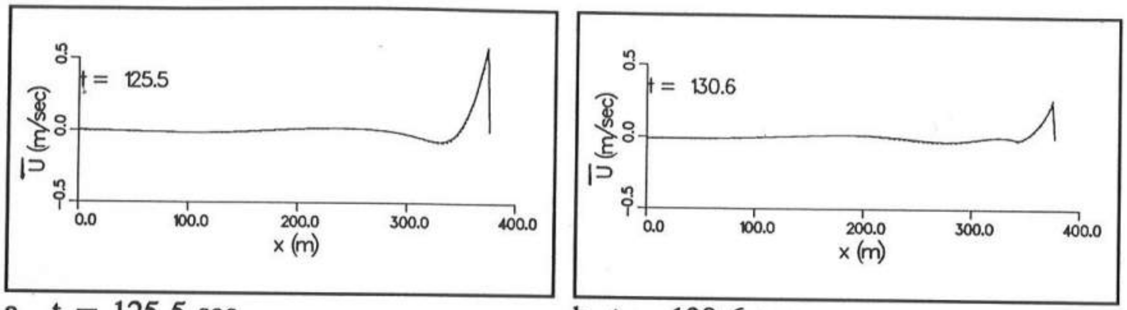

a. t = 125.5 sec

b. t = 130.6 sec

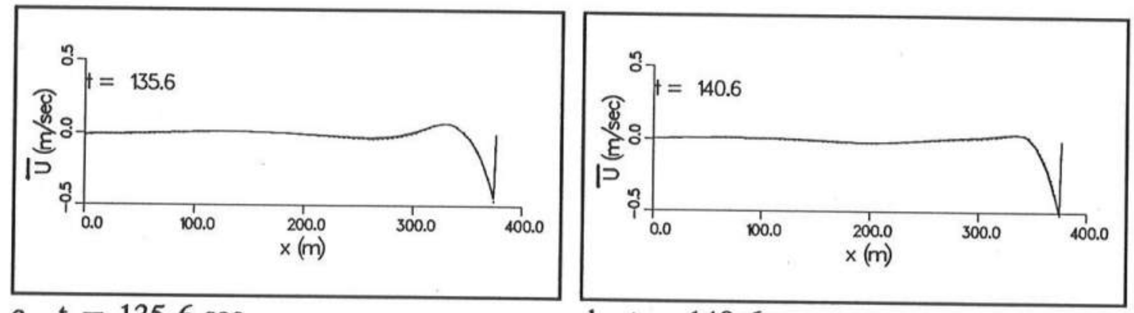

c. t = 135.6 sec

d. t = 140.6 sec

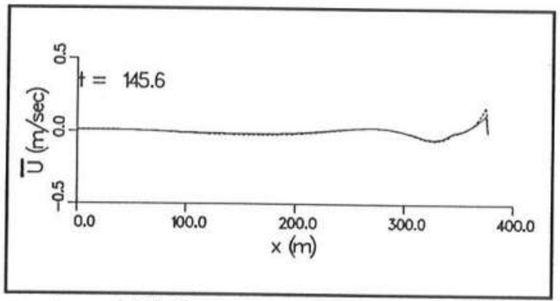

e. t = 145.6 sec

Figure 5.5. Case 1 snapshots of depth-integrated velocity from depth-integrated and analytic Schäffer-Svendsen models (solid line -- analytic surf beat solution, dashed line -- numerical solution)

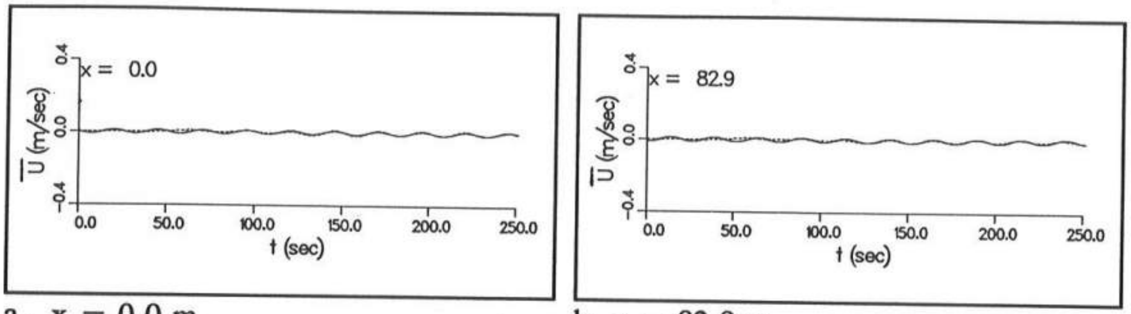

a. x = 0.0 m

b. x = 82.9 m

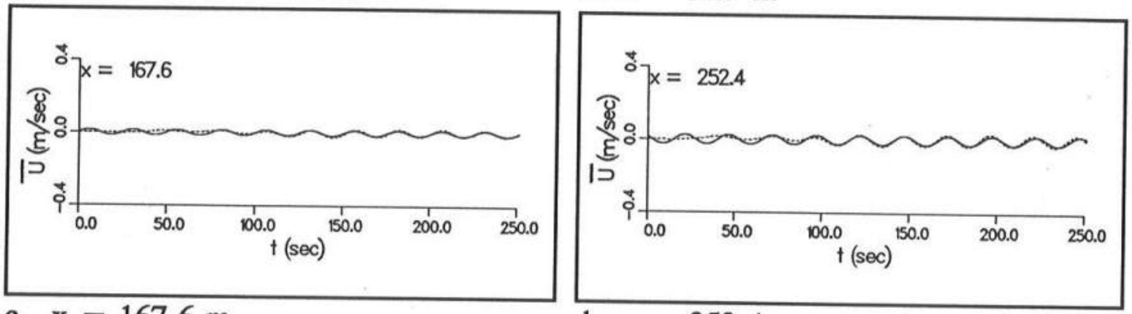

c. x = 167.6 m

d. x = 252.4 m

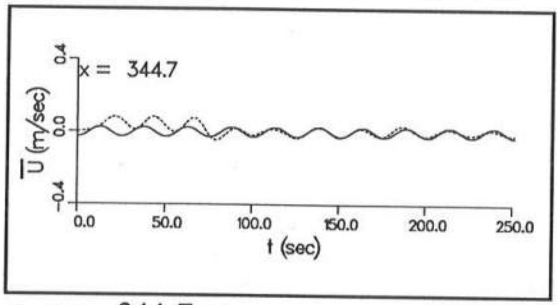

e. x = 344.7 m

Figure 5.6. Case 1 time series of depth-integrated velocity from depth-integrated and analytic Schäffer-Svendsen models for selected locations (solid line -- analytic surf beat solution, dashed line -- numerical solution)

Case 2

The configuration of Case 2 is somewhat similar to the wave channel at SUPERTANK, with an offshore depth of approximately 3 m and a surf zone width on the order of 25 m (for no nearshore bar). The surf beat input parameters for Case 2 are also listed in Table 5.1. The surf beat output is shown in Figure 5.7. The grid spacing used in both the surf beat and Lax-Wendroff models was $\Delta x =$ 0.25 m and $nx = 150$. The time step used in the Lax-Wendroff model was $\Delta t =$ 0.033 sec. The maximum Courant number was 0.71.

The infragravity periods at SUPERTANK were typically in the range of 20 to 40 sec. The period of the infragravity wave for Case 2 is 39 sec. A value of $\kappa = 0$ was selected because wave groupiness was observed in the surf zone at SUPERTANK. Remember that for $\kappa = 1$, the time-varying short-wave amplitude in the surf zone is zero and wave groupiness is destroyed (Equation 5.9). For $\kappa = 0$, the time-varying amplitude is reduced as function of depth, but maintains its grouped nature. Note that for $\kappa = 0$ (Figure 5.7), that the discontinuity in the surface elevation envelope is only in the slope and not in magnitude, due to the constant break point. The main feature of the surf beat solution is a partial node in the mid surf zone. Since the envelope is fairly flat, the solution does not vary greatly across the grid.

Figures 5.8a-e give snapshots of the infragravity surface elevations over one wave period. As expected from the fact that the short-wave frequency perturbation ϵ is small and thus the infragravity wave is long compared to the

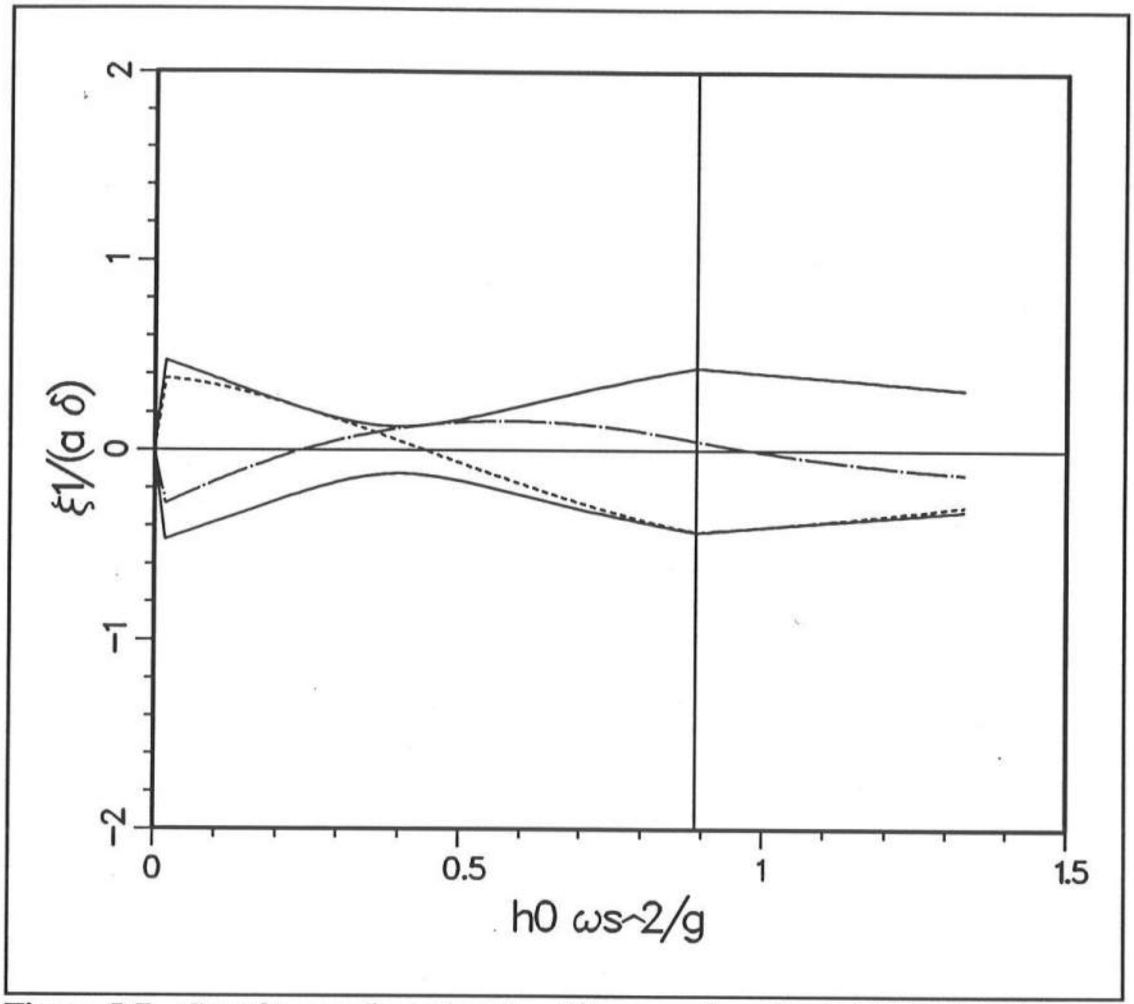

Figure 5.7. Case 2: nondimensional surf beat envelope for Schäffer-Svendsen model, $\pm|\xi_1/(\delta a_\infty)|$ -- solid line, $\xi_1/(\delta a_\infty)$ at $t = 0$ and $-T/4$ -- dashed and chain-dot lines

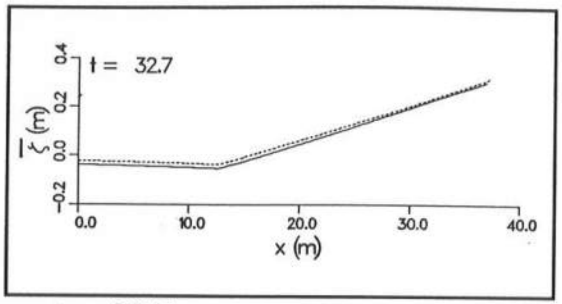

a. t = 32.7 sec

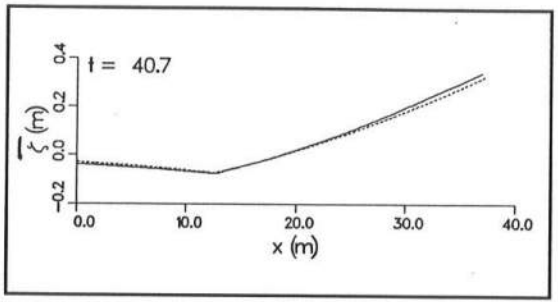

b. t = 40.7 sec

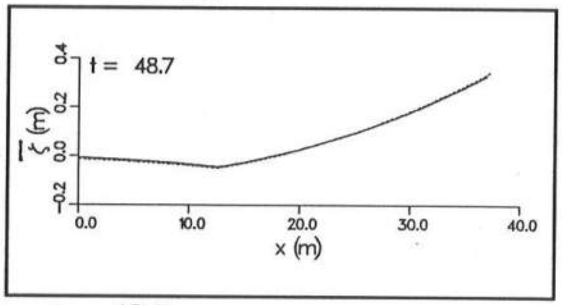

c. t = 48.7 sec

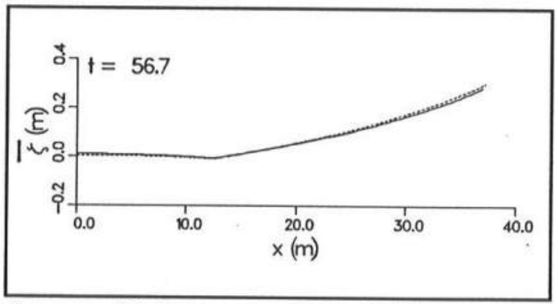

d. t = 56.7 sec

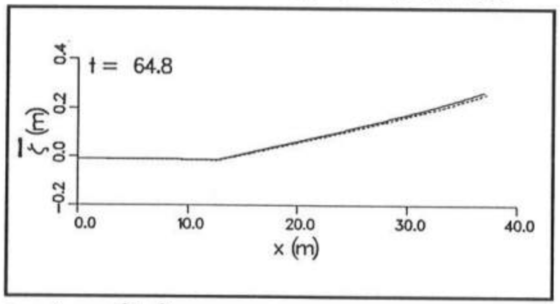

e. t = 64.8 sec

Figure 5.8. Case 2 snapshots of water surface elevation from depth-integrated and analytic Schäffer-Svendsen models (solid line -- analytic surf beat solution, dashed line -- numerical solution)

domain, the solution is fairly bland, with small oscillations around the mean setdown/setup solution. The water surface is rocking like a teeter-totter around the central node. There is a small mean bias in the numerical solution which increases near the shoreline. Figure 5.9 shows time series for five locations. In this case, the surf beat amplitude at the shoreline is relatively small. The phase difference between the solutions is also small, but increases near the shoreline. Mean and rms errors in elevation are reported in Table 5.3.

Figures 5.10 and 5.11 give snapshot and time series plots for the depth-integrated velocity for Case 2. The velocities are low and also rock around the central node in the solution. Again, the largest errors occur near the shoreline. Errors are given in Table 5.3.

Table 5.3. Lax-Wendroff error for Case 2

x, m	7.5	17.5	22.5	28.8	35.0
$E_{\overline{\zeta},m}$, %	-0.004	-0.009	0.01	0.04	0.19
$E_{\overline{\zeta},rms}$, %	0.82	0.53	0.59	0.75	1.00
$E_{\overline{U},m}$, %	0.01	-0.002	-0.007	-0.01	-0.007
$E_{\overline{U},rms}$, %	0.87	0.70	0.78	0.69	0.67

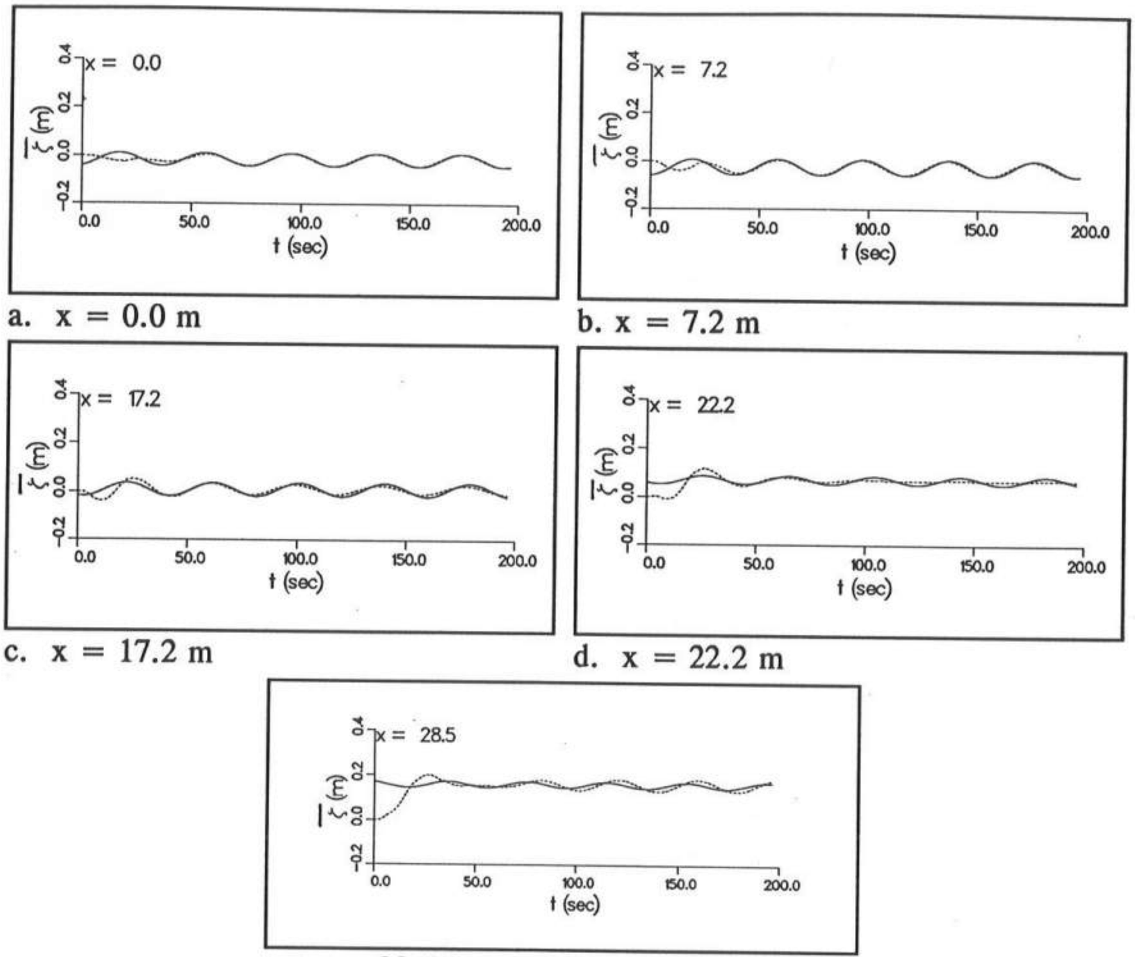

a. x = 0.0 m

b. x = 7.2 m

c. x = 17.2 m

d. x = 22.2 m

e. x = 28.5 m

Figure 5.9. Case 2 time series of water surface from depth-integrated and analytic Schäffer-Svendsen models for selected locations (solid line -- analytic surf beat solution, dashed line -- numerical solution)

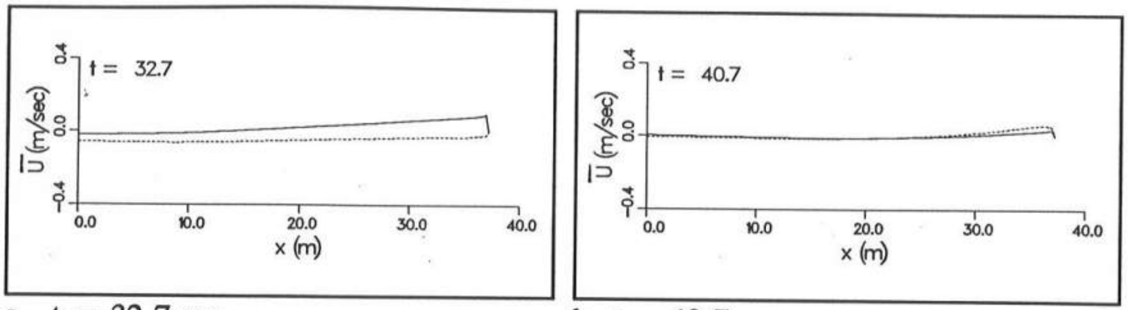

a. t = 32.7 sec

b. t = 40.7 sec

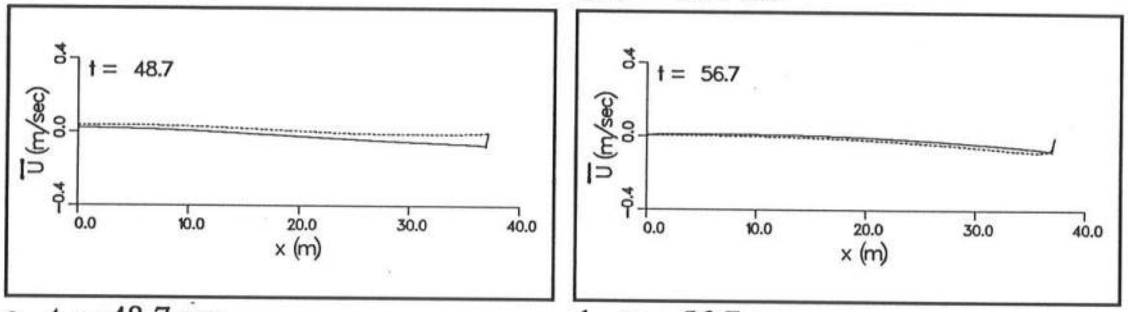

c. t = 48.7 sec

d. t = 56.7 sec

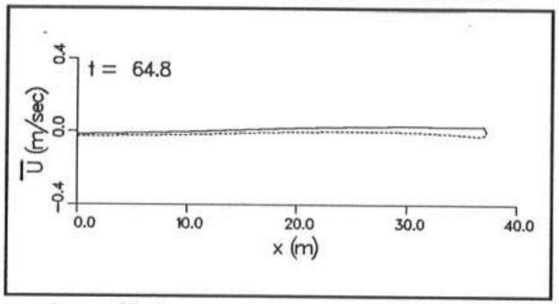

e. t = 64.8 sec

Figure 5.10. Case 2 snapshots depth-integrated velocity from depth-integrated and analytic Schäffer-Svendsen models (solid line -- analytic surf beat solution, dashed line -- numerical solution)

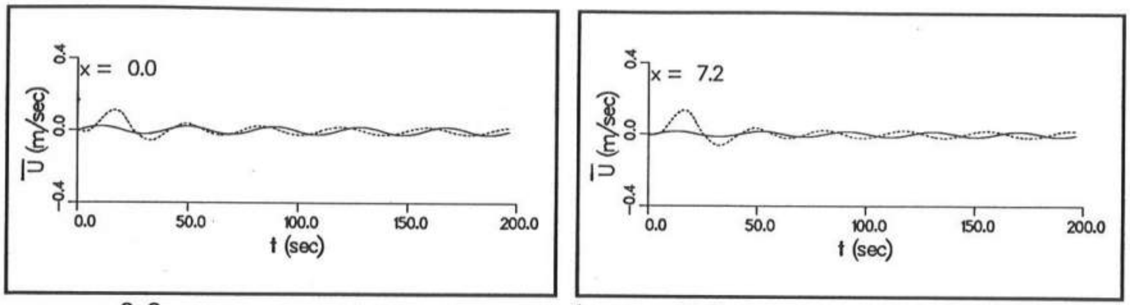

a. x = 0.0 m

b. x = 7.2 m

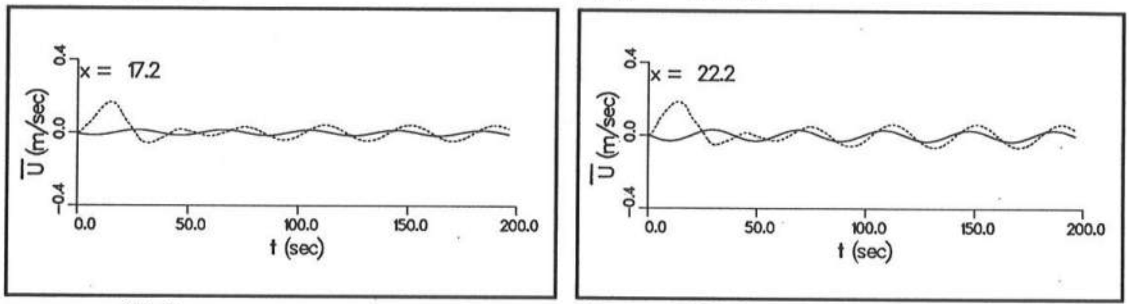

c. x = 17.2 m

d. x = 22.2 m

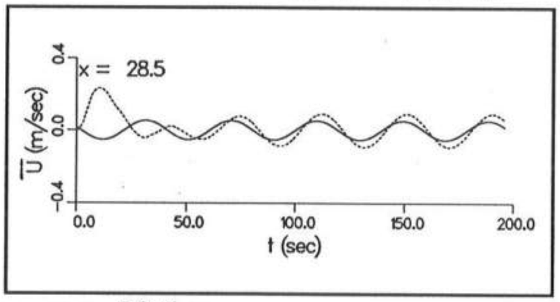

e. x = 28.5 m

Figure 5.11. Case 2 time series of depth-integrated velocity from depth-integrated and analytic Schäffer-Svendsen models for selected locations (solid line -- analytic surf beat solution, dashed line -- numerical solution)

Case 3

The surf beat input parameters for Case 3 are listed in Table 5.1. The surf beat output is shown in Figure 5.12. The grid spacing used in both the surf beat and Lax-Wendroff models was $\Delta x = 0.25$ m and $nx = 150$. The time step used in the Lax-Wendroff model was $\Delta t = 0.035$ sec. The maximum Courant number was 0.76. The configuration of Case 3 is similar to Case 2, but the period of the infragravity wave is 21 sec, versus 39 sec for Case 2. Consequently, the infragravity wave is shorter and the surf beat solution, shown in Figure 5.12 now has both a node and anti-node in the surf zone.

Figures 5.13a-e give snapshots of the infragravity surface elevations over one wave period. The solution is similar to Case 2, although the gradients in water surface are greater. Figure 5.14 shows time series for five locations. The time series show good agreement in phase and magnitude. The errors in elevation are reported in Table 5.4. Figures 5.15 and 5.16 give snapshot and time series plots for the depth-integrated velocity for Case 3. Errors are given in Table 5.4. As seen in Case 2, errors in velocity increase near the shoreline. Generally, the agreement is good.

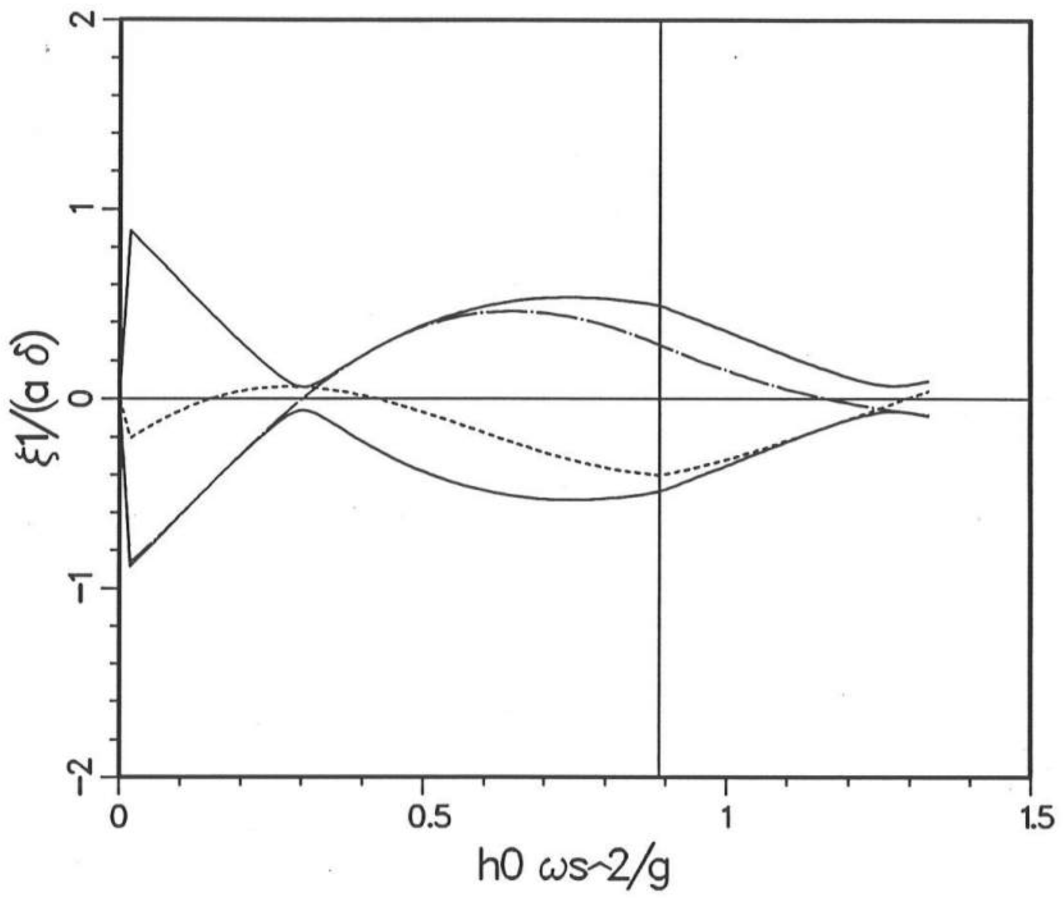

Figure 5.12. Case 3: nondimensional surf beat envelope for Schäffer-Svendsen model, $\pm|\xi_1/(\delta a_\infty)|$ -- solid line, $\xi_1/(\delta a_\infty)$ at $t = 0$ and $-T/4$ -- dashed and chain-dot lines

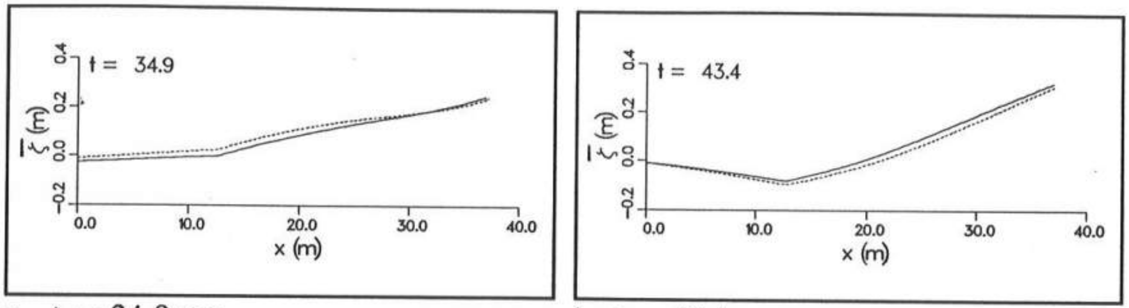

a. t = 34.9 sec

b. t = 43.4 sec

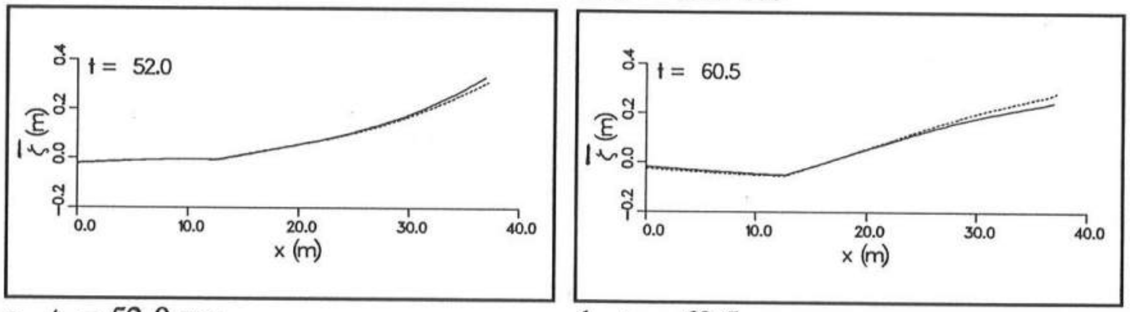

c. t = 52.0 sec

d. t = 60.5 sec

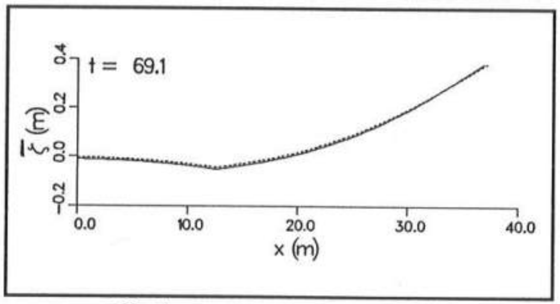

e. t = 69.1 sec

Figure 5.13. Case 3 snapshots of water surface elevation from depth-integrated and analytic Schäffer-Svendsen models (solid line -- analytic surf beat solution, dashed line -- numerical solution)

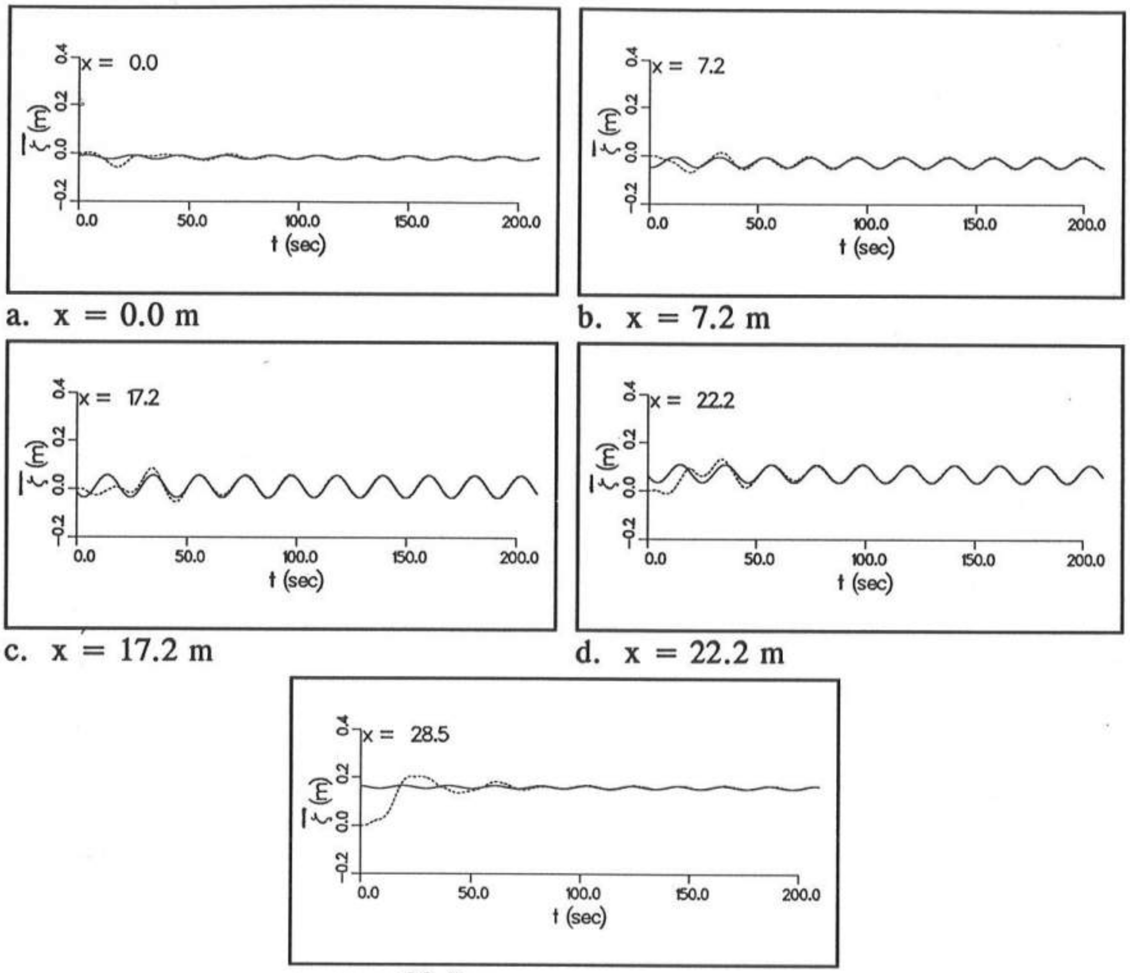

a. x = 0.0 m

b. x = 7.2 m

c. x = 17.2 m

d. x = 22.2 m

e. x = 28.5 m

Figure 5.14. Case 3 time series of water surface from depth-integrated and analytic Schäffer-Svendsen models for selected locations (solid line -- analytic surf beat solution, dashed line -- numerical solution)

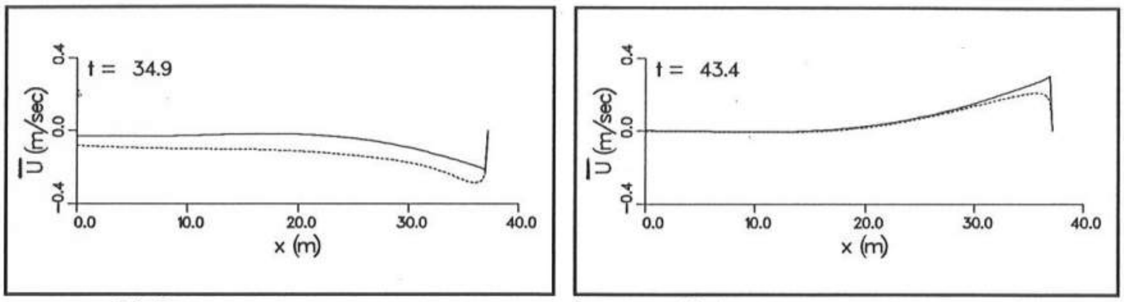

a. t = 34.9 sec b. t = 43.4 sec

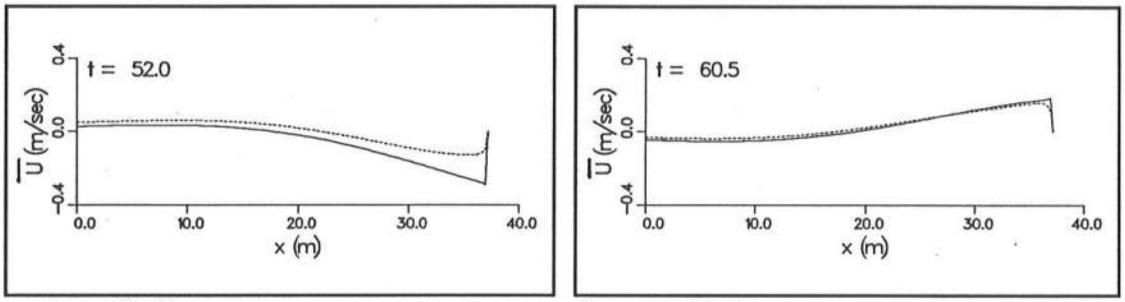

c. t = 52.0 sec d. t = 60.5 sec

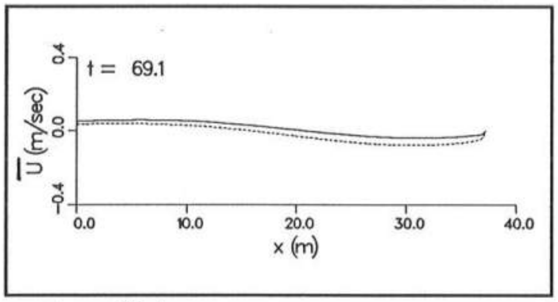

e. t = 69.1 sec

Figure 5.15. Case 3 snapshots of depth-integrated velocity from depth-integrated and analytic Schäffer-Svendsen models (solid line -- analytic surf beat solution, dashed line -- numerical solution)

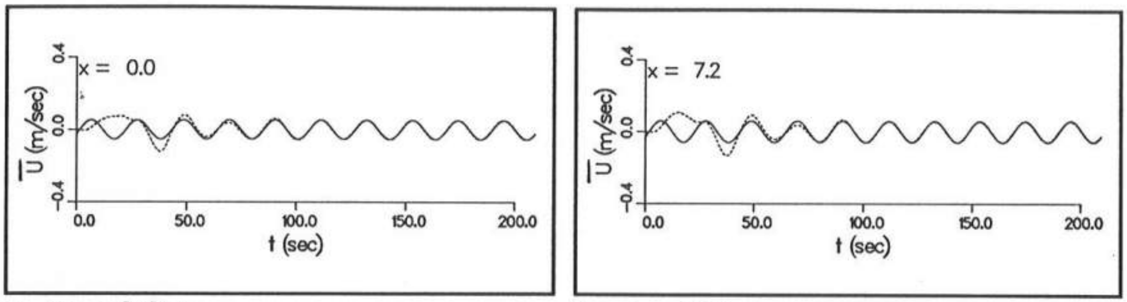

a. x = 0.0 m

b. x = 7.2 m

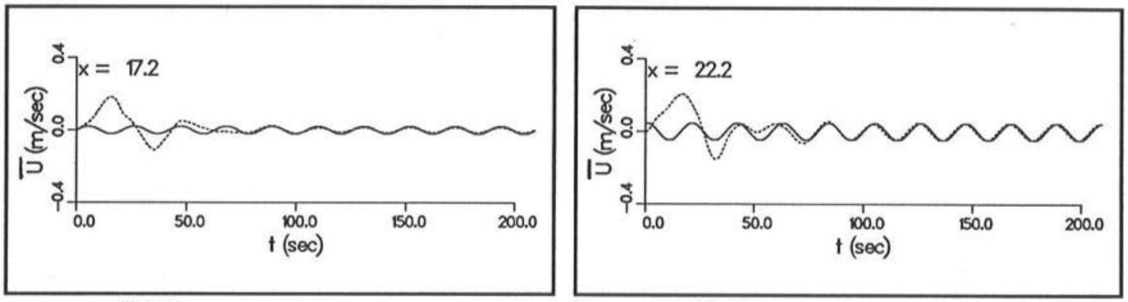

c. x = 17.2 m

d. x = 22.2 m

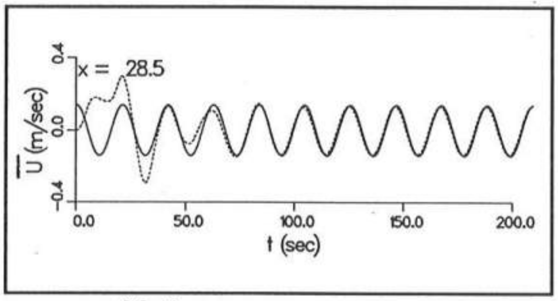

e. x = 28.5 m

Figure 5.16. Case 3 time series of depth-integrated velocity from depth-integrated and analytic Schäffer-Svendsen models for selected locations (solid line -- analytic surf beat solution, dashed line -- numerical solution)

Table 5.4. Lax-Wendroff error for Case 3

x, m	7.5	17.5	22.5	28.8	35.0
$E_{\overline{\zeta},m}$, %	0.02	-0.03	0.01	0.03	0.05
$E_{\overline{\zeta},rms}$, %	0.78	0.39	0.36	0.43	0.63
$E_{\overline{U},m}$, %	0.04	0.02	0.001	-0.01	-0.03
$E_{\overline{U},rms}$, %	0.62	0.46	0.45	0.53	0.78

5.1.4 Profile model surf beat results

The profile model, described in Chapter 4, was also run for Cases 2 and 3. The model was driven with output from the Lax-Wendroff model. The number of eigenvectors used was 20, and the number of points solved over the depth was 21. Results for Cases 2 and 3 are given in Figures 5.17 and 5.18, respectively. Both figures show similar trends. The figures show velocity profiles over an entire infragravity wave cycle. Both mean and time-varying forcing have been applied.

In the region outside the surf zone ($x = 7.25$ m), the velocity profiles "lean" offshore at the surface and are fairly uniform over the lower two-thirds of the depth. This is due to an increasing amplitude of the short waves, and thus a

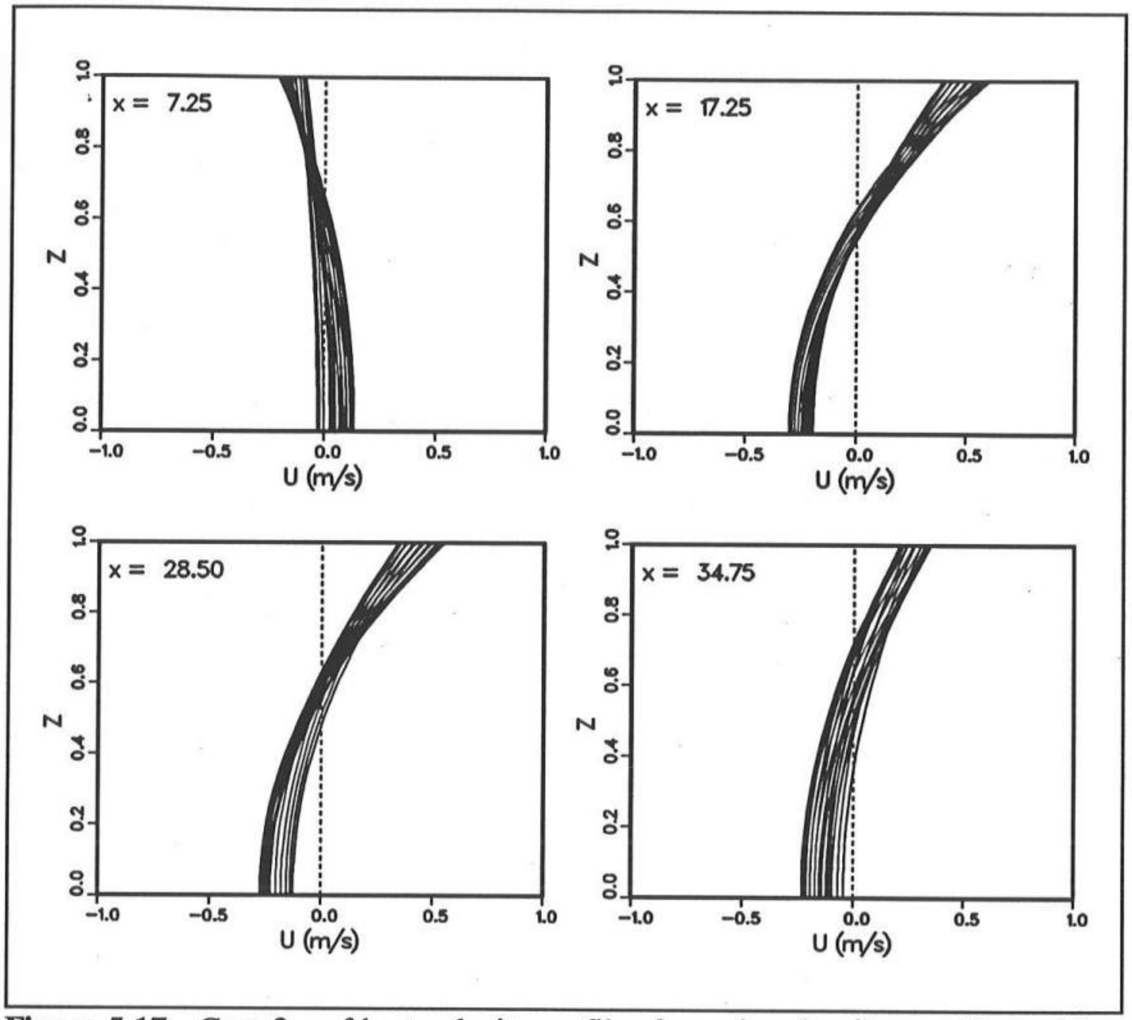

Figure 5.17. Case 2 surf beat velocity profiles from eigenfunction profile model at locations outside and through the surf zone

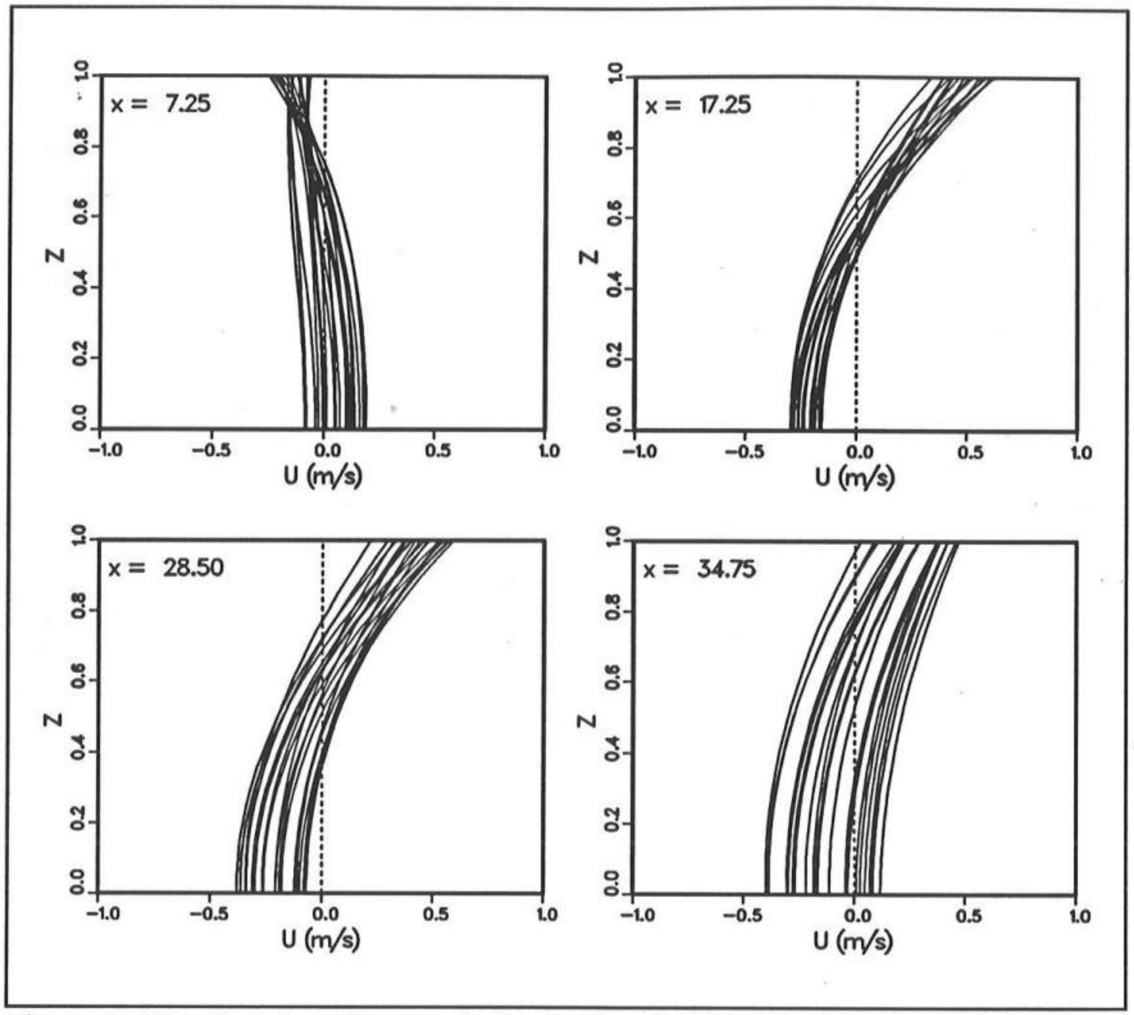

Figure 5.18. Case 3 surf beat velocity profiles from eigenfunction profile model at locations outside and through the surf zone

positive gradient in the radiation stress. Since the water depth is relatively deep in this region, the surface stress does not greatly impact the velocity distribution near the bottom.

In the region from the outer to mid surf zone ($x = 17.25$ m and $x = 28.5$ m), the velocity profiles exhibit the classical parabolic undertow shape with offshore flow near the bottom and onshore flow near the surface. The shape is driven by the breaking-induced decrease in the radiation stress. The mean radiation stress gradient is dominant. The mean flows are zero since this is a closed system with no inflow or outflow. The surface stress continues to dominate the velocity profiles in this region. The surface stress is strong and depths are shallower, so the surface effects reach near the bottom.

In the very nearshore region ($x = 34.75$ m), the behavior of the profiles changes again. In this region, the time-varying radiation stress forcing is reduced because the short waves are small. The dominant forcing is depth uniform and due to the gradients in the infragravity wave elevation (strong nodes and antinodes in the inner surf zone). The resultant velocity profiles are less curved. The top and bottom of the profiles also tend to be in phase.

In the next section, the mean forcing will be neglected. The time-varying results will be discussed in greater detail.

5.2 Putrevu and Svendsen Periodic Profile Model

Putrevu and Svendsen (1995) developed an infragravity velocity profile model for the surf zone which assumes periodicity in the forcing functions. The velocity profiles are driven by radiation stress gradients and free and forced infragravity waves. The model assumptions and governing equations are similar to the profile model described in Chapter 3. The solution method is different in that it assumes periodicity in all driving forces (i.e., periodic wave groups). Although the periodicity is the same in all driving forces, the relative phase of the surface stress forcing and the depth uniform forcing can vary and must be specified.

5.2.1 Putrevu-Svendsen model description

The governing equation for the Putrevu-Svendsen profile model is Equation 4.1. The model was developed assuming a gently sloping beach, a long straight coast (longshore homogeneity) with normal wave incidence, shallow water (pressure variation in the infragravity waves is hydrostatic under the free surface), and Reynolds' stresses are parameterized by an eddy viscosity ν_t . Only the time-varying solution, $U_1(z)$, is developed by Putrevu and Svendsen, mean water surface elevations and velocities are neglected. The steady solution could be linearly added. The boundary conditions in z are given by Equations 4.2 and 4.3, with a slight difference in the bottom friction formulation ($\tau_b = 0.5 \rho f_{cw} u_o U_{-ho}$). The initial condition, Equation 4.4, is replaced with the assumption of periodicity in time.

All components of the infragravity wave problem, U_1, $\overline{\zeta}_1$, τ_s, u_w^2, and f (see Chapter 4 for definitions) are assumed to have the form

$$\psi = \psi_a \, e^{-i\omega t} \tag{5.18}$$

where ω is the infragravity wave frequency, ψ is a dummy variable which represents any of the components listed above, and ψ_a is the component amplitude, which may be a function of x and z. The radiation stress forcing terms τ_s and u_w^2 are in phase with the short-wave temporal variation. The surface elevation gradient term will not in general be in phase with the short-wave variation. The surface elevation includes both forced- and free-wave components. The component phasing is selected so that f_a is maximum at $t = 0$ and the surface stress is defined

$$(\tau_s)_a = T_s \, e^{-i\Delta} \tag{5.19}$$

where Δ is the phase of τ_s relative to f_a and T_s is the surface stress amplitude.

The infragravity velocity profile amplitude, U_a, is split into three parts

$$U_a = U_{a1} + U_{a2} + U_{a3} \tag{5.20}$$

and the time-varying velocity profile is given by $U_1 = \mathrm{Re}(U_a \, e^{-i\omega t})$. The first part of the solution, U_{a1} , represents the depth uniform response to the depth uniform forcing and is given by

$$U_{a1} = \frac{-f_a}{i\,\omega} \tag{5.21}$$

This is a particular solution to the governing equation.

The second and third components of the solution, U_{a2} and U_{a3} , are homogeneous solutions which are subject to the inhomogeneous boundary conditions at the bottom and surface (Equations 4.2 and 4.3), respectively. The solution for U_{a2} is given by

$$U_{a2} = \frac{T_s}{\rho\, \nu_t\, \beta \sqrt{2}}\, F_2(z)\, e^{i(\phi_B + \phi_2)} \tag{5.22}$$

where

$$\beta = \sqrt{\frac{\omega}{2\,\nu_t}} \tag{5.23}$$

$$F_2 = \frac{\sqrt{\cos^2(\beta\,(z+h_0)) + \sinh^2(\beta\,(z+h_0))}}{\sqrt{\sinh^2(\beta\,h_0) + \sin^2(\beta\,h_0)}} \tag{5.24}$$

$$\phi_B = -\left(\Delta + \frac{5\,\pi}{4} + \tan^{-1}\left(\frac{\sinh\beta\,h_0\,\cos\beta\,h_0}{\cosh\beta\,h_0\,\sin\beta\,h_0}\right)\right) \tag{5.25}$$

$$\phi_2 = \tan^{-1}\left(\frac{-\sinh\beta\,(z+h_0)\ \sin\beta\,(z+h_0)}{\cosh\beta\,(z+h_0)\ \cos\beta\,(z+h_0)}\right) \tag{5.26}$$

The solution for U_{a3} is given by

$$U_{a3} = \frac{f_{cw}u_o U_{1B}}{2\nu_t\beta}\,F_3(z)\,e^{-i(\Delta_B+\phi_F-\phi_3)} \tag{5.27}$$

where

$$F_3(z) = \frac{\sqrt{\cos^2\beta\,(z-\overline{\zeta_0}) + \sinh^2\beta\,(z-\overline{\zeta_0})}}{\sqrt{2(\sinh^2\beta h_0+\sin^2\beta h_0)+\left(\frac{f_{cw}u_o}{2\nu_t\beta}\right)^2(\cos^2\beta h_0+\sinh^2\beta h_0)-\left(\frac{f_{cw}u_o}{2\nu_t\beta}\right)(\sin 2\beta h_0-\sinh 2\beta h_0)}} \tag{5.28}$$

$$\phi_F = \tan^{-1}\left(\frac{\sin\beta h_0\cosh\beta h_0 + \cos\beta h_0\sinh\beta h_0 + \frac{f_{cw}u_o}{2\nu_t\beta}\sin\beta h_0\sinh\beta h_0}{\sin\beta h_0\cosh\beta h_0 - \cos\beta h_0\sinh\beta h_0 - \frac{f_{cw}u_o}{2\nu_t\beta}\cos\beta h_0\cosh\beta h_0}\right) \tag{5.29}$$

$$\phi_3 = \tan^{-1}\left(\frac{-\sinh\beta\,(z-\overline{\zeta_0})\sin\beta\,(z-\overline{\zeta_0})}{\cosh\beta\,(z-\overline{\zeta_0})\cos\beta\,(z-\overline{\zeta_0})}\right) \tag{5.30}$$

and where $\overline{\zeta_0}$ is the mean water surface elevation, and U_{1B} and Δ_B are determined by the solutions for U_{a1} and U_{a2}

$$U_{1B}\, e^{-i\Delta_B} = U_{a1} + U_{a2}(z=-h_0) \tag{5.31}$$

The full solution for the velocity profile is then given by

$$\begin{aligned} U_1 = {} & \frac{f_a}{\omega}\cos\left(\omega t - \frac{\pi}{2}\right) + \frac{\sqrt{2}\,T_s\,\beta}{\omega\,\rho}F_2\cos(\omega t - \phi_B - \phi_2) + \\ & \frac{f_{cw}\,u_o\,U_{1B}}{2\,\nu_t\,\beta}F_3\cos(\omega t + \Delta_B + \phi_F - \phi_3) \end{aligned} \tag{5.32}$$

The shape of the velocity profiles is determined by the relative magnitudes of the three velocity terms U_{a1}, U_{a2}, and U_{a3} , the depth variation given by F_2 and F_3 , and the relative phase between terms determined by Δ.

5.2.2 Application of Putrevu-Svendsen and eigenfunction profile models to surf beat

Putrevu and Svendsen (1995) present three dimensionless parameters that determine the relative importance of the three terms in Equation 5.32. The first parameter is f_a/g, which is the forcing that is uniform over depth. The depth-uniform forcing is composed of gradients in the infragravity water surface elevations and the radiation stress below the mean water level (gradient of the first term on the right-hand side of Equation 4.46 or by Equation 4.47). The second parameter is $P_1 = \sqrt{2}\ T_s\ \beta/(\rho\ g)$, which is the surface stress forcing. The surface stress forcing is the shear at the mean water level due to the radiation stress above the mean water level and is the gradient of the second term on the right-hand side of Equation 4.46 or by Equation 4.48. The third parameter is $P_2 = f_{cw}\, u_o/(2\, \nu_t\, \beta)$, which is the bottom stress forcing (Equation 2.37) which resists the flow. In this section we will look at the relative importance of these three parameters for the surf beat Cases 2 and 3. Also, the results from the Putrevu-Svendsen model will be compared with the eigenfunction model derived in Chapter 4.

Case 2

Figure 5.19 shows the three parameters discussed above as a function of x for surf beat Case 2. The top figure shows the relationship of the two major parameters, f_a/g (solid line) and P_1 (dashed line). For orientation, the bottom plot shows the dimensionless envelope of the infragravity wave, $BA = |\xi_1|/(\delta a)$. A discontinuity occurs in the parameters at the breaker point. The surface stress term dominates the depth-uniform forcing outside the surf zone meaning that there is significant depth-variation in the velocity profiles. As the short waves decay in the surf zone, the surface stress term loses dominance because the surface stress is decaying in proportion to $H\, \partial H/\partial x$. In the inner surf zone there is a crossover point, and from there to the shoreline the depth uniform forcing dominates. This is because the short waves have decayed in this region, and the infragravity wave is approaching an anti-node at the shoreline (the gradient in the infragravity wave surface elevation is the main depth-uniform forcing).

Figure 5.20 shows the ratio of the surface forcing to the depth uniform forcing (solid line). The cross-over point from surface forcing dominance to the

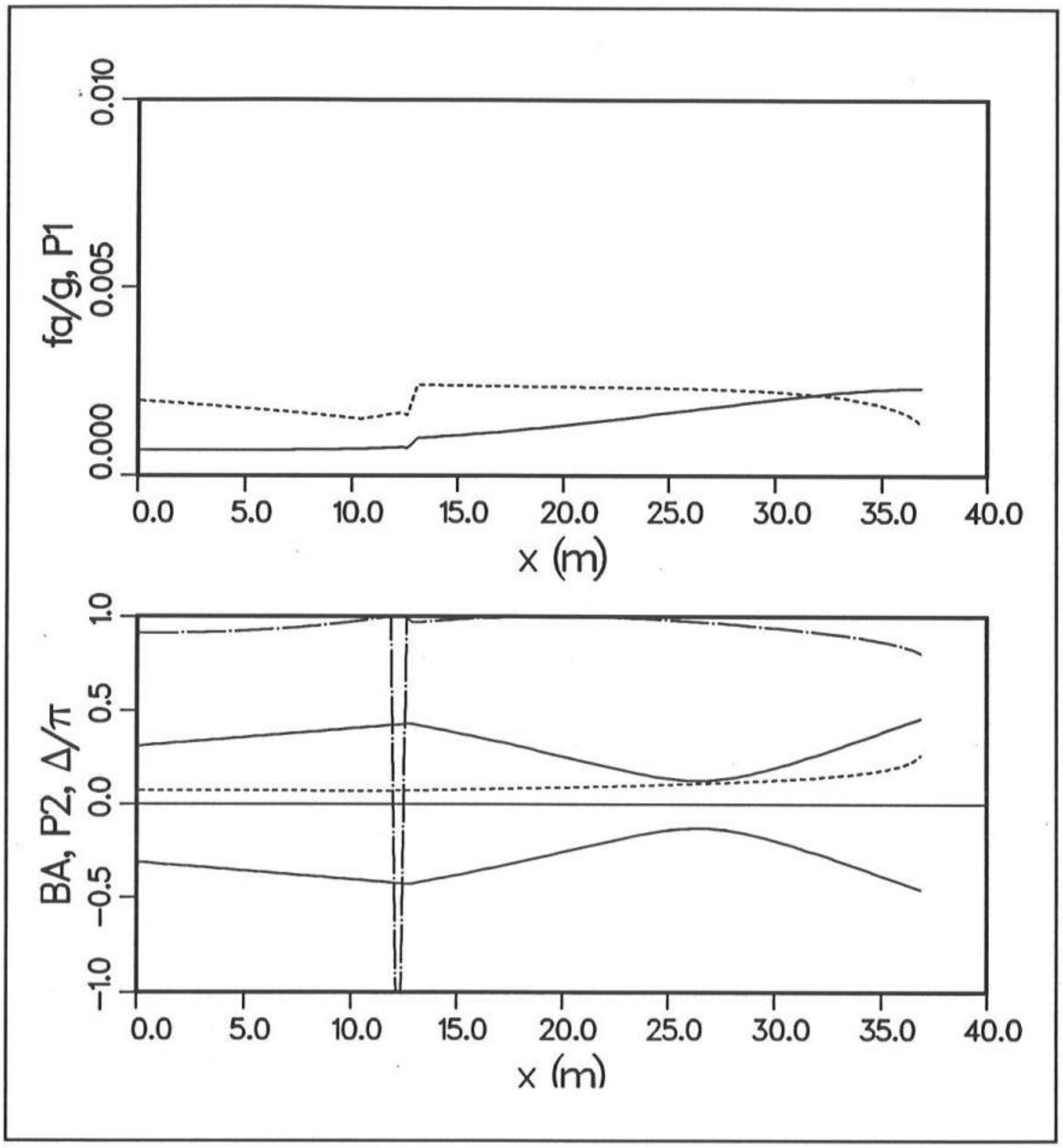

Figure 5.19. Case 2: velocity profile parameters, top: solid line -- f_a/g (depth-uniform forcing), dashed line -- $P_1 = \sqrt{2}\, T_s\, \beta/(\rho g)$ (surface stress forcing), bottom: solid line -- *BA* (surf beat envelope), dashed line -- $f_{cw}\, u_o/(2\, \nu_t\, \beta)$ (bottom friction), chain dot line -- Δ/π (relative phase of surface stress and depth-uniform forcing)

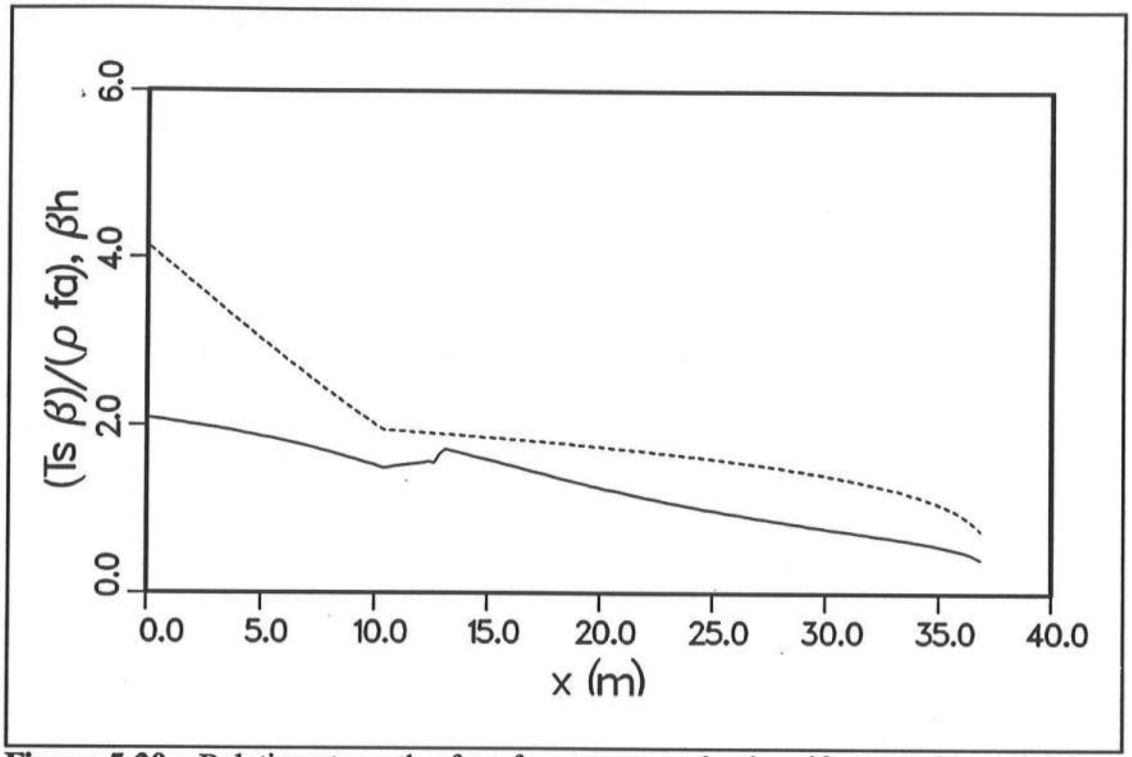

Figure 5.20. Relative strength of surface stress to depth-uniform surf beat forcing for Case 2 (dashed line -- βh, solid line -- $(T_s \beta)/(\rho f_a)$)

depth-uniform forcing dominance occurs at a ratio equal to $1/\sqrt{2}$, as seen from taking the ratio of the amplitudes of Equations 5.21 and 5.22.

The lower plot in Figure 5.19 shows the parameter P_2 , which is approximately constant through the surf zone. The relative phase, Δ, between f_a and P_1 is also shown in Figure 5.19. The typical value of Δ is approximately π, meaning that the depth-uniform and surface stress forcing are out of phase. This is expected for a case with $\kappa = 0$, since the infragravity wave would setdown under high wave groups and vice versa. The relative phase changes at the breaker line and at the shoreline.

The dashed line in Figure 5.20 shows the variation of βh with x. The parameter β (Equation 5.23) is analogous to the parameter used in the solution for wave boundary layers (Putrevu and Svendsen 1995, Longuet-Higgins 1953). The parameter βh is inversely related to the depth to which surface and bottom stresses influence the velocity profiles. Small values of βh indicate surface and bottom stress impact the entire water column, and large values indicate the impacts are localized near the boundary.

To compare the Putrevu-Svendsen and eigenfunction models, the surf beat model described in Section 5.1 was used to determine the variation of short- and long-wave amplitudes and phases in the profile models. Only the time-varying forcing was applied, so mean forcing was neglected. The results of the Putrevu-Svendsen model are given in Figure 5.21, and the results of the eigenfunction model are given in Figure 5.22. In the plots, the velocities have been

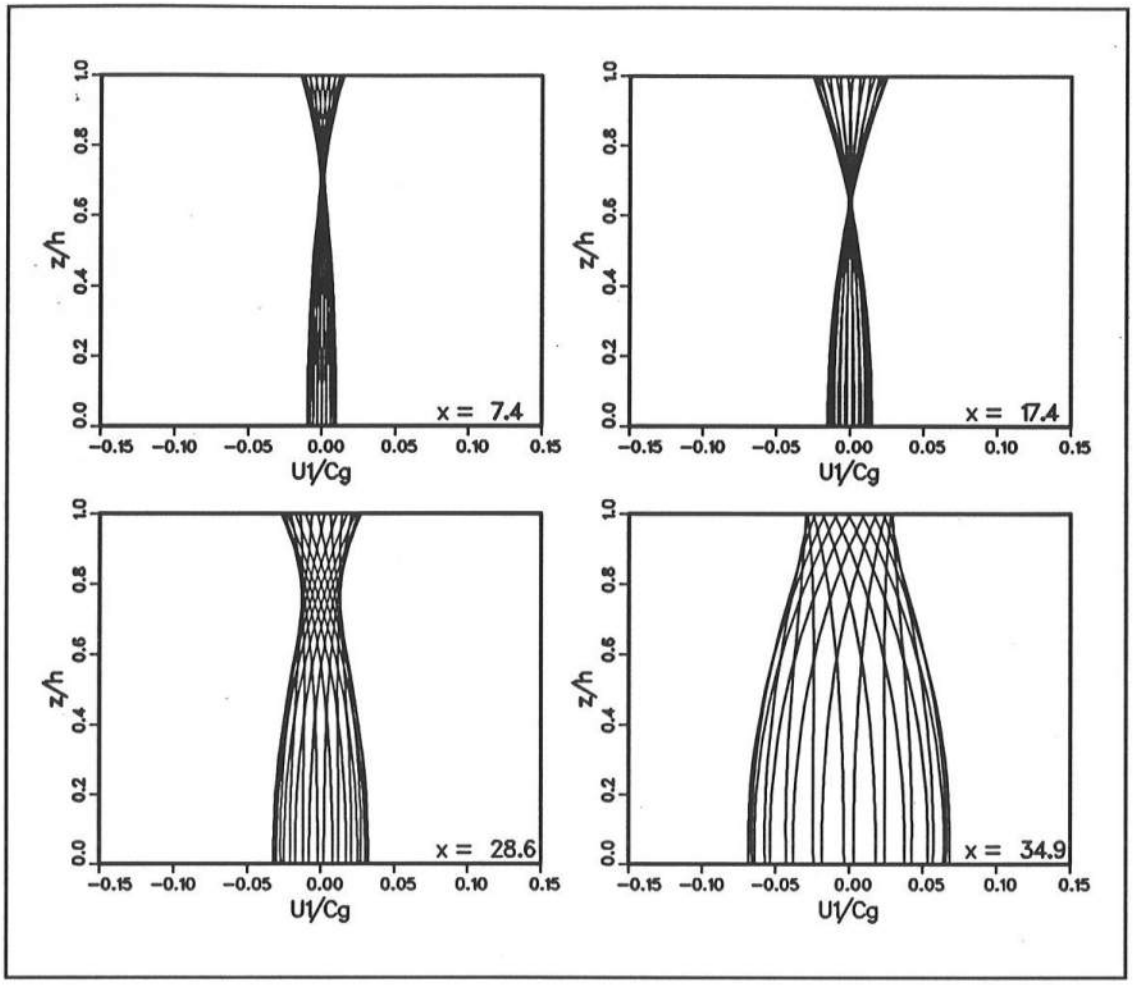

Figure 5.21. Putrevu-Svendsen time-varying velocity profiles for Case 2 surf beat forcing for locations outside and through the surf zone

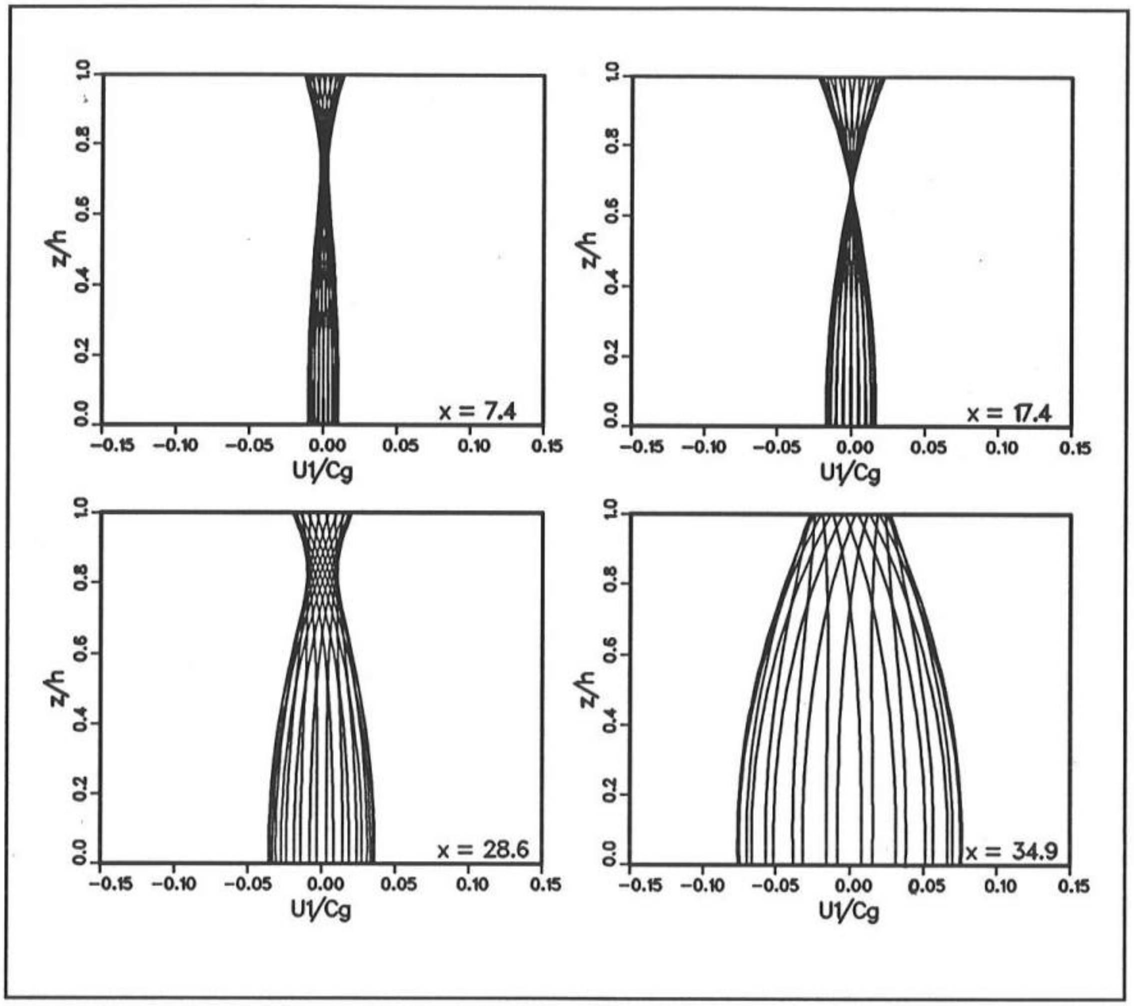

Figure 5.22. Eigenfunction time-varying velocity profiles for Case 2 surf beat forcing for locations outside and through the surf zone

nondimensionalized by the group velocity and the elevation, measured from bottom, has been nondimensionalized by the still-water depth.

Both models produce expected results. Outside the surf zone, the profiles are fairly uniform over depth with greater variation near the surface. The surface stress forcing is dominant, but the effect reaches only about one quarter of the water column. Progressing through the surf zone, the depth-uniform forcing becomes more and more important, and the profile variation becomes more uniform over depth.

The results from the two models are the same. The major difference between the models is that the Putrevu-Svendsen model assumes that all forcing components have the same periodicity, while the eigenfunction model does not. For the Schäffer-Svendsen surf beat input, the forcing components do have the same periodicity.

Case 3

The parameters for Case 3 are shown in Figures 5.23 and 5.24. The difference between Cases 2 and 3 is the long-wave period for Case 3 is approximately half the period for Case 2. This means that the wave length for Case 3 is shorter, and thus, nodes and antinodes for both the long-wave surface elevation and the short-wave groups are captured in the surf zone. This gives larger gradients in the long-wave elevations and short-wave groups and greater forcing. The short-wave breaking characteristics are similar in both cases. For Case 3, the dominance of the surface stress term is more pronounced outside the

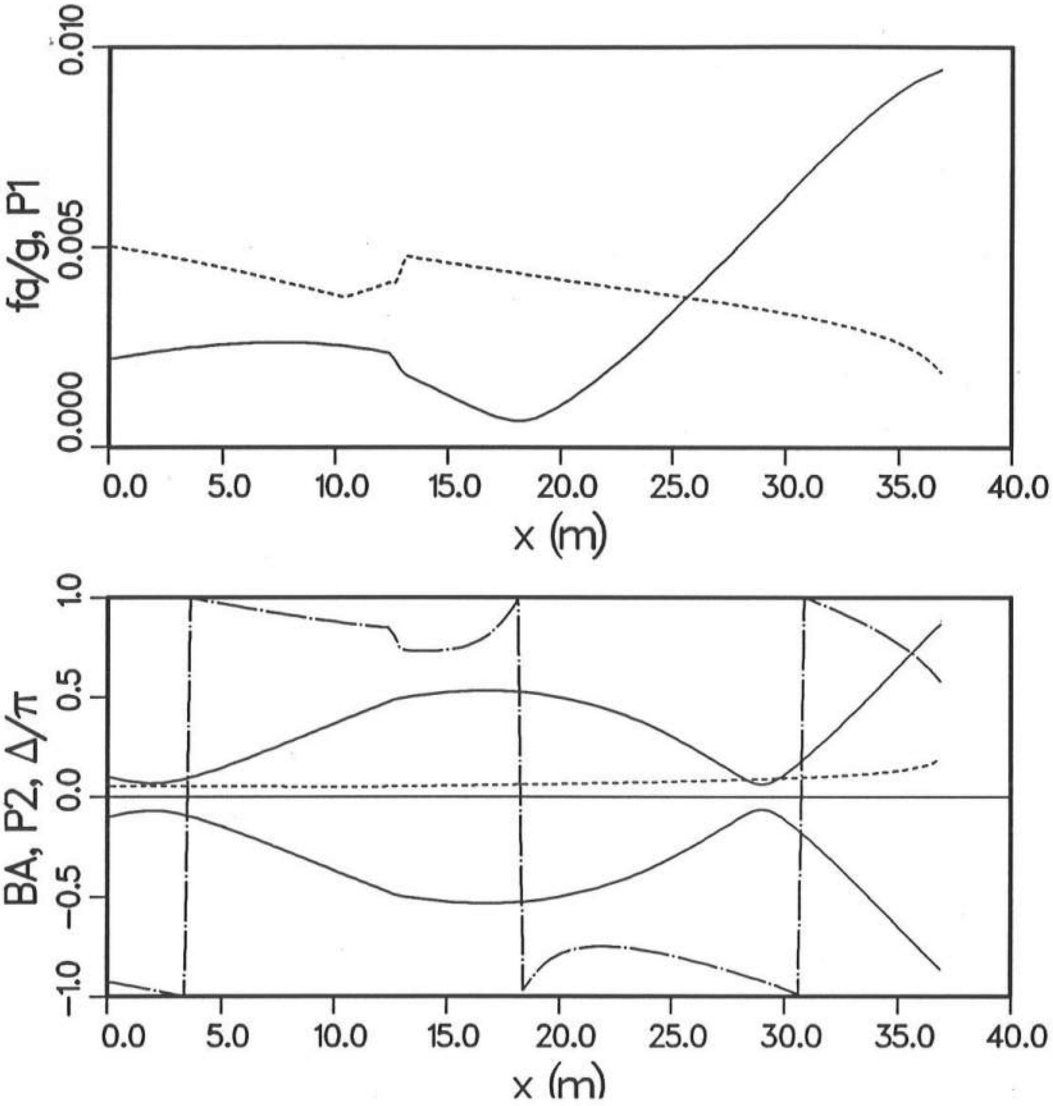

Figure 5.23. Case 3: velocity profile parameters, top: solid line -- f_a/g (depth-uniform forcing), dashed line -- $P_1 = \sqrt{2}\ T_s\ \beta/(\rho g)$ (surface stress forcing), bottom: solid line -- *BA* (surf beat envelope), dashed line -- $f_{cw}\ u_o/(2\ \nu_t\ \beta)$ (bottom friction), chain dot line -- Δ/π (relative phase of surface stress and depth-uniform forcing)

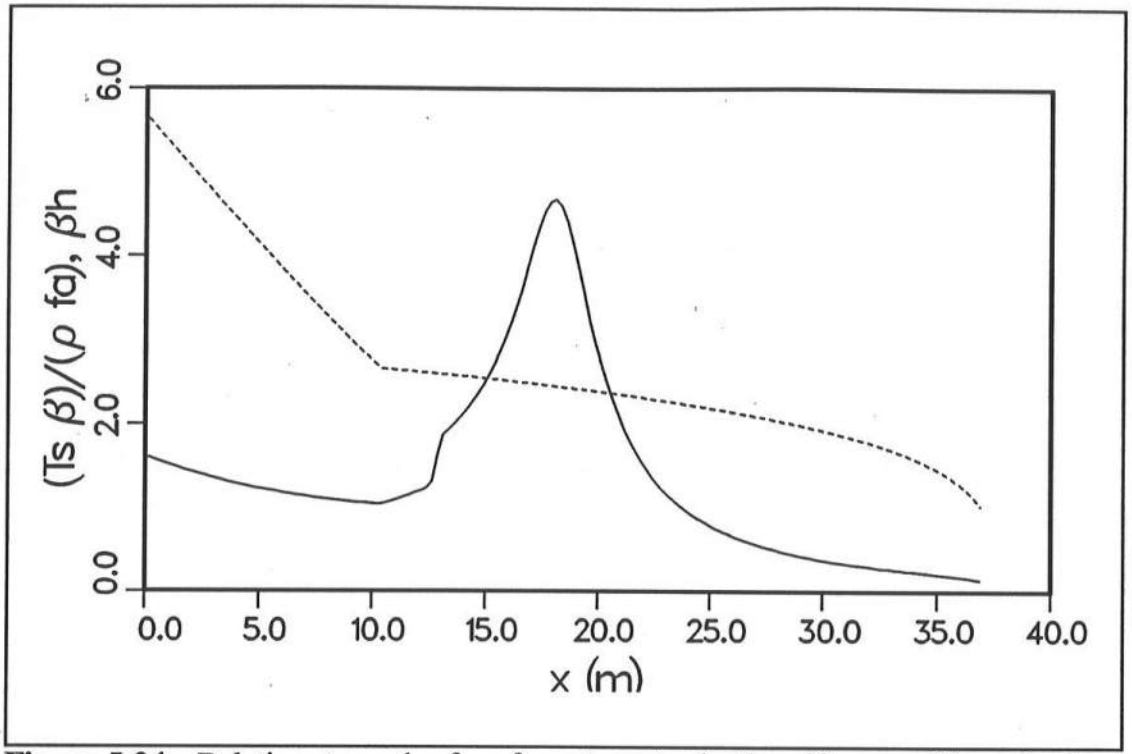

Figure 5.24. Relative strength of surface stress to depth-uniform surf beat forcing for Case 3 (dashed line -- βh, solid line -- $(T_s \beta)/(\rho f_a)$)

surf zone and in the outer surf zone. Also, the switch to dominance of the depth-uniform forcing is also more pronounced. The overall trends for Case 3 are similar to Case 2.

The plots of the velocity profiles (Figures 5.25 and 5.26) show the progression from surface stress dominance to depth-uniform forcing dominance from outside the surf zone to the shoreline.

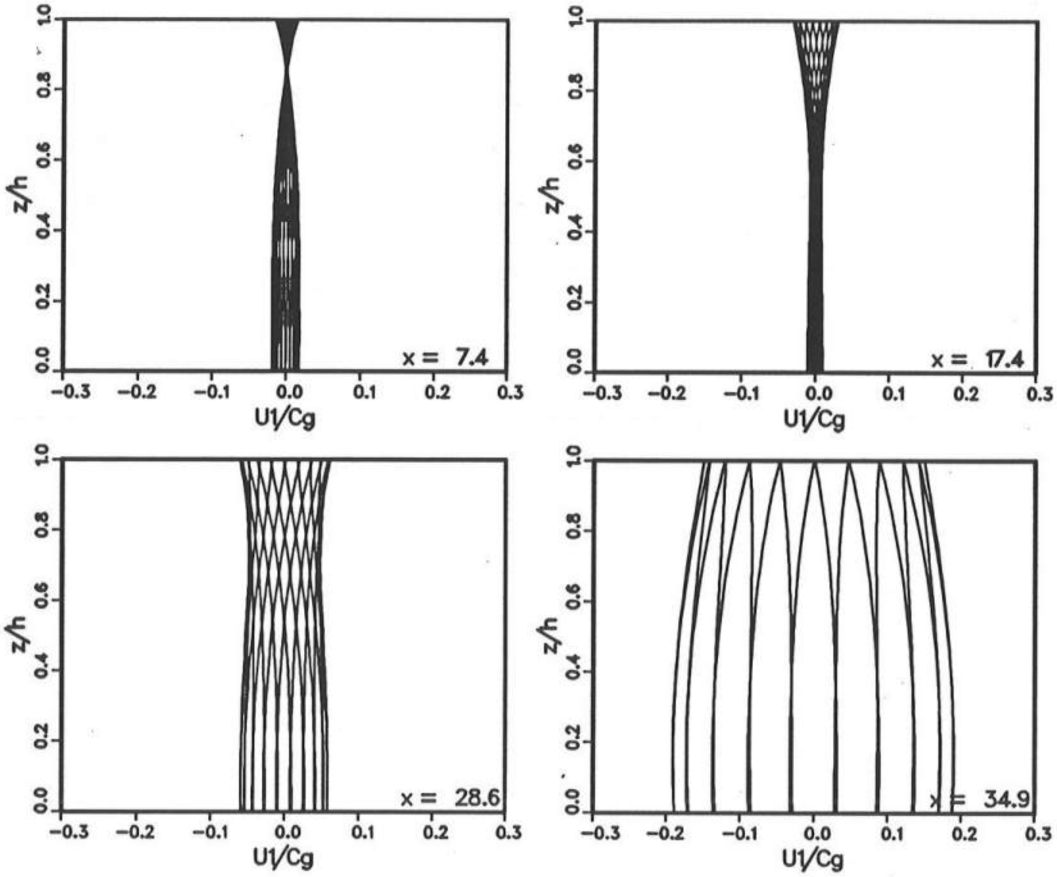

Figure 5.25. Putrevu-Svendsen time-varying velocity profiles for Case 3 surf beat forcing for locations outside and through the surf zone

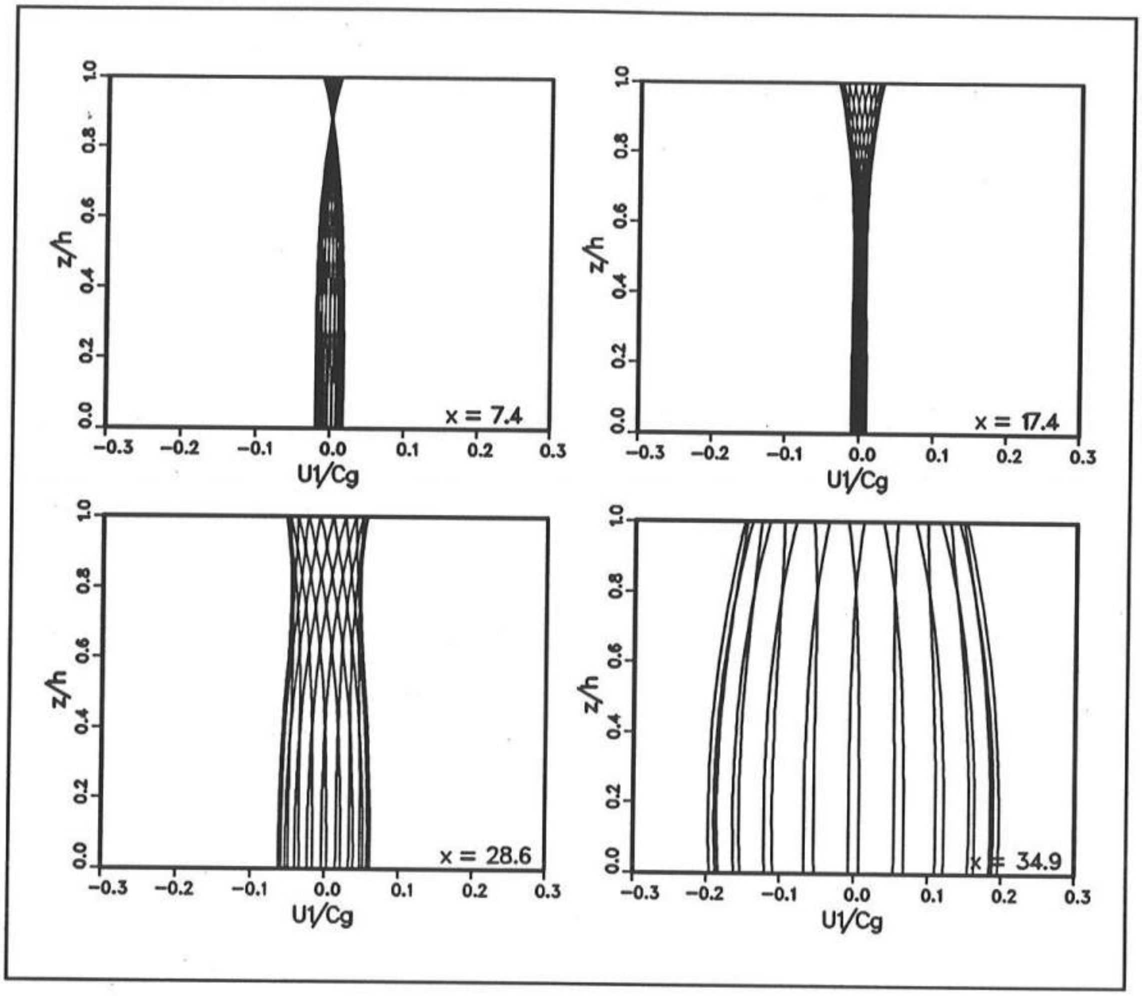

Figure 5.26. Eigenfunction time-varying velocity profiles for Case 3 surf beat forcing for locations outside and through the surf zone

Chapter 6

SUPERTANK LABORATORY DATA COLLECTION PROJECT

The SUPERTANK Laboratory Data Collection Project was conducted by the U.S. Army Engineer Waterways Experiment Station, Coastal Engineering Research Center (CERC), in the large wave channel at O.H. Hinsdale Wave Research Laboratory, Oregon State University (OSU), during August and September 1991 (Kraus et al. 1992, Kraus and Smith 1994, Smith and Kraus 1995). The purpose of SUPERTANK was to collect data unbiased by scaling distortions to verify and refine existing predictive technology and provide data and insight on detailed physical processes for development of the next generation of coastal processes numerical and physical models. The specific objectives of SUPERTANK were to: (a) collect data to verify and improve existing macro-scale beach profile change numerical simulation models; (b) collect data to develop advanced hydrodynamic, cross-shore sand transport, and meso-scale beach profile change numerical simulation models; (c) collect data to quantify performance of sandbars constructed offshore as a beneficial use of dredged material; (d) test and compare sediment-sensing acoustic instruments in a controlled, field-scale environment in support of dredging research; and (e) collect data to improve understanding of micro-scale fluid and sand motion. SUPERTANK was conducted as a multi-institutional effort, pooling expertise, instrumentation, and a wide range of research interests.

This chapter gives an overview of SUPERTANK, and then describes hydrodynamic data collection and data analysis. SUPERTANK data were used to test the model components developed in Chapters 3 and 4. Model comparisons using the data are made in Chapter 7.

6.1 Experiment Overview

SUPERTANK was conducted in the large wave channel at OSU. The channel is 104 m long, 3.7 m wide, and 4.6 m deep and is enclosed in a building. For SUPERTANK, sand was trucked from the Oregon coast and placed in the channel. The channel was first partially filled with water so that the sand would fall through the water and become wetted and somewhat washed. The sand was very well-graded with a median diameter of 0.22 mm and a fall speed of 3.3 cm/sec. Some tree bark and other organic matter were contained in the sand. The sand was washed by running waves on the beach, then draining the tank, and repeating the procedure. Organic matter on the sand surface was removed. The beach was composed of approximately 600 m^3 of sand that formed a 76-m-long beach. Figure 6.1 shows a view of the wave channel during SUPERTANK.

Figure 6.1. View of the OSU wave channel during SUPERTANK

Waves were generated in the wave channel with a hydraulically-driven, hinged-flap wave board. The generator has direct digital control and is equipped to actively absorb reflected waves at the peak spectral period. Broad- and narrow-band random and monochromatic waves were run with zero-moment wave heights in the range 0.2 to 1.0 m and with peak spectral periods in the range of 3 to 10 sec. The TMA spectral shape (Bouws et al. 1985), applicable to finite water depths, was used to design random-wave tests, with spectral width parameter γ between 1 (broad-banded) and 100 (narrow-banded).

Waves were typically run in segments of 10-, 20-, 40- and 70-min duration. The choice of these run lengths was determined by the competing factors of long runs for efficiency and statistical confidence versus short runs to capture the beach profile evolution, prevent long-wave buildup, and produce reasonable data file sizes. Profile change proceeded rapidly at first and gradually slowed as the profiles assumed an equilibrium shape, therefore, the wave run intervals in a test series were short at first and gradually increased to record the change with profile surveys. Kriebel and Smith (1994) showed that long-period oscillations did occur during runs, but did not grow as a function of run length. The magnitudes of low-frequency wave heights were similar to those observed in the field.

Over a six-week period, 228 data runs were completed for a total of approximately 130 hours of wave action. The major test series were erosional waves, accretional waves, dune erosion, seawall impacts, suspended sediment transport, berm flooding, and wave attenuation by offshore mounds. At the peak of data collection activities, the wave channel was instrumented with 16 resistance wave gauges, 10 capacitance wave gauges, 18 two-component electromagnetic current meters, 34 optical backscatter sensors, 10 pore-pressure gauges, 3 acoustic sediment concentration profilers, 1 acoustic Doppler current profiler, 1 four-ring acoustic benthic stress gauge, 1 laser Doppler velocimeter, 5 video cameras, and 2 underwater video cameras. Synchronous sampling by separate data acquisition systems was accomplished by digital input of a WWV time code (broadcast by the National Institute of Standards and Technology, Fort Collins, Colorado) to all computer clocks.

The beach profile was surveyed with an auto-tracking, infrared Geodimeter positioned at the shoreward end of the wave channel. The Geodimeter targeted a prism attached to the top of a survey rod mounted on a manually operated carriage. The survey rod, which moved freely in a supporting roller guide, made contact with the bed through a pair of wide-tread rubber wheels. x, y, z survey coordinates were collected automatically on a personal computer connected to the Geodimeter. The nominal horizontal survey spacing was 0.3 m, with finer resolution of steep features such as bars and dunes. The beach profile was surveyed along the center line of the channel. Occasionally, additional lines located 0.9 m from each of the channel walls were surveyed to assess uniformity of the profile across the channel. Beach profile data were visually checked for obvious errors (e.g., occasionally, the survey rod would stick and the wheels were not touching the bottom). These points were removed and replaced through nearest neighbor interpolation.

6.2 Hydrodynamic Data Collection

At SUPERTANK, waves and currents were measured along the wave channel with 16 resistance wave gauges and 18 electromagnetic current meters. Wave gauges were deployed at 3.66 m intervals from the mid surf zone to the wave paddle. The wave gauges measured the water surface elevation as a function of time to give wave height, wave period, and mean and time-varying water level throughout the channel. Current meters were deployed in vertical arrays inside and just outside the surf zone. The current meters measured the cross-shore and vertical water velocities as a function of time to give mean and time-varying current velocities.

6.2.1 Instrument description

Resistance wave gauges

Sixteen resistance wave gauges measured the elevation of the water surface to determine water level and wave parameters. The resistance wave gauges were fabricated by the staff of the O.H. Hinsdale Wave Research Laboratory (Dibble and Sollitt 1989). Each gauge was 2.1 m tall and consisted of two 0.69-mm seven-strand stainless steel cables, spaced 6.4 cm apart. The resistance gauges use the conductivity of the water to determine the water elevation. The resistance between the two wires is inversely proportional to the depth of water.

By monitoring the change in resistance, the water surface elevation was determined. Each gauge was driven by a constant amplitude AC voltage source and the current drawn by the gauge was measured. By Ohm's law, with the voltage held constant, the current is inversely proportional to the resistance or directly proportional to the water elevation. Current sensing is accomplished by measuring the voltage drop across a 1-ohm resistor placed in series with the gauge. The conversion from volts to engineering units is determined by calibration of the gauges, as described in Section 6.2.5.

Electromagnetic current meters

Cross-shore and vertical water velocities were measured with 18 Marsh-McBirney Model 512 electromagnetic current meters. Each current meter sensor consists of a 3.8-cm diameter sphere, which contains an electromagnet. Four electrodes are equally spaces around the sphere. The electromagnet generates a magnetic field, and, as the water (a conductor) flows through the magnetic field, it produces a voltage that is proportional to its velocity (Faraday principle). The voltage is detected with the electrodes. A rod containing the instrument cable is attached to the sphere, which in turn is attached to a flat metal mounting bar.

6.2.2 Instrument location

Resistance wave gauges

Wave gauges were deployed at 3.66-m intervals on the west wall of the wave channel. Gauges were attached to the tank wall using existing 2.54-cm wall inserts (threaded holes). Gauge mounts consisted of 2.54-cm aluminum rods, threaded on one end to attach to the wall inserts. The other end of each rod was machined to accept a Delrin plate, to which the wave gauge wires were attached. The gauge mounts extended horizontally out from the wall approximately 0.46 m and the gauges extended vertically from z = -0.3 m to -2.4 m, where z is measured vertically from the top of the wave tank. The typical still-water level was at z = -1.52 m. The top mount incorporated an adjustable eyebolt to set wire tension.

Electromagnetic current meters

Fourteen current meters were deployed on the east wall of the wave channel in vertical arrays of one to four gauges. The arrangement of the current meters varied from week to week, with some changes from run to run, to meet measurement objectives. Four additional current meters were deployed in a vertical array (approximate 0.3-m vertical spacing) off a mobile carriage. The position of the carriage and elevation of the meters on the carriage were varied from run to run.

The current meter mounts consisted of aluminum plates and rods. The plates were bolted into the wall inserts with 2.54-cm bolts. Spacers welded to the back of the plates set the plates approximately 5 cm out from the wall. A vertical array of rectangular slots was machined into the plates at 16.2-cm spacings. Aluminum rods of 1.9-cm diameter, threaded and keyed on one end, slid into the slots in the plate and were fastened with a nut on the backside of the plate (the space between the wall and plate allowed access behind the plate). The elevation of the rods could be easily adjusted between runs by removing the nut behind the plate and refastening the rod into another slot. The opposite end of the rod was machined flat on one side, and the mounting bar of the current meter was attached to the flat portion of the rod with two small hose clamps. Current meter cables were secured to the plate with cable ties attached through small holes punched into the plate for that purpose. The meters extended approximately 0.6 m out from the channel wall. Figure 6.2 shows an example of the current meter mounting configuration. The current meters deployed off the carriage were hose clamped to angles bolted to an aluminum wing-shaped section hanging down from the carriage. The wing elevation was adjusted with a winch and clamped into place to provide a steady platform for the meters.

6.2.3 Instrument characteristics

Resistance wave gauges

The largest source of error in the resistance wave gauge is expected to be the change in resistivity (change in conductivity of the water, contamination of the probes, or residual errors in the calibration procedure), typically 2 percent. The range of the gauges was fixed by the vertical range of the wires, z = -0.3 to -2.4 m. Occasionally, waves exceeded the top of a gauge (produced by a combination of large wave height and high water level) and saturated the signal. Gauge calibrations were linear.

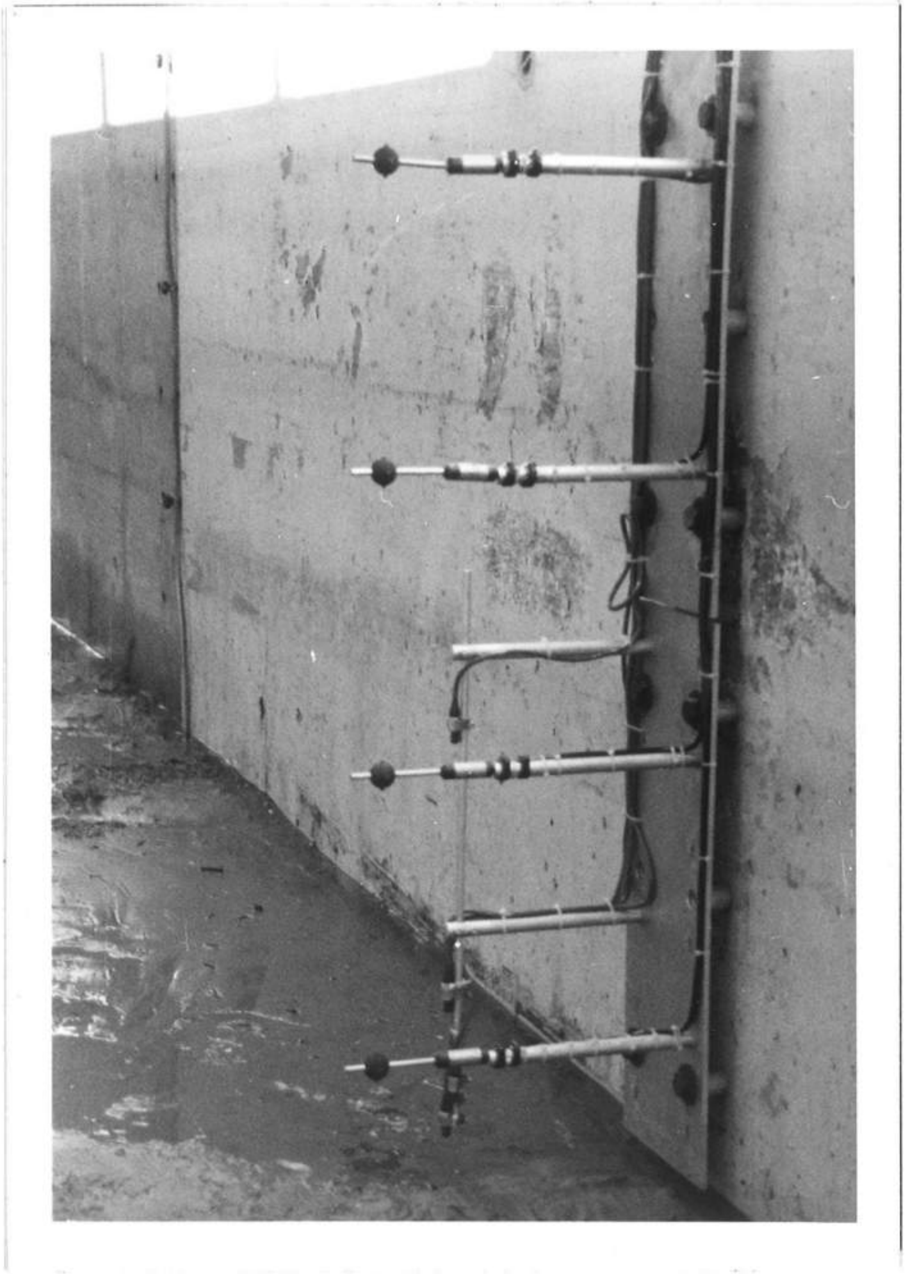

Figure 6.2. Current meter mounting configuration

Electromagnetic current meters

The manufacturer's specifications state that the current meters have an accuracy of ±2 percent. The range of the meter is ±5 V, which translates to ± 5 m/sec or 3 m/sec (depending on factory calibrations). The meters were deployed in groups of two or four using the close proximity option. This reduced interference between closely spaced meters by driving all meters in a group with one timing pulse.

6.2.4 Experiment procedures

The sequence of a typical run was:

a. Specify wave conditions and data collection parameters. The wave conditions were either monochromatic (specified wave height and period) or random (specified target zero-moment wave height H_{mo}, peak period T_p, and peakedness parameter γ to generate a TMA spectrum). Data collection parameters included sampling frequency and run length.

b. Check gauges and water level. Checks were made of the gauges (checking gauge voltages to ensure they were operating properly) and the water level.

c. Position the carriage. The carriage with the current meters was positioned at a strategic location (e.g., in the expected incipient breaking zone, adjacent to wall-mounted meters, in the trough).

d. Begin wave action and data collection. One computer program controlled both the wave generation and the collection of the resistance wave gauge and electromagnetic current meter data. The data collection began as soon as the wave generation program began (although wave action did not begin immediately) and ended when the wave action ceased. Typically, wave action lasted 10 to 70 min.

e. Lab notes. Notes were kept documenting significant features of the run, e.g., breaker type and approximate position, instrument status, and visual observation of sand ripples.

f. beach profile survey. At the beginning of the day and following each run, the beach profile was surveyed (the post-run survey typically served as the pre-run survey for the next run). Divers also measured the elevation of the lowest current meter in each vertical array and made any necessary meter adjustments. Current meter positions were surveyed once a week and after major changes in configuration.

g. Preliminary analysis of data for quality control. For at least one run a day (typically the first run of the day), plots were made of the time series and spectra for all gauges to ensure that the gauges were operating properly.

6.2.5 Calibration and zero reference

Resistance wave gauges

Wave gauges were calibrated once a week during the project. They were calibrated by slowly raising and lowering the water level (approximately 0.3 m/hr) and recording the water level change with the gauges. Simultaneously, a video camera recorded the water level relative to a 0.3-m-increment scale painted on the tank wall. Wave gauge data were linearly regressed with the video measurements to estimate gauge gains and offsets. Calibration gains for each day of the experiment were linearly interpolated between the weekly calibrations. Gauge offsets were calculated in the analysis software as the average water surface elevation during the quiescent period at the beginning of a run (average over the first 200 points in random wave runs, average over the first 20 points in monochromatic wave runs). The run-by-run offsets were calculated to adjust for small changes in water level between runs (leaking or filling of the tank) and changes in the sand level on the most shoreward gauges (due to beach profile change).

Electromagnetic current meters

Current meters were calibrated between September 24 and 27, 1991 at the U.S. Geological Survey Indoor Hydraulic Laboratory Facility in Bay St. Louis, Mississippi. Although most of the meters had been calibrated within one year prior to the project, the post-project calibrations were used for all analyses. As with the wave gauges, the current meter offsets for submerged meters were calculated from the beginning of the data record. For gauges that were out of the water at the beginning of the run, the calibration offsets were applied.

6.2.6 Sampling

Analog signals from the wave gauges and electromagnetic current meters were conditioned to a 0- to 10-V DC dynamic range. Each signal was low-pass filtered through a fifth-order, 10-Hz Bessel filter at the input to the data acquisition system to eliminate noise and avoid aliasing. Analog signals were digitized at 16 Hz, optically encoded, and transmitted to a VAX 3400 server. Digitized records were serially recorded in 256 time unit blocks to random access memory and transferred to a hard drive.

6.3 Data Analysis

The analysis routines for the resistance wave gauge and electromagnetic current meter data were nearly the same, with additional preprocessing required for the current meter data. The data were filtered to separate short-wave motions from low-frequency motions, and then spectral and zero up-crossing analyses were performed on the raw, low-pass, and high-pass signals. Sample time series, spectra, and mean data plots are presented. Analysis of wave reflection and wave groups are also given.

6.3.1 Analysis procedure

Preprocessing

The electromagnetic current meter data required two types of processing prior to analysis. First, a low-pass filter with a 2-Hz cutoff was applied to remove high-frequency noise. High-frequency noise was present in some data records for deployments with the current meters spaced less than 30 cm apart due to interference between the gauges. Second, the elevation of each current meter was compared with the water surface elevation (estimated from a resistance wave gauge at the same cross-shore location) to determine if the current meter was sufficiently submerged. The criterion for submergence was that the water level was 5 cm or more above the surveyed current meter elevation. Current meter readings were set to zero for the portion of the record when the gauge was out of the water. The current meters deployed on the carriage and current meters shoreward of the most shoreward resistance gauge could not be checked for submergence because there was not a co-located resistance wave gauge. These gauge outputs were analyzed assuming 100 percent submergence; thus, the results are viewed with healthy skepticism.

Filtering

To separate short-wave motions from low-frequency motions, a non-recursive, low-pass filter was applied. The period cutoff for the filter was set to twice the peak period of the incident short waves (the peak period of the long-period motion was generally 20 sec or longer as compared to typically 3 to 5 sec for the short waves). The period response of the filter is shown in Figure 6.3 for a cutoff period of 6 sec. The filter was applied beginning with the 1009th data point. The first 1008 points were skipped to ensure that the waves had reached the most shoreward gauge. Two hundred points were sacrificed at the beginning (in addition to the 1008 points that were skipped) and end of the data record in constructing the filter. The low-pass time series was output directly from the filter. The high-pass time series was obtained by subtracting the low-pass time series from the preprocessed data.

Spectral analysis

Spectral analysis was performed using a standard Fast Fourier Transform (Press et al. 1989). Data were divided into blocks of 4096 points and the spectrum was calculated for each block. The total number of blocks per run was determined by the run length (20-min run = 4 blocks, 40-min run = 8 blocks, and 70-min run = 15 blocks). The average spectrum for each run was calculated by averaging the spectra over all blocks within the run. The confidence bands for each spectrum become tighter as the number of averages increases. The degrees of freedom (DOF) for the spectra are approximately twice the number of averages (20-min run = 8 DOF, 40-min run = 16 DOF, and 70-min run = 30 DOF).

Mean water elevation, standard deviation, root-mean-square wave height, H_{mo}, and peak period were determined from the calculated spectra for the wave gauges. Similarly, mean velocities and standard deviations were estimated from the calculated spectra for the current meters.

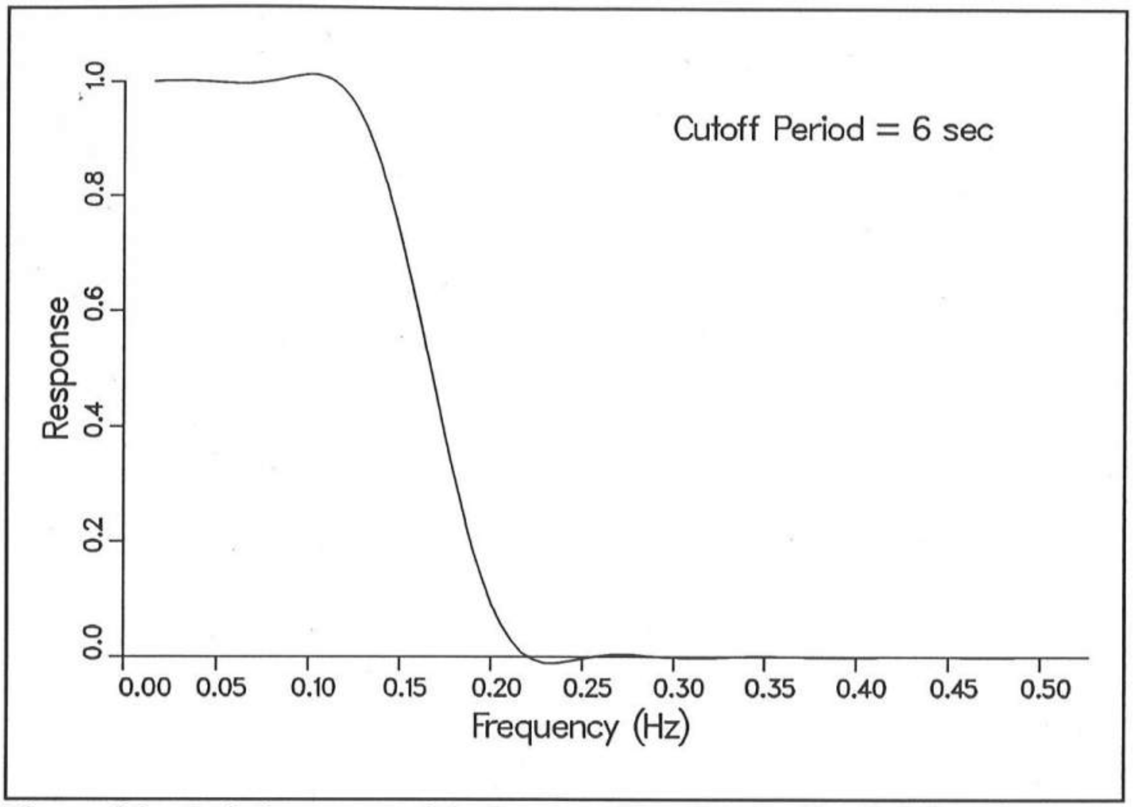

Figure 6.3. Period response of the low-pass filter for cutoff period 6 sec

Time series analysis

Time series analysis was performed with a zero-upcrossing definition of a wave. A wave is defined between two successive upward crossings of the water surface about the mean water elevation. The upcrossing definition was chosen because the saw-tooth shape of the nearshore wave profile gives distinct upward crossings, whereas downcrossings vary from wave to wave. The wave height H of an individual wave is defined as the difference between the highest and lowest water elevation between two zero upcrossings. The wave period T of an individual wave is defined as the time between two zero upcrossings. Very small waves ($H < 0.6$ cm), associated with small surface variations near the mean water elevation, were not identified as individual waves. These very small waves were included as part of the preceding wave.

The mean, standard deviation, skewness, and kurtosis of the water surface and the mean, root-mean-square, significant (H_s), one-tenth, and maximum (H_{max}) wave height and period were calculated from the wave gauges. Mean and maximum velocities, standard deviation, skewness, kurtosis, and percent of measurements with the gauge submerged were calculated for the current meters.

6.3.2 Long-wave motion in two SUPERTANK runs

Data for SUPERTANK Runs A2007B and A0509A are analyzed with particular emphasis on determining the long-wave motion. These runs will be studied in greater detail in Chapter 7. The data provide insight into the

SUPERTANK results as well as background for the modeling results discussed in Chapter 7. The beach profiles for Runs A2007B and A0509A are shown in Figures 6.4 and 6.5, respectively

Water surface elevations

A sample of the raw resistance wave gauge data is shown in Figure 6.6 for Gauge 3, Run A2007B. The vertical axis is the water surface elevation ζ and the horizontal axis is time. Every fourth data point of the time series is plotted. The low-pass signal is also included in Figure 6.6. The target wave conditions for Run A2007B were $T_p = 5.0$ sec and $H_{mo} = 0.7$ m. The wave spectrum was very narrow with $\gamma = 100$. Wave groups are evident in the time series, as would be expected with the relatively narrow incident spectrum. Gauge 3 is located in approximately 0.7 m water depth on the shoreward side of a bar, within the surf zone (Figure 6.4). The mean water surface elevation for the record was 0.02 m.

The smoothed spectra for the raw, low-pass, and high-pass signals for Gauge 3, Run A2007B, are given in Figure 6.7. For this example, the spectral peak is located at 0.2 Hz (5 sec) and higher harmonics are apparent at 0.4, 0.6, and 0.8 Hz. Both the wave kurtosis and skewness increase in shallower depths, as harmonics grow and waves become asymmetric. A low-frequency peak at 0.023 Hz (43 sec) is also apparent. At Gauge 3, 91 percent of the wave energy is contained in the high-pass signal and 9 percent is contained in the low-pass signal. The energy in the low-pass signal tends to increase close to shore.

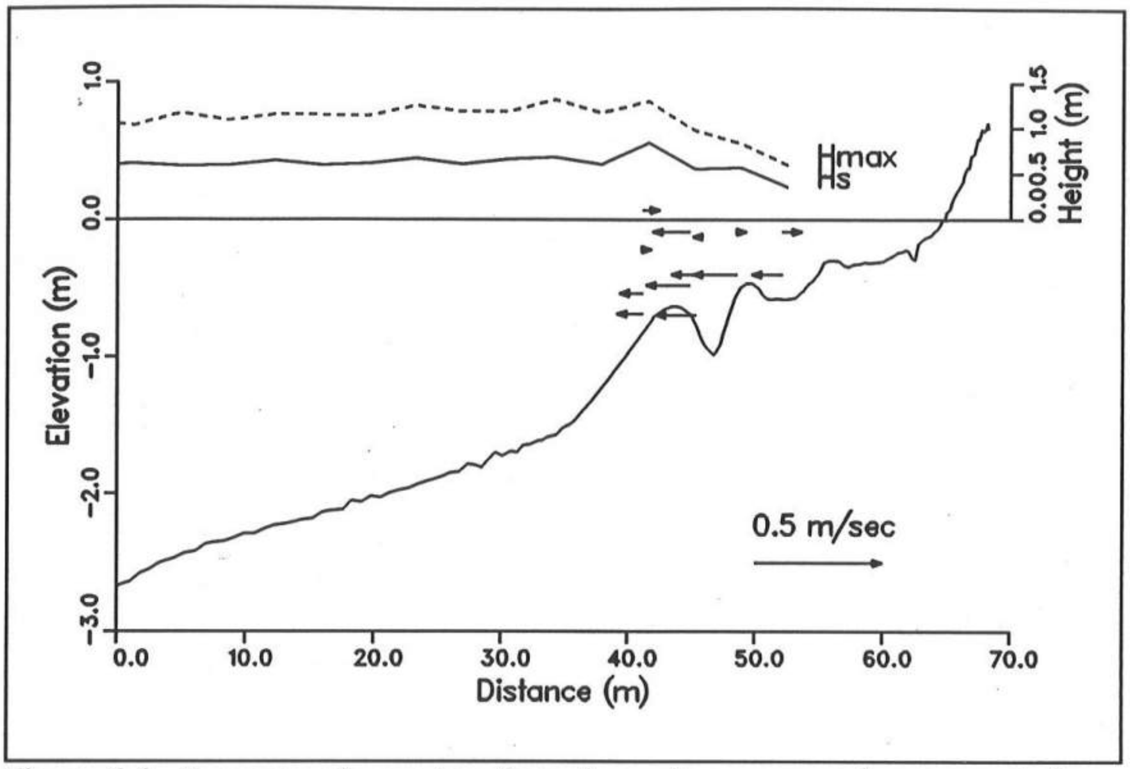

Figure 6.4. Summary of wave transformation and mean cross-shore currents for Run A2007B

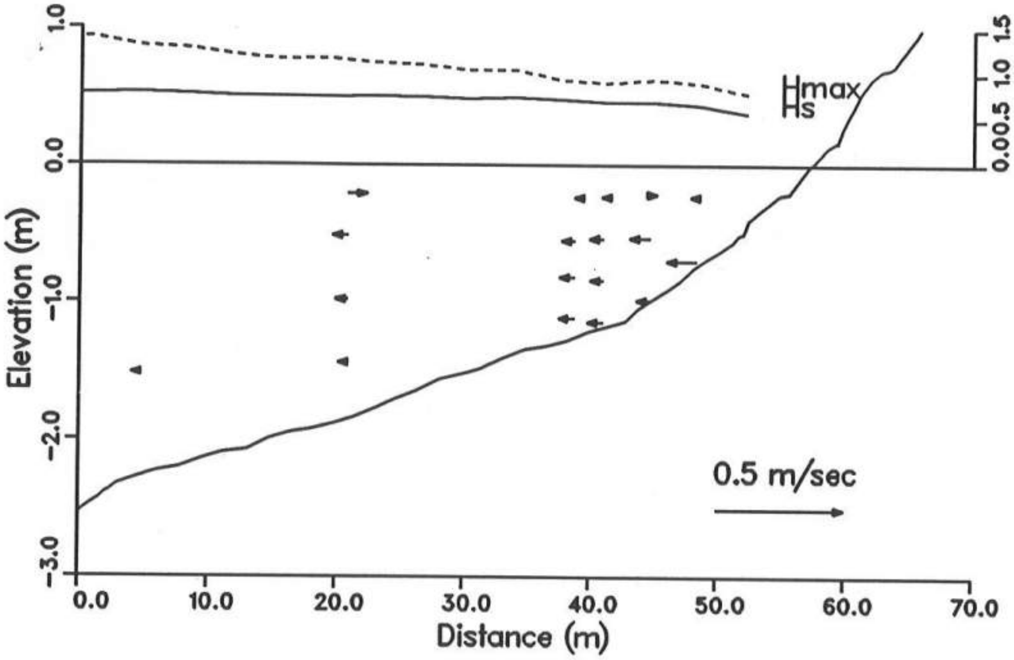

Figure 6.5. Summary of wave transformation and mean cross-shore currents for Run A0509A

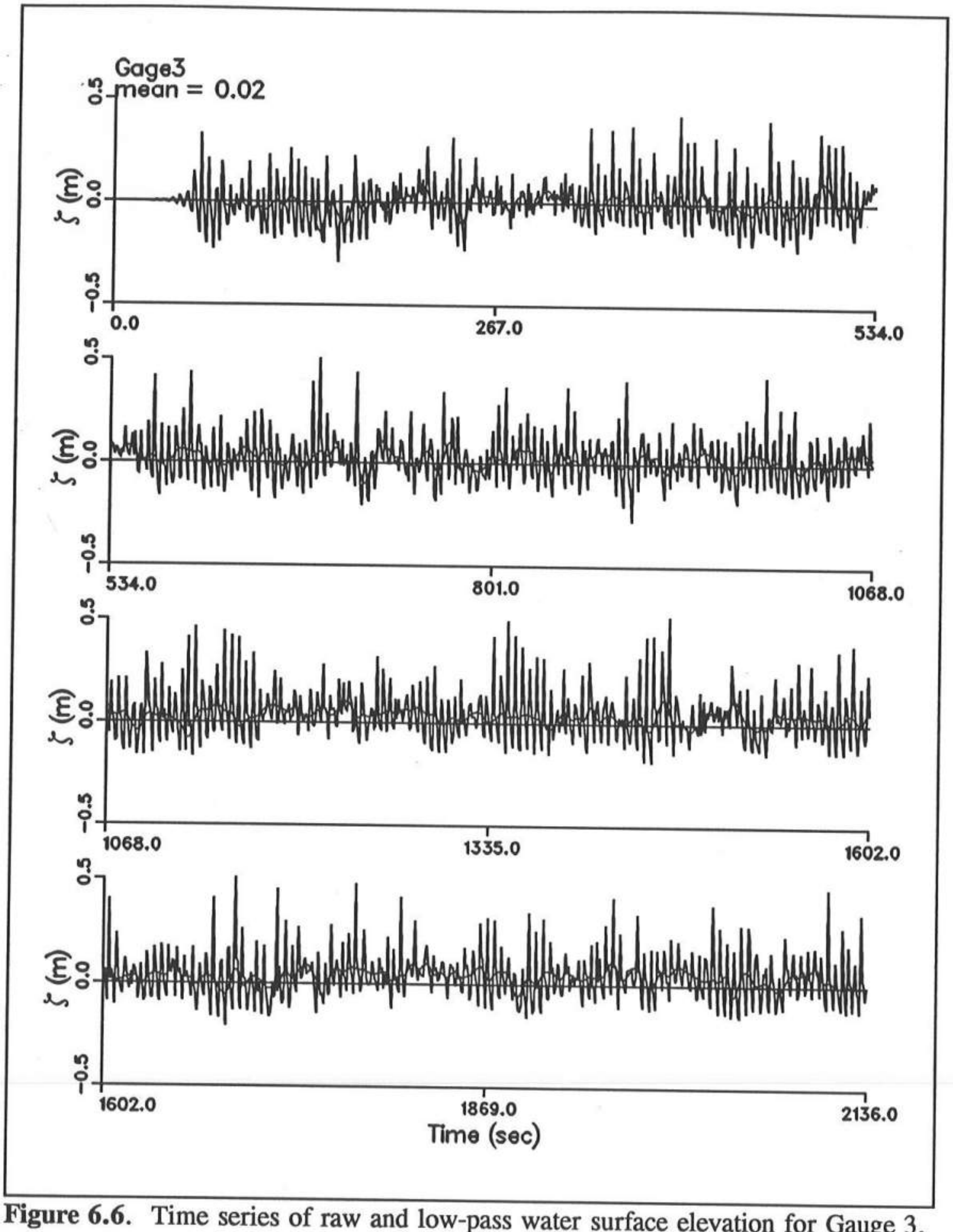

Figure 6.6. Time series of raw and low-pass water surface elevation for Gauge 3, Run A2007B

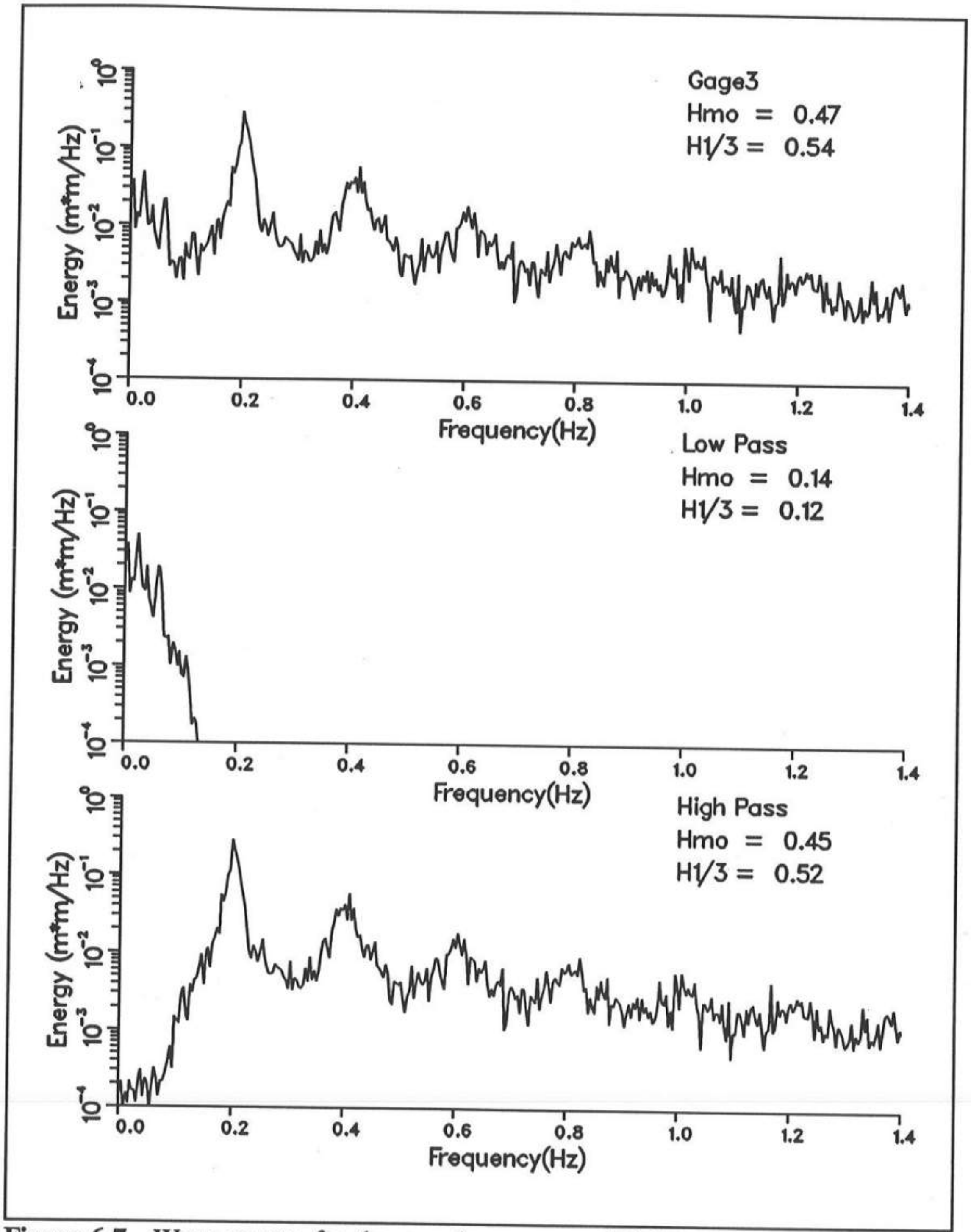

Figure 6.7. Wave spectra for the raw, low-pass, and high-pass water surface elevation for Gauge 3, Run A2007B

Velocities

Figure 6.8 shows the spectrum for the raw signal and the raw and low-pass time series for Channel 30 (cross-shore velocity component, located approximately 0.3 m below the still-water surface) for Run A2007B. This current meter is located at the same cross-shore location as wave Gauge 3 shown in Figures 6.6 and 6.7. The general appearance of the raw time series is similar to the wave time series in Figure 6.6. The positive velocities are onshore directed (corresponding to the passage of a wave crest) and the negative velocities are offshore (corresponding to the passage of a wave trough). The mean velocity at this gauge was -0.12 m/sec. The energy spectrum of the velocity is similar to the wave spectrum in Figure 6.7. The primary peak is at 0.2 Hz with harmonics at 0.4 and 0.6 Hz. Approximately 28 percent of the energy is contained in the low-pass signal and the low-frequency peak is at 0.02 Hz (50 sec).

Figure 6.4 and 6.5 give example summaries of the wave and current data for Runs A2007B and A0509A, respectively. The incident wave conditions for Run A0509A were $T_p = 3$ sec, $H_{mo} = 0.8$ m, and $\gamma = 20$. Run A0509A was the first SUPERTANK run, and it started from an equilibrium profile shape. The beach profile for Run A2007B was formed from a week of erosional wave conditions (generating multiple bars moving offshore) followed by a week of accretional wave conditions (in which the bars moved onshore). The top of the figures shows the wave transformation as measured by the resistance wave gauges and calculated from the zero-upcrossing analysis. H_{max} is given by the dashed line

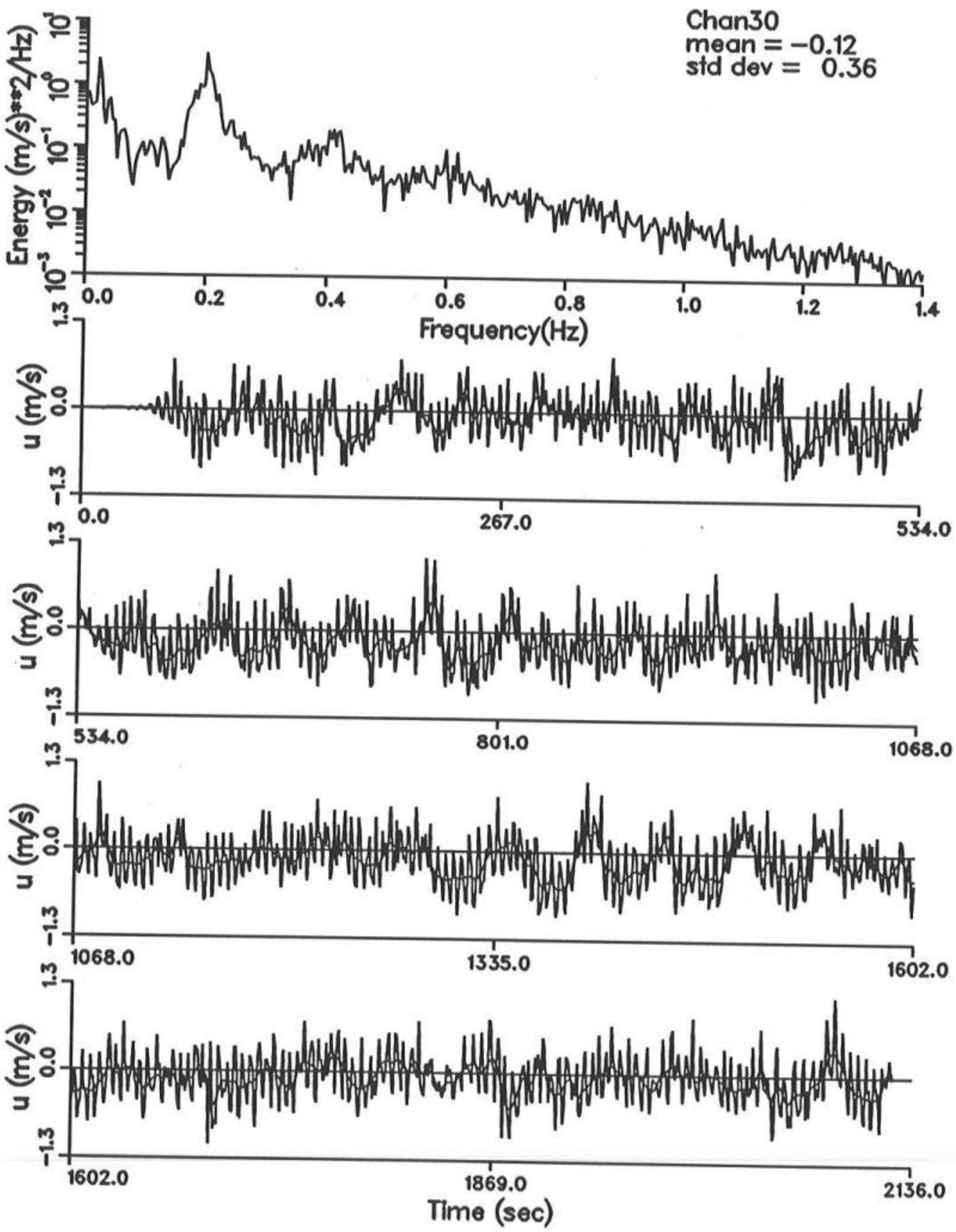

Figure 6.8. Current meter raw spectrum and time series of the raw and low-pass signal for Channel 30, Run A2007B

and H_s is given by the solid line. Note that the wave height scale is on the right-hand side of the plot. For Run A2007B, waves are breaking on the outer bar and decaying as they travel shoreward. For Run A0509A, the incipient wave breaking zone was located at the two most shoreward wave gauges. Figure 6.9 shows the decay of the high-pass wave height (solid line) and the growth of the low-pass wave height (dashed line) for Run A0509A.

The mean cross-shore current velocities are shown in Figures 6.4 and 6.5 as vectors. The plots illustrate the tendency for offshore flow below trough level and onshore flow above trough level. The maximum mean cross-shore velocities at SUPERTANK were 0.5 m/sec, shoreward of the bar. Velocities in the offshore region of the channel were typically less than 0.05 m/sec, in the range 0.2 to 0.5 $(H/h)^2(gh)^{0.5}$ (an estimate of the flow required to balance mass transport). The velocity profiles in the offshore region are linear in shape (constant over depth or slightly increasing offshore-directed velocity from the bottom to the surface). In the nearshore region, the mean velocity profile tended to be parabolic in shape, with greatest velocities near the bottom and lower velocities near trough level. The SUPERTANK cross-shore flow measurements show trends similar to field measurements at the DELILAH experiment (Smith et al. 1992), conducted at the CERC Field Research Facility in North Carolina. The velocity profile shape offshore of breaking and across the bar crest are similar in the laboratory and field measurements. However, measured undertow velocities in the trough at DELILAH are generally smaller than those measured at

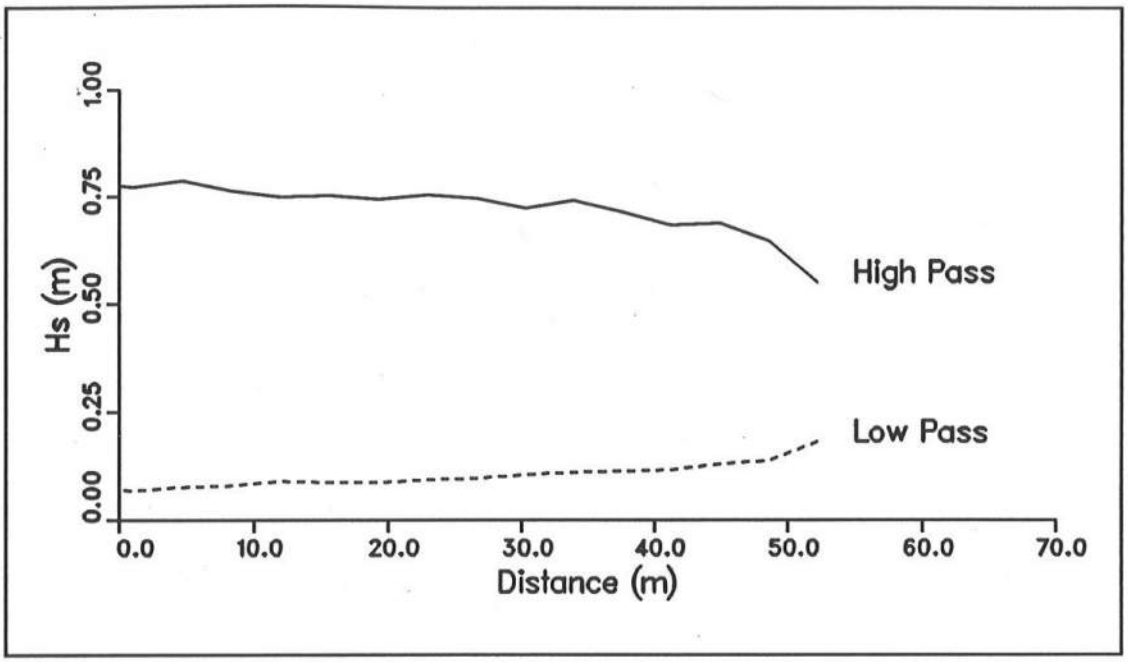

Figure 6.9. High-pass and low-pass significant wave heights for Run A0509A

SUPERTANK. This may be because the trough was deeper and wider and the foreshore steeper at DELILAH than at SUPERTANK or due to three-dimensional circulation at DELILAH.

6.3.3 Short- and long-wave reflection

Wave reflection from the nearshore (beach and bars) was calculated for selected wave runs at several locations in the channel. Reflection estimates were calculated with a frequency-domain linear theory analysis technique using synoptic time series of cross-shore velocity and water surface elevation (Hughes 1993). This method assumes normally-incident waves.

Hughes represents the water surface elevation and cross-shore velocity as the sum of incident and reflected irregular linear waves

$$\zeta = \sum_{i=0}^{N} [a_{Ii} \cos(\Phi_{Ii} - \sigma_i t) + a_{Ri} \cos(\Phi_{Ri} + \sigma_i t)] \tag{6.1}$$

$$u = \sum_{i=0}^{N} [a_{Ii} Z_i \cos(\Phi_{Ii} - \sigma_i t) - a_{Ri} Z_i \cos(\Phi_{Ri} + \sigma_i t)] \tag{6.2}$$

where

$$\Phi_{Ii} = (k_i x + \epsilon_{Ii}) \tag{6.3}$$

$$\Phi_{Ri} = (k_i x + \epsilon_{Ri}) \tag{6.4}$$

$$Z_i = \frac{g k_i}{\sigma_i} \frac{\cosh k_i (h + z)}{\cosh k_i h} \tag{6.5}$$

N is the number of frequencies, k is the wavenumber, σ is the angular wave frequency, ϵ is the phase angle, a is the wave amplitude, and the subscripts I and R denote incident and reflected wave components. Using trigonometric identities, Equations 6.1 and 6.2 can be rewritten

$$\zeta = \sum_{i=0}^{N} [A_i \cos \sigma_i t + B_i \sin \sigma_i t] \tag{6.6}$$

$$u = \sum_{i=0}^{N} [C_i Z_i \cos \sigma_i t + D_i Z_i \sin \sigma_i t] \tag{6.7}$$

where

$$A_i = a_{Ii} \cos \Phi_{Ii} + a_{Ri} \cos \Phi_{Ri} \tag{6.8}$$

$$B_i = a_{Ii} \sin \Phi_{Ii} - a_{Ri} \sin \Phi_{Ri} \tag{6.9}$$

$$\frac{C_i}{Z_i} = a_{Ii} \cos \Phi_{Ii} - a_{Ri} \cos \Phi_{Ri} \tag{6.10}$$

$$\frac{B_i}{Z_i} = a_{Ii} \sin \Phi_{Ii} + a_{Ri} \sin \Phi_{Ri} \tag{6.11}$$

Fourier analysis is used to calculate A, B, C, and D from the time series. Then, Equations 6.8-11 are solved to calculate the incident and reflected wave amplitudes and phases

$$a_{Ii} = \frac{1}{2} \sqrt{\left(A_i + \frac{C_i}{Z_i}\right)^2 + \left(B_i + \frac{D_i}{Z_i}\right)^2} \qquad (6.12)$$

$$a_{Ri} = \frac{1}{2} \sqrt{\left(A_i - \frac{C_i}{Z_i}\right)^2 + \left(B_i - \frac{D_i}{Z_i}\right)^2} \qquad (6.13)$$

$$\Phi_{Ii} = \tan^{-1} \left(\frac{B_i + \dfrac{D_i}{Z_i}}{A_i + \dfrac{C_i}{Z_i}} \right) \qquad (6.14)$$

$$\Phi_{Ri} = \tan^{-1} \left(\frac{-B_i + \dfrac{D_i}{Z_i}}{A_i - \dfrac{C_i}{Z_i}} \right) \qquad (6.15)$$

The reflection coefficient is the ratio of the reflected wave amplitude to the incident wave amplitude. The incident and reflected wave time series are given by

$$\zeta_I = \sum_{i=1}^{N} a_{Ii} \cos(\Phi_{Ii} - \sigma_i t) \qquad (6.16)$$

$$\zeta_R = \sum_{i=1}^{N} a_{Ri} \cos(\Phi_{Ri} + \sigma_i t) \qquad (6.17)$$

An example of the reflection analysis output is shown in Figure 6.10. The figure shows time series of the total, incident, and reflected long-wave water

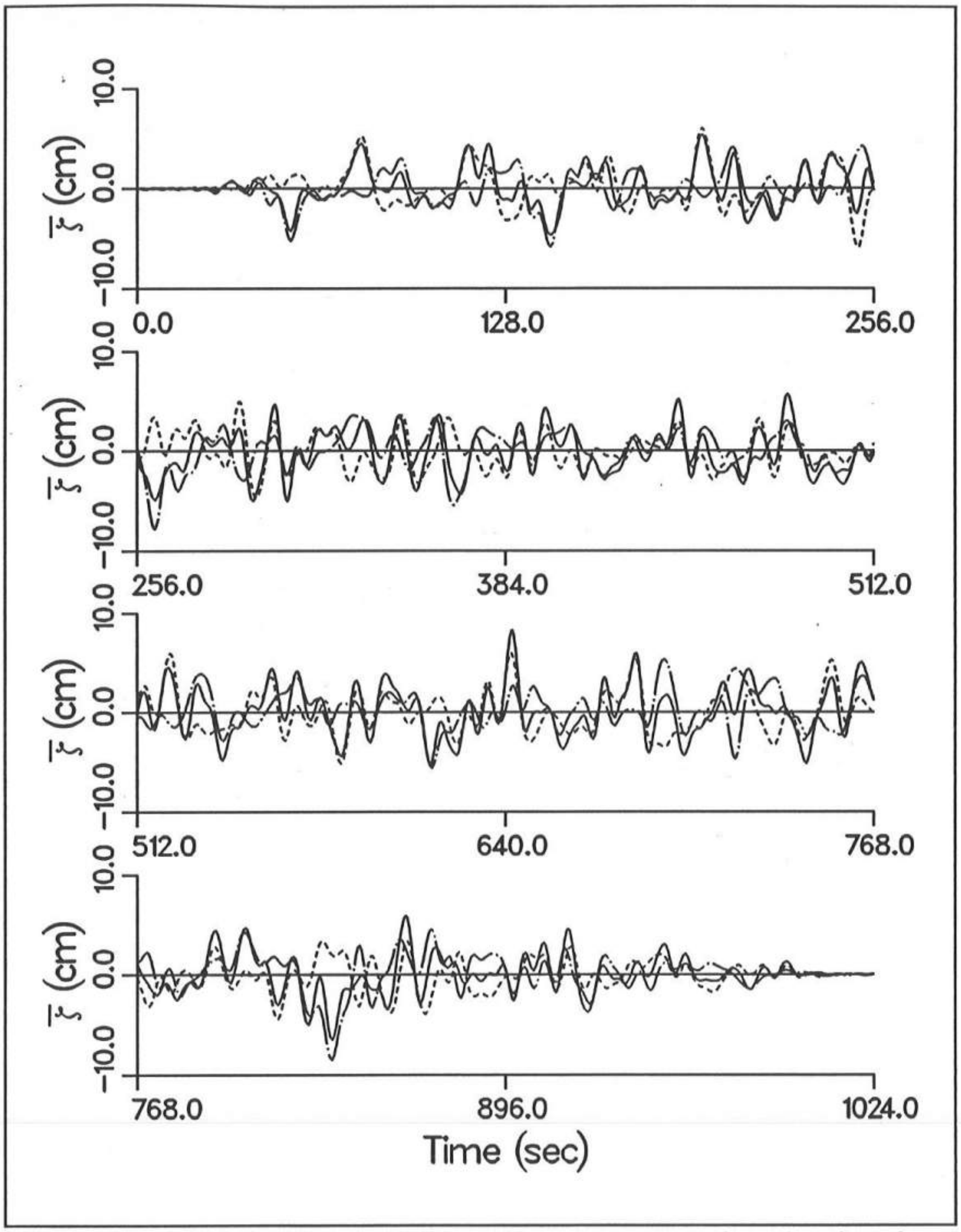

Figure 6.10. Total, incident, and reflected low-pass water surface elevations for Run A2007B (total -- solid line, incident -- chain-dot line, reflected -- dashed line)

surface elevation for Run A2007B. Separation of incident and reflected long waves is required to drive the depth-integrated model discussed in Chapter 3.

Reflection coefficients were generally 0.20 to 0.45 (all frequencies) for the SUPERTANK runs. Coefficients for the low-pass frequencies were in the range 0.4 to 1.0. The reflection coefficient was strongly related to the incident short-wave peak period, with greater reflection for longer peak periods. The wave generator used at the wave channel was equipped to absorb reflected waves at the peak frequency, so re-reflection of wave energy from the wavemaker was suppressed. Figure 6.11 shows total wave height calculated in 6-min segments for the high-pass and low-pass signals over a 70-min run. The solid lines are surf zone wave gauges (depth less than 1 m), the chain-dot lines are gauges in the deepest portion of the channel (depth approximately 3 m), and the dotted and dashed lines are at intermediate depths. There is a variation in long-wave height with time, but there is not a consistent increase in height with time from re-reflection of waves from the wavemaker, as might be expected.

6.3.4 Wave groups

The incident wave spectra at SUPERTANK included narrow-banded spectral shapes (TMA spectra with $\gamma = 20$ and 100). The narrow spectra produced wave groups which induced time variations in the low-pass surface elevations and velocities. The time series of high-pass wave energy (*E*) and low-pass surface elevation ($\overline{\zeta}$) for Run A2007B are given in Figure 6.12 for three

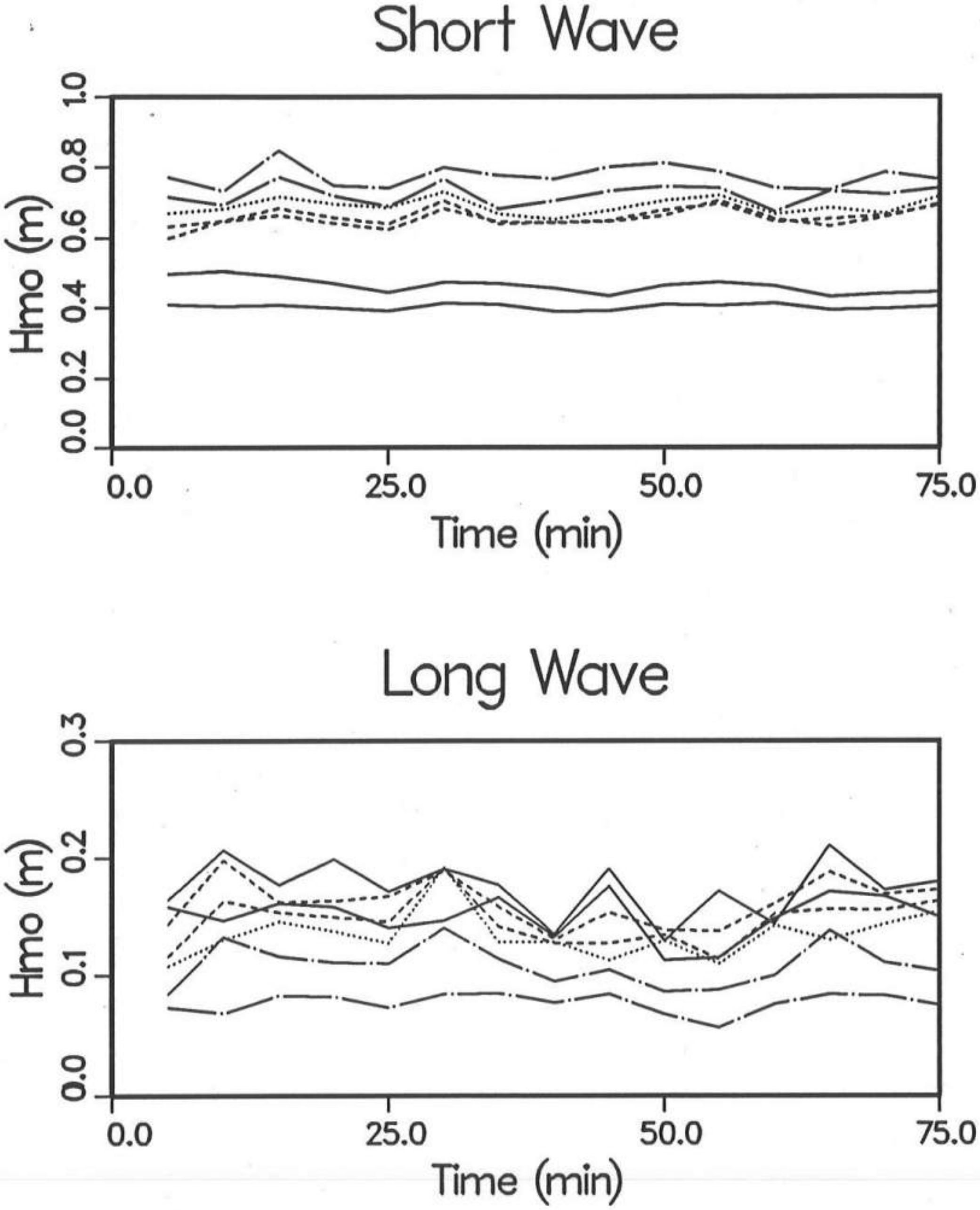

Figure 6.11. High-pass and low-pass wave heights as a function of time (surf zone -- solid line, deep -- chain-dot lines, intermediate depth -- dashed and dotted lines)

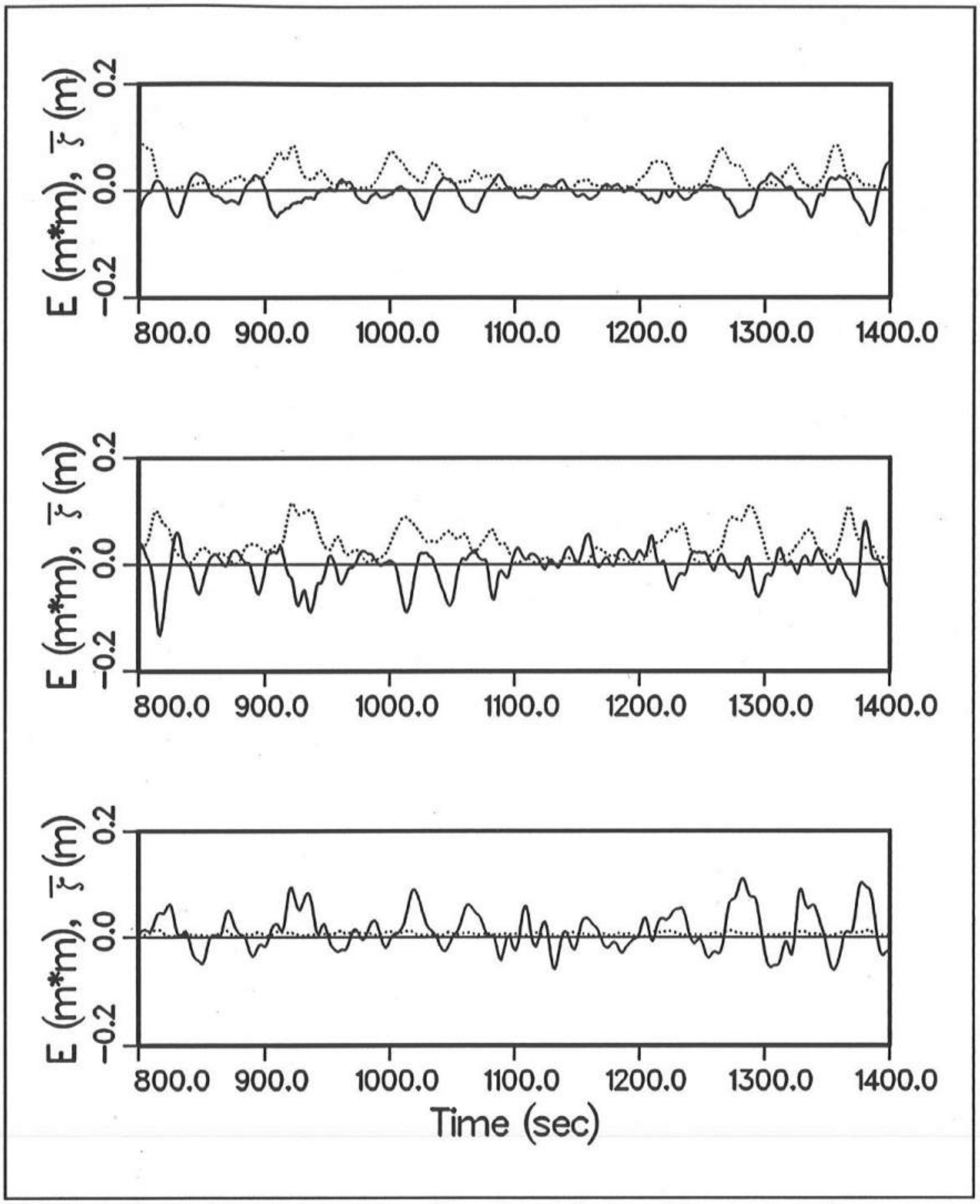

Figure 6.12. Incident wave energy (*E* -- dotted line) and low-pass surface elevation ($\overline{\zeta}$-- solid line) offshore (x = 0 m, top), seaward of incipient breaking (x = 40 m, middle), and surf zone (x = 51 m, bottom)

locations in the tank (x = 0, 40, and 51 m in Figure 6.4). The high-pass wave energy was calculated by squaring the high-pass surface elevation and then low-pass filtering the squared elevation to get the envelope of the energy. The top panel of Figure 6.12 is a location near the wave generator, the middle panel is a location just seaward of the incipient breaking zone, and the bottom panel is in the mid surf zone. The middle panel shows strong correlation between the high-pass wave energy and the low-pass surface elevation. The bottom panel, however, shows that in the mid surf zone, most of the short-wave energy has been dissipated due to wave breaking. The long-wave surface elevation maintains its structure and represents a system of free waves propagating towards the shoreline superimposed on similar outgoing waves which are the long-wave motion reflected from the shore.

As shown in the middle panel of Figure 6.12, the strongest correlation between the short-wave energy and the long-wave water surface elevation occurs just seaward of the breaker zone. The correlation of these two signals is shown in Figure 6.13 as a function of lag time. A strong negative correlation occurs at a time lag of approximately zero (short-wave energy leads slightly in time), as would be expected if the long-wave motion was generated by radiation stress forcing (Longuet-Higgins and Stewart 1964). The negative correlation means that high wave groups force a setdown of the low-pass water surface elevation, and low wave groups force a setup.

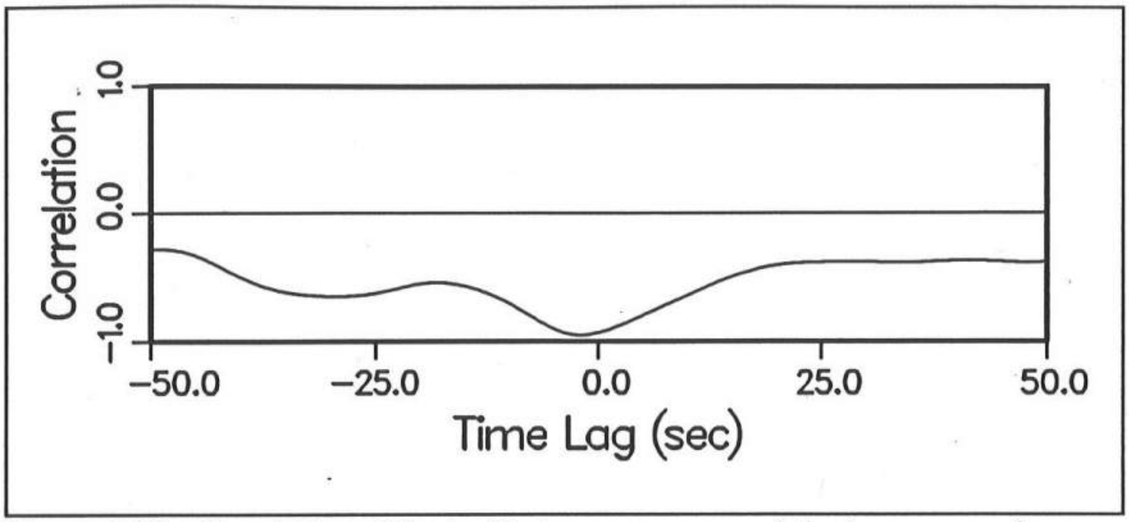

Figure 6.13. Correlation of the incident wave energy and the low-pass surface elevation at a location just seaward of the incipient breaker zone

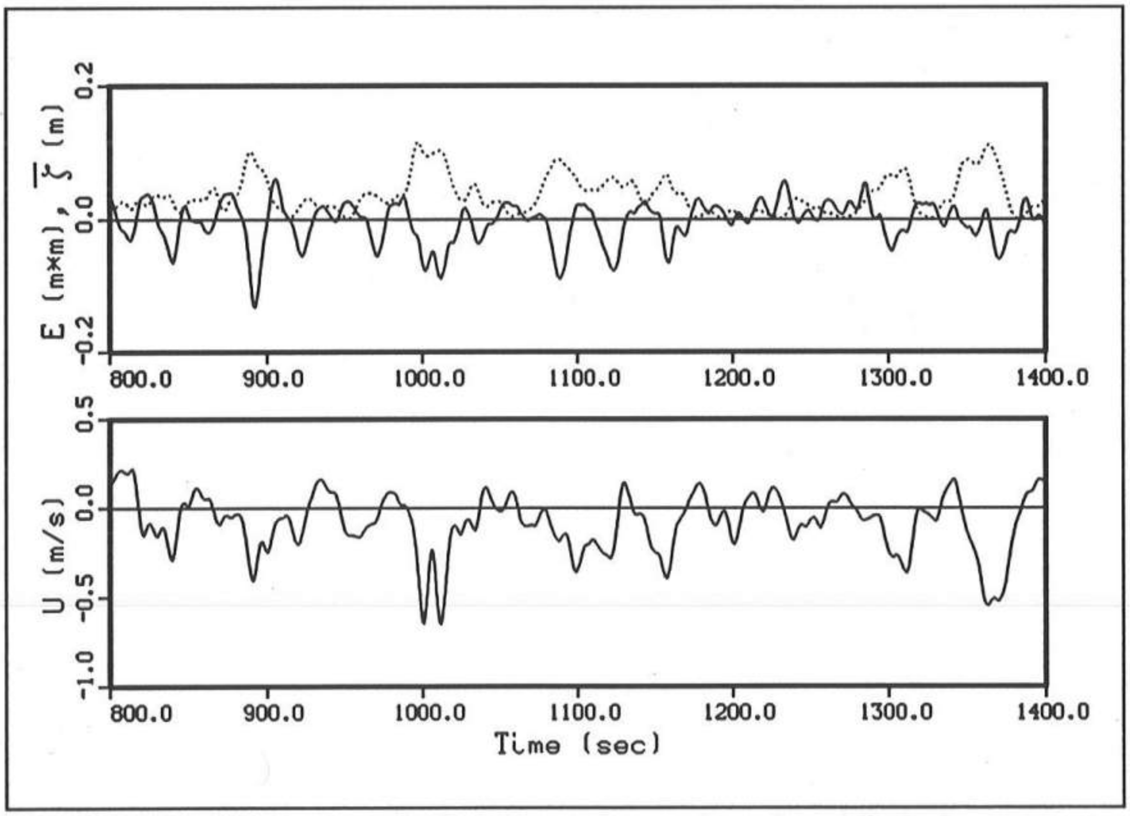

Figure 6.14. Time series of incident wave energy (*E* -- dotted line), low-pass surface elevation ($\overline{\zeta}$ --solid line), and low-pass velocity (*U*)

Figure 6.14 shows a repeat of the time series of short-wave energy (E) and long-wave water surface elevation ($\overline{\zeta}$) from the center panel of Figure 6.12 with the low-pass velocity measured with a co-located current meter (just outside the incipient breaker zone). Offshore flow is correlated with the high wave groups and depressions in the low-pass surface elevation. The time series show there is a mean setdown in the water surface in this location and a mean offshore flow at this mid-depth current measurement location. Figure 6.15 shows the correlation between the long-wave water surface elevation and the long-wave cross-shore velocity corresponding to Figure 6.14. The positive correlation is fairly strong, with the water surface elevation lagging the velocity by a few seconds. The similar correlation of the long-wave water surface elevation and velocity in the mid surf zone is shown in Figure 6.16. In the surf zone, the correlation is negative, and the water surface leads the cross-shore velocity by approximately one fourth of the low-pass wave period.

The very narrow spectra generated at SUPERTANK correspond to time series with significant wave groups. The wave groups generate long waves similar to the surf beat model of Schäffer and Svendsen discussed in Chapter 5.

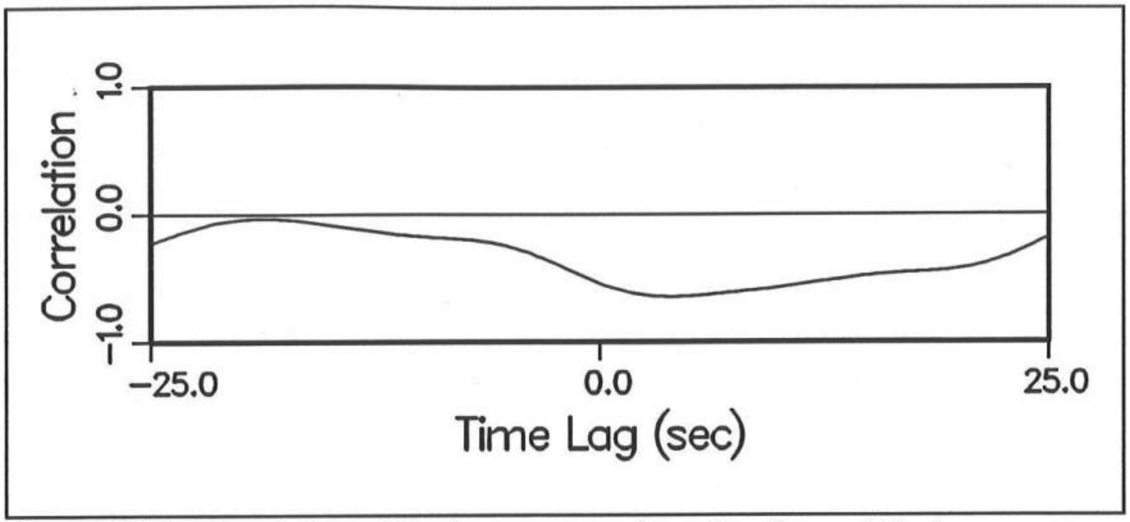

Figure 6.15. Correlation of the long-wave surface elevation and the long-wave velocity at a location just seaward of the incipient breaker zone

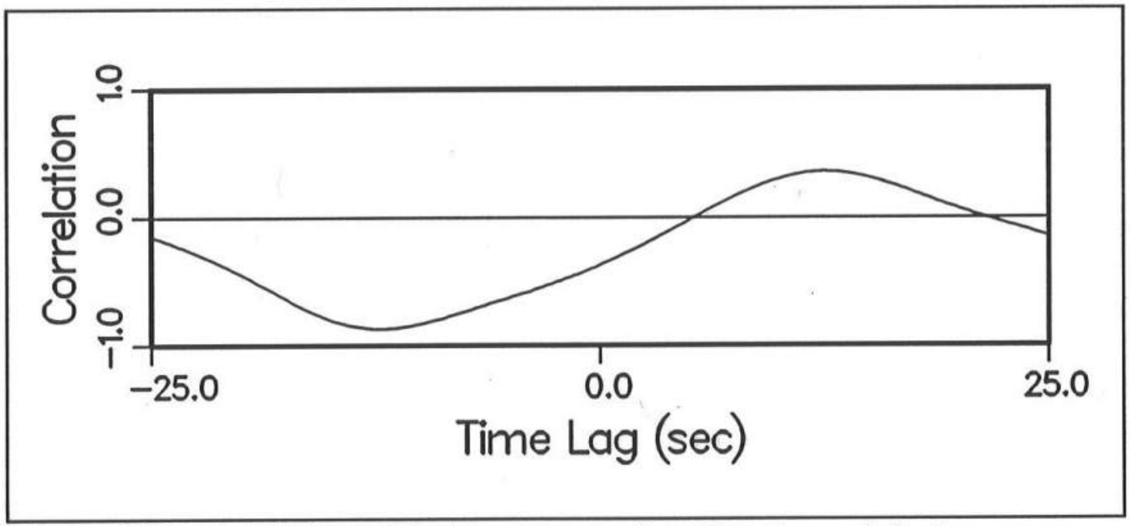

Figure 6.16. Correlation of the long-wave surface elevation and the long-wave velocity at a location in the mid surf zone

Chapter 7

MODELING TIME- AND DEPTH-VARYING CURRENTS AT SUPERTANK

Chapters 3 and 4 described the depth-integrated and profile models, respectively, and Chapter 6 described the SUPERTANK Laboratory Data Collection Project data set. This chapter pulls together both the modeling components and the laboratory data. Measurements made at SUPERTANK are used to drive the numerical models for predicting time-varying velocity profiles and to evaluate model results. To drive the numerical models, SUPERTANK measurements provided the incident infragravity wave time series at the offshore model boundary, time series of radiation stress throughout the grid domain, and the still-water depth. Low-pass measurements of velocity and water surface elevation were used to evaluate the models.

7.1 SUPERTANK Runs A0509A and A2007B

SUPERTANK Runs A0509A and A2007B were selected for simulation with the models. The bathymetry for Run A0509A has an equilibrium shape, as shown in Figure 7.1. The positions of current meters are shown with triangles in the figure. The short-wave parameters for Run A0509A were zero-moment wave height of 0.8 m, peak period of 3 sec, and a spectral peakedness parameter of 20,

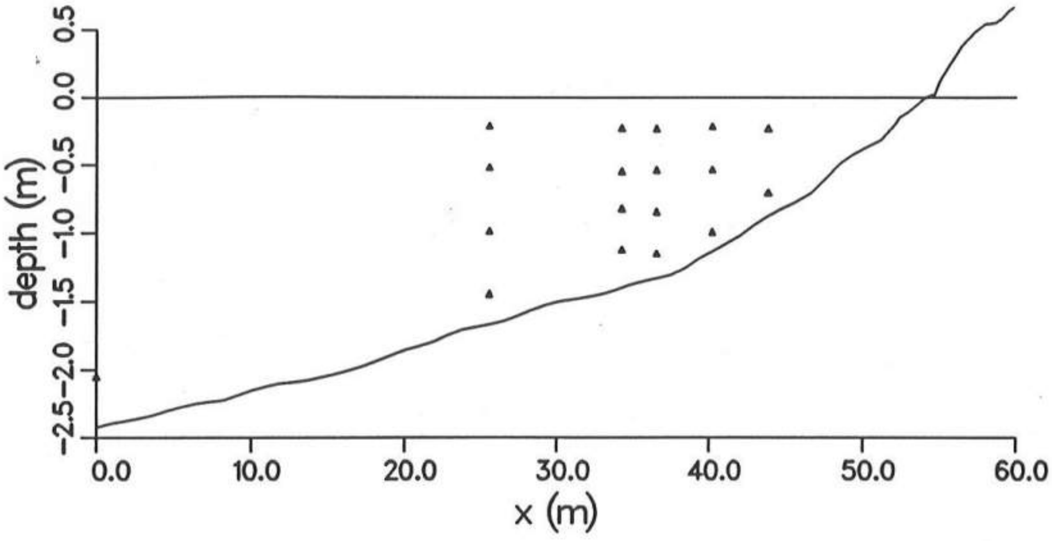

Figure 7.1. Bathymetry and current meter positions for SUPERTANK Run A0509A

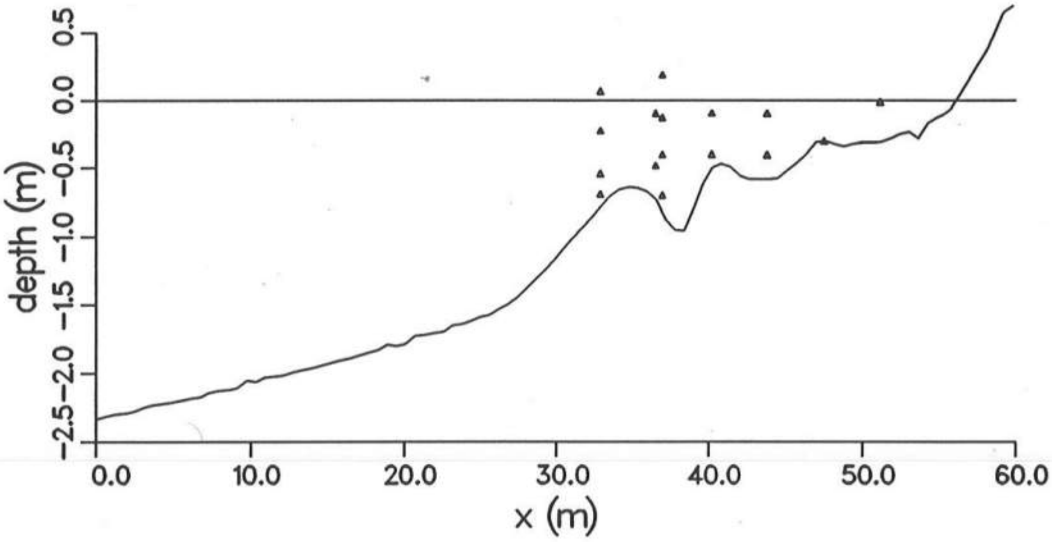

Figure 7.2. Bathymetry and current meter positions for SUPERTANK Run A2007B

a relatively narrow spectrum. The incident wave conditions are summarized in Table 7.1 The significant infragravity wave period was approximately 26 sec. This run was selected because it includes measurements both outside and inside the surf zone and illustrates several typical features of model results. Also, this is the only SUPERTANK run with a simple, non-barred bathymetry.

The bathymetry for Run A2007B has a complex barred shape, as shown in Figure 7.2. The multiple-bar shape was formed under a series of accretionary wave runs (low steepness waves). The positions of current meters are shown with triangles in the figure. The short-wave parameters for Run A2007B were zero-moment wave height of 0.7 m, peak period of 5 sec, and a spectral peakedness parameter of 100, a very narrow spectrum. The significant infragravity wave period was approximately 37 sec. This run was selected because of the very narrow spectrum and the resulting strong infragravity modulation. The current measurements were made just outside the surf zone and in the surf zone.

The following sections describe the application of the depth-integrated and profile models to SUPERTANK Runs A0509A and A2007B and evaluation of model results.

Table 7.1. Wave and grid parameters for Runs A0509A and A2007B

Run	H_{mo}, m	T_p, sec	γ	nx	ny	Δx, m	Δt, sec
A0509A	0.8	3.0	20.	57	5	0.91	0.125
A2007B	0.7	5.0	100.	37	5	0.61	0.125

7.2 Depth-Integrated Model

The two-dimensional-horizontal, depth-integrated Predictor-Corrector model described in Chapter 3 is used to calculate the long-wave water surface elevations for SUPERTANK. The governing equations are continuity and momentum (Equations 3.1-3). The offshore boundary condition is an incident long-wave time series, and the boundary condition at the shoreline is full reflection of the long wave. Radiation stress forcing, calculated from the SUPERTANK short-wave measurements, is applied throughout the nearshore. The depth-integrated model provides the long-wave water surface elevation throughout the nearshore to drive the time-varying velocity profile model (Section 7.3).

7.2.1 Model input and set up

As input, the depth-integrated Predictor-Corrector model requires the incident infragravity wave surface elevation time series at the offshore boundary, the time series of radiation stress throughout the domain, bottom friction information, initial conditions, and specification of the grid domain.

Offshore boundary condition

As described in Section 6.3.1, the SUPERTANK water surface and current measurements were filtered to separate short-wave motions from infragravity-wave motions using a low-pass filter. The low-passed signal includes wave-group forced long waves and free long waves that are reflected from the beach and wave generator (the generator absorbed reflected waves only at the incident short-wave peak period). The short-wave measurements are used to calculate radiation stress, and the infragravity wave measurements are used to drive the model at the offshore boundary and to evaluate model output within the domain.

Incident infragravity-wave time series at the offshore boundary were calculated using a linear technique to separate the incident and reflected waves using co-located measurements of cross-shore velocity and water surface elevation (Hughes 1993, Section 6.3.3). This required that the offshore model boundary be located at a position with co-located wave and current gauges. The offshore boundary for Run A0509A is at $x = 0.0$ m in Figure 7.1, in a water depth of 2.42 m. The offshore boundary for Run A2007B is at $x = 32.9$ m in Figure 7.2, in a water depth of 0.78 m. This boundary location was selected for Run A2007B because it was the deepest location with a current meter. The separated incident and reflected water surface elevations for Run A2007B are given in Figure 6.10.

Note that both forced and free infragravity waves existing in the tank are included in the offshore water surface boundary condition. The offshore boundary time series was applied uniformly across the offshore boundary (in the longshore direction).

Radiation stress forcing

The radiation stress forcing throughout the domain is the most difficult input to supply. Using the SUPERTANK water surface elevation measurements, radiation stress is calculated from the measured envelope of short-wave energy using linear wave theory (Equation 3.31), and assuming shallow-water conditions for the short-wave motion. The envelope of the short-wave energy ($\overline{\eta^2}$) was calculated by squaring the measured short-wave water surface elevation (η), low-pass filtering using the same filter used to separate the short-wave and infragravity wave motions, multiplying by two, and applying Equation 3.31, which results in

$$S_{xx} = \frac{3}{2}\,\rho g\,\overline{\eta^2}(t) \tag{7.1}$$

The spacing of the SUPERTANK water surface measurements was 3.66 m, which is coarser than the grid spacing used in model applications. To fill the spatial gaps, the short-wave energy envelope was linearly interpolated between gauges. The most shoreward wave gauge was located at x = 47.59 for Run A0509A and at x = 43.9 m for Run A2007B, so the wave energy envelope was linearly interpolated from the measured value at the most shoreward gauge to zero at the shoreline. The gauge spacing does not resolve the incipient breaker region well. Numerical or analytical models of the transformation and breaking of the short-wave groups could be used to provide the short-wave energy based on the energy equation. Additional empirical assumptions would be required to specify wave breaking for the wave groups. The approach taken here is to use the laboratory measurements. Thus, the short-wave breaker region is not well represented due to a lack of resolution in the measurements. The radiation stress forcing was applied uniformly across the grid in the longshore direction. The envelope of the short-wave energy is used in Equation 7.1 to calculate the time-varying radiation stress.

Bottom friction

Bottom friction is specified using Equation 2.37. A constant bottom friction coefficient of $f_{cw} = 0.01$ is used for all simulations. The model results were insensitive to the choice of f_{cw} in the typical range of values between 0.01-0.05. The short-wave velocity amplitude, u_o, is calculated using linear theory

$$u_o = \frac{a}{h} \frac{\sigma}{\sinh(kh)} \tag{7.2}$$

where a is the short-wave amplitude, σ is the short-wave radial frequency, and k is the short-wave wave number. To simplify the calculation of the velocity amplitude, the local wave amplitude was assumed equal to half the incident H_{mo}, outside the surf zone. To approximate breaking, a limiting amplitude of 0.4 h_0

was applied. Progressing from the offshore boundary to the shore, amplitudes clipped by 0.4 h_0 were passed shoreward as the base amplitude in place of 0.5 H_{mo}. The short-wave amplitude was assumed constant in time for the calculation of bottom friction.

Initial conditions

The initial conditions for the depth-integrated model (Equation 3.4-12) were specified as $Q_x = 0$ m^2/sec and $\overline{\zeta} = 0$ m throughout the domain. The infragravity wave forcing at the offshore boundary and the radiation stress forcing throughout the domain were also initiated at zero and linearly increased to their full measured values over the first 500 time steps. This ramping of the forcing reduces artificial oscillations generated by the initial conditions.

Grid domain

For Run A0509A, the region modeled extends from a depth of 2.42 m to 0.20 m. The cross-shore and longshore grid spacing was 0.91 m, and the time step used was 0.125 sec. With $\Delta x = 0.91$ m, there were 57 grid cells in the cross-shore (5 cells in the longshore). For Run A2007B, the region modeled extends from a depth of 0.78 m to 0.12 m. The cross-shore and longshore grid spacing was 0.61 m, resulting in 37 cells in the cross-shore and 5 cells in the longshore. For both SUPERTANK runs, the time step used was 0.125 sec. The grid spacings were selected so measurement points aligned with grid cells and the Courant criterion of $\Delta t \leq \Delta x/C$ was met. The time step was selected to equal twice the measurement sampling rate. The grid information for each run is summarized in Table 7.1. Water depths were specified from the SUPERTANK bathymetry surveys.

7.2.2 Model results

Results for the infragravity wave water surface elevation and depth-integrated velocities ($\overline{U} = Q_x/h$) are given in Figures 7.3-7.8 for Run A0509A and Figures 7.9-7.14 for Run A2007B. The figures show time series results for four x locations. The solid lines are the low-pass filtered wave and current measurements and the dashed lines are the model results. Infragravity surface elevations are relative to the still-water level, with negative values below still-water level and positive values above still-water level. Positive velocities are directed onshore and negative velocities are offshore. The measured velocities are determined as the average of the long-wave velocities over all gauges below the still-water level, not taking into account that the sensors are unevenly distributed over depth. Error statistics and mean values at all measurement locations are given in Tables 7.2 and 7.3 for Runs A0509A and A2007B, respectively. The dimensionless mean measured and calculated infragravity-wave surface elevations are given by

$$\overline{\zeta_{mm}} = \frac{\sum_{i=1}^{N} \overline{\zeta_m}}{N\, H_{rms}} \; X\ 100 \tag{7.3}$$

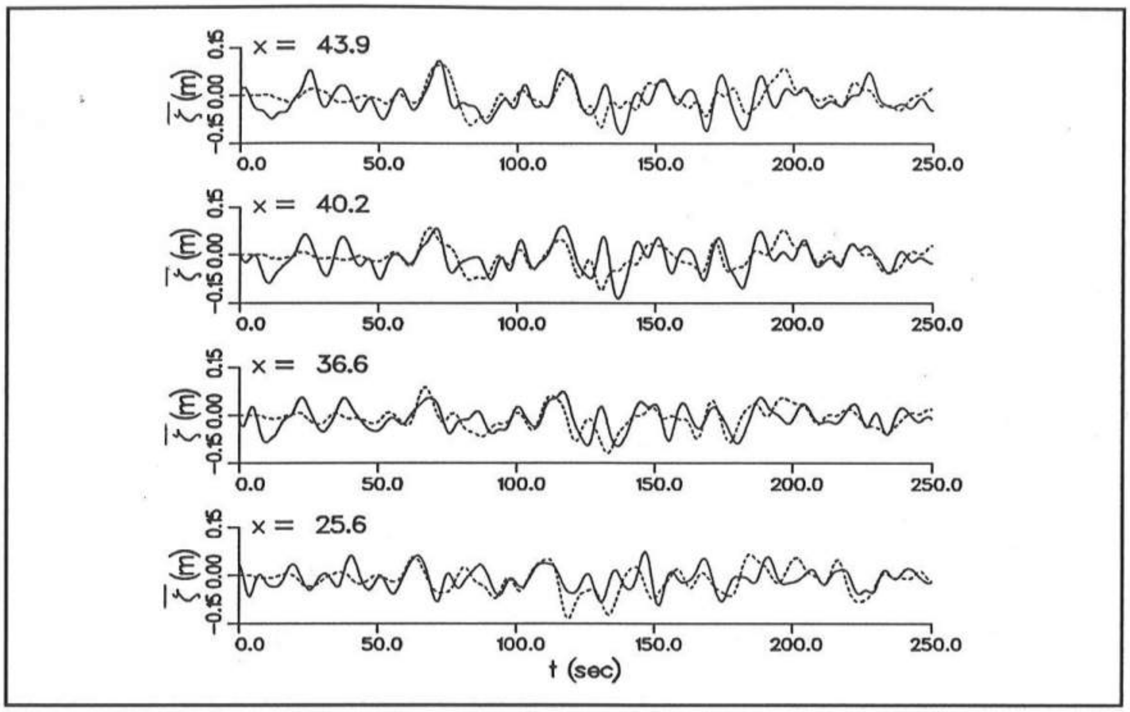

Figure 7.3. Infragravity surface elevations (solid -- measured, dashed -- calculated) for Run A0509A, t = 0-250 sec

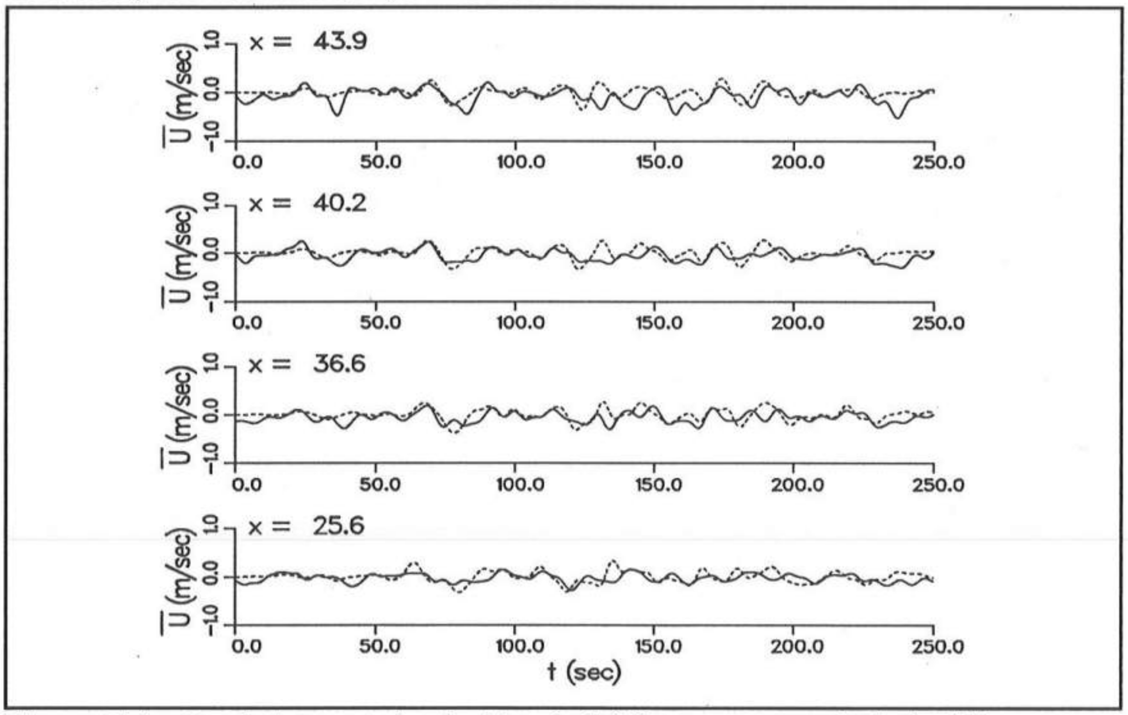

Figure 7.4. Depth-integrated velocities (solid line -- measured, dashed line -- calculated) for Run A0509A, t = 0-250 sec

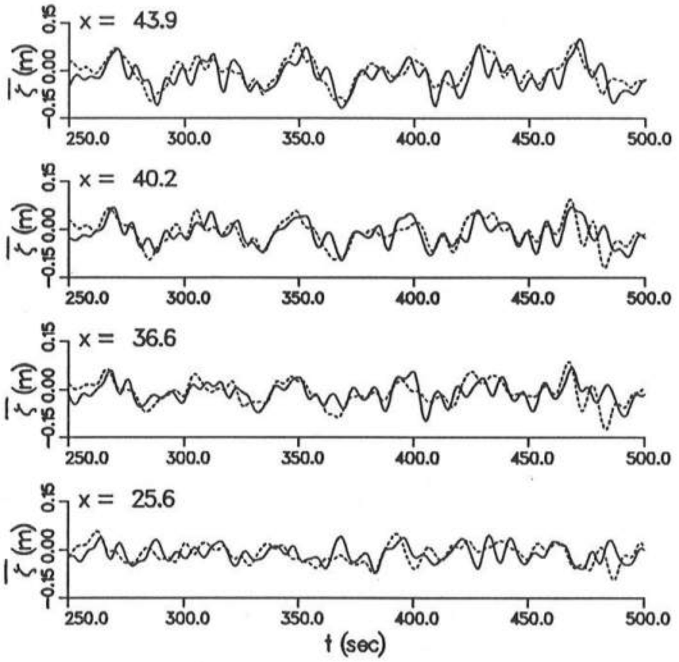

Figure 7.5. Infragravity surface elevations (solid -- measured, dashed -- calculated) for Run A0509A, t = 250-500 sec

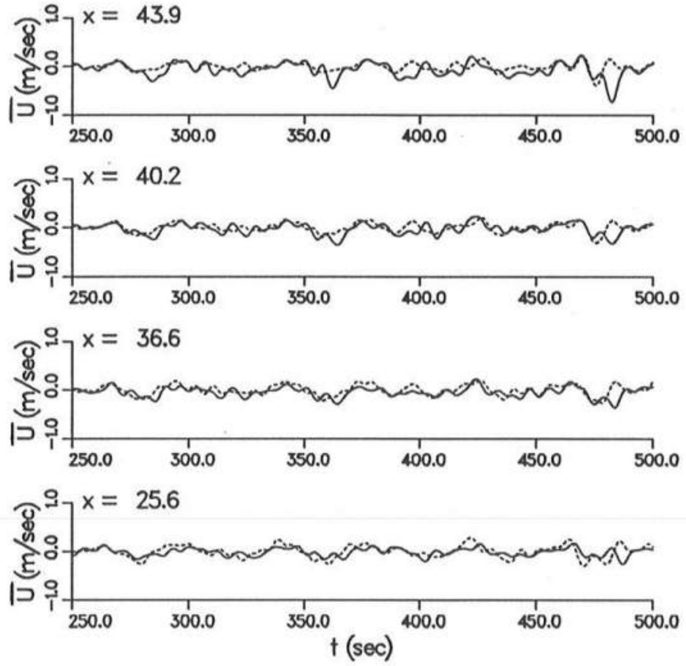

Figure 7.6. Depth-integrated velocities (solid line -- measured, dashed line -- calculated) for Run A0509A, t = 250-500 sec

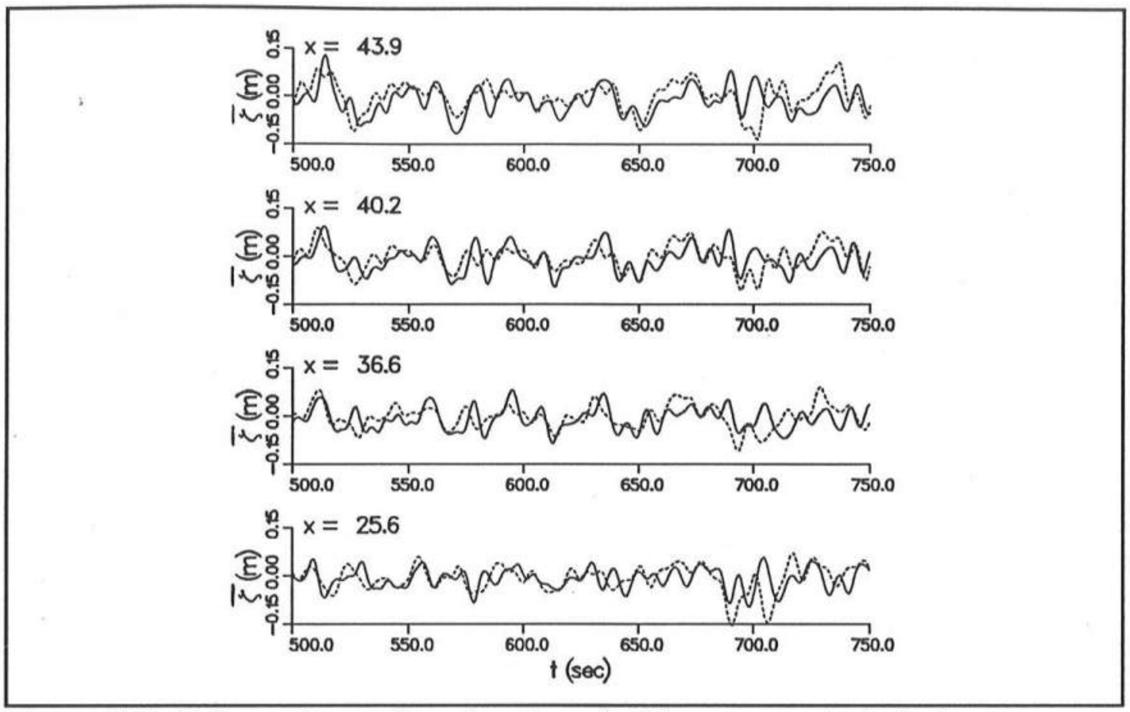

Figure 7.7. Infragravity surface elevations (solid -- measured, dashed -- calculated) for Run A0509A, t = 500-750 sec

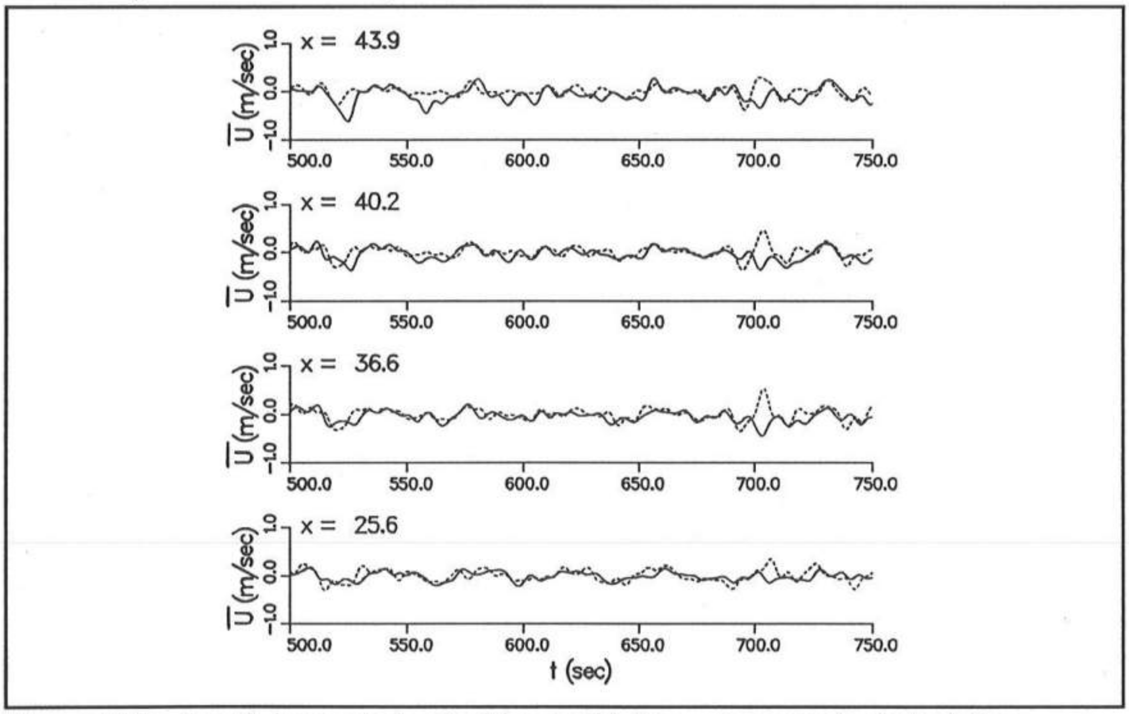

Figure 7.8. Depth-integrated velocities (solid line -- measured, dashed line -- calculated) for Run A0509A, t = 500-750 sec

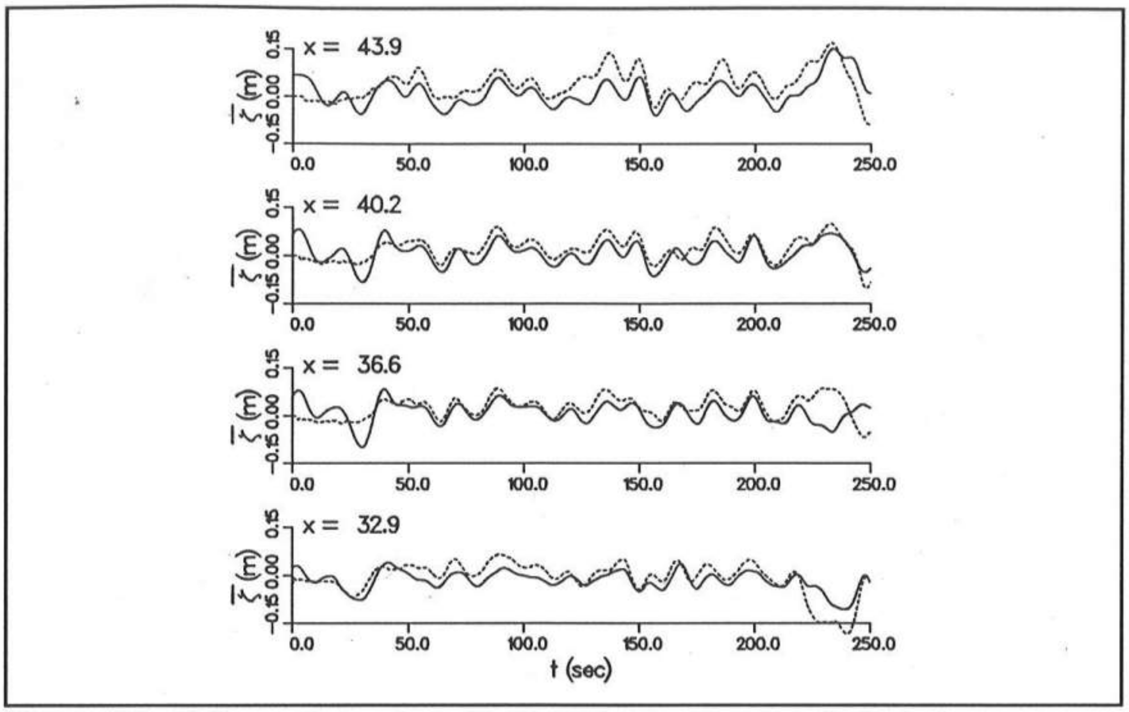

Figure 7.9. Infragravity surface elevations (solid -- measured, dashed -- calculated) for Run A2007B, *t* = 0-250 sec

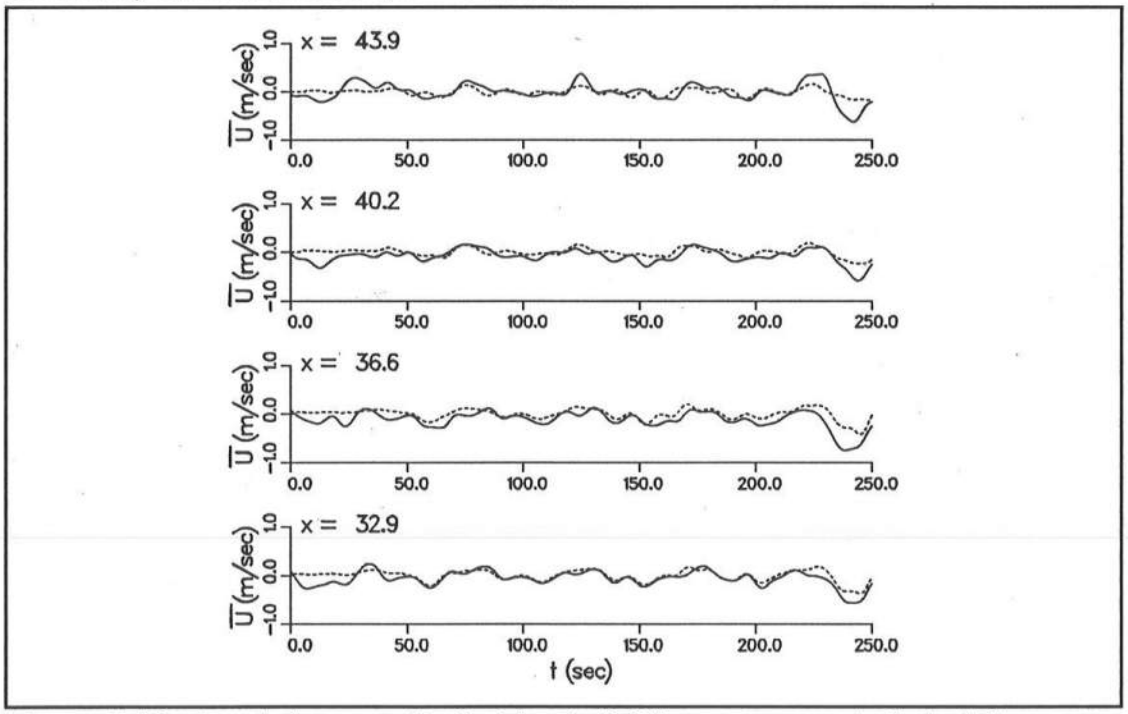

Figure 7.10. Depth-integrated velocities (solid line -- measured, dashed line -- calculated) for Run A2007B, *t* = 0-250 sec

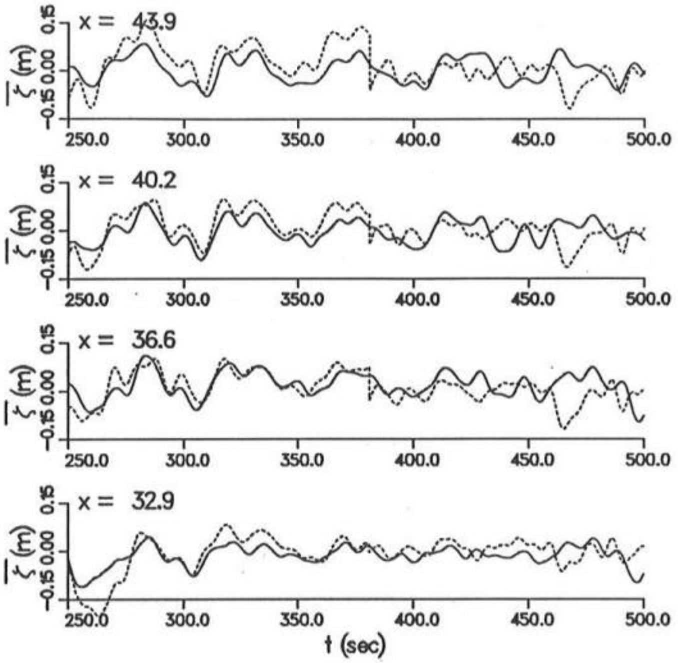

Figure 7.11. Infragravity surface elevations (solid -- measured, dashed -- calculated) for Run A2007B, t = 250-500 sec

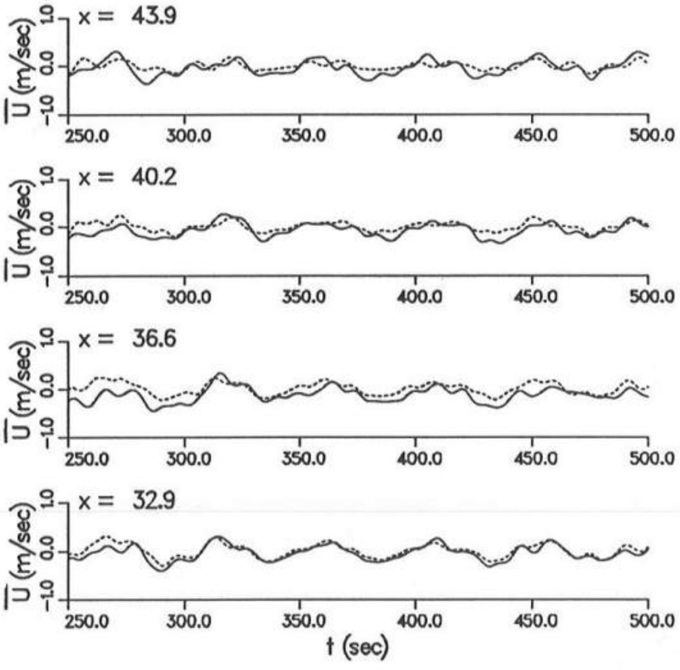

Figure 7.12. Depth-integrated velocities (solid line -- measured, dashed line -- calculated) for Run A2007B, t = 250-500 sec

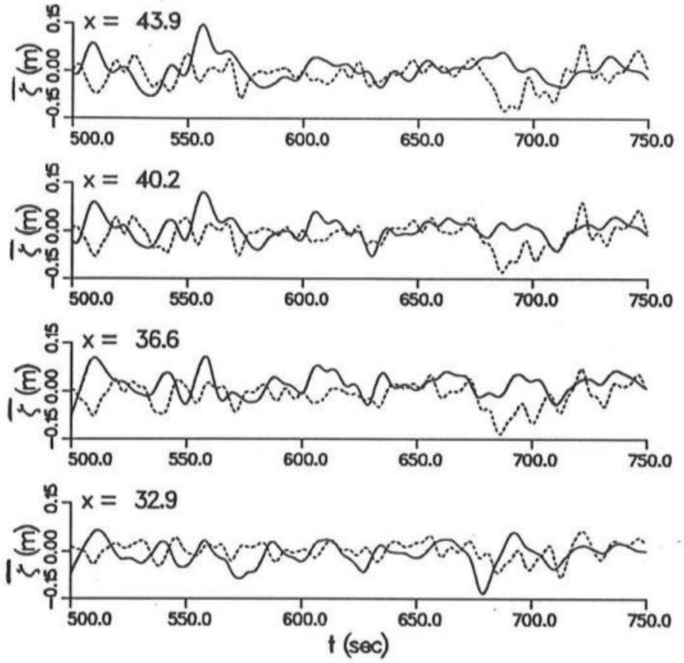

Figure 7.13. Infragravity surface elevations (solid -- measured, dashed -- calculated) for Run A2007B, t = 500-750 sec

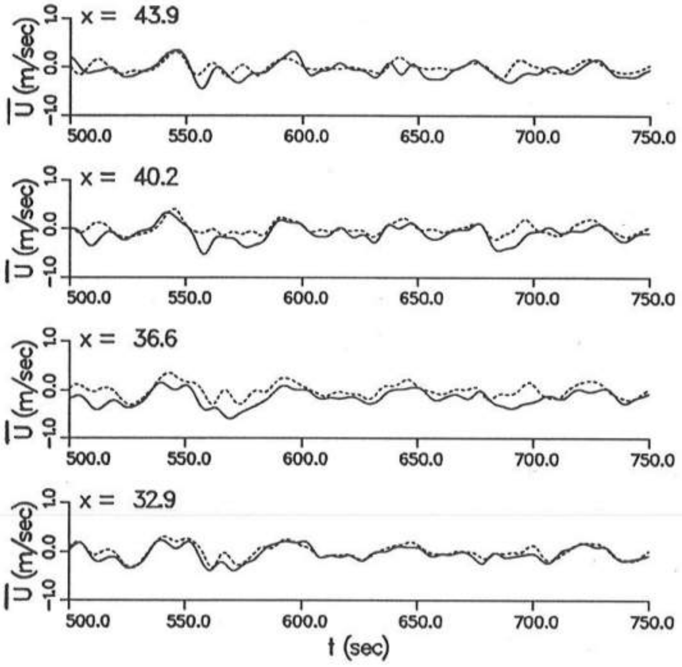

Figure 7.14. Depth-integrated velocities (solid line -- measured, dashed line -- calculated) for Run A2007B, t = 500-750 sec

Table 7.2. Depth-integrated model means and rms errors for Run A0509A

x, m	$\overline{\zeta}_{mm}$, %	$\overline{\zeta}_{mc}$, %	$E_{\overline{\zeta},rms}$, %	$\overline{U}_{mm}$, %	$\overline{U}_{mc}$, %	$E_{\overline{U},rms}$, %
0.0	-0.94	0.14	3.75	-0.30	0.02	2.50
3.66	-1.08	-2.13	1.15	---	---	---
7.32	-0.98	-2.01	4.64	---	---	---
10.97	-1.05	-1.99	4.66	---	---	---
14.63	-1.06	-1.89	4.65	---	---	---
18.29	-1.02	-1.99	4.72	---	---	---
21.95	-1.02	-1.93	4.92	---	---	---
25.60	-1.47	-1.66	5.14	-0.43	0.00	2.78
29.26	-1.30	-1.73	5.16	---	---	---
32.92	-1.34	-1.49	5.24	---	---	---
34.75	---	---	---	-1.75	-0.01	3.87
36.58	-1.57	-1.18	5.28	-1.30	-0.01	3.62
40.23	-1.66	-1.15	5.58	-1.20	-0.01	3.97
43.89	-2.15	-0.35	6.42	-2.35	-0.003	5.65
47.59	-13.74	3.71	19.48	---		---

Table 7.3. Depth-integrated model means and rms errors for Run A2007B

x, m	$\overline{\zeta}_{mm}$, %	$\overline{\zeta}_{mc}$, %	$E_{\overline{\zeta},rms}$, %	$\overline{U}_{mm}$, %	$\overline{U}_{mc}$, %	$E_{\overline{U},rms}$, %
32.92	-1.60	-0.43	4.41	-1.80	-0.05	2.98
36.58	3.26	7.89	7.56	-5.00	-0.04	6.44
37.19	---	---	---	-2.80	-0.04	4.31
40.23	0.57	6.76	7.79	-3.72	-0.05	5.94
43.89	2.82	20.68	21.50	-1.41	-0.03	5.38

$$\overline{\zeta_{cm}} = \frac{\sum_{i=1}^{N} \overline{\zeta_c}}{N\, H_{rms}} \; X\ 100 \qquad \mathbf{(7.4)}$$

where $\overline{\zeta}_m$ is the depth-averaged measured velocity, $\overline{\zeta}_c$ is the velocity calculated using the depth-integrated model, N is the number of measurements in the time series, and H_{rms} is the local rms wave height. The dimensionless rms error in long-wave water surface elevation is defined

$$E_{\overline{\zeta},rms} = \sqrt{\frac{\sum_{i=1}^{N} (\overline{\zeta_m} - \overline{\zeta_c})^2}{N\ H_{rms}^2}}\ X\ 100 \tag{7.5}$$

The dimensionless mean measured and calculated depth-integrated velocities are given by

$$\overline{U_{mm}} = \frac{\sum_{i=1}^{N} \overline{U_m}}{N \sqrt{g h_0}}\ X\ 100 \tag{7.6}$$

$$\overline{U_{cm}} = \frac{\sum_{i=1}^{N} \overline{U_c}}{N \sqrt{g h_0}}\ X\ 100 \tag{7.7}$$

where $\overline{U}_m$ is the depth-averaged measured velocity and $\overline{U}_c$ is the velocity calculated using the depth-integrated model. The dimensionless rms error in velocity is defined

$$E_{U,rms} = \sqrt{\frac{\sum_{i=1}^{N} (U_m - U_c)^2}{N\ g h_0}}\ X\ 100 \tag{7.8}$$

Dashes in the columns of Tables 7.2 and 7.3 indicate that a measurement was not made at the given x location.

Surface elevations

Comparison of the mean calculated infragravity surface elevations to the measured elevations illustrates clearly the inaccuracies in calculating the mean radiation stress. The mean setdown and setup are driven by the gradients in the mean radiation stress (caused by wave shoaling and breaking). As discussed previously, the wave height variation around breaking is not well captured in the measurements due to the fairly coarse spacing of the wave gauges (3.66 m). This results in a similar inaccuracy in the estimation of the radiation stress forcing. Linear theory used to calculate radiation stress is known to be inaccurate. Furthermore, the simple method used to calculated radiation stress does not account for the transition region between incipient breaking and wave setup (Svendsen 1984a) where changes in wave shape counteract the rapidly decreasing wave height to produce essentially constant radiation stress. This is illustrated by looking at the most shoreward points in Tables 7.2 and 7.3. For Run A0509A, the calculations show significant wave setup at x = 47.59 m, and the maximum setdown occurring at x = 29.26 m. The measurements show the maximum setdown is much further shoreward at x = 43.89 m and only a small setup at x = 47.59 m. The over estimation of setup at the shoreline in the numerical model results in exaggerated setdown in the offshore region (in the closed calculation domain, overprediction of the mean wave level in one area will cause an underprediction in other areas). The mean setdown is approximately twice the measured values, although the maximum calculated setdown is about equal to the measured value. For Run A2007B where all the gauges except the most seaward is in the surf zone, the setup calculated at the gauge locations is as much as an order of magnitude larger than the measurements.

Next, looking at the rms error in the infragravity wave calculations, the average rms error in surface elevation is 5.8% of H_{rms} (0.040 m) for Run A0509A and 10.3% of H_{rms} (0.044 m) for Run A2007B. The error increases in the shallowest depths. The reason for the increase in error at shallower depths is three-fold: (a) again, the linear radiation stress calculations are less accurate in shallower depths as the waves become more nonlinear, (b) the measurements are less accurate in shallower depths as the sand depth at the gauge changes during the run, potentially causing a change in the gauge offset calculated at the beginning of the run, and (c) the error in mean water level increases substantially in shallow water. Up to 55 percent of the rms error accounts for the mean errors previously discussed. The error in the mean setup accounts for a large percentage of the rms error in all locations with a positive mean water level, where large mean errors occurred. Removing the mean setup from the total water surface elevations reduced the average rms errors to 5.1% (0.035 m) and 7.3% (0.031 m) for Runs A0509A and A2007B, respectively.

Velocities

The calculated time means of the depth-integrated cross-shore velocities are approximately zero, as would be expected from a depth-integrated model with no net inflow or outflow. However, the depth-averaged measured mean velocities do show a net offshore flow or undertow. This is due to the fact that all measurements used were below the still-water level and the wave mass flux, which is included in the calculated volume flux, occurs above that level. Data from gauges shown in Figure 7.2 that were at or above the still-water level tended to be unreliable and were neglected. The measurements are capturing, to varying degrees depending on the measurement elevation, the return flow (undertow) from the wave-driven mass transport. The return flow is generally expressed as

$$U_{mass} = C_{mass} \sqrt{gh} \frac{H^2}{h^2} \tag{7.9}$$

where U_{mass} is the return flow velocity and C_{mass} is a variable coefficient (see Svendsen 1984b). The values of C_{mass}, based on the depth-averaged measured velocities and significant wave heights, range from 0.02 to 0.13, with the larger values in the surf zone. The model cannot represent the mean measured undertow without explicitly specifying the mass transport, which is not done here.

The average rms error in depth-averaged velocity is 3.7% of $\sqrt{gh}$ (0.13 m/sec) for Run A0509A and 5.0% of $\sqrt{gh}$ (0.13 m/sec) for Run A2007B. Removing the mean from the velocities reduced the average rms error for Run A0509A slightly (6 percent) and the error for Run A2007B was reduced 22 percent to 3.9% (0.10 m/sec). The errors were generally fairly constant throughout the domain.

7.3 Profile Model

7.3.1 Model input and set up

The profile model requires the water surface gradient, radiation stress, bottom friction coefficient, eddy viscosity, grid-like parameters, and initial conditions as input.

Water surface gradient, radiation stress, and bottom friction

The input parameters of the water surface gradient and the radiation stress are closely tied to the depth-integrated model. As described in Section 4.2.1, the infragravity water surface elevations are obtained from the output of the depth-integrated model. The radiation stress calculated within the depth-integrated model is saved along with the water surface elevations. Input for the profile model are gradients of $\overline{\zeta}$ and radiation stress which are calculated with second-order finite differences within the profile model. Note that the Δx for the derivatives is the same as used in the depth-integrated model, although the velocity profiles can be calculated anywhere within the grid used for the depth-integrated model without determining the solution for the entire domain. The bottom friction is calculated using Equation 2.37 with a constant bottom friction coefficient of $f_{cw} = 0.01$, as in the depth-integrated model. It is very important that forcing in the depth-integrated and profile models be consistent. Otherwise, the water surface gradient calculated in the depth-integrated model will not be in equilibrium with the other profile model forcing.

Eddy viscosity

The eddy viscosity is calculated using Equation 4.49. For complicated cross-shore bathymetry, such as SUPERTANK Run A2007B, the "inside surf zone" formulation for eddy viscosity is applied for all points shoreward of the most offshore point where $H_{mo}/h = 0.8$.

Grid-like parameters and initial conditions

The profile model was applied at all x locations in the depth-integrated grid, using the central point in y. Profiles were determined using 10 eigenfunctions and specifying output at 21 locations over the vertical. The initial condition was $U = 0$ m/sec for all x and z.

7.3.2 Model results

Example profile model results are shown in Figures 7.15-7.24. In Figures 7.15-7.22, the solid line is the profile model output, the dashed line is the depth-integrated model output, and the symbols are measurements. The vertical axis is the dimensionless depth Z, where

$$Z = \frac{h_0 + z}{h_0} \qquad \textbf{(7.10)}$$

The six panels in each figure represent six snapshots in time at 3-sec intervals. Figures 7.15-7.18 are results from Run A0509A, and Figures 7.18-7.22 are results from Run A2007B. Figures 7.23 and 7.24 are overlays of calculated velocity profiles at 3-sec time increments from $t = 500$ to 750 sec, for Runs A0509A and

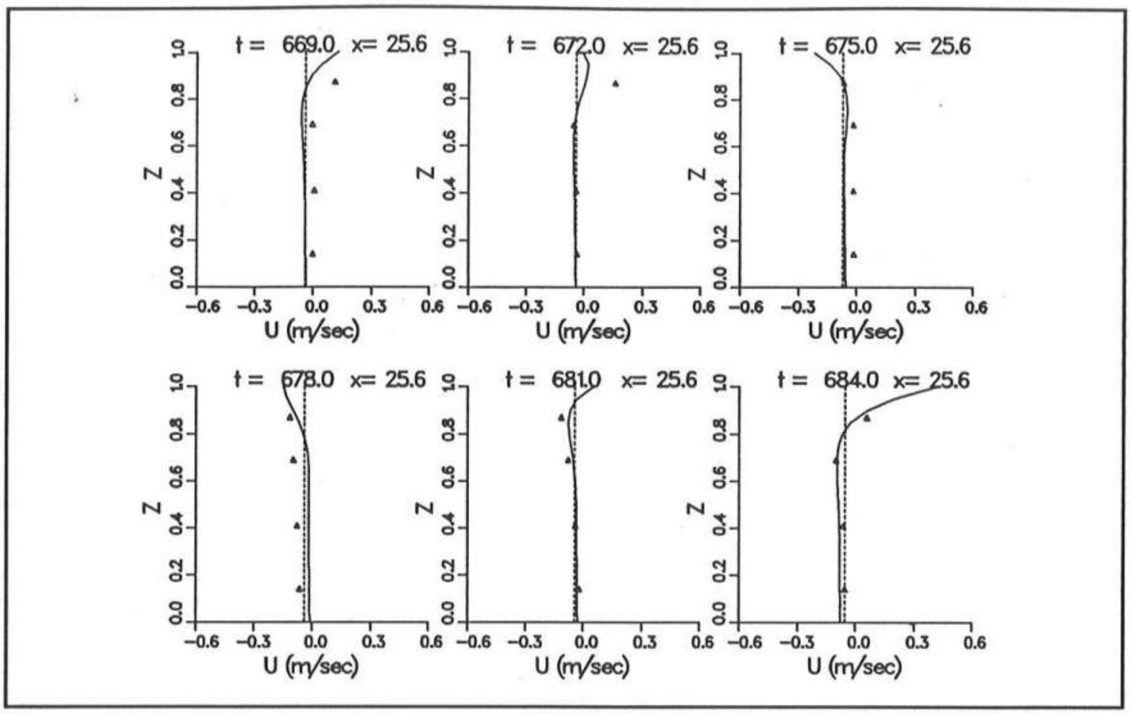

Figure 7.15. Velocity profiles at x = 25.6 m (solid -- profile model, dashed -- depth-integrated model, symbols -- measurements) for Run A0509A

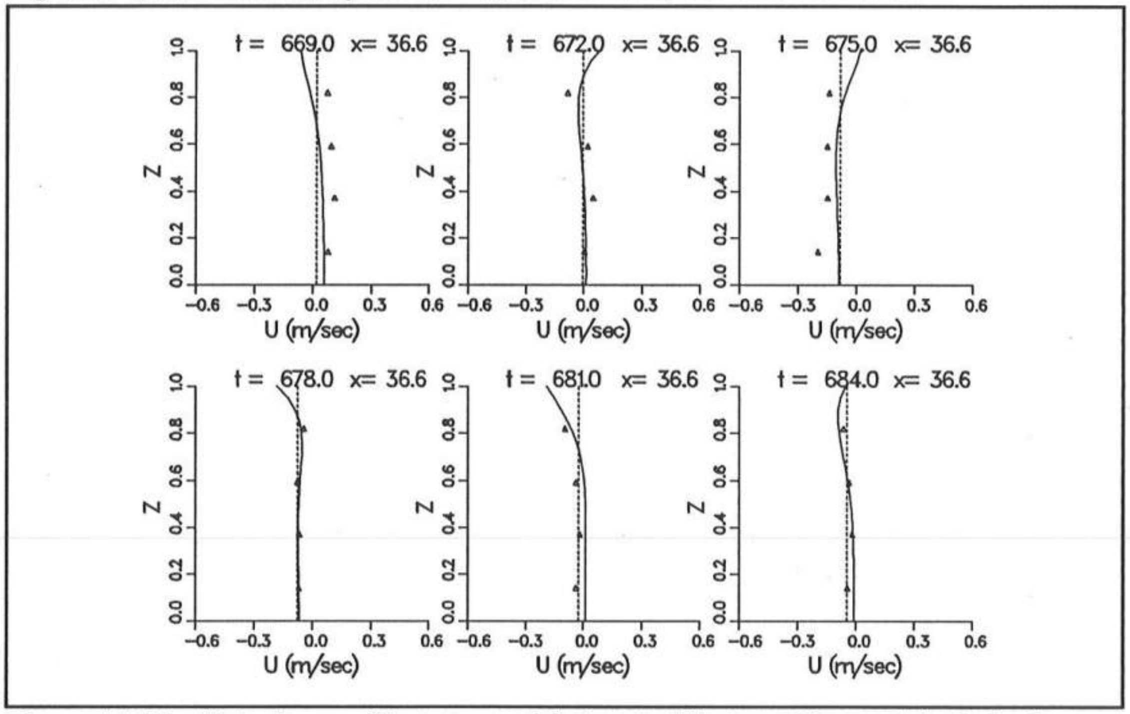

Figure 7.16. Velocity profiles at x = 36.6 m (solid -- profile model, dashed -- depth-integrated model, symbols -- measurements) for Run A0509A

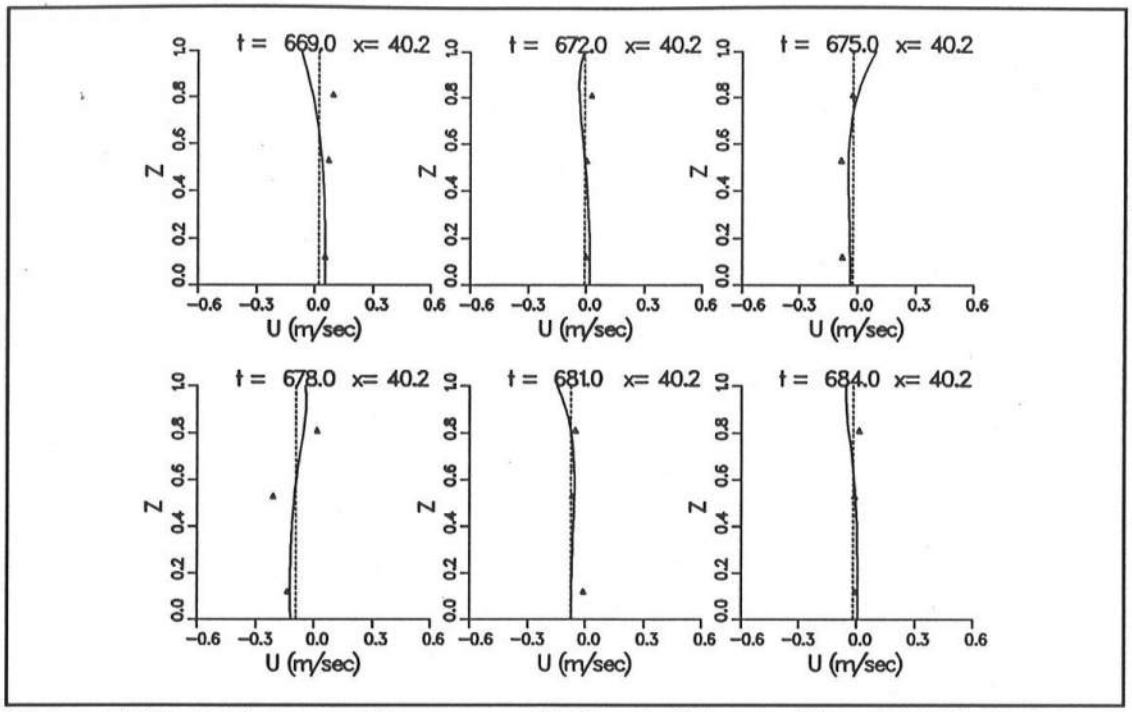

Figure 7.17. Velocity profiles at $x = 40.2$ m (solid -- profile model, dashed -- depth-integrated model, symbols -- measurements) for Run A0509A

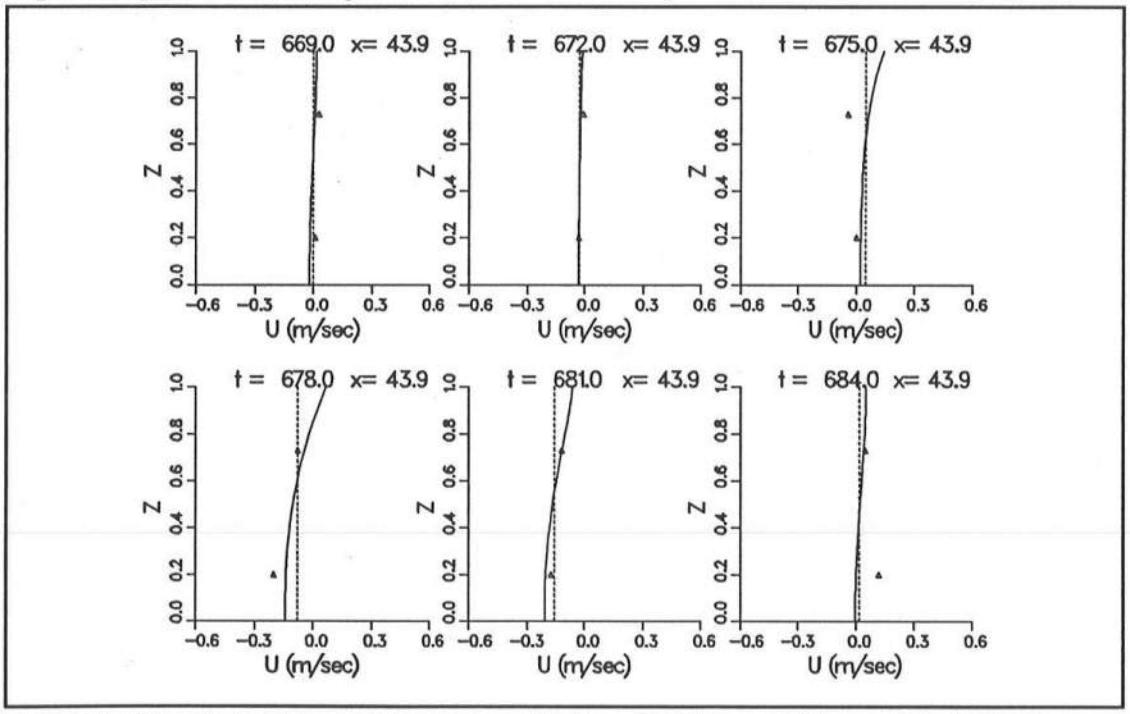

Figure 7.18. Velocity profiles at $x = 43.9$ m (solid -- profile model, dashed -- depth-integrated model, symbols -- measurements) for Run A0509A

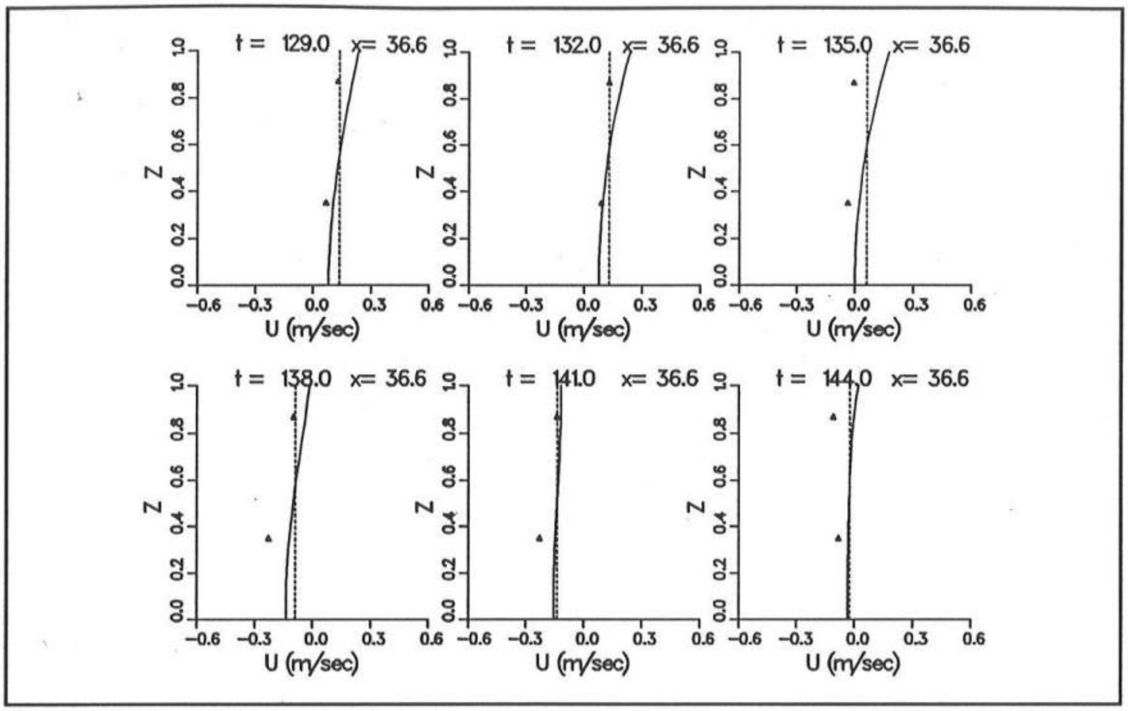

Figure 7.19. Velocity profiles at x = 36.6 m (solid -- profile model, dashed -- depth-integrated model, symbols -- measurements) for Run A2007B

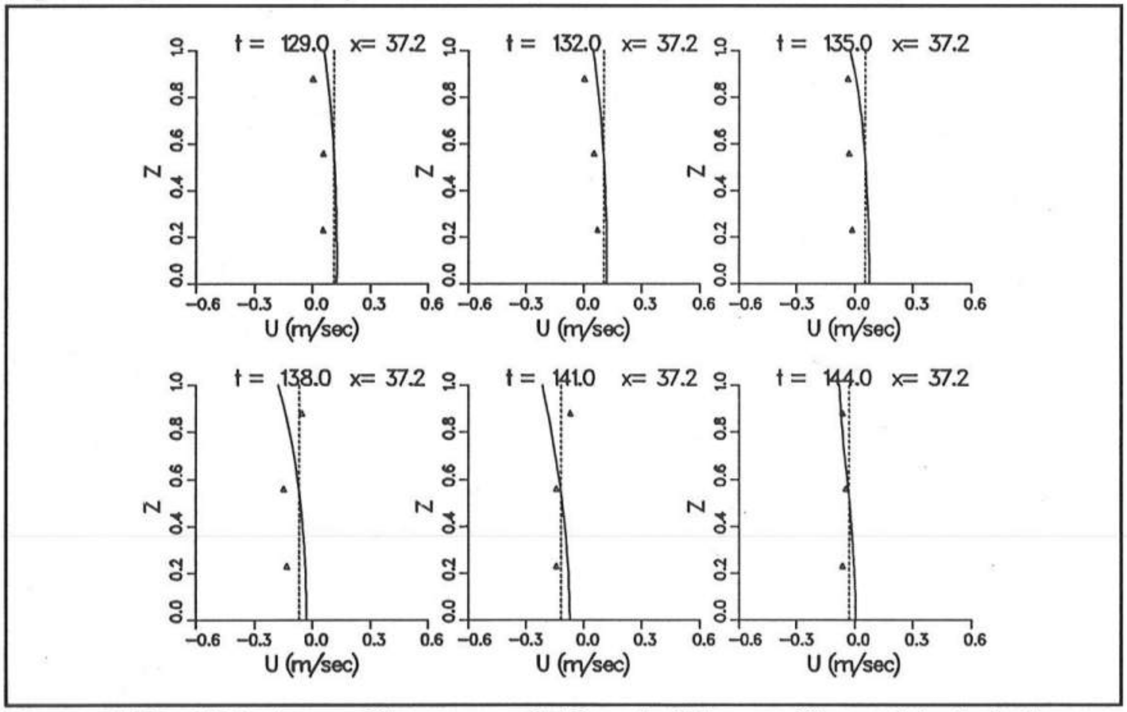

Figure 7.20. Velocity profiles at x = 37.2 m (solid -- profile model, dashed -- depth-integrated model, symbols -- measurements) for Run A2007B

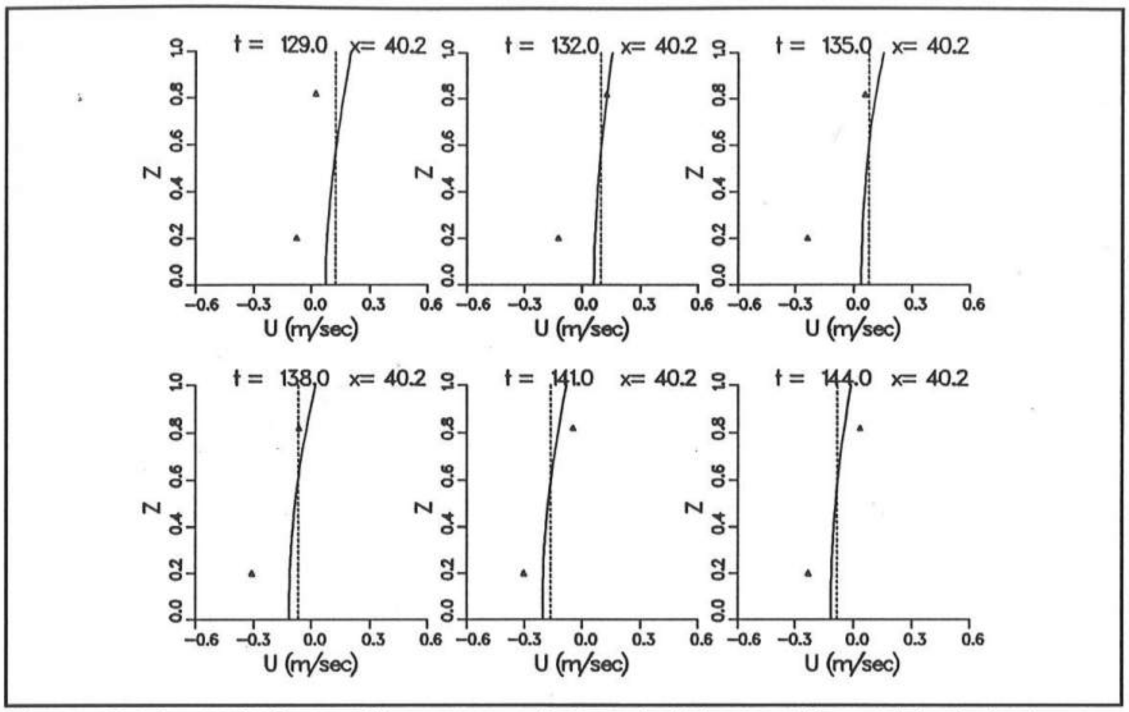

Figure 7.21. Velocity profiles at $x = 40.2$ m (solid -- profile model, dashed -- depth-integrated model, symbols -- measurements) for Run A2007B

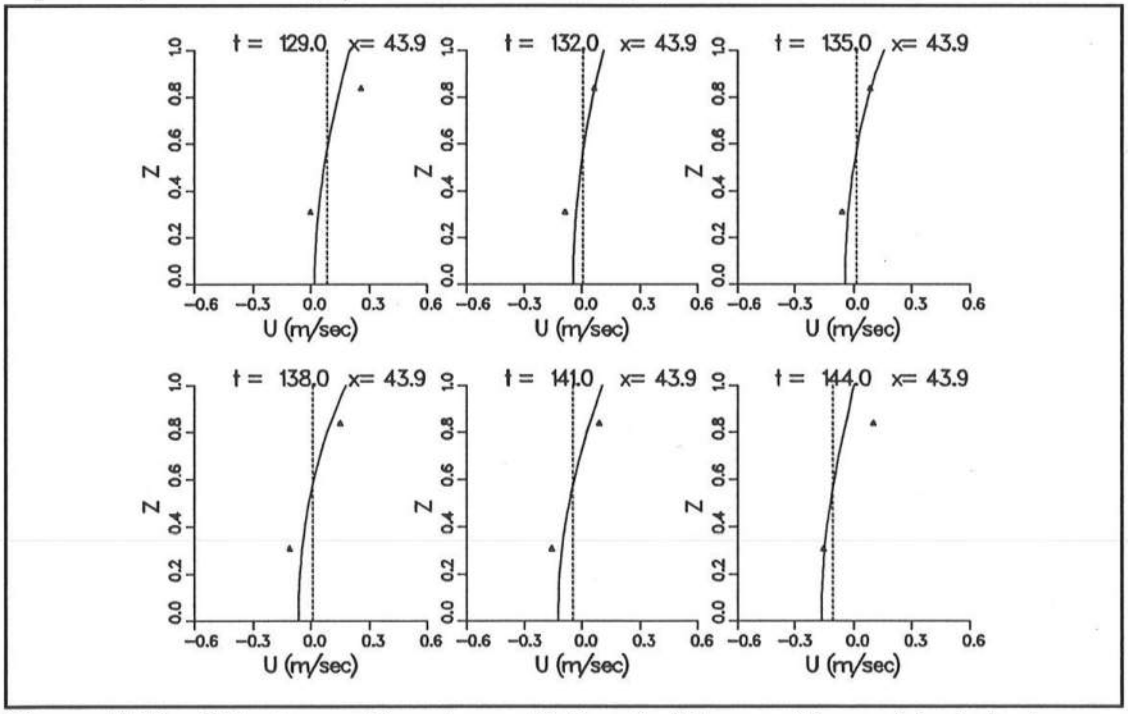

Figure 7.22. Velocity profiles at $x = 43.9$ m (solid -- profile model, dashed -- depth-integrated model, symbols -- measurements) for Run A2007B

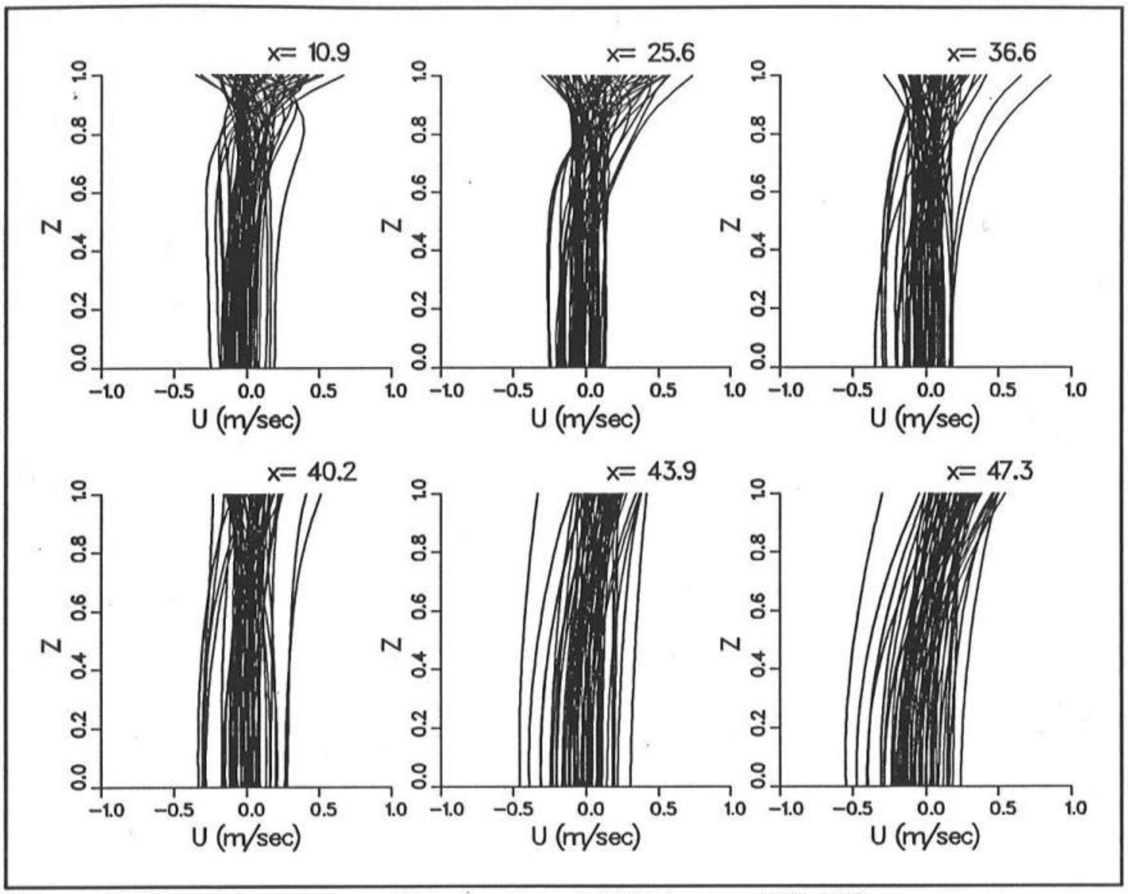

Figure 7.23. Calculated profiles for Run A0509A, t = 500-750 sec

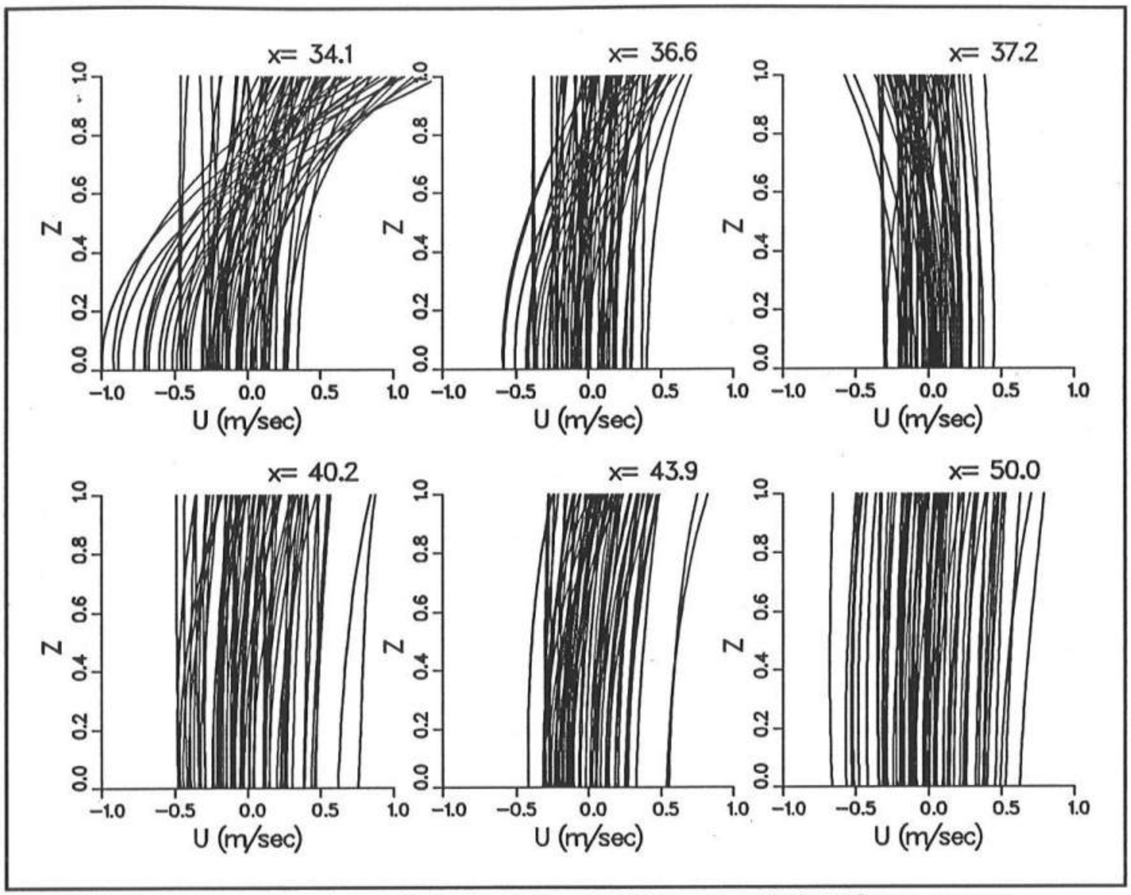

Figure 7.24. Calculated profiles for Run A2007B, t = 500-750 sec

A2007B, respectively. Error statistics and mean velocities at the measurement locations are given in Tables 7.4 and 7.5 for Runs A0509A and A2007B, respectively. The tables give the x locations (see Figures 7.1-7.2), water depths, and dimensionless vertical positions Z (Equation 7.10) at which the measurements were made. The dimensionless mean measured and calculated velocities are defined

$$U_{mm} = \frac{\sum_{i=1}^{N} U_m}{N\sqrt{g h_0}} \text{ X } 100 \tag{7.11}$$

$$U_{cm} = \frac{\sum_{i=1}^{N} U_c}{N\sqrt{g h_0}} \text{ X } 100 \tag{7.12}$$

where U_m is the measured velocity, U_c is the velocity calculated using the profile model, and N is the number of measurements in the time series. The dimensionless rms error in velocity is defined

$$E_{U,rms} = \sqrt{\frac{\sum_{i=1}^{N} (U_m - U_c)^2}{N g h_0}} \text{ X } 100 \tag{7.13}$$

Table 7.4. Profile model mean values and rms errors for Run A0509A

x, m	h, m	Z	U_{mm}, %	U_{cm}, %	$E_{U,rms}$, %	$E_{U,rms}^{*}$, %
25.60	1.67	0.14	-0.82	-0.71	2.24	2.24
25.60	1.67	0.41	-1.18	-0.39	2.28	2.14
25.60	1.67	0.69	-1.60	0.49	3.28	2.54
25.60	1.67	0.87	1.77	1.15	3.20	3.14
34.75	1.38	0.20	-1.85	-1.08	3.56	3.50
34.75	1.38	0.41	-1.85	-0.62	3.08	2.83
34.75	1.38	0.61	-1.66	0.19	3.60	3.09
34.75	1.38	0.84	-0.05	1.73	4.56	4.20
36.58	1.33	0.14	-1.75	-0.51	3.28	3.03
36.58	1.33	0.37	-1.56	-0.32	3.57	3.35
36.58	1.33	0.59	-1.58	0.16	4.01	3.62
36.58	1.33	0.82	-0.38	0.75	3.37	3.17
40.23	1.13	0.12	-1.71	-0.56	3.98	3.81
40.23	1.13	0.53	-2.60	-0.003	5.09	4.38
40.23	1.13	0.81	0.65	0.70	3.80	3.80
43.89	0.88	0.20	-4.03	-1.62	6.87	6.44
43.89	0.88	0.73	-0.69	1.41	5.68	5.28

*rms error with mean removed

Table 7.5. Profile model mean values and rms errors for Run A2007B

x, m	h, m	Z	U_{mm},	U_{cm},	U_{rms}, m/sec	U_{rms}^*, m/sec
36.58	0.74	0.35	-6.02	-1.55	7.17	5.62
36.58	0.74	0.87	-4.07	-2.82	9.87	7.07
37.19	0.88	0.23	-4.68	0.61	7.64	5.52
37.19	0.88	0.56	-3.19	-0.07	5.98	5.11
37.19	0.88	0.88	-0.58	-1.53	5.31	5.22
40.23	0.50	0.20	-8.18	-1.23	9.90	7.07
40.23	0.50	0.82	0.71	1.18	8.85	8.84
43.89	0.59	0.31	-5.79	-1.59	6.97	5.57
43.89	0.59	0.84	2.95	2.64	6.58	6.58

*rms error with mean removed

Run A0509A

Profiles for Run A0509A are given in Figures 7.15 - 7.18 and range from locations well outside the surf zone at x = 25.6 m to the outer surf zone at x = 43.9 m. These figures show a short sequence of profiles at a time when the depth-integrated model performed well in terms of predicting the infragravity motion (see Figures 7.7 and 7.8). Figure 7.23 gives an overview of profile shapes outside and inside the surf zone.

Outside the surf zone ($x < 40$ m), typical velocity profiles exhibit three characteristics: (a) the greatest velocity variation generally occurs near the surface, (b) the velocities near the surface and bottom are out of phase (note the "braided" appearance of the profiles near the surface), and (c) the profile variation over depth is relatively symmetric about $U = 0$ m/sec (time mean of the velocity at any elevation is near zero). These characteristics are illustrated in Figures 7.15 - 7.17 and 7.23. The velocity profiles are uniform over the lower two-thirds of the depth. Near the surface, the velocity magnitude is greater and the direction is often opposite that of the lower part of the water column. Typically, in the offshore region the time-varying surface stress is the dominant forcing. Since the mean forcing is small, the profiles are approximately symmetric about $U =$ 0 m/sec. The water depth is relatively large, so the surface stress causes higher velocities near the surface.

Inside the surf zone ($x > 40$ m), velocity profiles have the following characteristics: (a) the mean undertow profile is the dominant feature, and (b) the time-variation is fairly constant in magnitude and phase over depth (the profiles are approximately parallel, instead of the braided pattern outside the surf zone). The mean velocity profile inside the surf zone is the classic parabolic shape (see Figures 7.18 and 7.23), unlike outside the surf zone where the mean profile is approximately vertical. This implies that the dominant forcing in the outer surf zone is the mean surface stress (mean surface stress portion of the radiation stress gradient due to wave breaking). The typical time variation of the profile in the surf zone is an oscillation about the mean undertow profile, although there is a small phase difference between the surface the bottom. Figures 7.18 and 7.23 show that the velocity profiles are relatively vertical for positive (onshore) velocities and more parabolic for negative (offshore) velocities.

The average rms error in the calculated velocities is 3.9% of $\sqrt{g\,h}$ (0.14 m/sec), which is approximately equal to the error in the depth-integrated model. Considering only the time-varying solution, the rms error decreases slightly. Mean velocities are in general not well represented in the model. The reasons for the disagreement are the same as discussed in Section 7.2.2 for the depth-integrated model. The error is uncorrelated with elevation in the water column, but error does increase in the surf zone. The profile model reproduces the characteristics and the profile shapes measured in the SUPERTANK runs.

Run A2007B

Profiles for Run A2007B are given in Figures 7.19-7.22 and 7.24, and range from locations just outside the surf zone through the outer and mid surf zone. The profile characteristics discussed in the surf zone for Run A0509A apply here as well, i.e., dominance of parabolic profile shape, and time-varying phase and magnitude are constant over depth. In addition, in the mid to inner surf zone (x > 40 m), model results and measurements show less velocity variation over the vertical as the time-varying, depth-uniform forcing (surface elevation gradient) becomes dominant. This is shown clearly in Figure 7.24 at $x = 50.0$ m.

The average rms error in the calculated velocities for Run A2007B is 7.6% of $\sqrt{g\,h}$ (0.20 m/sec), which is about 50 percent greater that the depth-integrated model results. Considering only the time-varying solution, the rms error decreased to 6.3% (0.16 m/sec). Both Runs A0509A and A2007B show an increase in calculated velocity errors in and near the surf zone.

The main source of error in the calculations is inaccuracies in the forcing (linear radiation stress calculation and omission of the transition zone in the region of incipient wave breaking, see Section 7.2.2). Additional errors stem from the linear separation of the incident and reflected long wave used to drive the depth-integrated model, the linear separation of the short- and long-wave components, and the lack of resolution in the water surface measurements for calculating radiation stress. Laboratory measurement errors are also a factor.

7.3.3 Profile parameters

As discussed in Section 5.2.2, Putrevu and Svendsen (1995) identified dimensionless parameters that together describe infragravity wave profiles: βh which determines the depth to which the effect of the surface and bed shear stresses are felt ($\beta = (\omega/(2\,\nu_t))^{0.5}$, ω is the infragravity wave frequency, and h is water depth); Δ which is the relative phase between the surface stress and depth-uniform forcing; and $T_s\,\beta/(\rho\,f_a)$ which is the relative importance of the surface stress and depth-uniform forcing, where T_s and f_a are the amplitudes of the surface stress and depth-uniform forcing, respectively. A summary of estimated parameter values for the SUPERTANK Runs A0509A and A2007B are shown in Figures 7.25 and 7.26. The parameters are estimated using peak infragravity wave frequencies of 0.039 Hz for Run A0509A and 0.027 Hz for Run A2007B. The peak frequencies for the surface stress and depth-uniform forcing were not exactly the same. Also, the peak frequencies varied somewhat across the grid. The interpretation of parameters values illustrates the mechanisms behind the trends discussed previously, including penetration of surface stresses, the relative phasing of the forcing, and the dominant forcing.

Parameter βh

The larger value of βh outside the surf zone implies that surface stress forcing will impact a smaller percentage of the water column than at locations inside the surf zone, and thus, the greatest vertical variation will be near the surface. For Run A0509A, βh varies from 10 to 1, which is reflected in the difference between the profiles with greater variations near the surface outside the surf zone (large βh) and profiles with a uniform variation in magnitude over depth in the surf zone (small βh). For Run A2007B, βh is relatively constant (1.5 to 1.0), and the profile variation over depth is similar to the surf zone profiles of Run A0509A which have similar values of βh.

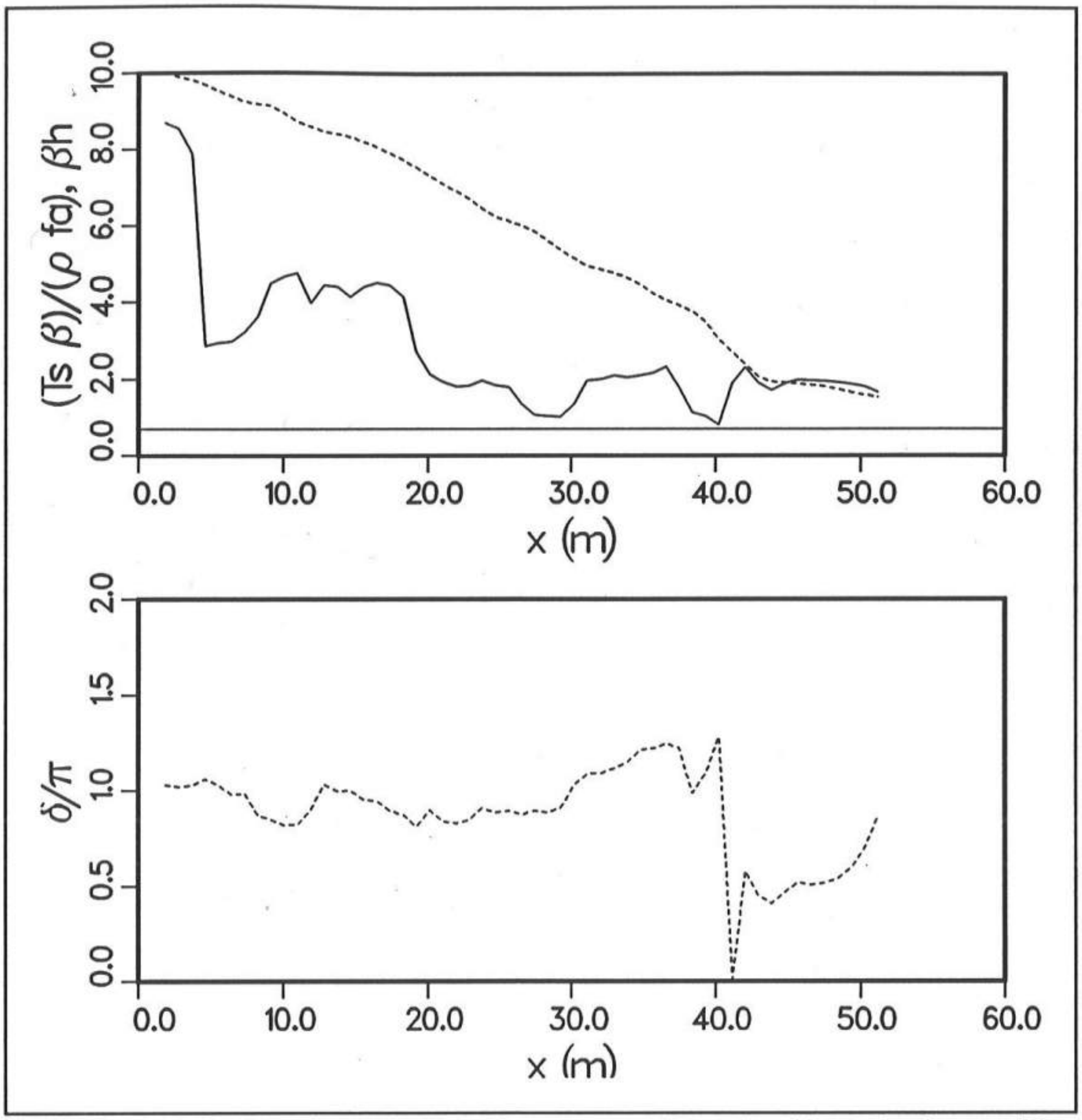

Figure 7.25. Relative strength of surface stress and depth-uniform forcing (solid line), *βh* (dashed line), and relative phase of surface stress and depth-uniform forcing for Run A0509A

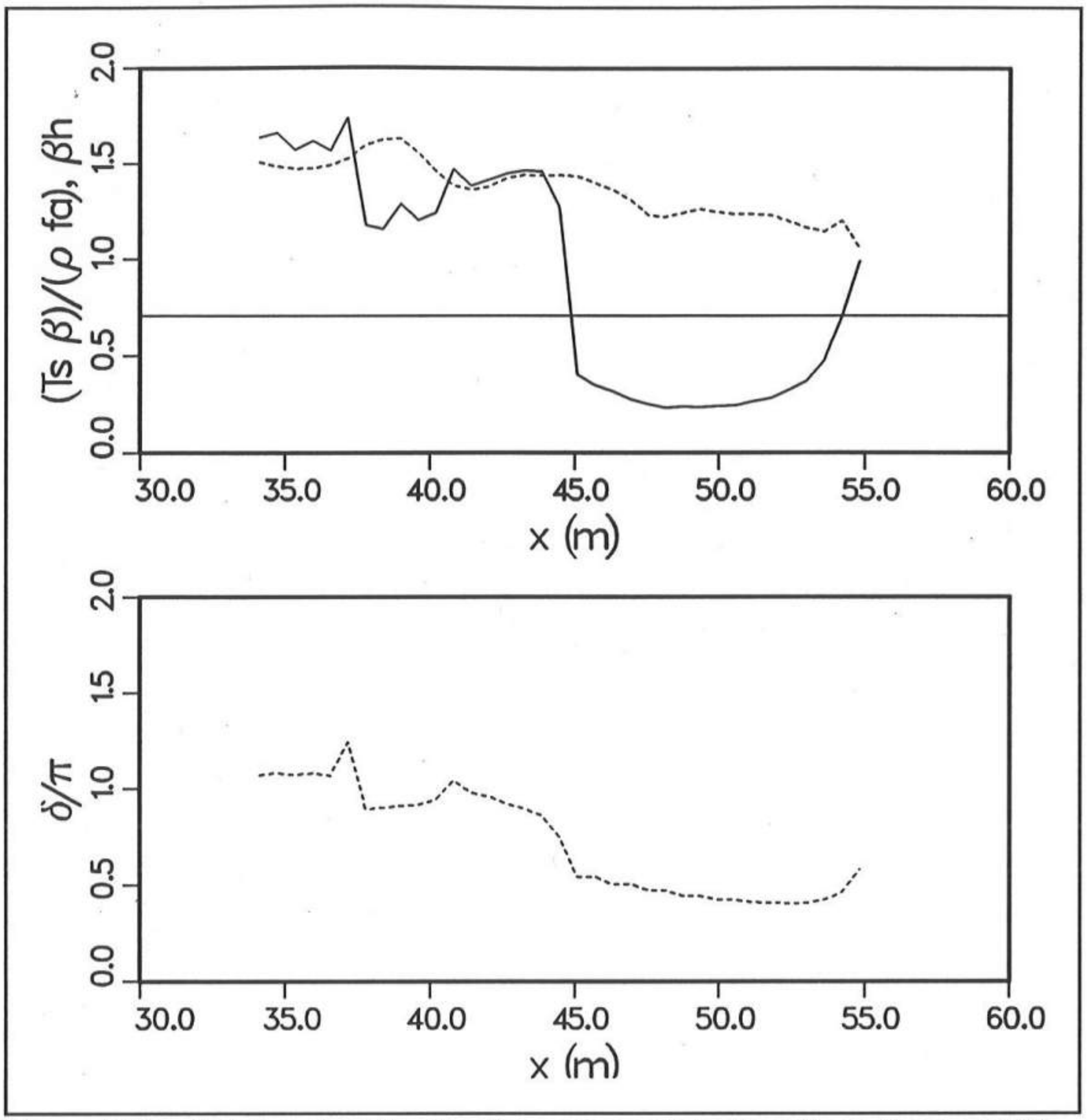

Figure 7.26. Relative strength of surface stress and depth-uniform forcing (solid line), βh (dashed line), and relative phase of surface stress and depth-uniform forcing for Run A2007B

Parameter Δ

The relative phase between the surface stress and depth-uniform forcing is the parameter Δ. This parameter gives the simplest interpretation of the results. Physically, however, this parameter is difficult to predict because the depth-uniform component of the forcing is composed of both the pressure gradient from the long-wave motion and the depth-uniform part of the variation of the radiation stress due to the modulation of the short-wave motion. For the cases of pure surf beat analyzed in Chapter 5, the value of Δ was approximately constant and equal to π outside the surf zone and 0.5-0.8 π inside the surf zone. The trend was dependent on the choice of $\kappa = 0$.

The SUPERTANK measurements show similar trends in Δ. For both Runs A0509A and A2007B, $\Delta \approx \pi$ outside the surf zone (same as for the surf beat model) and in the outer surf zone. Inside the surf zone ($x \geq 40$ m for Run A0509A and the inner surf zone, $x \geq 45$ m, for Run A2007B) Δ decreases to $\pi/2$. Thus, inside the surf zone, the surface stress and depth-uniform forcing are closer to being in phase. The decease in Δ in the surf zone indicates that the upper and lower portions of the velocity profile should also be less out of phase, as seen previously.

Parameter $T_s\, \beta/(\rho\, f_a)$

The last parameter, $T_s\, \beta/(\rho\, f_a)$, is a measure of the ratio of the surface stress (part of the radiation stress due to short-wave modulation) to the depth-uniform forcing (contribution of the pressure gradient due to the infragravity motion and the modulation of the short-wave radiation stress below trough level, which is assumed to be depth uniform). The parameter shows that the forcing outside the surf zone tends to be surface stress dominated ($T_s\,\beta/(\rho\,f_a) > 0.7$), while in the surf zone the forcing is balanced between surface stress and depth-uniform forcing. In Run A2007B (Figure 7.26) the depth-uniform forcing dominates ($T_s\,\beta/(\rho\,f_a) < 0.7$) in the inner surf zone. In the relatively long, flat inner surf zone in Run A2007B the short-wave energy is dissipated (T_s becomes small) and the profile shape is vertical (depth-uniform forcing dominates, see Figure 7.24, $x = 50$ m). Surface stress dominated profiles vary over depth, and depth-uniform dominated profiles are linear and vertical in shape.

The model results for SUPERTANK Runs A0509A and A2007B exhibit the following characteristics. Outside the surf zone, the greatest velocity variation occurred near the surface (large βh and large $T_s\,\beta/(\rho\,f_a)$). Also, velocities near the surface and the bottom were out of phase ($\Delta = \pi$). The profile variation over depth was fairly symmetric about $U = 0$ m/sec because the time-mean forcing was small. Inside the surf zone, the mean undertow profile was the dominant feature due to the dominance of the time-mean forcing. The time-variation of the velocity was fairly constant over depth (small βh and small Δ). Small values of Δ indicate that the surface and depth-uniform forcing are in phase, so the velocities at the surface and through the water column are also in phase. In the inner surf zone or a flat surf zone, the velocity profile was vertical due to the small value of $T_s\,\beta/(\rho\,f_a)$.

Chapter 8

SUMMARY AND CONCLUSIONS

The purpose of this study was to numerically model time- and depth-varying cross-shore currents forced by gravity and infragravity waves in the nearshore. The study included numerical model development, laboratory data collection, and model application and evaluation with the laboratory data.

8.1 Research Results

Both depth-integrated and depth-varying models were developed and linked. The depth-integrated model includes the propagation, generation, and reflection of long waves in a nearshore domain. The output water surface elevations from the depth-integrated model were used to drive a local eigenfunction solution of the velocity over depth. Both models are time dependent.

Using the depth-integrated equations of mass and momentum, two depth-integrated, finite-difference flow models were developed based on the Predictor-Corrector (two-dimensional) and Lax-Wendroff (one-dimensional) methods. The Predictor-Corrector model was a modification of the SHORECIRC model. Model forcing terms included radiation stress, bottom friction, and a specified incoming long wave. The Predictor-Corrector model exhibited spurious water elevation and velocity oscillations in time when it was executed without bottom friction and depth nonlinearity. This problem is similar to spatial oscillations in a Leap-Frog model.

The velocity profile model is an analytical eigenfunction solution for the cross-shore momentum equation, assuming longshore uniformity. Eddy viscosity was assumed constant for a given depth, but varied across shore as a function of local water depth and breaker location. Both the depth-integrated and profile models shared the same radiation stress and bottom friction formulations, to ensure equilibrium between the solutions.

The depth-integrated and profile models were applied to the analytical, depth-integrated surf beat solution of Schäffer and Svendsen (1988) and Schäffer (1990, 1993). The Schäffer-Svendsen solution includes a forced infragravity wave propagating across a plane beach. The infragravity wave is released through breaking and reflects from the shoreline. The Schäffer-Svendsen solution was modified to include both mean and time-varying forcing (original model included only the time-varying component). Three test cases simulated one condition published by Schäffer (1993) and two conditions similar to the SUPERTANK configuration. The Lax-Wendroff depth-integrated model was applied since the analytical surf beat solution was linear and neglected bottom friction. The depth-integrated model results compared well to the analytical solution. Root-mean-square errors in $\overline{\zeta}$ ranged from 0.25 to 1.0% of H_0 (0.002 to 0.01 m) and rms errors in $\overline{U}$ ranged from 0.02 to 0.9% of $\sqrt{g\,h}$ (0.002 to 0.04 m/sec). The greatest errors were typically near antinodes in the solution at the shoreline. The solutions showed antinodes in elevation at the shoreline and near the breaker line.

The profile model was also run with the Schäffer-Svendsen surf beat forcing. The velocity profiles outside the surf zone leaned offshore at the surface and were fairly uniform over the lower two-thirds of the depth. This was due to the shoaling of the short waves and the relatively large water depth. In the mid surf zone, the velocity profiles exhibited a parabolic undertow shape with offshore flow near the bottom and onshore flow near the surface. This shape was due to the gradient in wave height caused by wave breaking. In the very nearshore, the velocity profiles varied uniformly over depth because the depth-uniform forcing (water surface gradients) dominated.

Putrevu and Svendsen (1995) developed an infragravity wave velocity profile model, assuming a constant periodicity in all forcing functions. This condition is satisfied in the Schäffer-Svendsen surf beat model. Using only the time-varying portion of the forcing (neglecting the mean forcing), the eigenfunction profile model results were compared to the Putrevu-Svendsen solution. The profiles were the same, as would be expected.

Putrevu and Svendsen (1995) identify three dimensionless parameters that represent the relative importance of the surface stress forcing, depth-uniform forcing, and the bottom stress. For the surf beat examples, the parameters elucidated the following trends: (a) outside the surf zone, the surface stress term dominated and profiles showed the greatest variation near the surface,

(b) progressing through the surf zone, the depth-uniform forcing became more important and the profile became uniform over depth, and (c) bottom stress was fairly constant through the nearshore and was less important than the surface stress and depth-uniform forcing terms.

Two additional factors introduced by Putrevu and Svendsen, βh and Δ, indicate the depth to which surface stress forcing penetrates and the phase difference between the depth uniform and surface stress terms, respectively. The parameter βh decreases from offshore to nearshore indicating greater penetration of the surface stress forcing near the shoreline. This reinforces the trend toward depth uniform profiles in shallow depths and greater vertical nonuniformity in deeper depths. For the surf beat results, Δ was approximately equal to π. In the inner surf zone, the value of Δ decreased to $0.5 - 0.8\ \pi$. Since in the inner surf zone the short-wave energy is dissipated (surface stress forcing near zero), the change in Δ did not appear to impact the profile shape.

Water surface elevation and cross-shore current data were collected during the large-scale SUPERTANK Laboratory Project to provide measurements to evaluate the depth-integrated and profile models. SUPERTANK was performed in the large wave tank at Oregon State University with a sand beach. A range of near-prototype wave conditions were run, and waves, water levels, currents, and beach profile evolution were measured. SUPERTANK hydrodynamic data were filtered with a cut off of half the peak frequency to separate short- and long-wave components. Details of the analysis and sample data were presented in Chapter 6.

Two SUPERTANK runs were identified to simulate with the models, Runs A0509A and A2007B. The runs differed from each other in peak period (3 versus 5 sec), bathymetry (non-barred versus barred), spectral peakedness ($\gamma = 20$ versus 100), and gauge positions (outside the surf zone and outer surf zone versus outer to mid surf zone).

The depth-integrated Predictor-Corrector model grid was set up so that gauge locations aligned with grid cells. Still-water depths were specified using the pre-run profile surveys. The depth-integrated model was forced with measured incident long-wave time series at the offshore boundary and radiation stress throughout the domain calculated from measured or interpolated short-wave time series. The radiation stress was calculated using linear theory. A constant bottom friction coefficient of $f_{cw} = 0.01$ was applied.

The average rms errors for the depth-integrated model were 1 to 21% of H_{rms} (0.04 m) for $\overline{\zeta}$ and 2 to 6% of $\sqrt{g\,h}$ (0.13 m/sec) for $\overline{U}$. The rms errors in surface elevation increased in shallow depths. This increase in shallow water was due to the linear calculation of radiation stress (due to increased wave linearity) and an increase in mean gauge errors at shallow depths (due to sand bed changes). Up to 22 percent of the rms error in $\overline{U}$ is due to mean errors. The measured depth-averaged velocities are weighted toward the lower water column and thus tended to show a net offshore flow, instead of the net zero flow expected for a closed system.

The profile model was executed with 10 eigenfunctions for 21 locations over depth. The water elevations and radiation stress were supplied by the depth-integrated model. The same bottom friction coefficient was used as used in the depth-integrated model. The rms error in the calculated velocities was 4% of $\sqrt{gh}$ (0.14 m/sec) for Run A0509A (most gauges outside the surf zone) and 8% of $\sqrt{gh}$ (0.20 m/sec) for Run A2007B (most gauges inside the surf zone). Errors increased in and near the surf zone for both runs. Mean errors again accounted for as much as 20 percent of the rms error. Velocity errors were larger for the profile model than the depth-integrated model. Mean velocities are generally not represented well by the model. Errors were uncorrelated with elevation in the water column. The profile model results were quite good during times when the depth-integrated results were good

The overall trends in the profiles were similar to those seen in the surf beat simulations. The profile model results for SUPERTANK exhibited the following characteristics:

a) outside the surf zone

- the greatest velocity variation occurs near the surface (large βh and surface stress dominating)
- velocities near the surface and the bottom are out of phase ($\Delta = \pi$)
- profile variation over depth is fairly symmetric about $U =$ 0 m/sec (small mean forcing)

b) inside the surf zone

- mean undertow profile is the dominant feature (mean forcing is dominating)
- the time variation of the velocity is fairly constant over depth (small βh and small Δ)
- in the inner surf zone or a flat surf zone, the velocity profile is uniform over depth (small surface stress forcing)

8.2 Future Work

The greatest limitation of the present study was the specification of radiation stress using linear theory and coarsely spaced water surface measurements. Svendsen (1984a) and Svendsen and Putrevu (1993) show the limitations of linear theory in the surf zone, but the ease of application for a broad range of conditions has kept linear theory as the tool of choice. The coarsely spaced wave gauges at SUPERTANK did not capture the breaker position for model application. Future experiments need closely spaced gauges in the surf zone to catch the important transition processes in the breaker zone. A model of the time-varying nearshore wave transformation and breaking would also fill this void. Until such a model is available, use of the depth-integrated and profile model will be limited to cases with dense wave measurements or use of ad-hoc assumptions about the relationships between short waves and infragravity waves (e.g., Symonds et al. 1982, Schäffer and Svendsen 1988).

Another improvement to the depth-integrated model would be to formulate a wetting and drying boundary condition at the shoreline to replace the present fixed shoreline location. Prediction of swash processes is useful, but not necessarily important to study velocity profiles away from the shoreline.

The models developed in this study focused on cross-shore processes. The next step would be to generalize the solution to include both the longshore and cross-shore. The complications in doing this include more complicated boundary conditions, refraction processes, and solution methods. Application of such a quasi-three-dimensional model could be used to represent cell circulation and rip current generation, which are still poorly understood. Edge-wave and shear-wave forcing could also be applied.

For coastal engineers, calculation of hydrodynamic processes is usually an intermediate step in the calculation of sediment transport and bathymetry change. The depth-integrated and profile models are useful tools for studying cross-shore transport of suspended sediment. Together with the sediment concentration and beach profile data from SUPERTANK, the models could be applied to study sediment transport rates and quantities under controlled conditions.

REFERENCES

Battjes, J. A., R. J. Sobey, and M. J. F. Stive, 1990. Nearshore circulation. *The Sea*, B. Le Mehaute and D. M. Hanes, ed., John Wiley & Sons, New York, 467-493.

Birkemeier, W. A., and R. A. Dalrymple, 1975. Nearshore water circulation induced by wind and waves. *Proceedings, Modeling'75*, ASCE, 1062-1081.

Bouws, E., H. Gunther, W. Rosenthal, and C.L. Vincent, 1985. Similarity of the wind wave spectrum in finite depth water; 1. spectral form. *Journal of Geophysical Research*, 90(C1), 975-986.

Bowen, A. J., 1969. The generation of longshore currents on a plane beach. *Journal of Marine Research*, 73(8), 2569-2577.

Cialone, M. A., D. J. Mark, L. W. Chou, D. A. Leenknecht, J. E. Davis, L. S. Lillycrop, R. E. Jensen, E. F. Thompson, M. B. Gravens, J. D. Rosati, R. A. Wise, N. C. Kraus, P. M. Larson, and J. M. Smith, 1994. Coastal Modeling System (CMS) User's Manual. Technical Report CERC-91-1, U.S. Army Engineer Waterways Experiment Station, Vicksburg, MS, 201 pp.

Dally, W. R., and R. G. Dean, 1984. Suspended sediment transport and beach profile evolution. *Journal of Waterway, Port, Coastal, and Ocean Engineering*, 110(1), 15-33.

Dally, W. R., R. G. Dean, and R. A. Dalrymple, 1985. Wave height variation across beaches of arbitrary profile. *Journal of Geophysical Research*, 90(C6), 11,917-11,927.

Davies, A. M., 1980. Application of the Galerkin method to the formulation of a three-dimensional nonlinear hydrodynamic numerical sea model. *Applied Mathematical Modelling*, 4, 245-256.

__________, 1987. On extracting current profiles from vertically integrated numerical models. *Coastal Engineering*, 11, 445-477.

de Vriend, H. J., and M. J. F. Stive, 1987. Quasi-3D modelling of nearshore currents. *Coastal Engineering*, 11, 565-601.

de Vriend, H. J., J. Zyserman, J. Nicholson, J. A. Roelvink, P. Pechon, and H. N. Southgate, 1993. Medium-term 2DH coastal area modelling. *Coastal Engineering*, 21, 193-224.

Dibble, T. L., and C. K. Sollitt, 1989. New designs for acoustic and resistive wave profiles. *Proceedings, Workshop on Instrumentation for Hydraulic Laboratories*, IAHR.

Dyhr-Nielsen, M., and T. Sorensen, 1970. Some sand transport phenomena on coasts with bars. *Proceedings, 12th Coastal Engineering Conference*, ASCE, 1993-2004.

Ebersole, B. A., and R. A. Dalrymple, 1979. A numerical model for nearshore circulation including convective accelerations and lateral mixing. Ocean Engineering Report No. 21, University of Delaware, Newark, DE, 87 pp.

Elgar, S., T. H. C. Herbers, M. Okihiro, J. Oltman-Shay, and R. T. Guza, 1992. Observations of infragravity waves. *Journal of Geophysical Research*, 97, 15,573-15,577.

Gallagher, B., 1971. Generation of surf beat by non-linear wave interaction. *Journal of Geophysical Research*, 49, Part 1, 1-20.

Greenberg, M. D., 1988. *Advanced Engineering Mathematics*, Prentice-Hall, Inc., 946 pp.

Guza, R. T., and E. B. Thornton, 1982. Swash oscillations on a natural beach. *Journal of Geophysical Research*, 87(C1), 483-491.

Hansen, J. B., and I. A. Svendsen, 1984. A theoretical and experimental study of undertow. *Proceedings, 19th Coastal Engineering Conference*, ASCE, 2246-2262.

Herbers, T. H. C., S. Elgar, R. T. Guza, and W. C. O'Riley, 1992. Infragravity frequency motions on the shelf. *Proceedings, 23rd Coastal Engineering Conference*, ASCE, 846-859.

Holman, R. A., 1986. Extreme value statistics for wave run-up on a natural beach. *Coastal Engineering*, 9(6), 527-544.

Holman, R. A., and A. H. Sallenger, 1985. Setup and swash on a natural beach. *Journal of Geophysical Research*, 90(C1), 945-953.

Houston, J. R., 1995a. Beach nourishment. *Shore and Beach*, January 1995, 21-24.

__________, 1995b. The economic value of beaches. *The CERCular*, CERC-95-4, U.S. Army Engineer Waterways Experiment Station, Vicksburg, MS, 1-4.

Hughes, S. A., 1993. Laboratory wave reflection analysis using co-located gages. *Coastal Engineering*, 20, 223-247.

Huntley, D. A., R. T. Guza, and E. B. Thornton, 1981. Field observations of surf beat; 1. Progressive edge waves. *Journal of Geophysical Research*, 86(C7), 6451-6466.

Jonsson, I. G., 1966. Wave boundary layers and friction factors. *Proceedings, 10th Coastal Engineering Conference*, ASCE, 127-148.

Keely, J. R., and A. J. Bowen, 1977. Longshore variation in longshore currents. *Canadian Journal of Earth Science*, 14(8), 1897-1905.

Kobayashi, N., A. K. Otta, and I. Roy, 1987. Wave reflection and run-up on rough slopes. *Journal of Waterway, Port, Coastal, and Ocean Engineering*, 113(3), 282-298.

Kraus, N. C., and J. M. Smith, 1994. SUPERTANK laboratory data collection project, volume I: main text. Technical Report CERC-94-3, U.S. Army Engineer Waterways Experiment Station, Vicksburg, MS, 285 pp.

Kraus, N. C., J. M. Smith, and C. K. Sollitt, 1992. SUPERTANK laboratory data collection project. *Proceedings, 23rd Coastal Engineering Conference*, ASCE, 2191-2204.

Kriebel, D. L., and J. M. Smith, 1994. Wave transformation measurements at SUPERTANK. *Proceedings, Coastal Dynamics'94*, 233-247.

Larson, M., and N. C. Kraus, 1991. Numerical model of longshore current over bar and trough beaches. *Journal of Waterway, Port, Coastal, and Ocean Engineering*, 117(4), 326-247.

Longuet-Higgins, M. S., 1953. Mass transport in water waves. *Philosophical Transactions of the Royal Society*, 345, 535-581.

__________, 1970a. Longshore currents generated by obliquely incident sea waves, 1. *Journal of Geophysical Research*, 75(33), 6778-6789.

__________, 1970b. Longshore currents generated by obliquely incident sea waves, 2. *Journal of Geophysical Research*, 75(33), 6790-6801.

Longuet-Higgins, M. S., and R. W. Stewart, 1962. Radiation stress and mass transport in gravity waves. *Journal of Fluid Mechanics*, 13, 481-504.

__________, 1963. A note on wave set-up. *Journal of Marine Research*, 21, 4-10.

__________, 1964. Radiation stresses in water waves; a physical discussion, with applications. *Deep Sea Research*, 11, 529-562.

Mase, H., 1988. Spectral characteristics of random wave runup. *Coastal Engineering*, 115(5), 649-661.

Mei, C. C., 1989. *The Applied Dynamics of Ocean Surface Waves*, World Scientific Publishing, Singapore, 740 pp.

Noda, E. K., 1974. Wave-induced nearshore circulation. *Journal of Geophysical Research*, 79(27), 4097-4106.

Oltman-Shay, J., and K. K. Hathaway, 1989. Infragravity energy and its implications is nearshore sediment transport and sandbar dynamics. Technical Report CERC-89-8, U.S. Army Engineer Waterways Experiment Station, Vicksburg, MS, 34 pp.

Press, W. H., B. P. Flannery, S. A. Teukolsky, and W. T. Vetterling, 1989. *Numerical Recipes*, Cambridge University Press, Cambridge, England, 702 pp.

Putrevu, U., and I. A. Svendsen, 1993. Vertical structure of undertow outside the surf zone. *Journal of Geophysical Research*, 98(C12), 22,707-22,716.

__________, 1995. Infragravity velocity profiles in the surf zone. *Journal of Geophysical Research*, 100(C8), 16,131-16,142.

Roache, P. J., 1982. *Computational Fluid Dynamics*, Hermosa Publishers, Albuquerque, New Mexico, 446 pp.

Sanchez-Arcilla, A., F. Collado, and A. Rodriguez, 1992. Vertically varying velocity field in q-3d nearshore circulation. *Proceedings, 23rd Coastal Engineering Conference*, ASCE, 2811-2824.

Schäffer, H. A., 1990. Infragravity waves induced by short-wave groups. Series Paper 50, Institute of Hydrodynamics and Hydraulic Engineering, Technical University of Denmark, 168 pp.

__________, 1993. Infragravity water waves induced by short-wave groups. *Journal of Fluid Mechanics*, 247, 551-588.

Schäffer, H. A., and I. A. Svendsen, 1988. Surf beat generation on a mild-slope beach. *Proceedings, 21st Coastal Engineering Conference*, ASCE, 1058-1072.

Senate Coastal Coalition, 1995. Letter to President Clinton, December 22, 1995.

Smith, J. M., and N. C. Kraus, 1995. SUPERTANK laboratory data collection project, volume II: appendices A-I, Technical Report CERC-94-3, U.S. Army Engineer Waterways Experiment Station, Vicksburg, MS, 241 pp.

Smith, J. M., I. A. Svendsen, and U. Putrevu, 1992. Vertical structure of the nearshore current at DELILAH: measured and modeled. *Proceedings, 23rd Coastal Engineering Conference*, ASCE, 2825-2838.

Stive, M. J. F., and H. G. Wind, 1982. A study of radiation stress and set-up in the nearshore region. *Coastal Engineering*, 6(1), 1-26.

__________, 1986. Cross-shore mean flow in the surf zone. *Coastal Engineering*, 10(4), 325-340.

Svendsen, I. A., 1984a. Wave heights and set-up in a surf zone. *Coastal Engineering*, 8(4), 303-329.

__________, 1984b. Mass flux and undertow in a surf zone. *Coastal Engineering*, 8(4), 347-365.

Svendsen, I. A., and R. S. Lorenz, 1989. Velocities in combined undertow and longshore currents. *Coastal Engineering*, 13, 55-79.

Svendsen, I. A., and U. Putrevu, 1990. Nearshore circulation with 3-d profiles. *Proceedings, 22nd Coastal Engineering Conference*, ASCE, 241-254.

__________, 1993. Surf zone wave parameters from experimental data. *Coastal Engineering*, 19, 283-310.

__________, 1994. Nearshore mixing and dispersion. *Proceeding of the Royal Society of London, Series A*, 445, 561-576.

__________, 1996. Surf zone hydrodynamics. Review paper to appear in *Advances in Coastal and Ocean Engineering*, World Scientific Publishing, Singapore, 76 pp.

Svendsen, I. A., H. A. Schaffer, and J. B. Hansen, 1987. The interaction between the undertow and the boundary layer flow on a beach. *Journal of Geophysical Research*, 92(C11), 11,845-11,856.

Symonds, G., D. A. Huntley, and A. J. Bowen, 1982. Two-dimensional surf beat: long wave generation by a time-varying break point. *Journal of Geophysical Research*, 87(C1), 492-498.

Thornton, E. B., 1970. Variation of longshore current across the surf zone. *Proceedings, 12th Coastal Engineering Conference*, ASCE, 291-308.

Thornton, E. B., and R. T. Guza, 1981. Longshore Currents and bed shear stress. *Proceedings, Directional Wave Spectra Applications*, ASCE, 147-164.

__________, 1986. Surf zone longshore currents and random waves: field data and models. *Journal of Physical Oceanography*, 16, 1165-1178.

Van Dongeren, A. R., F. E. Sancho, I. A. Svendsen, and U. Putrevu, 1994. SHORECIRC: a quasi 3-d nearshore model. *Proceedings, 24th Coastal Engineering Conference*, ASCE, 2741-2754.

Vemulakonda, S. R., 1984. Erosion control of scour during construction, report 7, CURRENT - a wave-induced current model. Technical Report HL-80-3, U.S. Army Engineer Waterways Experiment Station, Vicksburg, MS, 101 pp.

Wind, H. G., and C. B. Vreugdenhill, 1986. Rip current generation near structures. *Journal of Fluid Mechanics*, 171, 459-476.

Wright, L. D., R. T. Guza, and A. D. Short, 1982. Surf zone dynamics on a high energy dissipative beach. *Marine Geology*, 45, 41-62.